

## Main Group Secondary Bonding

EXPERIMENTAL AND COMPUTATIONAL STUDIES ON THE EFFECT OF  
SECONDARY BONDING INTERACTIONS ON THE SPECTROSCOPIC  
PROPERTIES AND REACTIVITY OF ORGANO-CHALCOGEN COMPOUNDS

BY

PHILIP J. W. ELDER, B.SC.

A THESIS

SUBMITTED TO THE SCHOOL OF GRADUATE STUDIES

IN PARTIAL FULFILLMENT OF THE REQUIREMENTS

FOR THE DEGREE

DOCTORATE OF PHILOSOPHY

MCMASTER UNIVERSITY

© COPYRIGHT BY PHILIP J. W. ELDER, NOVEMBER 2011

Ph.D (2011)  
(Chemistry)

McMaster University  
Hamilton, ON

TITLE:      Experimental and Computational Studies on the Effect of Secondary Bonding Interactions on the Spectroscopic Properties and Reactivity of Organo-Chalcogen Compounds.

AUTHOR:    Philip J. W. Elder

SUPERVISOR: Professor Ignacio Vargas-Baca

NUMBER OF PAGES: xxxii, 202

**ABSTRACT**

This thesis presents the results of investigations on the application of modern spectroscopic techniques to the characterisation of secondary bonding interactions (SBIs) in selected organo-chalcogen compounds. Although the research was mostly focused on two families of compounds, ditellurides and chalcogen-substituted azodyes, the observations and conclusions are applicable to a wide variety of compounds. Because the effects of the SBIs are subtle, great care was taken to carefully distinguish contributions from other factors. DFT computational studies showed that the molecular conformation influences the electronic excitations observable in the UV-vis spectrum and the frequency of resonance in  $^{125}\text{Te}$  NMR of organoditellurides. In the absence of protection to shield the chalcogen from intermolecular interactions, the  $^{125}\text{Te}$  NMR chemical shift is dependent on the concentration of ditellurides; intramolecular SBIs attenuate the concentration dependency and steric protection cancels it entirely. The nature of the solvent impacts the results of both spectroscopic techniques through several mechanisms, including the solvatochromic effect, conformational changes due to the polarity of the medium and solvation. Solution  $^{125}\text{Te}$  NMR spectroscopy is sensitive to all those contributions but, for the same reason, it cannot be applied in an unambiguous way to identify the presence of SBIs.

Conversely, the use of intramolecular SBIs to modify the spectroscopic properties of a conjugated chromophore was investigated. Push-pull azobenzenes were derivatised with functional groups containing divalent chalcogen atoms through metathesis with a mercurated derivative of the azodye. The regiochemistry of formation of the intermediate

was shown to be under kinetic control. In the chalcogen-substituted molecules, the efficiency of electron delocalisation through the SBIs was assessed by calculations of the nucleus independent chemical shift (NICS). The linear (UV-vis absorption) and nonlinear (second harmonic-generation) optical responses of the modified chromophore were investigated and interpreted in the context of the SBIs. Substitution with the chalcogen groups, and the consequent perturbation of the  $\pi$ -system, cause a blue shift in the first absorption maxima but little change was observed in the hyperpolarisability of the chromophore ortho-functionalised with the phenylselenenyl group. The sensitivity of the electronic spectrum to the SBI was applied to monitor the process of halide exchange in the halo-chalcogenyl derivatives of the push-pull azobenzene.

Very strong SBIs can result in interatomic distances so short that they are difficult to distinguish from hypervalent covalent bonds. This is the situation observed in the structure of the first 2,5,8,11,1,4,7,10,3,6,9,12-tetraoxatetratelluratetrazacyclododecane. DFT calculations showed that this unusual macrocycle is stable with respect to dissociation into isotellurazole oxide and VT NOESY experiments indicate it remains intact in solution.

## ACKNOWLEDGEMENTS

I would like to thank my supervisor, Dr. Ignacio Vargas-Baca, for his helpful guidance and enthusiasm during my time as a summer researcher, my undergraduate senior thesis, and throughout this entire Ph. D. thesis project.

My gratitude is extended toward my supervisory committee members, Dr. G. Schrobilgen and Dr. D. Emslie, for their helpful suggestions, guidance, and technical expertise over the course of my studies at McMaster University.

I thank both former and present lab group members for laying some of the groundwork for these experiments, and for making the lab environment an enjoyable and inspirational place to work.

I would like to acknowledge the optical spectroscopy, NMR, mass spectrometry and X-ray diffraction facilities as well as the helpful contributions from their staff.

In gratitude, I acknowledge the staff and facilities of the Shared Hierarchical Academic Research Computing Network (SHARCNET:[www.sharcnet.ca](http://www.sharcnet.ca)).

I would like to recognize my funding sources: Natural Science and Engineering Research Council of Canada (NSERC), McMaster University, the Canada Foundation for Innovation (CFI) and the Ontario Innovation Trust (OIT).

I express my heart-felt gratitude to my family, without whom none of this would have been possible. The constant love, concern, support and strength they have provided me all these years cannot be understated.

## TABLE OF CONTENTS

ABSTRACT.....	iii
ACKNOWLEDGEMENTS .....	v
TABLE OF CONTENTS .....	vi
LIST OF FIGURES .....	xii
LIST OF SCHEMES .....	xviii
LIST OF TABLES .....	xix
LIST OF COMPOUNDS.....	xxii
LIST OF ABBREVIATIONS AND SYMBOLS .....	xxx
<b>1 Introduction.....</b>	<b>1</b>
<b>1.1 Supramolecular Chemistry .....</b>	<b>1</b>
<b>1.1.1 Closed-Shell Interactions .....</b>	<b>1</b>
<b>1.1.2 Secondary Bonding Interactions .....</b>	<b>2</b>
<b>1.1.3 Supramolecular Synthons .....</b>	<b>5</b>
<b>1.2 The [Te-m-D]<sub>2</sub> Supramolecular Synthons and 1,2,5-Chalcogenadiazoles.....</b>	<b>7</b>
<b>1.3 The [Te-m-D] Supramolecular Synthons and "Intramolecular Coordination" .....</b>	<b>9</b>
<b>1.4 Purpose, Scope and Overview of the Thesis .....</b>	<b>12</b>
<b>2 Experimental .....</b>	<b>14</b>

<b>2.1</b>	<b>Instrumental Methods .....</b>	<b>14</b>
2.1.1	Dispersive Raman Spectroscopy .....	14
2.1.2	Fourier Transform Infrared Spectroscopy .....	14
2.1.3	Ultraviolet-Visible Spectroscopy .....	15
2.1.4	Electron Ionization Mass Spectrometry .....	16
2.1.5	Chemical Ionization Mass Spectrometry .....	17
2.1.6	Melting Points.....	17
2.1.7	Single Crystal X-ray Diffraction.....	18
2.1.8	Nuclear Magnetic Resonance Spectroscopy .....	19
2.1.9	Second Harmonic Generation.....	21
2.1.10	High-Performance Liquid Chromatography .....	24
<b>2.2</b>	<b>Materials and Methods.....</b>	<b>25</b>
2.2.1	Syntheses .....	26
2.2.1.1	Ditellurides.....	26
2.2.1.2	Azodyes .....	29
2.2.1.3	3,9,15,21-tetrakis(1,1-dimethylethyl)-1,7,13,19-tetramethyl- 1,4,7,10,2,5,8,11,3,6,9,12-tetraoxatetratelluratetraazacyclododecane .....	38
<b>2.3</b>	<b>Computational Details .....</b>	<b>40</b>
<b>3</b>	<b>A Detailed Study of the <sup>125</sup>Te NMR Shielding of Organo-Ditellurides in Solution.....</b>	<b>42</b>
3.1	Motivation.....	42

<b>3.2</b>	<b>Objective and Method .....</b>	<b>44</b>
<b>3.3</b>	<b>NMR Shielding.....</b>	<b>45</b>
<b>3.4</b>	<b>Results and Discussion.....</b>	<b>49</b>
<b>3.4.1</b>	<b>Choice of Model Compounds.....</b>	<b>49</b>
<b>3.4.2</b>	<b>Synthesis of Ditellurides .....</b>	<b>52</b>
<b>3.4.3</b>	<b>Conformational Effects Assessed by Computational Modeling .....</b>	<b>53</b>
<b>3.4.3.1</b>	<b>Structural Benchmarking and Basis Set Selection .....</b>	<b>53</b>
<b>3.4.3.2</b>	<b>Electronic Excitations.....</b>	<b>58</b>
<b>3.4.3.3</b>	<b><sup>125</sup>Te NMR Chemical Shift .....</b>	<b>62</b>
<b>3.4.3.4</b>	<b>Molecular Conformation, Electronic Excitations and NMR Shielding.....</b>	<b>64</b>
<b>3.4.4</b>	<b>Environmental Effects through Computational and Experimental Studies .....</b>	<b>66</b>
<b>3.4.4.1</b>	<b>Dielectric Properties .....</b>	<b>66</b>
<b>3.4.4.2</b>	<b>Explicit Solvation Models.....</b>	<b>73</b>
<b>3.4.4.3</b>	<b>Summary of solvent effects .....</b>	<b>78</b>
<b>3.4.5</b>	<b>Dynamic Effects .....</b>	<b>79</b>
<b>3.4.5.1</b>	<b>Auto-association Models.....</b>	<b>79</b>
<b>3.4.5.2</b>	<b>Concentration and Temperature Dependence .....</b>	<b>81</b>
<b>3.5</b>	<b>Summary and Conclusions .....</b>	<b>96</b>

<b>4</b>	<b>Investigations of the Reactivity, Electronic Structure and Optical Properties of Dipolar Azobenzenes that Feature Intramolecular E··N SBIs (E = S, Se, Te) .....</b>	<b>99</b>
4.1	Introduction.....	99
4.1.1	Proposed System of Study and Objectives.....	101
4.1.2	Proposed Methods and Scope of this Chapter .....	103
4.2	Mercuration of a Push-Pull Azobenzene .....	105
4.2.1	Results and Discussion.....	108
4.2.1.1	Synthesis.....	108
4.2.1.2	Molecular Structure of 2,2'-Diiodo Azobenzene (28) .....	108
4.2.1.3	Mercuration of Dipolar Azodyes .....	109
4.2.1.4	Structures of the Isolated Compounds.....	111
4.2.1.5	Molecular Structure of 30 .....	112
4.2.1.6	Temporal Distribution of Products .....	115
4.2.1.7	Computational modeling .....	117
4.2.2	Summary of the Mercuration Studies.....	122
4.3	Spectrophotometric Study of the 2-Halochalcogenyl-Substituted Azobenzenes and their Halide Exchange Reaction.....	122
4.3.1	Experimental Design.....	123
4.3.2	Results and Discussion.....	124
4.3.2.1	Preparation of 2-Halochalcogenyl-Azobenzenes.....	124
4.3.2.2	Exchange Reactions .....	125

<b>4.4</b>	<b>Second Harmonic Generation from 2-Arylchalcogenyl Azobenzenes .....</b>	<b>127</b>
4.4.1	Molecular Origin of Nonlinear Optical Properties.....	127
4.4.2	Results and Discussion.....	134
4.4.2.1	Syntheses.....	134
4.4.2.2	Hyperpolarisability determination.....	135
<b>4.5</b>	<b>Computational Studies of Chalcogenyl-Substituted Azobenzenes .....</b>	<b>136</b>
4.5.1	Molecular Structures .....	136
4.5.2	Electronic Structure.....	140
4.5.3	Electron Delocalization Through the SBIs .....	143
4.5.4	Analysis of the Excitation Spectra.....	149
4.5.5	Calculated SHG Hyperpolarisabilities .....	152
<b>4.6</b>	<b>Summary and Conclusions .....</b>	<b>152</b>
<b>5</b>	<b>Synthetic, Structural and Computational Investigations of a Macrocycle Featuring -O-Te-N- Catenation.....</b>	<b>155</b>
5.1	Introduction.....	155
5.2	Results and Discussion.....	157
5.2.1	Synthesis and Isolation .....	157
5.2.2	Structure .....	159
5.2.3	Modeling the Assembly from the Isotellurazole Oxide .....	163
5.2.4	Stability .....	166
5.2.5	Bonding .....	167

<b>5.3</b>	<b>Summary.....</b>	<b>169</b>
<b>6</b>	<b>Conclusions and Suggestions for Future Work .....</b>	<b>170</b>
<b>6.1</b>	<b>Conclusions.....</b>	<b>170</b>
<b>6.2</b>	<b>Suggestions of Future Work .....</b>	<b>172</b>
<b>6.2.1</b>	<b><sup>125</sup>Te NMR Spectroscopy of Ditellurides.....</b>	<b>172</b>
<b>6.2.2</b>	<b>UV-vis Studies of Chalcogen-Substituted Azodyes.....</b>	<b>173</b>
<b>6.2.3</b>	<b>Nonlinear Optical Properties .....</b>	<b>174</b>
<b>6.2.4</b>	<b>Delocalization of Electron Density by SBI formation.....</b>	<b>175</b>
<b>6.2.5</b>	<b>Stability of the (-Te-O-N)<sub>4</sub> Macrocycle.....</b>	<b>176</b>
<b>6.2.6</b>	<b>Coordination Complexes of the (-Te-O-N)<sub>4</sub> Macrocycle.....</b>	<b>176</b>
	<b>Appendix.....</b>	<b>178</b>
	<b>References.....</b>	<b>179</b>

**LIST OF FIGURES**

<b>Figure 1.1</b> Mixing of molecular orbitals in an E <sup>π</sup> D secondary bonding interaction. For simplicity, only p atomic orbitals are considered. Reproduced with permission from reference 23.....	4
<b>Figure 1.2</b> Idealized VSEPR geometries for tellurium in the a) II and b) IV oxidation states. The arrows denote the positions preferred for the formation of secondary bonding interactions. Reproduced with permission from reference 23. ....	7
<b>Figure 2.1</b> Schematic of the Hyper-Rayleigh scattering SHG experiment. ....	23
<b>Figure 3.1</b> Comparison of calculated and experimental <sup>125</sup> Te NMR chemical shifts for selected organotellurium compounds. Reproduced with permission from reference 136.....	49
<b>Figure 3.2</b> The effect of the dihedral angle on I) the relative energy, and II) the dipole moment of <b>17</b> ( --- Trajectory A, — Trajectory B). The shaded area highlights the dihedral angles of 90% of crystallographically characterized ditellurides. ....	57
<b>Figure 3.3</b> Two distinct optimized geometries of <b>17</b> obtained at the C-Te-Te-C torsion angle of 90° for trajectories A and B. ....	58
<b>Figure 3.4</b> Kohn-Sham frontier molecular orbitals of <b>14</b> . Isosurfaces plotted at 0.05 au. ....	59
<b>Figure 3.5</b> Effect of the dihedral angle on the energy of the first electronic excitation of <b>17</b> . ( --- Trajectory A, — Trajectory B) The shaded area highlights the dihedral angles of 90% of crystallographically characterized ditellurides. ....	60

**Figure 3.6** Walsh diagram illustrating the effect of the C-Te-Te-C dihedral angle on the frontier orbitals of **17**. Orbitals are labelled according to  $C_2$  molecular symmetry (--- dihedral angle for energetic minimum).....61

**Figure 3.7** The relative contributions of the components of the shielding constant for each calculated geometry of trajectory B (— — — occupied-occupied ( $s^{(1)}$ ), — occupied-virtual ( $u^{(1)}$ ), ••• virtual-virtual ( $b^{(1)}$ ), --- gauge tensor ( $g$ )).....63

**Figure 3.8** The effect of the dihedral angle on the  $^{125}\text{Te}$  chemical shift of **17**. ( --- Trajectory A, — Trajectory B) The shaded area represents the dihedral angles of 90% of crystallographically characterized ditellurides.....64

**Figure 3.9** Correlation between the magnitude of the calculated paramagnetic shielding and the calculated transition energy of **17** as a result of changes in the molecular geometry (Trajectory B). .....65

**Figure 3.10** Experimentally determined energy of excitation of **14** (0.137 M, 303.0 K) as a function of solvent dielectric constant. ....69

**Figure 3.11** Calculated excitation energy of **17** as a function of solvent dielectric constant. ....69

**Figure 3.12** Comparison of calculated and experimental excitation energies for the first transition of **17** and **14** in a number of solvents.....70

**Figure 3.13** Experimentally determined  $^{125}\text{Te}$  chemical shift of **14** (0.137 M, 303.0 K) as a function of solvent dielectric constant. ....72

**Figure 3.14** Experimental  $^{125}\text{Te}$  chemical shift as a function of excitation energy for **14** in different solvents.....73

- Figure 3.15** Effect of the concentration on the  $^{125}\text{Te}$  NMR chemical shift of **14** in solution at 303.0 K. ( $\blacktriangle$  =  $\text{CCl}_4$ ,  $\circ$  = Hexanes,  $\blacksquare$  = Pyridine,  $\blacklozenge$  = DMSO). The error in the measured chemical shift ( $\leq 0.005$  ppm) is too small to be noticeable in this plot. ....83
- Figure 3.16** Effect of concentration and temperature on the  $^{125}\text{Te}$  NMR chemical shift of **14** in I) hexanes, II) toluene, and III) dichloromethane. The errors in the measured chemical shift ( $\leq 0.005$  ppm) and temperature ( $\leq 0.045$  K) are too small to be noticeable in this plot. ....85
- Figure 3.17** Effect of the temperature on the  $^{125}\text{Te}$  NMR chemical shift of **19**. The errors in the measured chemical shift ( $\leq 0.005$  ppm) and temperature ( $\leq 0.045$  K) are too small to be noticeable in this plot. ....88
- Figure 3.18** Effect of concentration and temperature on the  $^{125}\text{Te}$  NMR chemical shift of **13** in water. The errors in the measured chemical shift ( $\leq 0.005$  ppm) and temperature ( $\leq 0.045$  K) are too small to be noticeable in this plot. ....89
- Figure 3.19** Effect of concentration and temperature on the  $^{125}\text{Te}$  NMR chemical shift of **15** in I) hexanes, and II) toluene. The errors in the measured chemical shift ( $\leq 0.005$  ppm) and temperature ( $\leq 0.045$  K) are too small to be noticeable in this plot. ....91
- Figure 3.20** Effect of concentration and temperature on the  $^{125}\text{Te}$  NMR chemical shift of **16** in dichloromethane. The errors in the measured chemical shift ( $\leq 0.005$  ppm) and temperature ( $\leq 0.045$  K) are too small to be noticeable in this plot. ....93

<b>Figure 3.21</b> Effect of temperature on the $^{125}\text{Te}$ NMR chemical shift of <b>13-16</b> , and <b>19</b> . The chemical shift values have been divided by the number of atoms in the molecule. The errors in the measured temperature ( $\leq 0.045$ K) are too small to be noticeable in this plot. ....	96
<b>Figure 4.1</b> ORTEP of 2,2'-diiodo azobenzene, <b>28</b> (50% displacement ellipsoids). ....	109
<b>Figure 4.2</b> ORTEP of 4-nitro, 2-iodo, 4-dimethylamino azobenzene, <b>30</b> (50% displacement ellipsoids). For clarity, all hydrogen atoms are displayed as spheres of $\text{\AA} = 0.15$ . ....	113
<b>Figure 4.3</b> Amounts of the reactant and products of mercuration as a function of reaction time (— <b>27</b> , ••• <b>33</b> , --- <b>34</b> ). Spline lines highlight the trends but were not obtained by fitting. ....	117
<b>Figure 4.4</b> Differences of total bonding energies of the possible products of metallation of azobenzene, <b>24</b> . (The carbon atoms and the positions of substitution are numbered as in <b>Figure 4.1</b> ). ....	118
<b>Figure 4.5</b> Differences of total bonding energies of the possible products of metallation of <b>29</b> . (The carbon atoms and the positions of substitution are numbered as in <b>Scheme 4.5</b> ). ....	119
<b>Figure 4.6</b> HOMO of <b>29</b> projected onto the electron density (0.03 a.u. isosurface). ....	120
<b>Figure 4.7</b> Differences of total bonding energies of the transition states corresponding to the possible products of metallation of <b>24</b> . (The carbon atoms and the positions of substitution are numbered as in <b>Figure 4.1</b> ). ....	121

<b>Figure 4.8</b> Differences of total bonding energies of the transition states that would lead to each possible product of metallation of <b>29</b> . (The carbon atoms and the positions of substitution are numbered as in <b>Scheme 4.5</b> ). .....	121
<b>Figure 4.9</b> Changes in the UV-vis spectra and absorbance at 330 nm of <b>45</b> as a result of addition of $\Gamma$ (from 0 to 100 equivalents) at 25 °C. ....	127
<b>Figure 4.10</b> Schematic representation of polarisation as orbital mixing. ....	129
<b>Figure 4.11</b> A Comparison of Rayleigh scattering and SHG processes. ....	130
<b>Figure 4.12</b> Selected frontier orbitals of the azobenzenes <b>27</b> , <b>40</b> - <b>47</b> , <b>53</b> , and <b>54</b> . ....	141
<b>Figure 4.13</b> Composition of the I) HOMO and II) LUMO of <b>45</b> . ....	142
<b>Figure 4.14</b> Graphical representation of the HOMO-16 of <b>45</b> , which corresponds to the sigma stabilization interaction of the SBI. Isosurface plotted at 0.03 a.u. ....	143
<b>Figure 4.15</b> Representative structures of $C_6H_6$ , <b>27</b> , <b>33</b> , <b>58</b> , <b>61</b> , <b>45</b> , and <b>54</b> showing the location of calculated centroids used in NICS calculations. ....	145
<b>Figure 4.16</b> Calculated NICSs as a function of the halide X in compounds <b>36-47</b> and <b>59-61</b> . (■ = sulfur, ○ = selenium, Δ = tellurium).....	148
<b>Figure 4.17</b> Correlation between the SBI bond length of <b>36-47</b> on the calculated NICSs. (■ = sulfur, ○ = selenium, Δ = tellurium) .....	148
<b>Figure 4.18</b> Transition densities for the most intense transitions in the electronic spectra of <b>27</b> and <b>45</b> . The transition number (in order of increasing energy) is indicated beside each plot.....	150
<b>Figure 4.19</b> Calculated UV-vis absorption spectra and absorption bands for <b>27</b> , <b>44</b> , <b>45</b> , <b>46</b> , and <b>47</b> . ....	151

<b>Figure 5.1</b> ORTEP of two perspectives of the molecular structure of <b>63</b> (95% probability ellipsoids, methyl groups of t-butyl and hydrogen atoms omitted for clarity). Reproduced with permission from reference 263. ....	160
<b>Figure 5.2</b> SCF potential of <b>64b</b> projected onto the electron density (0.04 a.u. isosurface). ....	165
<b>Figure 5.3</b> LUMO of <b>64b</b> (0.03 a.u. isosurface). ....	165
<b>Figure 5.4</b> 2-D NOESY spectrum of <b>63</b> in dichloromethane-d <sub>2</sub> collected at 180 K. ( $\delta(\text{Me}) = 2.17$ ppm, $\delta(t\text{-Bu}) = 1.42$ ppm, $\delta(\text{C-H}) = 7.00$ ppm).....	167
<b>Figure 6.1</b> Two views of the DFT optimized structure of mercury (II) chloride bound by a (-Te-O-N) <sub>4</sub> macrocycle. ....	177

## LIST OF SCHEMES

<b>Scheme 1.1</b> Hydrogen-bonded supramolecular synthons. A and B denote acidic (H donor) and basic (H acceptor) sites.....	6
<b>Scheme 1.2</b> Schematic representation of the [Te-m-D] <sub>2</sub> supramolecular synthon.....	8
<b>Scheme 1.3</b> Schematic representation of the [Te-m-D] supramolecular synthon.....	9
<b>Scheme 3.1</b> Schematic representation of the structures of the pyridine solvates of <b>17</b> with 1:1 ( <b>I</b> ) and 2:1 ( <b>II</b> ) stoichiometries. ....	75
<b>Scheme 3.2</b> Auto-association bonding schemes present in the solid-state structures of ditellurides.....	80
<b>Scheme 4.1</b> Asymmetric methoxyselenenylation of an olefin. ....	100
<b>Scheme 4.2</b> Structural isomers of the type RSN=C(R')N=NC(R')=NSR.....	101
<b>Scheme 4.3</b> Classification of substituted azobenzenes.....	102
<b>Scheme 4.4</b> Azodye chalcogen-substituted <i>ortho</i> - to the azo bridge. ....	103
<b>Scheme 4.5</b> Atom numbering for <b>27</b> .....	111
<b>Scheme 5.1</b> Alternative bonding descriptions for the -O-Te-N sequence.....	156
<b>Scheme 5.2</b> 1,2-Chalcogenazole oxides. ....	157

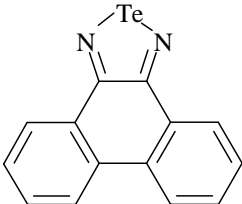
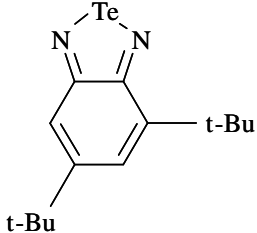
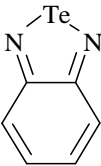
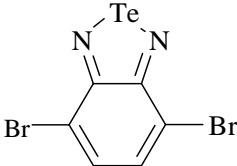
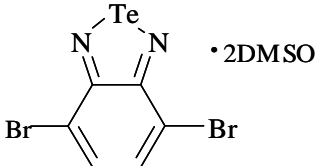
## LIST OF TABLES

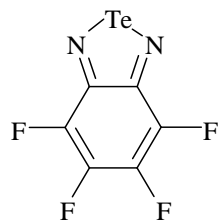
<b>Table 3.1</b> A comparison of calculated and experimental <sup>147</sup> bond lengths and angles of <b>17</b> .....	54
<b>Table 3.2</b> A comparison of calculated and experimental <sup>148</sup> bond lengths and angles of <b>14</b> .....	55
<b>Table 3.3</b> A comparison of optimized gas phase and COSMO structures of <b>17</b> .....	67
<b>Table 3.4</b> Calculated <sup>125</sup> Te chemical shifts for <b>17</b> using COSMO-optimized geometries.	71
<b>Table 3.5</b> Binding energies (not Zero Point Energy (ZPE) corrected) and selected structural parameters for <b>17</b> and its mono-solvates. ....	75
<b>Table 3.6</b> Binding energies (not ZPE corrected) and selected structural parameters for <b>17</b> and its di-solvates.....	76
<b>Table 3.7</b> Calculated <sup>125</sup> Te chemical shifts for the gas phase structure of <b>17</b> and explicit solvation models. $\Delta\delta$ refers to the change from the gas phase value.....	77
<b>Table 3.8</b> Calculated bond lengths, angles, and interaction energies of association models of <b>17</b> <sub>2</sub> . ....	81
<b>Table 3.9</b> Regression parameters* of the concentration dependence of the <sup>125</sup> Te NMR chemical shift of <b>14</b> at 303.0 K. ....	83
<b>Table 3.10</b> The dependence of the <sup>125</sup> Te NMR chemical shift on the concentration of <b>14</b> in hexanes.*.....	86
<b>Table 3.11</b> The dependence of the <sup>125</sup> Te NMR chemical shift on the concentration of <b>14</b> in toluene. *.....	86

<b>Table 3.12</b> The dependence of the $^{125}\text{Te}$ NMR chemical shift on the concentration of <b>14</b> in dichloromethane.* .....	86
<b>Table 3.13</b> The dependence of the $^{125}\text{Te}$ NMR chemical shift on the concentration of <b>13</b> in water. Corrections are applied according to Eq. <b>3.7</b> .* .....	89
<b>Table 3.14</b> The dependence of the $^{125}\text{Te}$ NMR chemical shift on the concentration of <b>15</b> in hexanes.* .....	91
<b>Table 3.15</b> The dependence of the $^{125}\text{Te}$ NMR chemical shift on the concentration of <b>15</b> in toluene.* .....	92
<b>Table 3.16</b> The dependence of the $^{125}\text{Te}$ NMR chemical shift on the concentration of <b>16</b> in dichloromethane.* .....	93
<b>Table 4.1</b> Summary of crystal data, collection and refinement conditions for <b>28</b> and <b>30</b> .	114
<b>Table 4.2</b> Selected bond lengths (Å) and bond angles (°) for <b>30</b> .	115
<b>Table 4.3</b> The relative yields of products of substitution. ....	116
<b>Table 4.4</b> Hyperpolarisabilities for a Series of Chalcogen Containing Heterocycles	132
<b>Table 4.5</b> The effect of chalcogen donation on the hyperpolarisability of a series of thiophene-based molecules ( <b>49</b> ). ....	132
<b>Table 4.6</b> Hyperpolarisabilities for a series of chalcogen-containing D- $\pi$ -A molecules. ....	133
<b>Table 4.7</b> A comparison of calculated bond lengths and angles of <b>27</b> and the sulfenyl halide substituted derivative. ....	137
<b>Table 4.8</b> A comparison of calculated bond lengths and angles of <b>27</b> and the selenenyl halide substitution. ....	138

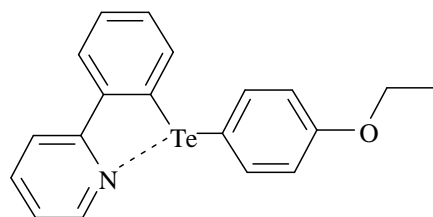
<b>Table 4.9</b> A comparison of calculated bond lengths and angles of <b>27</b> and the tellurenyl halide substitutions.....	138
<b>Table 4.10</b> A comparison of calculated bond lengths and angles of <b>27</b> and phenyl chalcogenyl substituted species <b>52</b> , <b>53</b> , and <b>54</b> .....	140
<b>Table 4.11</b> Calculated NICSs for compounds, <b>27</b> , <b>33,36-47</b> , <b>52-54</b> , <b>56-61</b> and C <sub>6</sub> H <sub>6</sub> ...	146
<b>Table 4.12</b> DFT and TD-DFT calculated values pertaining to NLO activity of <b>27</b> , the phenylchalcogenyl derivatives ( <b>52</b> , <b>53</b> , <b>54</b> ), and <b>55</b> . ....	152
<b>Table 5.1</b> Summay of crystal data, collection and refinement conditions for <b>63</b> .....	161
<b>Table 5.2</b> Selected bond lengths (Å) and bond angles (°) for <b>63</b> . ....	162
<b>Table 5.3</b> CSOV analysis for C <sub>2h</sub> dimers of <b>68a</b> and <b>68b</b> . ....	168

## LIST OF COMPOUNDS

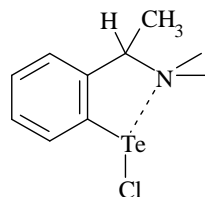
	<b>1</b>
	<b>2</b>
	<b>3</b>
	<b>4</b>
	<b>5</b>
	<b>6</b>



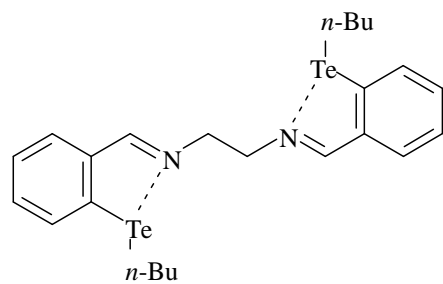
7



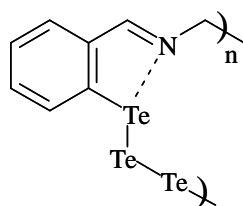
8



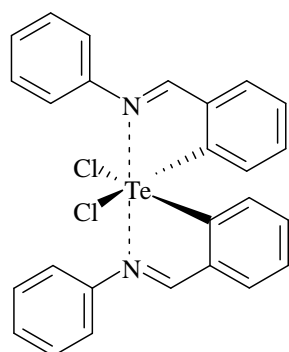
9



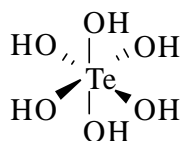
10



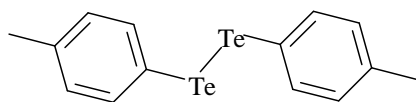
11



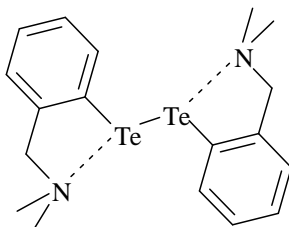
12



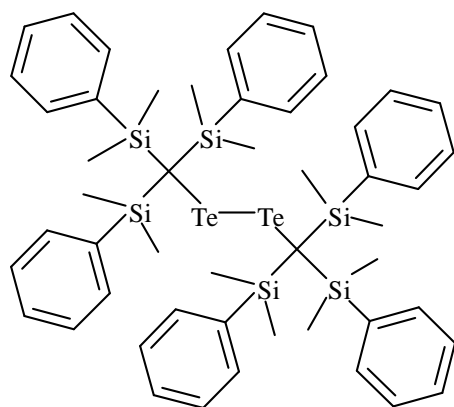
13



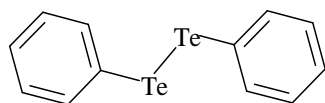
14



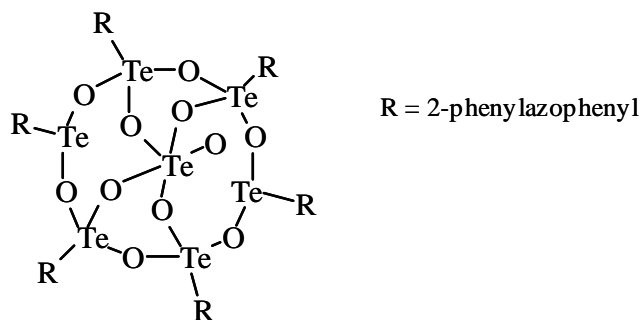
15



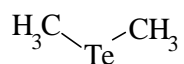
16



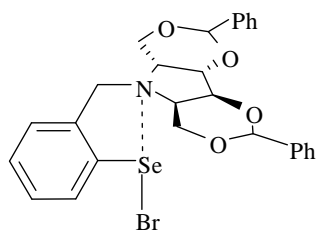
17



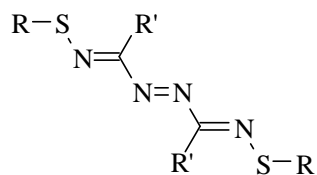
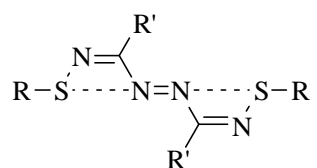
18



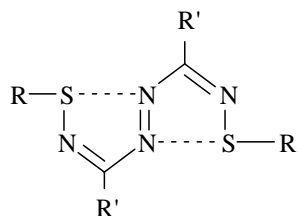
19



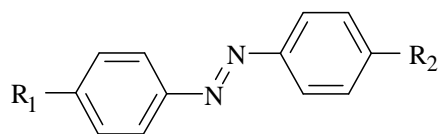
20

21 R = Ph, R' = 2-BrC<sub>6</sub>H<sub>4</sub>

22 R = Ph, R' = H



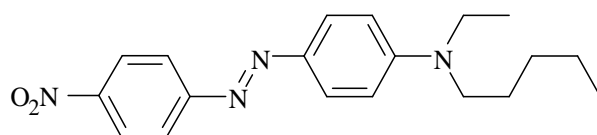
23 R, R'=Ph



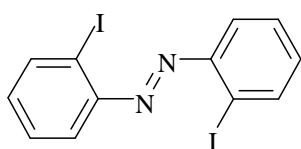
**24**  $R_1, R_2 = \text{Alkyl, H}$

**25**  $R_1 = \text{N(alkyl)}_2, R_2 = \text{Alkyl, H}$

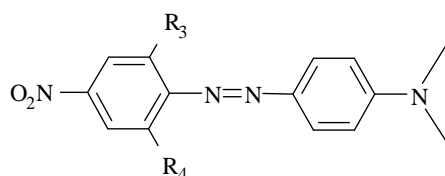
**26**  $R_1 = \text{N(alkyl)}_2, R_2 = \text{NO}_2, \text{F}, \text{S(O)}_2\text{Me}$



**27**

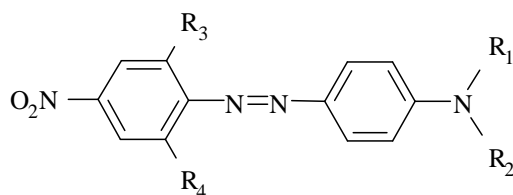


**28**



**29**  $R_3, R_4 = \text{H}$

**30**  $R_3 = \text{H}, R_4 = \text{I}$

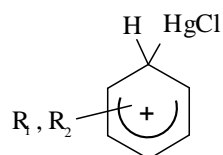


**31**  $R_1 = \text{C}_2\text{H}_5, R_2 = \text{n-C}_5\text{H}_{11}, R_3 = \text{H}, R_4 = \text{HgCl}$

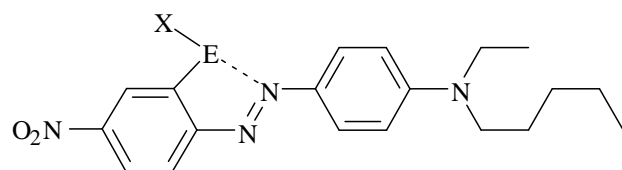
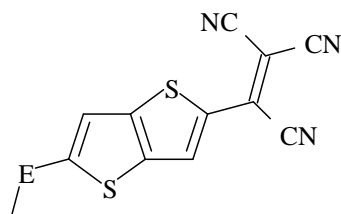
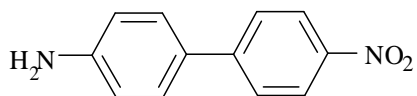
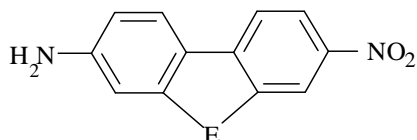
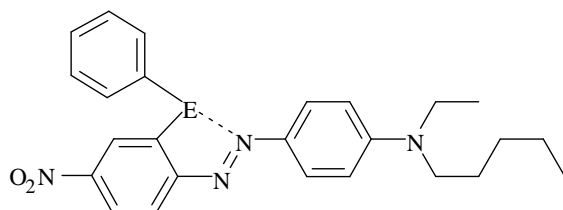
**32**  $R_1 = \text{C}_2\text{H}_5, R_2 = \text{n-C}_5\text{H}_{11}, R_3, R_4 = \text{HgCl}$

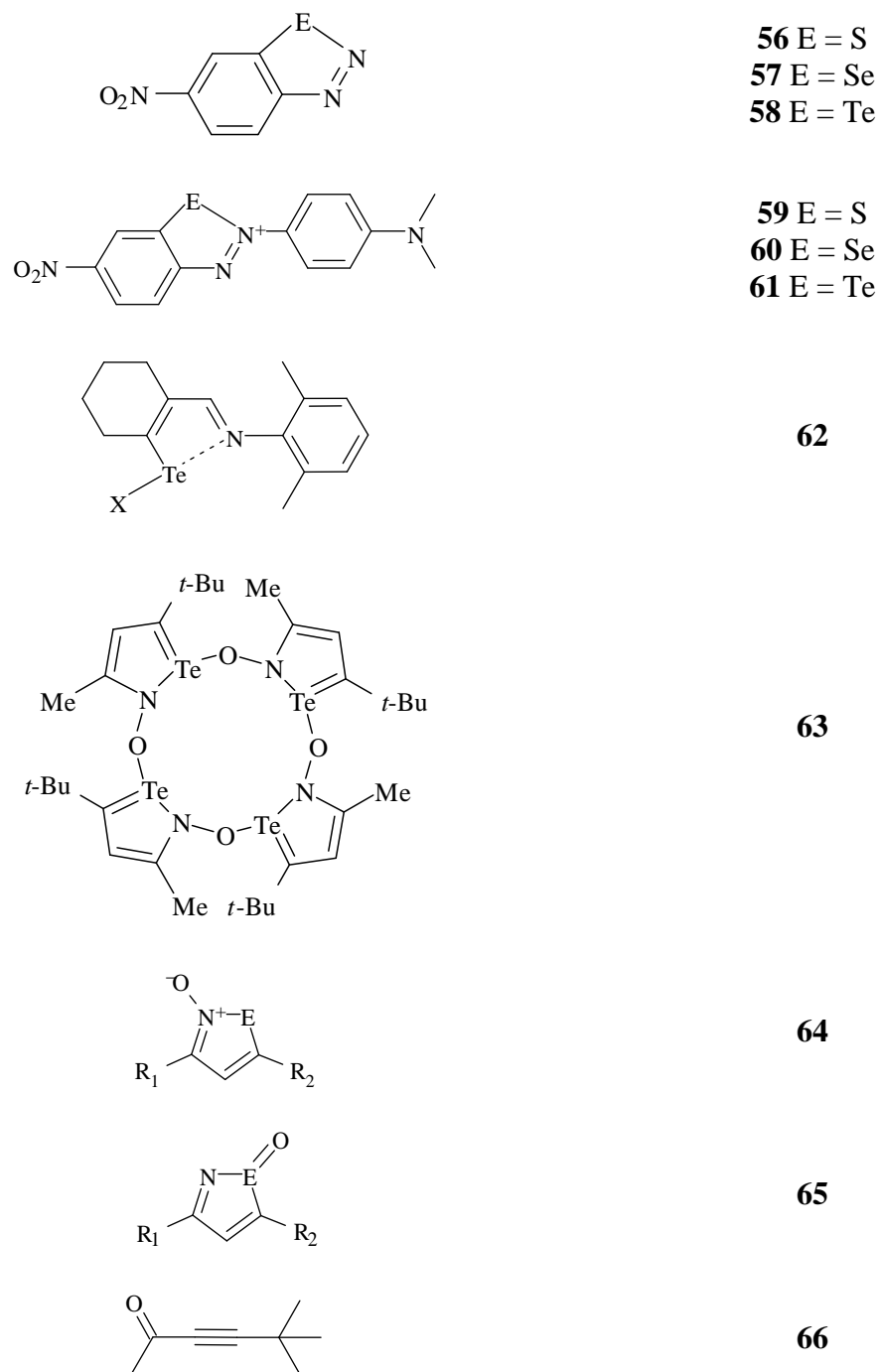
**33**  $R_1 = \text{C}_2\text{H}_5, R_2 = \text{n-C}_5\text{H}_{11}, R_3 = \text{H}, R_4 = \text{I}$

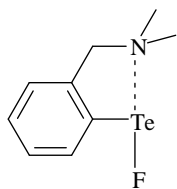
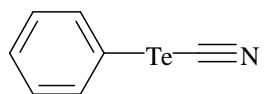
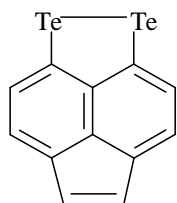
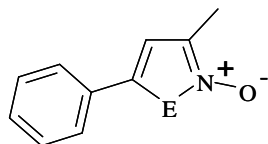
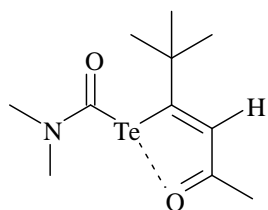
**34**  $R_1 = \text{C}_2\text{H}_5, R_2 = \text{n-C}_5\text{H}_{11}, R_3, R_4 = \text{I}$



**35**

**36** E = S, X = F**37** E = S, X = Cl**38** E = S, X = Br**39** E = S, X = I**40** E = Se, X = F**41** E = Se, X = Cl**42** E = Se, X = Br**43** E = Se, X = I**44** E = Te, X = F**45** E = Te, X = Cl**46** E = Te, X = Br**47** E = Te, X = I**48****49****50****51****52** E = S**53** E = Se**54** E = Te**55**





**LIST OF ABBREVIATIONS AND SYMBOLS**

$\beta$	Second-order hyperpolarizability tensor (in nonlinear optics)
$\delta$	chemical shift, ppm (parts per million)
$\lambda$	wavelength
$\mu$	linear absorption coefficient (in crystallography)
$\rho$	density of a material (in crystallography)
$\Sigma$	Shielding constant
Å	angstrom
a, b, c, $\alpha$ , $\beta$ , $\gamma$	unit cell parameters (in crystallography)
ACN	acetonitrile
ADF	Amsterdam Density Functional software
ALDA	Adiabatic Local Density Approximation
ASE	aromatic stabilization energy
a.u.	arbitrary units
au	atomic units
AU	absorbance units
B	magnetic field (in NMR spectroscopy)
BP86	GGA exchange correlation functional, Becke exchange and Perdew correlation
CI	chemical ionization (in mass spectrometry)
$\text{cm}^{-1}$	inverse centimetres (wavenumbers)
COSMO	conductor-like screening model
CSD	Cambridge Structural Database
CSOV	constrained space orbital variation
D	donor atom with an SBI
DCE	1,2-dichloroethane
DCM	dichloromethane
DFT	density functional theory
Diox	1,4-dioxane
DMF	dimethyl formamide
DMSO	dimethyl sulphoxide
DOSY	diffusion ordered spectroscopy (NMR experiment)
DZ	double- $\zeta$ (basis set)
DZP	double- $\zeta$ with one-polarization function (basis set)
E	a variable element within a structure, the acceptor element within an SBI

e	electrons (in crystallography)
EA	elemental analysis
EAS	electrophilic aromatic substitution
EI	electron impact (in mass spectrometry)
esu	electrostatic Units
FID	free induction decay
FT	Fourier transform
FWHM	full width at half maximum
GIAO	gauge-including atomic orbitals
GGA	generalized gradient approximation
GUI	graphical user interface
HF	Hartree-Fock
HOMA	harmonic oscillator model of aromaticity
HOMO	highest occupied molecular orbital
HMBC	heteronuclear multiple-bond coherence (pulse sequence)
HSQC	heteronuclear single quantum coherence (pulse sequence)
HRS	hyper-Rayleigh scattering
iPr	isopropyl
IR	infrared
IUPAC	International Union of Pure and Applied Chemistry
K	calibration factor (in second harmonic generation)
K	Kelvin
KS	Kohn-Sham
LB	Lorentzian broadening
LUMO	lowest unoccupied molecular orbital
$L_z$	angular momentum operator
MALDI	matrix-assisted laser desorption/ionization
Me	methyl
MO	molecular orbital
MS	mass spectrometry
nBu	n-butyl
NICS	nucleus independent chemical shift
NLO	nonlinear optical
nm	nanometer
NMR	nuclear magnetic resonance (spectroscopy)
NOE	nuclear Overhauser effect

NOESY	nuclear Overhauser effect spectroscopy (NMR experiment)
pm	picometer
PMT	photomultiplier tube
ppm	parts per million
PTFE	polytetrafluoroethylene
PW91	GGA exchange correlation functional, Perdew and Wang
Py	pyridine
QZ4P	quadruple- $\zeta$ with four-polarization functions (basis set)
$R_1$	unweighted residual factor (in crystallography)
$r_{vdW}$	van der Waals radii
SAOP	statistical average of orbital potentials
SBI	secondary bonding interaction
SHG	second harmonic generation
SZ	single- $\zeta$ (basis set)
T	temperature
TD-DFT	time-dependant density functional theory
THF	tetrahydrofuran
TMS	tetramethylsilane
TOF	time-of-flight (in mass spectrometry)
TZ2P	triple- $\zeta$ with two-polarization functions (basis set)
TZP	triple- $\zeta$ with one polarization function (basis set)
UV-Vis	ultraviolet-visible (spectroscopy)
V	unit cell volume (in crystallography)
VT	variable temperature (in NMR)
$wR_2$	weighted residual factor (in crystallography)
Z	molecules per unit cell (in crystallography)
ZORA	zeroth-order regular approximation

## 1 Introduction

### 1.1 Supramolecular Chemistry

In view of the wide extent of the achievements attained in over 40 years of research in supramolecular chemistry and its subfields (e.g. self-assembly, host-guest chemistry, solid-state inclusion chemistry, crystal engineering, supramolecular machines/devices and soft/smart materials), it is surprising that the vast majority of large, complex and sometimes functional *polymolecular entities*<sup>1</sup> have been obtained through the use of just a few types of supramolecular interactions: hydrogen bonding, the coordination of metal ions and, to a lesser extent,  $\pi$ -stacking and hydrophobic effects. Under the premise that different interactions would lead to distinct architectures and/or elicit unique properties, other interactions have stimulated interest as alternative means of assembling these structures. For example, *aurophilic* (or more generally *metallophilic*) interactions between d<sup>10</sup> metal ions continue to attract interest because of the intriguing structures and photophysical properties of the compounds that feature them.<sup>2</sup> Such contacts are stabilized by relativistic effects and belong to the broad category of *closed-shell* interactions,<sup>3</sup> meaning that the participating atoms had already satisfied their valences and – based on the simple arguments of Lewis bonding theory – were not expected to require more bonding electrons and/or form additional bonds.

#### 1.1.1 Closed-Shell Interactions

Closed-shell interactions are a pervasive feature in structural main-group chemistry;<sup>4</sup> crystallographic determinations often reveal short distances between a heavy p-block

element and one or more atoms which typically possess lone pairs of electrons. Heavy main-group elements are of course able to “expand their valence shell” forming *hypervalent bonds* that are accurately described by multicenter orbital interactions. The distances in closed-shell interactions, however, are much longer than the typical hypervalent single bond and yet they are so much shorter than the sum of corresponding van der Waals radii that they cannot be dismissed as “non-bonded contacts” or “packing accidents” stabilized only by “van der Waals forces”.\* Over time this phenomenon has received attention under several labels including: soft-soft interactions,<sup>5</sup> closed-shell interactions,<sup>3</sup> nonbonding interactions,<sup>6</sup>  $\sigma$ -hole interactions,<sup>7</sup> semibonding interactions,<sup>8</sup> halogen bonds,<sup>9</sup> noncovalent interactions<sup>10</sup> and weakly-bonding interactions.<sup>11-13</sup>

### 1.1.2 Secondary Bonding Interactions

Arguably the most appropriate name, *secondary bonding interaction* (SBI), was proposed in the 1970’s by Alcock<sup>14</sup> making distinction from the Lewis and hypervalent *primary* bonds. His concept was based on crystallographic data, including not only distances but angles as well. Considering that typically the secondary bond axis is nearly collinear with a (primary) bond between the central heavy atom (E) and a more electronegative atom (X), Alcock realized that such interactions are stabilized by electrostatic and covalent contributions. The former arises from local partial charges and

---

\* Considering its origin in modeling gas behaviour, the term “van der Waals forces” is in principle applicable to *any* intermolecular interactions but it is most frequently used to describe those arising from dipole-dipole, dipole-induced dipole or dispersion forces. On the other hand, the van der Waals radius is an arbitrary cutoff distance, beyond which intermolecular contacts are regarded as the result of those weak interactions only. However, such interpretation is in conflict with the asymptotic radial decay of electron density from the atomic nucleus; in other words, there is always some degree of orbital interaction between neighbouring molecules.

the later consists of the donation of electrons from a donor (D) into the  $\sigma^*$  molecular orbital corresponding to the primary E-X bond (**Figure 1.1**). The fundamentals of this model derived from empirical observation have been validated by modern quantum mechanical methods<sup>15-18</sup> but a complete bonding description does require the inclusion of all orbital, electrostatic and dispersion contributions.<sup>8</sup> While mixing of occupied and unoccupied orbitals corresponds to the donor acceptor character of the interaction and confers directionality to the SBI, an unavoidable destabilizing contribution (the Pauli repulsion) results from the mixing of all-occupied orbitals. In certain cases, the electrostatic contribution could add to the directional nature of the SBI.<sup>7,10,19</sup> The dispersion force is always attractive and arises from the instantaneous correlation of electrons in the interacting atoms. The strength of the dispersion force increases as the electron clouds become more polarizable; it is therefore more important for systems with the heaviest elements.<sup>20,21</sup> Although SBIs are not fundamentally different from “regular” hypervalent bonds – and in certain instances can approach their strength<sup>22</sup> – it is convenient to distinguish SBIs as the interactions or bonds which can be manipulated for the purposes of supramolecular synthesis.

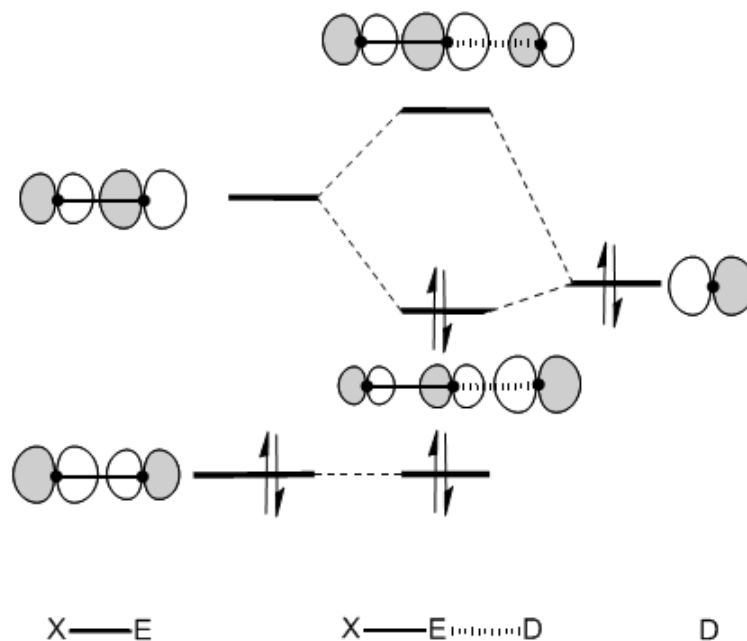


**Figure 1.1** Mixing of molecular orbitals in an  $E \cdots D$  secondary bonding interaction. For simplicity, only p atomic orbitals are considered. Reproduced with permission from reference 23.

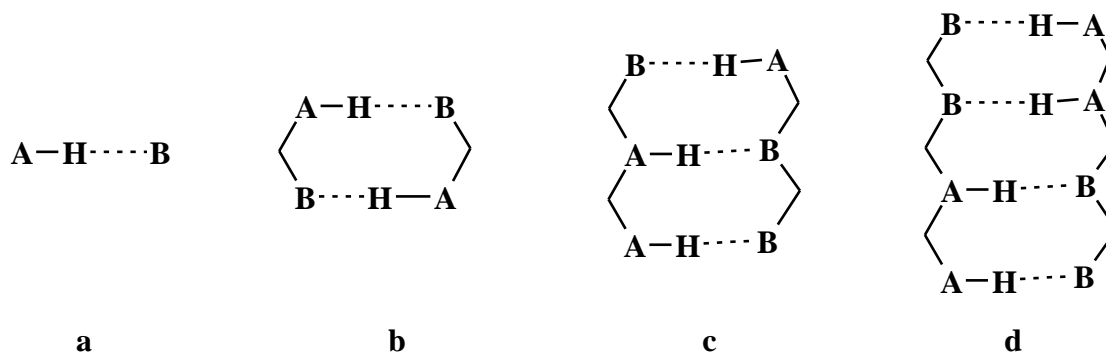
Compared to other supramolecular interactions, there have been rather few attempts to systematically use SBIs as design elements in supramolecular chemistry. Notwithstanding, some noteworthy cases illustrate the potential of main-group SBIs in this context: pnictogen-centered SBIs<sup>24</sup> can link ribbon polymers;<sup>25</sup> chalcogen-chalcogen contacts<sup>26</sup> assemble supramolecular tubes;<sup>27-29</sup> and applications of halogen SBIs have been demonstrated in the design of noncentrosymmetric lattices capable of second harmonic generation (SHG),<sup>30</sup> the resolution of a racemic perfluoroalkyl bromide,<sup>31</sup> the separation of mixtures of diiodoperfluoroalkanes,<sup>32</sup> and the organization of 1-dimensional molecular magnets with attenuation of antiferromagnetic coupling.<sup>33</sup>

### 1.1.3 Supramolecular Synthons

Making an analogy to hydrogen bonding, Starbuck and Orpen<sup>24</sup> noted that the rational design of SBI supramolecular systems would greatly benefit from the application of Desiraju's concept of supramolecular synthon: "*a structural unit within a supermolecule which can be formed and/or assembled by known or conceivable synthetic operations involving intermolecular interactions*".<sup>34</sup> **Scheme 1.1** depicts some important examples of dimeric supramolecular synthons that are based on hydrogen bonding. The key to the efficient application of main-group SBIs in supramolecular chemistry would be the identification of the most efficient supramolecular synthons, i.e. those which are:

- Strong enough to hold the building blocks in place;
- Directional, to guide the formation of the supramolecular structure;
- Reversible, in order to allow error self-correction;
- Synthetically accessible by methods applicable to a wide variety of derivatives.

The case of hydrogen bonding **Scheme 1.1** does illustrate how supramolecular synthons with multiple points of attachment achieve great stability and directionality, as in the synthons that are formed by the pairing of bases in nucleic acids (**Scheme 1.1 b and c**) and a motif which is so strong that it generates true supramolecular polymers (**Scheme 1.1 d**).<sup>35</sup>



**Scheme 1.1** Hydrogen-bonded supramolecular synthons. A and B denote acidic (H donor) and basic (H acceptor) sites.

Chalcogens (S, Se, Te) are especially interesting as SBI centres because their VSEPR geometries in oxidation states II and IV typically have two positions available for the formation of SBIs (**Figure 1.2**); such a geometric attribute encourages chelation and/or the formation of planar supramolecular synthons. Because of the antibonding character of the electron-acceptor orbitals, the heaviest member of the family, tellurium, makes the strongest SBIs. Tellurium is also synthetically versatile as it makes stable bonds with most main-group elements.<sup>36</sup> The ability of some tellurium compounds to form adducts with organic Lewis bases has long been recognized;<sup>37</sup> Haiduc and Zuckerman-Schpector<sup>26,38</sup> have reviewed a number of supramolecular structures assembled by tellurium-centred SBIs. A recent review of the data deposited in the Cambridge Crystallographic Database (CSD, version 5.31, Nov. 2009 with 490,902 entries)<sup>39</sup> extended those earlier findings with a comparison of the relative strengths of tellurium-centred SBIs and the identification of most frequent and strongest supramolecular synthons.<sup>23</sup> This study showed that the shortest distances, and likely the

strongest interactions, occurred when N, O, or Cl act as donor atoms, and when these same elements, or the CN pseudohalogen group, take the place of X (**Figure 1.1**).<sup>23</sup>

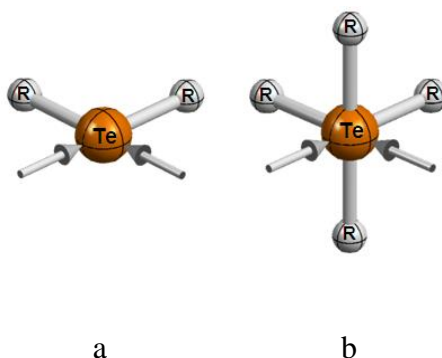
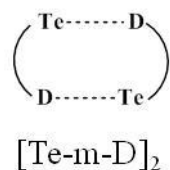


**Figure 1.2** Idealized VSEPR geometries for tellurium in the a) II and b) IV oxidation states. The arrows denote the positions preferred for the formation of secondary bonding interactions. Reproduced with permission from reference 23.

## 1.2 The [Te-m-D]<sub>2</sub> Supramolecular Synthons and 1,2,5-Chalcogenadiazoles

The [Te-m-D]<sub>2</sub> synthon<sup>23</sup> is a virtual heterocycle formed by two antiparallel SBIs (**Scheme 1.2**). It is in principle stronger than the simple single-SBI case as there are twice as many supramolecular interactions. The shortest distances are observed when N or O donate electrons into Te-X bonds and X is also N or O. Within this group, there are fifteen structures with Te...D SBIs shorter than 80% of the sum of  $r_{vdw}$  and in each case the actual supramolecular synthon is the virtual four-membered heterocycle [Te-D]<sub>2</sub>. Six of these crystal structures (1,2,5-telluradiazole (**1**),<sup>40</sup> phenanthro(9,10-c)-1,2,5-telluradiazole (**2**),<sup>41</sup> 4,6-di-t-butylbenzo-2,1,3-telluradiazole (**3**),<sup>42</sup> benzo-2,1,3-telluradiazole (**4**),<sup>43</sup> 4,7-dibromobenzo-2,1,3-telluradiazole (**5**),<sup>43</sup> and the DMSO adduct of 4,7-dibromobenzo-

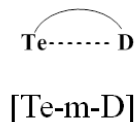
2,1,3-telluradiazole (**6**)<sup>43</sup>) feature the [Te-N]<sub>2</sub> synthon assembled by 1,2,5-telluradiazole heterocycles as building blocks.



**Scheme 1.2** Schematic representation of the [Te-m-D]<sub>2</sub> supramolecular synthon.

Of all tellurium-containing supramolecular synthons, the [Te-N]<sub>2</sub> has been studied in the greatest detail. A thorough bonding description was provided by DFT<sup>16</sup> and when combined with crystallographic data, these results were used to parameterize a force field for the design of new supramolecular assemblies.<sup>44</sup> Steric effects on the formation of the synthon have also been examined.<sup>43</sup> The chromotropism of two polymorphs of 4,5,6,7-tetrafluorobenzo-2,1,3-telluradiazole (**7**)<sup>45</sup> was explained in terms of changes of the local symmetry of distorted [Te-N]<sub>2</sub> synthons. A noncentrosymmetric distortion of the supramolecular synthon was used to induce the crystallization of lattices with nonlinear optical properties.<sup>46</sup> In addition to the strength of their Te-N SBIs, telluradiazoles have received attention due to their convenient synthesis, and the many applications of their lighter analogues.<sup>47-49</sup> The selenium rings associate in this fashion most frequently when they are N-substituted with alkyl groups.<sup>50, 51</sup>

### 1.3 The [Te-m-D] Supramolecular Synthons and "Intramolecular Coordination"



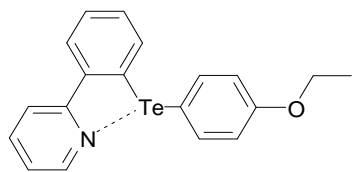
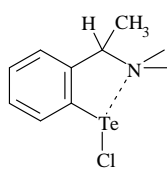
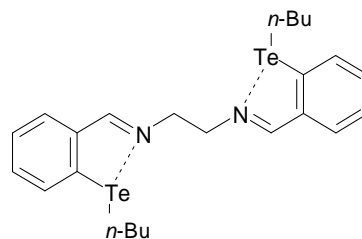
**Scheme 1.3** Schematic representation of the [Te-m-D] supramolecular synthon.

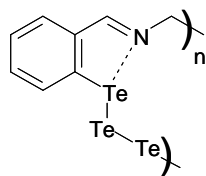
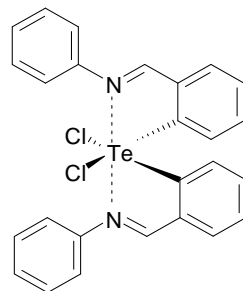
The [Te-m-D] supramolecular synthon<sup>23</sup> is the virtual heterocycle (usually four-, five- or six-membered) formed by an SBI between tellurium and donor atoms within the same molecule (**Scheme 1.3**). In this case, the shortest SBI lengths are observed when the acceptor (X) atom is N, O, Cl, or the pseudohalogen group CN. This is consistent with Alcock's bonding description for a SBI as the Te contribution to the Te-X  $\sigma^*$  orbital increases with the electronegativity of X. In addition, the energy of the acceptor orbital decreases with the Te-X electronegativity difference and leads to a stronger orbital interaction with the lone pair of D. The electrostatic component of the interaction is further enhanced by increasing the polarization of the Te-X bond.

Although this supramolecular synthon is the simplest case, its SBI has been studied in less detail than more complex intermolecular cases. The effect of intramolecular SBIs on organotellurium compounds were the focus of a review,<sup>52</sup> which included descriptions of structure, chemical consequences and spectroscopic evidence to support the presence of short contacts. Despite the large number of compounds described, the majority of the information was summarized from structural studies and the review predominantly consists of a description of molecular geometries. Donation from P, O, S, Cl and N were

each considered, of which nitrogen examples constitute the largest body of information and present the greatest structural variety.

The most common structures containing nitrogen donors can be classified into one of four groups: azobenzenes, benzylamines, imines, and those containing heterocycles. The azobenzene group has provided information into the effect of X on the bonding of the molecule; in the solid state the tellurenyl halides exhibit three-coordinate tellurium atoms, while the perchlorate analogue exists as a salt.<sup>53</sup> A reverse trans metallation has been reported in the reaction of **8** with  $\text{HgCl}_2$ <sup>54</sup> and similar transfer of organic groups from tellurium to copper (I) has been observed.<sup>55</sup> The optically pure chiral tellurenyl halide, **9**, shows inequivalent resonances for methyl groups suggesting a strong  $\text{Te}\cdots\text{N}$  interaction persists in solution.<sup>56</sup> The tellurated Schiff base **10** has been used as a bi- and tridentate ligand for coordination with platinum and rhodium centers respectively.<sup>57</sup> Treatment of the same compound with excess  $\text{SOCl}_2$  leads to the formation of the poly-tritelluride, **11**, stabilized through SBI formation.<sup>58</sup> Despite this progress, much of the understanding of such intramolecular SBIs comes from the study of the analogues made with lighter chalcogens.

**8****9****10**

**11****12**

On occasion, some spectroscopic results (infrared, nuclear magnetic resonance and Mössbauer) have been interpreted in view of the formation of intramolecular Te-D SBIs. Shifts in the position of the C=N stretch band of tellurated Schiff bases are similar to those observed in substituted azobenzenes; the presence of the SBI has been inferred due the similarities with the known coordination of the chalcogen by azobenzene N in the solid state.<sup>59</sup> NMR spectroscopy on the <sup>15</sup>N labeled compound **12** showed coupling between N and Te (61 Hz, 122 Hz), indicating the presence of strong intramolecular association in solution.<sup>60</sup> The extent of delocalisation of electron density into the virtual heterocycle formed by an *ortho*-tellurated azobenzene was examined using Mössbauer spectroscopy; the quadrupole splitting is larger than expected for a two-coordinate tellurium atom.<sup>61</sup> In spite of these data, there is clearly the need for a systematic study to establish unequivocal correlations between spectral changes and the formation of SBIs.

#### 1.4 Purpose, Scope and Overview of the Thesis

The study of organo-chalcogen compounds capable of forming intramolecular secondary bonds has primarily consisted of structural characterization. Although there have been some studies which have demonstrated (and exploited) the effect of such interactions on spectroscopic properties and reactivity of some selenium compounds<sup>62-65</sup> there is a significant lack of fundamental understanding in this area, especially in the case of tellurium. The purpose of the investigations described in this Thesis has been to fill that void. The proposed goals of this project were:

1. Probe the viability of  $^{125}\text{Te}$  NMR as a means of conclusive identification of SBIs in solution.
2. Understand the effect of an intramolecular chalcogen-centred SBI on the electronic structure and spectra of a conjugated chromophore.
3. Use such effects to modify useful properties of the chromophore and/or monitor a chemical process centred on the chalcogen.

The results of these investigations are presented as follows. Chapter 2 contains all of the experimental and computational details. A detailed experimental and computational study into the chemical shielding of the  $^{125}\text{Te}$  nucleus of organoditellurides is presented in Chapter 3. Chapter 4 discusses the incorporation of a chalcogen into a chromophore and the effect of an intramolecular SBI on the electronic structure, reactivity, and nonlinear polarisability of the molecule. The incidental discovery of an  $(-\text{O}-\text{Te}-\text{N}-)_4$  macrocycle provided an example of a molecule featuring a bonding pattern that corresponds to the

covalent extreme of an intramolecular SBI; the synthesis, structure, bonding, and stability studies of this system are described in Chapter 5. Chapter 6 summarizes the significance of these results and presents some avenues for future research.

## **2 Experimental**

### **2.1 Instrumental Methods**

#### **2.1.1 Dispersive Raman Spectroscopy**

##### **Sample Preparation**

Moisture sensitive samples were sealed in Pyrex melting point capillaries under a nitrogen atmosphere. When the samples scattered weakly, the sample tube was opened and contents placed on a glass slide immediately prior to acquisition. Air-stable samples were placed directly on a glass slide for measurements.

##### **Data Acquisition**

Spectra were acquired on a Renishaw inVia Raman microscope with the WiRE 3 software package at ambient temperature. The sample was excited with a 785 nm laser source (Renishaw HPNIR785) using 30 mW of power using a 1200 line/nm grating. Typically 10 ten-second scans were averaged to produce the final spectrum. A multi-point background correction was applied to each spectrum using the Grams software package.

#### **2.1.2 Fourier Transform Infrared Spectroscopy**

##### **Sample Preparation**

Air sensitive samples were prepared in the glove box under nitrogen as either compressed KBr or polyethylene pellets. These samples were transported under nitrogen

to the instrument and placed in a nitrogen purged sample housing. Air-stable compounds were prepared as compressed KBr pellets on the benchtop prior to being placed in the nitrogen purged sample housing.

### **Data Acquisition**

IR spectra were recorded at room temperature using a Bio-Rad FTS-40 FT-IR spectrometer. Each spectrum was acquired with a resolution of  $4\text{ cm}^{-1}$  in the region of  $4000\text{-}400\text{ cm}^{-1}$  and the background was recorded prior to spectral acquisition. Background subtraction and a multi-point background correction were applied to the spectra using the Grams software package.

## **2.1.3 Ultraviolet-Visible Spectroscopy**

### **Sample Preparation**

Solutions of air sensitive compounds were prepared using carefully weighed materials and calibrated volumetric glassware in the glove box under nitrogen.

### **Data Acquisition**

The ultraviolet-visible (UV-vis) absorption spectra were measured in quartz cuvettes on either a Varian Cary 50 spectrometer or a Varian Cary 300 spectrometer with a temperature-controlled stage. These instruments were run in dual beam mode by scanning from  $200\text{-}800\text{ nm}$  with a scan rate of  $10\text{ nm/s}$ . The solvent background was manually subtracted using external blank samples.

## **2.1.4 Electron Ionization Mass Spectrometry**

### **Sample Preparation**

Pure samples were dissolved in appropriate solvents prior to introduction into the mass spectrometer. Samples that were prone to hydrolysis were sealed in capillaries under nitrogen and opened immediately before acquisition.

### **Data Acquisition**

Low- and high-resolution electron-impact and chemical ionization mass spectrometry experiments were performed on a Micromass GCT (GC-EI/CI Time of Flight) Mass Spectrometer in probe mode. High-resolution mass spectra were obtained in a Waters/Micromass Q-ToF Ultima Global (ES TOF) Mass Spectrometer. In each case, the sample was introduced directly into the ionization chamber in a shortened borosilicate glass capillary on a probe rod. The sample was heated by ramping to 300 °C; the temperature range that exhibited the most intense parent ion peaks was used for acquisition. The sample was ionized by a 70 eV electron stream. The positively charged ions were detected by a time-of-flight detector. The final spectrum consisted of the time averaged spectra from regions of the chromatogram where the desired signal was maximized without saturating the detector.

### **2.1.5 Chemical Ionization Mass Spectrometry**

#### **Sample Preparation**

Pure samples were dissolved in appropriate solvents prior to introduction into the mass spectrometer. Samples that were prone to hydrolysis were sealed in capillaries under nitrogen, and opened immediately before acquisition.

#### **Data Acquisition**

Low resolution electron-impact and chemical ionization mass spectrometry experiments were performed on a Micromass GCT (GC-EI/CI Time of Flight) Mass Spectrometer in probe mode. In each case, the sample was introduced directly into the ionization chamber in a shortened borosilicate glass capillary on a probe. Typically, ionized ammonia reagent gas was used to form a positively charged even electron analyte ion which was detected by a time-of-flight detector. The final spectrum consisted of the time averaged spectra from regions of the chromatogram where the desired signal was maximized without saturating the detector.

### **2.1.6 Melting Points**

Melting points were measured on a Thomas-Hoover melting point apparatus and are reported uncorrected.

## 2.1.7 Single Crystal X-ray Diffraction

### Sample Preparation

Samples were handled at room temperature coated in Paratone-n oil. Crystals were mounted on nylon loops (Hampton, CA) or MiTeGen Micromounts (Ithica, NY) using Paratone-n oil.

### Data Acquisition

Redundant data sets were collected on one of the following instruments:

1) A P4 Bruker diffractometer upgraded with a Bruker SMART 1K CCD detector and a rotating anode utilizing Mo-K $\alpha$  radiation ( $\lambda=0.71073$  Å, graphite monochromator) equipped with an Oxford cryostream 700 low temperature accessory.

2) A SMART APEX II diffractometer utilizing Mo-K $\alpha$  radiation ( $\lambda=0.71073$  Å, graphite monochromator) from a fine-focus sealed X-ray tube with a CCD area detector and equipped with an Oxford cryostream 700 low temperature accessory.

### Data treatment

Typically, after a sufficient number of frames were collected, the reciprocal lattice was visualized with RLATT<sup>66</sup> or the reciprocal lattice viewer in the APEX 2 software suite.<sup>67</sup> If the data consisted of only one set of reflections a preliminary unit cell and orientation matrix was determined from this raw data. The complete dataset was integrated using either SAINT<sup>68</sup> or the integration feature of the APEX 2 software suite. The final cell parameters were obtained by refinement on the positions of the integrated reflections with  $I > 10\sigma(I)$ . The data were empirically corrected for absorption and other

effects using SADABS<sup>69</sup> or the absorption correction feature in the APEX 2 software suite. The structures were solved by direct methods using SHELXS<sup>70</sup> and refined by full-matrix least squares on all  $F^2$  data using SHELXL<sup>70</sup> as part of the WinGX software package.<sup>71</sup> The non-H atoms were refined anisotropically, while H atoms were constrained to idealized positions using appropriate riding models. Molecular graphics were produced using either ORTEP-3<sup>72</sup> or Mercury 2.2.<sup>73</sup> Crystallographic information files have been included in a separate supplementary information file.

## 2.1.8 Nuclear Magnetic Resonance Spectroscopy

### Sample Preparation

A typical sample was prepared by dissolving ca. 15 mg of compound in 0.7 mL of a deuterated solvent. Solutions of air sensitive compounds were prepared using deuterated solvents which had been previously dehydrated through activated alumina. Ditelluride samples used in <sup>125</sup>Te concentration-dependent studies were prepared using non-deuterated solvents, with an external sample used as a lock.

### Data Acquisition

**Low field:** A Bruker Avance 200 (200.13 MHz) spectrometer was used to acquire routine low-field NMR spectra at ambient temperature. A 5-mm QNP ('quad') probe was used for <sup>1</sup>H, and <sup>13</sup>C{<sup>1</sup>H} spectra operating in locked mode using the deuterium signal from the solvent. The <sup>1</sup>H and <sup>13</sup>C{<sup>1</sup>H} spectra were referenced to tetramethylsilane (TMS) using the deuterated solvent peaks as secondary references.

**High field:** A Bruker DRX (AVANCE) 500 (500 MHz) spectrometer was used to acquire high field nuclear magnetic resonance spectra. A Bruker 5-mm broad band inverse probe was used to acquire  $^1\text{H}$  spectra and a 5-mm broad band probe was used to acquire  $^{13}\text{C}\{^1\text{H}\}$  and  $^{125}\text{Te}$  spectra. Variable temperature spectra were acquired using either a cold or ambient temperature gas flow with a BV-T 2000 variable temperature controller. In experiments where accurate temperature measurements were necessary, a chemical shift thermometer was employed: 4% methanol in methanol- $d_4$  for 178-300 K and 100% ethylene glycol for 300-380 K.<sup>74</sup> Occasionally, a Bruker AVANCE II 600 (600 MHz) with 5-mm broad band observe probe and autotune was used to assess the purity of compounds through  $^1\text{H}$  and  $^{13}\text{C}\{^1\text{H}\}$  spectra. Structural assignments were facilitated by the heteronuclear single quantum coherence (HSQC) and heteronuclear multiple-bond coherence (HMBC) pulse sequences. All samples were run locked to the deuterium signal of the solvent if applicable. The  $^1\text{H}$  and  $^{13}\text{C}\{^1\text{H}\}$  spectra were referenced to TMS using the deuterated solvent peaks as secondary references. Unless otherwise indicated, all spectra were obtained at 303.0 K.

#### **Referencing of $^{125}\text{Te}$ NMR measurements**

The resonance frequency of pure  $\text{Me}_2\text{Te}$  ( $\delta$  0.00 ppm) was determined at 303.0 K and used as the primary reference. A secondary standard of  $\text{Ph}_2\text{Te}_2$  in  $\text{CD}_2\text{Cl}_2$  ( $3.73 \times 10^{-4}$  M) was then measured giving  $\delta=420.36$  ppm; all other measurements were performed against this sample. The secondary standard was locked on the proton channel, and the shims manipulated to maximize the signal and ensure field homogeneity. At this point

the field was brought to a prescribed value of -4554 based on the results of early experiments before the lock was turned off. The broad band probe was tuned and matched to the  $^{125}\text{Te}$  resonance frequency of 157.79 MHz, and the field confirmed to have remained constant. In each experiment, the temperature was confirmed using the corresponding chemical shift thermometer to ensure accuracy in the reference. The data presented within this thesis is reported uncorrected for instrument drift, which was experimentally determined to result in a decrease in the chemical shift of 0.5 Hz (0.003 ppm) per hour.

### **Data Processing**

Data were processed using the XWINNMR or TOPSPIN 2.1 software packages. In all cases the free induction decay (FID) was processed with exponential multiplication and zero-filling before being Fourier transformed. For  $^{125}\text{Te}$  NMR, the Lorentzian broadening (LB) parameter was modified as necessary, but most commonly set to 2.

### **2.1.9 Second Harmonic Generation**

#### **Sample Preparation**

Solution samples were prepared using sample preparation methods similar to those used for UV-vis spectroscopy. Dye solutions were prepared using carefully weighed materials and calibrated volumetric glassware to achieve concentrations consistent with absorptions of no more than 0.1 absorbance units at 532 nm. Prior to data collection, each sample was filtered through a PTFE membrane to remove particulate matter.

### Instrumentation

A custom-built harmonic-light spectrometer<sup>75</sup> was employed for these measurements. The layout of the optics for the modified hyper-Rayleigh scattering (HRS) experiment is shown in **Figure 2.1**. An Nd:YAG laser (Continuum Surelite II<sup>TM</sup>) was used as a light source. This system delivered IR pulses with a repetition frequency of 10 Hz and a width of 5-7 ns, producing up to 655 mJ of energy at a wavelength of 1064 nm. The combination of an iris, a half-wave achromatic retarder and a polarizer was used to modulate the intensity of the laser ( $I_{\omega}$ ), which was monitored by a photodiode with a 177 ps rise time (Newport Model 818-BB-30) and a beam splitter. The intensity of light scattered in the visible was measured with an end-on photomultiplier tube (Oriel 773346) with an operating range of 185-850 nm, a gain above  $5 \times 10^5$ , a responsivity of  $3.4 \times 10^4$  A/W and a rise time of 15 ns. This detector received light through an assembly consisting of an 850 nm cut-off short-pass filter (CVI); a crown-glass plano-convex lens of diameter 25.4 mm and focal length 50 mm, and an interferential filter (CVI) centered at 532 nm with a nominal 10 nm full-width half-maximum (FWHM) spectral band. The photomultiplier tube (PMT) was normally operated under a 1000 V bias provided by a regulated power supply (Oriel 70705). The PMT output was delivered to a 350 MHz voltage amplifier (Oriel 70723). The responses of the two detectors were independently calibrated with a power meter (Melles Griot 13PEM001). The response of each detector was kept within its calibration range by means of neutral density filters (CVI) and

measured with a boxcar integrator (Stanford Research 250). The boxcar integrator output was acquired with a digital oscilloscope card (National Instruments NI 5112 PCI) installed in a PC and controlled with custom LabView Virtual Instrument software.

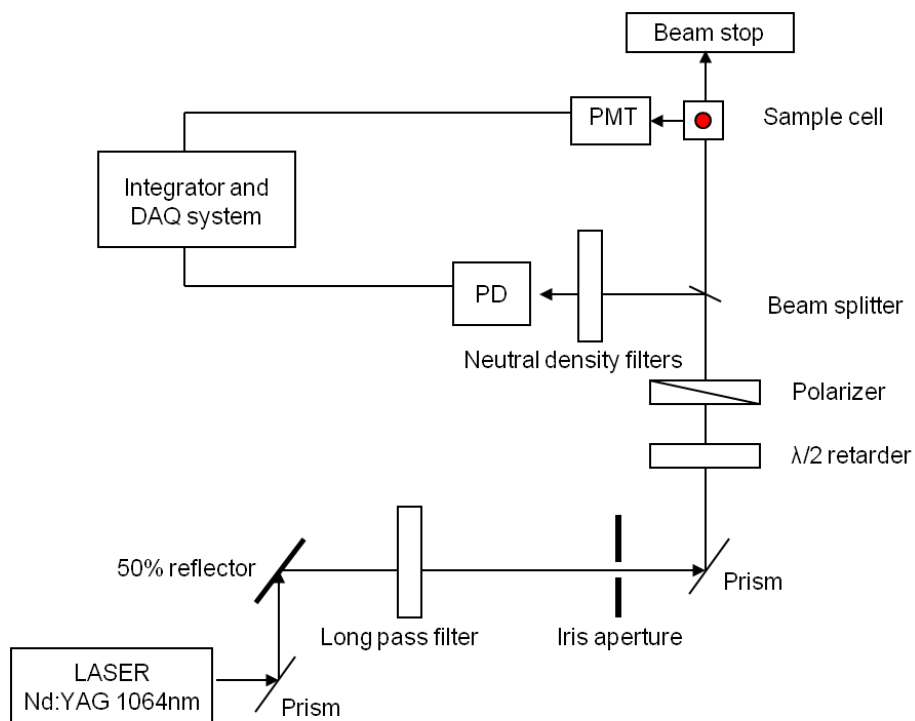


**Figure 2.1** Schematic of the Hyper-Rayleigh scattering SHG experiment.

A standard 5% (0.37 M) solution of *p*-nitroaniline in acetonitrile was used as a reference. In all cases, sample vials used for standardization were cleaned and re-used for sample trials. Special care was taken to ensure the incident beam was consistently striking the same location.

### Data Processing

The averaged intensity of the signal ( $I_{2\omega}$ ) was fitted to equation 2.1 where  $I_\omega$  is the averaged intensity of the pump measured at the reference photodiode,  $N$  is the *number density* (scattering units per unit of volume) and  $\langle \beta^2 \rangle$  the square of the orientational average of the hyperpolarisability tensor. The calibration factor,  $G$ , incorporates local field effects as well as geometric factors, it was determined for each cell by fitting the data from the reference standard to the equation.

$$I_{2\omega} = GN \langle \beta^2 \rangle I_\omega^2 \quad 2.1$$

#### 2.1.10 High-Performance Liquid Chromatography

##### Sample Preparation

Solutions were prepared using carefully weighed materials and calibrated volumetric glassware to achieve concentrations consistent with absorptions of 1.0 absorbance unit at the wavelength of maximum absorption observed in the UV-vis spectra. Prior to data collection, each sample was filtered through a polytetrafluoroethylene (PTFE) membrane to remove particulate matter. All solvents were filtered through PTFE or hydrophilic membranes and sparged with helium gas for 30 minutes before use. Prior to any injection, all lines were primed by repeatedly withdrawing solvent using a teflon syringe.

##### Separations

Analytical runs for method development were performed at room temperature on a Waters Spherisorb 5  $\mu\text{m}$  ODS2 analytical column (4.6 x 150 mm, flow rate 2 mL min<sup>-1</sup>)

using 20  $\mu\text{L}$  injections. Semipreparative runs were performed at room temperature on a Waters Spherisorb S5 ODS2 semipreparative column (10 x 250 mm, flow rate 4-8 mL  $\text{min}^{-1}$ ) using 100  $\mu\text{L}$  injections. In all injections, the Waters 600E Multisolvant Delivery System (Waters 600 Controller, Waters 600E Pump) was used, and separations were monitored with a Waters 2996 photodiode array detector in conjunction with the Empower control software. Eluted fractions were delivered to a Waters Fraction Collector II and recovered with an Eppendorf 5301 Centrifugal Concentrator.

## 2.2 Materials and Methods

All materials are reagent grade unless otherwise indicated. Trifluoroacetic acid (Caledon), 1,4-dioxane (BDH), and diethyl ether (Caledon) were freshly distilled prior to use. All other reagents were used as received from Sigma-Aldrich (p-nitroaniline, ethyl aniline, n-pentanol, mercury (II) trifluoroacetate, *p*-tolyl magnesium bromide, N,N-dimethyl benzenemethanamine, boron trifluoride etherate), Caledon (potassium hydroxide, zinc chloride, hydrochloric acid, sodium chloride, sodium acetate), Fisher (lithium chloride), Baker (iodine, sodium iodide), Alfa-Aesar (3,3-dimethylbutyne), Cerac (tellurium powder), EMD (sodium bicarbonate, sodium thiosulfate, sodium hydroxide, DMF), Acros (n-butyl lithium, acetic anhydride) and Shawinigan (sodium nitrite). Iodopentane,<sup>76,77</sup> Bipy•TeCl<sub>2</sub>,<sup>78</sup> tris(dimethylphenylsilyl)methane,<sup>79</sup> and bis(N,N-dimethylcarbamoyl)-ditelluride<sup>80</sup> were synthesized according to literature procedures.

Acetonitrile (Caledon, HPLC grade), dichloromethane (Caledon, HPLC grade), tetrahydrofuran (Caledon, HPLC grade) and toluene (Caledon, HPLC grade) were purified on an IT solvent purification system and stored over type 4Å molecular sieves. The silica gel used for column chromatography (EM Science) had a particle size of 40 – 63 µm. The manipulation of air-sensitive materials was performed under an atmosphere of nitrogen using standard Schlenk and glove box techniques. All manipulations of mercury and organomercury compounds were performed using methods designed to prevent exposure.

## 2.2.1 Syntheses

### 2.2.1.1 Ditellurides

**Bis(*p*-tolyl) ditelluride** (C<sub>14</sub>H<sub>14</sub>Te<sub>2</sub>) (**14**). The synthesis was performed with modifications to that reported by Irgolic<sup>81</sup> for bisphenyl ditelluride. To a sample of tellurium powder (3.12 g, 24.5 mmol) in a three-necked round-bottom flask connected to a vacuum line was added 15 mL anhydrous tetrahydrofuran (THF) prior to cooling with a liquid nitrogen/ethanol bath (-100 °C). A 1 M solution of *p*-tolyl magnesium bromide in THF (30 mL) was added dropwise with stirring and the system then warmed to room temperature. The vessel was stirred open to the atmosphere until a red colour persisted, then oxygen gas was slowly bubbled through the solution for 45 minutes, at which time the entire solution was dark red. This crude mixture was gravity filtered and extracted with ether. The combined ether layers were concentrated using a rotary evaporator and

the product was placed under dynamic vacuum overnight to remove traces of solvent. The product was further purified by sublimation under dynamic vacuum at 75 °C. Yield 2.48 g, 46%. mp: 50-52 °C. <sup>1</sup>H NMR (500.13 MHz, CDCl<sub>3</sub>, 7.26 ppm): δ = 2.38 (s, 6H, H<sub>C7</sub>), 7.01 (d, 4H, H<sub>C3</sub> H<sub>C3'</sub> H<sub>C5</sub> H<sub>C5'</sub>), 7.69 (d, 4H, H<sub>C2</sub> H<sub>C2'</sub> H<sub>C6</sub> H<sub>C6'</sub>). <sup>13</sup>C NMR (125.76 MHz, CDCl<sub>3</sub>, 77.2 ppm): δ = 21.2 (C7 C7'), 104.3 (C4 C4'), 130.3 (C3 C3' C5 C5'), 138.2 (C2 C2' C6 C6'), 138.4 (C1). <sup>125</sup>Te NMR (157.79 MHz, CDCl<sub>3</sub>): δ = 426.3. UV (CH<sub>2</sub>Cl<sub>2</sub>): λ<sub>max</sub> = 405 nm ε = 78,900 cm<sup>2</sup>/mol. HRMS (ES): m/z Calculated for [MH]<sup>+</sup> (C<sub>14</sub>H<sub>14</sub>Te<sub>2</sub>): 441.9220, Found 441.9216.

**2,2'-ditellurobis(N,N-dimethyl-benzenemethanamine)** (C<sub>18</sub>H<sub>24</sub>N<sub>2</sub>Te<sub>2</sub>) (**15**). This synthesis was performed using a modification of that reported by Kaur<sup>82</sup> and entirely under a red light to prevent photolysis. A sample of N,N-dimethyl-benzenemethanamine (1.53 mL, 10.1 mmol) was combined with 50 mL anhydrous ether in a side-arm round-bottom flask under a nitrogen atmosphere. To this was added dropwise a solution of n-butyl lithium (6.60 mL, 12.0 mmol) in cyclohexane, and the solution was left stirring for 24 h. Tellurium powder (1.29 g, 10.1 mmol) was placed inside a solid addition flask under an atmosphere of nitrogen, and added into the reaction mixture at once. The mixture was left to stir under nitrogen for an additional 4 hours, then poured into a beaker and stirred open to air for 10 min. Oxygen gas was then bubbled through the solution for 35 min, at which time a dark brown/yellow colour persisted. Distilled water (100 mL) was added to the beaker and oxygen bubbling was resumed for an additional 30 minutes.

The reaction mixture was then gravity filtered and extracted with ether. The product was purified by column chromatography with a 3:1 ether: toluene mixture. Yield = 1.240 g, 47%.  $^1\text{H}$  NMR (500.13 MHz,  $\text{CDCl}_3$ , 7.26 ppm): 2.31 ppm (s, 12H,  $\text{H}_{\text{C}8}$ ), 3.56 (s, 4H,  $\text{H}_{\text{C}7}$ ), 7.02 (m, 4H,  $\text{H}_{\text{C}3}$   $\text{H}_{\text{C}4}$ ), 7.11 (dd, 2H,  $\text{H}_{\text{C}5}$ ), 8.00 (d, 2H,  $\text{H}_{\text{C}6}$ ).  $^{13}\text{C}$ -DEPTq NMR (125.76 MHz,  $\text{CDCl}_3$ , 77.2 ppm): 44.2 ppm (C8), 66.7 (C7), 113.4 (C1), 126.5 (C5), 128.4 (C3), 139.3 (C6), 141.3 (C2).  $^{125}\text{Te}$  NMR (157.79 MHz,  $\text{CDCl}_3$ ):  $\delta = 352.6$  ppm.

**Bis(tris-dimethylphenylsilyl)methyl ditelluride** ( $\text{C}_{50}\text{H}_{66}\text{Si}_6\text{Te}_2$ ) (**16**): To a solution of 0.785 g (1.885 mmol) of tris-dimethylphenylsilylmethane<sup>79</sup> in 12.0 mL of THF was added 1.3 mL (2.08 mmol) of 1.6 M solution of methyl lithium in ether. After the ether was removed under vacuum, the remaining solution was refluxed 4 h prior to cooling to 25 °C. The solution was transferred by canula onto 0.24 g (1.88 mmol) of tellurium powder in one side of a double-flask, with an adjoining coarse frit. The slurry was stirred for 3 h at room temperature then filtered through the glass frit to remove unreacted tellurium. The filtrate was evacuated to dryness, re-dissolved in 5.0 mL fresh THF, then diluted with a solution of 0.235 g (0.924 mmol) iodine in 10.0 mL hexanes. After 1 h stirring at room temperature, the solvents were removed in vacuo then extracted with acetone until the extracts were colourless. To these combined extracts was added an equivalent volume of water, then the mixture was filtered by suction to obtain a dark coloured solid, which was rinsed repeatedly with MeOH and pentane to remove unreacted iodine. The crude product could be further purified by filtering DCM solutions through a layer of silica. Evaporation of these solvents yielded **16** as bright green prisms.

Yield = crude 0.359 g, 35%; after purification 0.091 g, 25%.  $^1\text{H}$  NMR (500.13 MHz,  $\text{CD}_2\text{Cl}_2$ , 5.32 ppm):  $\delta$  = 0.56 ppm (s, 32H,  $\text{CH}_3$ ), 7.09 (m, 12H,  $\text{H}_{\text{aryl}}$ ), 7.20 (m, 18H,  $\text{H}_{\text{aryl}}$ ). (Due to low solubility, the  $^{13}\text{C}$  spectra could not be obtained.)  $^{125}\text{Te}$  NMR (157.79 MHz, toluene- $d_8$ ):  $\delta$  = 427.0 ppm.

### 2.2.1.2 Azodyes

#### Preparation of the Dye

**N-Ethyl-N-pentyl aniline** ( $\text{C}_{13}\text{H}_{21}\text{N}$ ). N,-ethyl-N-pentyl aniline was prepared using a modification of Khan's procedure;<sup>83</sup> the iodinated alkane was used in place of the alkyl bromide. In a typical reaction a mixture of 1-iodopentane (20 mL, 0.153 mol) and ethylaniline (13 mL, 0.103 mol) was added to potassium hydroxide (6.192 g, 0.110 mol) under a nitrogen atmosphere. The mixture was refluxed with stirring for 6 h, and the product was isolated as a clear, colourless liquid after purification by distillation (68 °C, 0.4 torr). Yield: 15.03 g, 76%.  $^1\text{H}$  NMR (500.13 MHz,  $\text{CDCl}_3$ , 7.26 ppm):  $\delta$  = 0.93 (t, 3H), 1.16 (t, 3H), 1.32 (m, 2H), 1.36 (m, 2H), 1.60 (m, 2H), 3.25 (t, 2H), 3.38 (q, 2H), 6.64 (m, 2H), 6.68 (d, 2H), 7.22 (t, 1H).  $^{13}\text{C}$ -DEPTq NMR (125.76 MHz,  $\text{CDCl}_3$ , 77.1 ppm): 12.4 (s, 1C, C14), 14.1 (s, 1C, C19), 22.7 (s, 1C, C17), 27.1 (s, 1C, C16), 29.5 (s, 1C, C18), 44.8 (s, 1C, C13), 50.4 (s, 1C, C15), 111.6 (s, 2C, C9 C11), 115.2 (s, 2C, C8 C12), 129.2 (s, 1C, C7), 147.9 (s, 1C, C10). HRMS (EI, %):  $m/z$  Found: 191.1679 ( $\text{M}^+$ , 15) Calculated 191.1674.

**N-Ethyl-4-[4-nitrophenyl]diazenyl] N-pentylaniline** (C<sub>19</sub>H<sub>24</sub>N<sub>4</sub>O<sub>2</sub>) (27).

Synthesis was performed with minor modifications to the standard diazonium coupling method;<sup>84</sup> the addition of sodium nitrite was controlled by testing the solution periodically with starch-iodide paper, and a crystal of sodium sulphite was used to destroy any excess of nitrous acid. A sample of *p*-nitroaniline (1.79 g, 13.0 mmol) was placed in 40 mL of 5M HCl at 0 °C. A second sample containing sodium nitrite (0.897 g, 13.0 mmol) dissolved in water was then added, maintaining a constant temperature below 4 °C. The mixture was stirred for 15 min prior to the addition of N,-ethyl-N-pentyl aniline (2.502 g, 13.1 mmol). After stirring for 1 h, a minimal amount of sodium acetate (16.517 g, 0.201 mol) was added to neutralize the acid. The dark red product was isolated by filtration and purified by column chromatography (100% CHCl<sub>3</sub>). Yield: crude 4.22 g, 95%; after purification 3.889 g, 88%. <sup>1</sup>H NMR (500.13 MHz, CD<sub>2</sub>Cl<sub>2</sub>, 5.32 ppm): δ = 0.94 (t, 3H), 1.25 (t, 3H), 1.39 (m, 4H), 1.69 (q, 2H), 3.41 (t, 2H), 3.51 (q, 2H), 6.80 (d, 2H), 7.93 (d, 2H), 7.95 (d, 2H), 8.31 (d, 2H). <sup>13</sup>C-DEPTq NMR (125.76 MHz, CD<sub>2</sub>Cl<sub>2</sub>, 54.0 ppm): δ = 12.4 (s, 1C, C14), 14.1 (s, 1C, C19), 22.8 (s, 1C, C18), 27.4 (s, 1C, C16), 29.6 (s, 1C, C17), 45.6 (s, 1C, C13), 50.9 (s, 1C, C15), 111.6 (s, 2C, C9 C11), 122.8 (s, 2C, C3 C5), 125.1 (s, 2C, C2 C6), 126.7 (s, 2C, C8 C12), 143.6 (s, 1C, C7), 147.6 (s, 1C, C4), 152.3 (s, 1C, C10), 157.8 (s, 1C, C1). MP = 110 – 112 °C. UV (CH<sub>2</sub>Cl<sub>2</sub>): λ<sub>max</sub> = 498 nm, ε = 19000 cm<sup>2</sup>/mol. IR (cm<sup>-1</sup>): 3732w, 3098w, 2951m, 2926m, 2869m, 1598s, 1584s, 1557m, 1515s, 1465w, 1455w, 1420w, 1404w, 1376s, 1360s, 1337s, 1307s, 1270s, 1254s, 1216m, 1189m, 1151m, 1139s, 1126s, 1102s, 1072m, 984w, 858m, 830m, 795w,

754w, 735w, 725w, 687w, 666w, 637w, 614w, 585w, 563w, 537w, 510w. HRMS (EI, %):  $m/z$  Found: 340.1906 ( $M^+$ , 13) Calculated 340.1899.

### **Mercuration Procedure**

**CAUTION.** Mercury compounds are very toxic, exposure to them should be avoided at all times.

**N-Ethyl-4-[(2-chloromercurio-4-nitrophenyl)diazenyl]      N-pentylaniline**  
( $C_{19}H_{23}N_4O_2HgCl$ ) (**31**). In a typical reaction, dry **27** (0.064 g, 0.189 mmol) and mercury trifluoroacetate (0.159 g, 3.72 mmol) were combined with freshly distilled trifluoroacetic acid (0.13 mL) under a nitrogen atmosphere. The mixture was heated with stirring for 4 h in an oil bath at 68 °C, after which a concentrated solution of sodium chloride (0.055 g, 0.942 mmol) and sodium acetate (0.190 g, 2.31 mmol) was added and the entire sample was placed in an ultrasonic bath for 10 min. The crude product was extracted with dichloromethane and dried. Extraction of the residues with hexanes removed unreacted starting material, leaving spectroscopically pure mercurated dye. Yield = 0.067 g, 62%.  $^1H$  NMR (500.13 MHz,  $CD_2Cl_2$ , 5.32 ppm):  $\delta$  = 0.94 (t, 3H), 1.25 (t, 3H), 1.39 (m, 4H), 1.69 (q, 2H), 3.41 (t, 2H), 3.51 (q, 2H), 6.80 (d, 2H), 8.06 (d, 2H), 8.08 (d, 2H), 8.29 (dd, 2H), 8.39 (d, 2H).  $^{13}C$ -DEPTq NMR (125.76 MHz,  $CD_2Cl_2$ , 54.0 ppm):  $\delta$  = 12.6 (s, 1C, C14), 14.2 (s, 1C, C19), 23.2 (s, 1C, C18), 27.8 (s, 1C, C16), 29.6 (s, 1C, C17), 46.1 (s, 1C, C13), 51.4 (s, 1C, C15), 125.5 (s, 1C, C6), 127.5 (s, 2C, C9 C11), 130.2 (s, 1C, C5),

132.8 (s, C, C2), 137.5 (s, 1C, C7), 141.8 (s, 1C, C10), 148.1 (s, 1C, C4), 159.6 (s, 1C, C1).

### Metathesis Reactions

**Iodination of mercurials.** Iodine (0.202 g, 0.80 mmol) was added to the crude mercurated dye residues in a minimum amount of chloroform. This solution was stirred for 48 h and then extracted with concentrated sodium bicarbonate. A sodium thiosulphate solution was added and the mixture was stirred for 5 min. The organic phase was separated and dehydrated with sodium sulphate then evaporated to dryness. The residue was treated with a mixture of acetonitrile-water (85% v/v) and separated using semi-preparative HPLC with 100  $\mu$ L injections. The method employed a stepwise elution gradient that began isocratic 86% v/v for 14 min, before changing to 100% acetonitrile with a linear gradient over 1 min. Individual fractions were collected to recover the two major products, which were in order of elution:

**N-Ethyl-4-[(2,6-diiodo-4-nitrophenyl)diazenyl] N-pentylaniline** ( $C_{19}H_{22}N_4O_2I_2$ )  
**(34).**  $t_r = 12.4$  min.  $^1H$  NMR (500.13 MHz,  $CD_2Cl_2$ , 5.32 ppm):  $\delta = 0.94$  (t, 3H,  $H_{C19}$ ), 1.25 (t, 3H,  $H_{C14}$ ), 1.39 (m, 4H,  $H_{C17}$   $H_{C18}$ ), 1.69 (q, 2H,  $H_{C16}$ ), 3.41 (t, 2H,  $H_{C15}$ ), 3.51 (q, 2H,  $H_{C13}$ ), 6.68 (d, 2H,  $H_{C2}$   $H_{C6}$ ), 7.91 (d, 2H,  $H_{C3}$   $H_{C5}$ ), 8.76 (s, 2H,  $H_{C9}$   $H_{C11}$ ).  $^{13}C$ -DEPTq NMR (125.76 MHz,  $CD_2Cl_2$ , 54.0 ppm):  $\delta = 12.6$  (s, 1C, C14), 14.2 (s, 1C, C19), 23.0 (s, 1C, C18), 27.7 (s, 1C, C16), 29.9 (s, 1C, C17), 46.1 (s, 1C, C13), 51.4 (s, 1C,

C15), 87.8 (s, 2C, C8 C12), 111.8 (s, 2C, C2 C6), 127.2 (s, 2C, C3 C5), 135.9 (s, 2C, C9 C11), 145.7 (s, 1C, C4), 147.0 (s, 1C, C7), 152.9 (s, 1C, C1), 159.4 (s, 1C, C10). UV (CH<sub>2</sub>Cl<sub>2</sub>):  $\lambda_{\max}$  = 460 nm,  $\epsilon$  = 13000 cm<sup>2</sup>/mol. IR (cm<sup>-1</sup>): 3732w, 3363w, 3186w, 3088w, 3071w, 2957m, 2923s, 2852m, 1733w, 1646w, 1632w, 1605m, 1570w, 1556w, 1524w, 1508w, 1462w, 1410w, 1371w, 1333m, 1311w, 1275w, 1260w, 1216w, 1196w, 1184w, 1137m, 1114w, 1073w, 1043w, 995w, 946w, 914w, 893w, 879w, 822w, 795w, 749w, 739w, 720w, 703w, 525w, 503w. HRMS (EI, %): *m/z* Found: 591.9828 (M<sup>+</sup>, 100) Calculated: 591.9832.

**N-Ethyl-4-[(2-iodo-4-nitrophenyl)diazenyl] N-pentylaniline (C<sub>19</sub>H<sub>23</sub>N<sub>4</sub>O<sub>2</sub>I) (33).**

*t<sub>r</sub>* = 14.2 min. <sup>1</sup>H NMR (500.13 MHz, CD<sub>2</sub>Cl<sub>2</sub>, 5.32 ppm):  $\delta$  = 0.94 (t, 3H, H<sub>C19</sub>), 1.25 (t, 3H, H<sub>C14</sub>), 1.39 (m, 4H, H<sub>C17</sub> H<sub>C18</sub>), 1.69 (q, 2H, H<sub>C16</sub>), 3.41 (t, 2H, H<sub>C15</sub>), 3.51 (q, 2H, H<sub>C13</sub>), 6.82 (d, 2H, H<sub>C2</sub> H<sub>C6</sub>), 7.68 (d, 1H, H<sub>C12</sub>), 7.94 (d, 2H, H<sub>C3</sub> H<sub>C5</sub>), 8.24 (dd, 1H, H<sub>C11</sub>), 8.81 (d, 1H, H<sub>C9</sub>). <sup>13</sup>C-DEPTq NMR (125.76 MHz, CD<sub>2</sub>Cl<sub>2</sub>, 54.0 ppm):  $\delta$  = 12.7 (s, 1C, C14), 14.4 (s, 1C, C19), 23.1 (s, 1C, C18), 27.8 (s, 1C, C16), 29.8 (s, 1C, C17), 46.1 (s, 1C, C13), 51.4 (s, 1C, C15), 100.0 (s, 1C, C12), 112.0 (s, 2C, C2 C6), 117.5 (s, 1C, C8), 124.8 (s, 1C, C9), 127.7 (s, 2C, C5 C3), 135.4 (s, 1C, C11), 144.0 (s, 1C, C4), 147.7 (s, 1C, C7), 153.7 (s, 1C, C1), 156.3 (s, 1C, C10). UV (CH<sub>2</sub>Cl<sub>2</sub>):  $\lambda_{\max}$  = 520 nm,  $\epsilon$  = 27000 cm<sup>2</sup>/mol. IR (cm<sup>-1</sup>): 3186w, 3086w, 2953m, 2921s, 2851m, 1734w, 1645w, 1600s, 1570m, 1555m, 1515s, 1436w, 1400m, 1357m, 1325s, 1314s, 1307s, 1262s, 1233s, 1196w, 1139s, 1104s, 1073m, 1024m, 992w, 892w, 869m, 834w, 818m, 798w, 747w,

727w, 691w, 634w, 566w, 539w, 518w. HRMS (EI, %):  $m/z$  Found: 466.0866 ( $M^+$ , 65)  
Calculated: 466.0866.

**[(2-Iodo-4-nitrophenyl)diazenyl]N,N-dimethylaniline** ( $C_{14}H_{13}N_4O_2I$ ) (**30**). The compound was prepared using the above mercuration method from 4-nitroaniline (1.02 g, 7.39 mmol) and N,N-dimethylaniline (0.887 g, 7.33 mmol), followed by mercuration of a small amount of material (0.0317g, 0.117 mmol) with  $Hg(CF_3CO_2)_2$  (0.120 g, 0.281 mmol) and treatment with iodine (0.203 g, 0.798 mmol), yielding a dark red powder (0.245 g, 0.906 mmol, 48%). Crystals suitable for X-ray diffraction were grown by slow evaporation of a chloroform/toluene solution.  $^1H$  NMR (500.13 MHz,  $CD_2Cl_2$ , 5.32 ppm):  $\delta$  = 3.13 (s, 6H,  $N(CH_3)_2$ ), 6.78 (d, 2H, H2 H6), 7.66 (d, 2H, H9), 7.94 (d, 2H, H5 H3), 8.22 (dd, 2H, H8), 8.79 (d, 1H, H11).  $^{13}C$ -DEPTq NMR (125.76 MHz,  $CD_2Cl_2$ , 54.0 ppm): 40.6 (s, 2C,  $N(CH_3)_2$ ), 99.8 (s, 1C, C7), 112.2 (s, 2C, C2 C6), 117.5 (s, 1C, C8), 124.8 (s, 1C, C9), 127.4 (s, 2C, C3 C5), 135.4 (s, 1C, C11), 145.2 (s, 1C, C4), 148.4 (s, 1C, C12), 154.5 (s, 1C, C1), 156.0 (s, 1C, C10). UV ( $CH_2Cl_2$ ):  $\lambda_{max}$  = 502 nm,  $\epsilon$  = 25000  $cm^2/mol$ . IR ( $cm^{-1}$ ): 3732w, 3087w, 2901w, 2854w, 2816w, 1610s, 1571m, 1553m, 1518s, 1506s, 1441w, 1416m, 1409m, 1357s, 1327s, 1306s, 1258m, 1238m, 1196w, 1139s, 1105s, 1064m, 1028w, 995w, 940w, 899w, 886w, 832w, 820m, 747w, 725w, 699w, 690w, 634w, 549w, 537w, 520w, 511w. HRMS (EI, %):  $m/z$  Found: 396.0094 ( $M^+$ , 100) Calculated: 396.0083.

**2,2'-diiodo Azobenzene** ( $C_{12}H_8N_2I_2$ ) (**28**). Azobenzene (0.184 g, 1.01 mmol) and mercury trifluoroacetate (0.43 g, 1.01 mmol) were combined with freshly distilled trifluoroacetic acid (0.13 mL) under a nitrogen atmosphere. The mixture was heated with stirring for 4 h in an oil bath at 68 °C, after which a concentrated solution of sodium chloride (0.345 g, 5.90 mmol) and sodium acetate (2.085 g, 14.7 mmol) was added and the entire sample was placed in an ultrasonic bath for 20 min, then let settle. After decanting the solvent, a mixture of iodine (0.279 g, 1.10 mmol) in methanol was added. With time, crystals of **28** precipitated from solution and were collected by filtration. Yield = 0.047 g, 10%.  $^1H$  NMR (500.13 MHz,  $CD_2Cl_2$ , 5.32 ppm):  $\delta$  = 7.23 (dd, 2H, H5 H5'), 7.48 (dd, 2H, H4 H4'), 7.75 (d, 2H, H6 H6'), 8.06 (d, 2H, H3 H3').  $^{13}C$ -DEPTq NMR (125.76 MHz,  $CD_2Cl_2$ , 54.0 ppm):  $\delta$  = 103.4 (s, 2C, C1 C1'), 118.6 (s, 2C, C6 C6'), 129.6 (s, 2C, C4 C4'), 133.4 (s, 2C, C5 C5'), 140.6 (s, 2C, C3 C3'), 151.2 (s, 2C, C2 C2')

**Metathesis with Chalcogen Halides.** In a typical reaction, 0.39 mmol mercurated dye was combined with 0.47 mmol of the corresponding chalcogen source. Following the addition of 10 mL 1,4-dioxane, the mixture was heated at reflux for 5 h, then cooled and evaporated to dryness. The residues were then extracted with dichloromethane to remove the mercurated salts, and the extracts evaporated to dryness. Subsequent purification methods are described below.

**N-Ethyl-4-[(2-chloroselenenyl-4-nitrophenyl)diazenyl]****N-pentylaniline**

(C<sub>19</sub>H<sub>23</sub>N<sub>4</sub>O<sub>2</sub>SeCl) (**41**) This product was obtained from the general metathesis reaction using the 1:1 addition product of selenium tetrachloride and elemental selenium. The product was further purified by column chromatography using dichloromethane as an eluent. Yield = isolated 0.168 g, 95%; purified 0.157 g, 89%. <sup>1</sup>H NMR (500.13 MHz, CD<sub>2</sub>Cl<sub>2</sub>, 5.32 ppm): δ = 0.95 (t, 3H, H19), 1.27 (t, 3H, H14), 1.39 (m, 4H, H17 H18), 1.69 (m, 2H, H16), 3.43 (t, 2H, H15), 3.53 (q, 2H, H13), 6.77 (d, 2H, H9 H11), 8.07 (m, 2H, H8 H12), 8.32 (d, 1H, H3), 8.38 (dd, 1H, H6), 9.49 (d, 1H, H6). (Due to low concentrations, the <sup>13</sup>C spectra could not be obtained) UV (CH<sub>3</sub>CN): λ<sub>max</sub> = 590 nm, ε = 27000 cm<sup>2</sup>/mol.

**N-Ethyl-4-[(2-chlorotellurenyl-4-nitrophenyl)diazenyl]****N-pentylaniline**

(C<sub>19</sub>H<sub>23</sub>N<sub>4</sub>O<sub>2</sub>TeCl) (**45**) This product was obtained using the general metathesis reaction and the tellurium dichloride bipyridyl salt<sup>78</sup> as a chalcogen source. Yield = 0.189, 95%. <sup>1</sup>H NMR (600 MHz, CD<sub>2</sub>Cl<sub>2</sub>, 5.32 ppm): δ = 0.94 (t, 3H, H19), 1.26 (t, 3H, H14), 1.38 (m, 4H, H17 H18), 1.69 (m, 2H, H16), 3.41 (t, 2H, H15), 3.51 (q, 2H, H13), 6.73 (d, 2H, H9 H11), 7.97 (m, 2H, H8 H12), 8.34 (dd, 1H, H2), 8.38 (d, 1H, H3), 9.25 (d, 1H, H6). <sup>13</sup>C-DEPTq NMR (500.13 MHz, CD<sub>2</sub>Cl<sub>2</sub>, 54.0 ppm): δ = 12.1 (s, 1C, C14), 13.7 (s, 1C, C19), 22.4 (s, 1C, C18), 27.0 (s, 1C, C16), 29.1 (s, 1C, C17), 45.8 (s, 1C, C13), 50.9 (s, 1C, C15), 112.2 (s, 2C, C9 C11), 122.6 (s, 2C, C2), 121.5 (s, 1C, C2), 125.0 (s, 2C, C8 C12), 128.2 (s, 1C, C6), 129.6 (s, 1C, C3), 143.2 (s, 1C, C7). (Due to low concentrations,

the quaternary carbons were not observed.)  $^{125}\text{Te}$  NMR (157.79 MHz,  $\text{CD}_2\text{Cl}_2$ ):  $\delta = 1331.7$  ppm. UV ( $\text{CH}_3\text{CN}$ ):  $\lambda_{\text{max}} = 615$  nm,  $\epsilon = 18500$   $\text{cm}^2/\text{mol}$ .

**N-Ethyl-4-[(2-phenylselenenyl-4-nitrophenyl)diazenyl]      N-pentylaniline**

( $\text{C}_{25}\text{H}_{28}\text{N}_4\text{O}_2\text{Se}$ ) (**53**) This product was obtained from the general metathesis reaction using phenylselenenyl chloride as a chalcogen source. The product could be purified by HPLC using a stepwise elution gradient that began isocratic 80% v/v (water:acetone) for 10 min, before changing to 100% acetonitrile with a linear gradient over 1 min. Yield = 63% (based on multiple 100  $\mu\text{L}$  injections).  $t_r = 17.2$  min.  $^1\text{H}$  NMR (500.13 MHz,  $\text{CD}_2\text{Cl}_2$ , 5.32 ppm):  $\delta = 0.94$  (t, 3H, H19), 1.23 (t, 3H, H14), 1.39 (m, 4H, H17 H18), 1.67 (m, 2H, H16), 3.39 (t, 2H, H15), 3.49 (q, 2H, H13), 6.77 (d, 2H, H9 H11), 7.49 (t, 1H, H23), 7.53 (m, 2H, H22 H24), 7.70 (d, 1H, H6), 7.76 (d, 2H, H21 H25), 7.82 (d, 1H, H3), 7.93 (d, 2H, H8 H12), 8.01 (dd, 1H, H2).  $^{13}\text{C}$ -DEPTq NMR (125.76 MHz,  $\text{CD}_2\text{Cl}_2$ , 54.0 ppm):  $\delta = 12.6$  (s, 1C, C14), 14.4 (s, 1C, C19), 23.1 (s, 1C, C18), 27.6 (s, 1C, C16), 29.5 (s, 1C, C17), 45.8 (s, 1C, C13), 51.1 (s, 1C, C15), 111.7 (s, 2C, C9 C11), 120.6 (s, 2C, C3), 121.5 (s, 1C, C2), 124.3 (s, 1C, C6), 126.9 (s, 2C, C8 C12), 128.4 (s, 1C, C20), 130.1 (s, 1C, C23), 130.6 (s, 2C, C22 C24), 136.3 (s, 1C, C4), 137.6 (s, 2C, C21 C25), 143.2 (s, 1C, C7), 147.4 (s, 1C, C5), 152.2 (s, 1C, C10), 153.3 (s, 1C, C1). UV ( $\text{CH}_3\text{CN}$ ):  $\lambda_{\text{max}} = 526$  nm,  $\epsilon = 12000$   $\text{cm}^2 \text{mol}^{-1}$ . HRMS (ES, %):  $m/z$  Found: 497.1456 ( $\text{M} + \text{H}^+$ , 100) Calculated: 497.1757.

**2.2.1.3 3,9,15,21-tetrakis(1,1-dimethylethyl)-1,7,13,19-tetramethyl-  
1,4,7,10,2,5,8,11,3,6,9,12-tetraoxatetratelluratetraazacyclododecane**

**5,5-dimethyl, 3 hexyn-2-one, (C<sub>8</sub>H<sub>12</sub>O) (67):** A solution of 3,3-dimethyl butyne (5.0 mL in 50 mL anhydrous THF) was cooled to -78° C prior to the dropwise addition of n-butyl lithium (18.0 mL, 2.5 M solution in ether). This solution was stirred at low temperature for 1h, boron trifluoride etherate (4.7 mL, 4.5 mmol) was added, and the entire solution stirred for an additional 15 min. A separate solution of acetic anhydride (6.36 mL, 6.75 mmol) in 10 mL THF was then added at once, and the solution took on a vibrant yellow colour. After 20 min, an aqueous sodium hydroxide solution (7.0 mL) was added dropwise, then the flask was allowed to slowly warm to room temperature. The reaction was basified completely using aqueous sodium hydroxide, then extracted with ether and brine. The combined organic fractions were evaporated to dryness then distilled (20 mbar, 50 °C) to isolate the pure ynone. Yield = 2.059 g, 38%. <sup>1</sup>H NMR (500.13 MHz, CD<sub>2</sub>Cl<sub>2</sub>, 5.32 ppm): 1.27 (s, 12H), 2.27 (s, 3H).

**(Z)-Te-2,2-dimethyl-5-oxohex-3-en-3-yl dimethylcarbamotelluroate,**  
(C<sub>11</sub>H<sub>19</sub>O<sub>2</sub>N<sub>2</sub>Te) (**68**): An excess of sodium borohydride (63 mg in 5 mL of methanol, 2.2 equivalents) was slowly added to bis(N,N-dimethylcarbamoyl)-ditelluride<sup>80</sup> (300 mg in 10 mL of DMF, 0.75 mmol) at -78°. The mixture was warmed up to 0°C and **67** (342 mg, 2.2 equivalents) was added dropwise. After 7 h the reaction was quenched by careful

addition of 10 mL of water. The mixture was filtered and extracted with toluene multiple times. The organic layer was washed with water, dehydrated and evaporated to dryness. The residue was purified by column chromatography (silica, 95:5 CH<sub>2</sub>Cl<sub>2</sub>/MeOH). Solvent evaporation afforded a yellow oil. Yield = 0.12 g, 25%. <sup>1</sup>H NMR (500.13 MHz, CD<sub>2</sub>Cl<sub>2</sub>, 5.32 ppm): 6.80 (s, 1H, CH); 2.94 (s, 6H, N(CH<sub>3</sub>)<sub>2</sub>); 2.20 (s, 3H, CH<sub>3</sub>); 1.22 (s, 9H, C(CH<sub>3</sub>)<sub>3</sub>). <sup>13</sup>C-DEPTq NMR (125.76 MHz, CD<sub>2</sub>Cl<sub>2</sub>, 54.0 ppm): 199.6 (s, 1C, C(O)CH<sub>3</sub>), 156.9 (s, 1C, NC(O)), 151.6 (s, 1C, Te-C=C), 133.4 (s, 1C, Te-C=C), 41.4 (C(CH<sub>3</sub>)<sub>3</sub>), 35.9 (s, 2C, N(CH<sub>3</sub>)<sub>2</sub>), 31.2 (s, 1C, C(O)CH<sub>3</sub>), 30.7 (s, 3C, C(CH<sub>3</sub>)<sub>3</sub>) <sup>125</sup>Te NMR (157.79 MHz, CD<sub>2</sub>Cl<sub>2</sub>): 656 (d, |<sup>3</sup>J(<sup>125</sup>Te, <sup>1</sup>H)| = 13.6 Hz). MS (ES): m/z: 327.1 ([M]<sup>+</sup>, <sup>129</sup>Te), 325.0 ([M]<sup>+</sup>, <sup>127</sup>Te). HRMS (ES): m/z Calculated for [MH]<sup>+</sup> (C<sub>11</sub>H<sub>20</sub>O<sub>2</sub>N<sup>129</sup>Te): 328.0557, Found 328.0549.

**3,9,15,21-tetrakis(1,1-dimethylethyl)-1,7,13,19-tetramethyl- 1,4,7,10,2,5,8,11,3,6, 9,12-tetraoxatetratelluratetraazacyclododecane (C<sub>32</sub>H<sub>52</sub>O<sub>4</sub>N<sub>4</sub>Te<sub>4</sub>) (64).** An excess (4.4 equivalents) of hydroxylamine-O-sulfonic acid was added to the tellurocarbamate **68** (280 mg, 0.89 mmol) in 10 mL of anhydrous methanol. The mixture was refluxed for two hours and the resulting yellowish solution was cooled down to room temperature and diluted with water. The aqueous phase was extracted with toluene multiple times and the combined organic extracts were washed with water, dried and evaporated. The solid was extracted with ether two times. The remaining pale yellow solid can be recrystallized from hot chloroform to give small yellow crystals. Yield= 0.14 g, 60%. <sup>1</sup>H NMR (500.13

MHz, CD<sub>2</sub>Cl<sub>2</sub>, 5.32 ppm): 7.00 (s, <sup>1</sup>H, CH); 2.14 (s, 3H, CH<sub>3</sub>); 1.42 (s, 9H, C(CH<sub>3</sub>)<sub>3</sub>).  
<sup>13</sup>C-DEPTq NMR (125.76 MHz, CD<sub>2</sub>Cl<sub>2</sub>, 54.0 ppm): 168.9 (s, 1C, C-Te), 156.4 (s, 1C, C-N), 122.7 (s, 1C, C=C-C), 41.5 (s, 1C, C(CH<sub>3</sub>)), 32.1 (s, 3C, CH<sub>3</sub>), 16.0 (s, 1C, CH<sub>3</sub>).  
MS (CI<sup>+</sup>): 269 ([M<sup>1/4</sup>]<sup>+</sup>, <sup>129</sup>Te), 253.0 ([M<sup>1/4</sup>-O]<sup>+</sup>, <sup>129</sup>Te). HRMS (ES): m/z Calculated for [M<sup>1/4</sup>H]<sup>+</sup> (C<sub>8</sub>H<sub>14</sub>ON<sup>129</sup>Te): 270.0138, Found 270.0122. IR (cm<sup>-1</sup>): 2953(s), 2912(m), 2865(m), 1565(m), 1466(m), 1424(w), 1389(w), 1370(m), 1361(m), 1337(w), 1243(w), 1231(w), 1202(w), 1125(vs), 1030(w), 1001(w), 967(mw), 896(m), 842(w), 828(w), 794(w), 760(w), 756(w), 697(m).

### 2.3 Computational Details

The structures considered in these studies were optimized using the ADF DFT package (versions 2005.01 through 2010.02).<sup>85-87</sup> adiabatic local density approximation (ALDA) was used for the exchange-correlation kernel<sup>88,89</sup> and the differentiated static LDA expression was used with the Vosko-Wilk-Nusair parametrization.<sup>90</sup> Calculations of model geometries were gradient-corrected with the exchange and correlation functionals of the gradient correction proposed in 1988 by Becke<sup>91</sup> and Perdew<sup>92</sup> (BP86) or the exchange and correlation functionals of the gradient correction proposed in 1991 by Perdew and Wang (PW91).<sup>92,93</sup> Preliminary geometry optimisations were conducted using a small double- $\zeta$  basis set with frozen cores corresponding to the configuration of the preceding noble gas and no polarization functions; the resulting structures were further refined using a triple- $\zeta$  all-electron basis set with one polarization function and

applying the Zeroth Order Regular Approximation (ZORA)<sup>94-98</sup> formalism with the specially adapted basis sets. Symmetry constraints were used when a point group was applicable. Electronic excitations<sup>99-101</sup> and hyperpolarizabilities<sup>102-104</sup> were calculated using the time-dependent extension of density functional theory (TD-DFT)<sup>99-101</sup> as implemented within the ADF package; the Statistical Average of different model Potentials for occupied Kohn-Sham Orbitals (SAOP)<sup>105-107</sup> was used for the exchange-correlation potentials in the zeroth-order Kohn-Sham (KS) equations. Chemical shift calculations<sup>108-111</sup> were carried out on the <sup>125</sup>Te nucleus with the ZORA correction applied. The effect of solvent dielectric was approximated using the conductor-like screening model (COSMO);<sup>112-114</sup> in the case of hexanes and nitroethane, the appropriate constants for n-hexane and nitromethane were used as approximate models. Calculation of Fukui functions were performed with the ADF GUI (versions 2008.01 – 2010.02).<sup>115</sup> Additional visualization of the computational results was performed using Cerius2 (Accelrys) supplemented by the ADF SDK (SCM) interface and Molekel.<sup>116</sup>

### 3 A Detailed Study of the $^{125}\text{Te}$ NMR Shielding of Organo-Ditellurides in Solution

#### 3.1 Motivation

While SBIs are primarily characterized in the solid state through X-ray diffraction structural determinations, there are a variety of spectroscopic methods that offer an alternative for their study even outside of the crystalline state. For example, neutron diffraction of neat phosphorus tribromide provides evidence of strongly attractive interactions between the molecules in the liquid. These results are based on average distances between atoms, which are consistent with the presence of a significant amount of P-Br $\cdots$ P links.<sup>117</sup> It might be expected that if the SBIs significantly influence the electronic structures of the molecules, photoelectron spectroscopy could be used in the gas phase, but only individual molecules have been observed in such experiments, even when the interactions are strong.<sup>118</sup> Mass spectrometry has been able to detect aggregates of 1,2,5-telluradiazole derivatives in gas phase but the experiments are often complicated by side reactions.<sup>43</sup> Vibrational spectroscopy (IR and Raman) can provide valuable insight, but the large mass of the tellurium atom and the inherent weakness of these bonding interactions mean that the vibrations of interest would only appear at low wavenumbers. For their observation, one would need to go to the far IR, use low energy Raman or state-of-the-art terahertz spectrometers. The solutions of many organo-tellurium compounds are often coloured, making UV-vis spectroscopy an attractive alternative, but in some cases photoexcitation also leads to decomposition of the sample. Arguably the best and

most convenient method for the characterization of Te-centred SBIs in solution would be NMR, since it is non-destructive and  $^{125}\text{Te}$  nucleus has a spin of  $\frac{1}{2}$  with zero quadrupole moment, 6.99% natural abundance and relatively high receptivity ( $D^C = 12.7$ ).

Heavy elements commonly exhibit wide ranges of chemical shifts and are very sensitive to the environment. The  $^{125}\text{Te}$  nucleus itself has a range of resonances larger than 4000 ppm;<sup>119</sup> reported shifts range from -1214 ppm for  $(\text{Me}_3\text{Sn})_2\text{Te}^{120}$  to 3102 ppm for the  $\text{Se}_2\text{Te}_2^{2+}$  dication in 30% oleum.<sup>121</sup> Changes of environment resulting from SBI formation are a minor perturbation compared to the effect of covalent bond formation, so it is essential to consider all the factors that affect the chemical shift of  $^{125}\text{Te}$ . In this respect, modern computational methods could facilitate the analysis and interpretation of experimental spectra.

In the solid state, ditelluride and diselenide molecules are frequently associated through short contacts to the chalcogen, both intra- and intermolecular. Intramolecular secondary interactions are most commonly observed in the crystal structures of dichalcogenides substituted with functional groups that contain donor atoms; examples include short  $\text{Br}\cdots\text{Se}$  interactions (3.7356(4) Å) in bis[3-(bromomethyl)-2-naphthyl] diselenide,<sup>122</sup> and short  $\text{N}\cdots\text{E}$  contacts in the dialkyl-2-oxazolinyl substituted diarylditelluride (2.773 Å)<sup>123</sup> and diaryldiselenide (2.785 Å).<sup>124</sup>

In some cases, the effect of these interactions can be observed in solution NMR. There is an apparent correlation between the  $^{77}\text{Se}$  and  $^{125}\text{Te}$  chemical shifts and the  $\text{N}\cdots\text{E}$  SBI distance in the crystal structure for a number of diselenides<sup>123</sup> and ditellurides.<sup>124</sup> A

decrease in SBI bond length, and likely an increase in SBI strength, is accompanied by increases in the  $^{125}\text{Te}$  and  $^{77}\text{Se}$  chemical shift. The formation of multiple SBIs to the same nucleus results in a shift to lower resonance when comparing analogous mono- and diselenide species.<sup>125</sup> Intermolecular interactions in ditellurides are most commonly observed in the solid state with either Te atoms,<sup>126-129</sup> or aryl rings,<sup>130-132</sup> or through interactions with donor functional groups on adjacent molecules.<sup>133,134</sup> However, there is no information in the literature relating the effect of these intermolecular SBIs on the  $^{125}\text{Te}$  NMR chemical shift.

### 3.2 Objective and Method

The purpose of the studies described in this chapter was to establish whether the  $^{125}\text{Te}$  chemical shift could unequivocally be used to detect the formation and/or presence of secondary bonding interactions in solution. This would be possible if the magnitude of shielding changes induced by the SBIs is greater than the changes due to all other contributing factors. Therefore, this study included an examination of all variables that could affect the experimental determination of the  $^{125}\text{Te}$  chemical shift of a molecule prone to forming intermolecular SBIs. The most relevant principles of NMR are briefly reviewed next. This is followed by a justification of the experimental design, the results and their discussion.

### 3.3 NMR Shielding

The resonance frequency - and the chemical shift - of a nucleus in the NMR experiment is characteristic of the environment surrounding an active nucleus to an extent that this property is routinely used to demonstrate and monitor the deliberate transformation of functional groups in organic syntheses. The case of inorganic systems, especially those containing heavy elements, is much more complicated.

The application of an external magnetic field to a sample gives rise to a *chemical shift*, in that the local field experienced by a nucleus is not equal to the external field applied to the sample as a whole. This field attenuation is accounted for with the *shielding constant*  $\sigma$  (Eq. **3.1**).

$$B_{eff} = B_0(1 - \sigma) \tag{3.1}$$

By convention this shielding constant is usually reported in ppm with respect to a reference sample (Eq. **3.2**) in order to obtain a *chemical shift* ( $\delta$ ) corresponding to a specific nucleus.

$$\delta = \left( \frac{\sigma_{ref} - \sigma}{1 - \sigma_{ref}} \right) \tag{3.2}$$

The chemical shift of a nucleus depends on many factors, including effects of the medium, concentration and temperature, and large polarisable nuclei can be very sensitive to changes in the local environment. To fully understand how these factors affect the chemical shift, a detailed analysis of the shielding constant is presented next.

The shielding is described by a 3×3 tensor, the three diagonal terms of which are averaged to produce the *isotropic shielding constant* ( $\sigma$ ) that takes into account molecular rotations (tumbling) in solution. The  $\sigma_{zz}$  term in equation 3.3 refers to shielding parallel to the applied field, while the  $\sigma_{xx}$  and  $\sigma_{yy}$  terms arise due to circulation of electrons within the perpendicular  $xy$  plane.

$$\sigma = \frac{1}{3}(\sigma_{xx} + \sigma_{yy} + \sigma_{zz}) \quad 3.3$$

The three component terms can be expressed using the Ramsey equation, which treats the process of NMR as a perturbation on the ground-state molecular wave function.<sup>135</sup> Similar equations can be used to describe the  $\sigma_{xx}$  and  $\sigma_{yy}$  components, but for the sake of clarity this discussion will focus on the component aligned with the magnetic field ( $\sigma_{zz}$ ).

$$\sigma_{zz} = \frac{e^2}{2mc^2} \langle 0 | \frac{x^2 + y^2}{r^3} | 0 \rangle + \left( - \left( \frac{e\hbar}{2mc} \right)^2 \sum_n \left\{ \frac{\langle 0 | \hat{L}_z | n \rangle \langle n | \frac{2\hat{L}_z}{r^3} | 0 \rangle}{E_n - E_0} + \frac{\langle 0 | \frac{2\hat{L}_z}{r^3} | n \rangle \langle n | \hat{L}_z | 0 \rangle}{E_n - E_0} \right\} \right) \quad 3.4$$

Here the  $\sigma_{zz}$  component of the shielding constant is related to the orbital angular momentum operator,  $L_z$ , the energy difference between ground and excited states,  $E_n - E_0$ , and the average distance from the electron to the nucleus undergoing the transition,  $r$ . The first term in equation 3.4 describes the diamagnetic contribution to the shielding constant, which usually is interpreted as the result of the circulation of electrons around the nucleus as a result of the magnetic flux created by the applied field. The second term considers the paramagnetic contribution to the shielding constant, and is derived from the field-induced mixing of orbitals that results in asymmetric electron motion. This paramagnetic term can be greatly simplified using a mean excitation energy ( $\Delta E$ , the average of the energy difference between the ground and the most relevant excited states) and averaging the paramagnetic contributions to  $\sigma_{xx}$ ,  $\sigma_{yy}$ , and  $\sigma_{zz}$ .

$$\sigma_p = -\frac{2}{3} \left( \frac{e\hbar}{mc} \right)^2 \left\langle \frac{1}{r^3} \right\rangle \frac{1}{\Delta E} \quad 3.5$$

If the applied perturbation is small, the excitation can be approximated as the simple mixing of the ground and first excited state. This corresponds to the first excitation in the electronic spectrum, the energy of which can be calculated from the time-dependent

wavefunction or at least estimated from the HOMO-LUMO gap. Incorporation of this approximated paramagnetic constant and the diamagnetic terms for  $\sigma_{xx}$ ,  $\sigma_{yy}$ ,  $\sigma_{zz}$  into equation **3.3** yields the equation for the total (isotropic) shielding constant (Eq. **3.6**).

$$\sigma = \frac{1}{3} \left[ \frac{e^2}{2mc^2} \left( \langle 0 | \frac{y^2 + z^2}{r^3} | 0 \rangle + \langle 0 | \frac{x^2 + z^2}{r^3} | 0 \rangle + \langle 0 | \frac{x^2 + y^2}{r^3} | 0 \rangle \right) \right] + \left( -\frac{2}{3} \left( \frac{e\hbar}{mc} \right)^2 \left\langle \frac{1}{r^3} \right\rangle \frac{1}{\Delta E} \right) \quad \mathbf{3.6}$$

This equation has a linear form, with the shielding constant being proportional to the inverse of the approximated average transition energy. In this manner, a larger HOMO-LUMO gap results in a smaller paramagnetic shielding component, effectively increasing the overall shielding constant and the chemical shift. Equally, a smaller HOMO-LUMO gap should result in a smaller chemical shift.

Modern computational methods [Hartree Fock (HF) and Density Functional Theory (DFT)] allow for calculation of chemical shifts; the most accurate results are usually obtained for light elements. In the case of heavy nuclei, significant deviations from the experimental results are known for chemical shifts calculated by application of gauge-including atomic orbitals (GIAO) and DFT. For example, for the  $^{125}\text{Te}$  nucleus the average deviation is on the order of 200 ppm (**Figure 3.1**).<sup>136</sup> In good part the problem is due to the lack of modeling of local environmental effects such as solvation.<sup>137-139</sup> The chemical shift is known to be dependent on effects of the medium (possible structural changes, the solvent dielectric properties, solvent-solute interactions), concentration (auto-association, volume susceptibility) and temperature. All of these effects would have

to be considered in order to attempt bringing the calculated chemical shifts closer in line with experimental results.

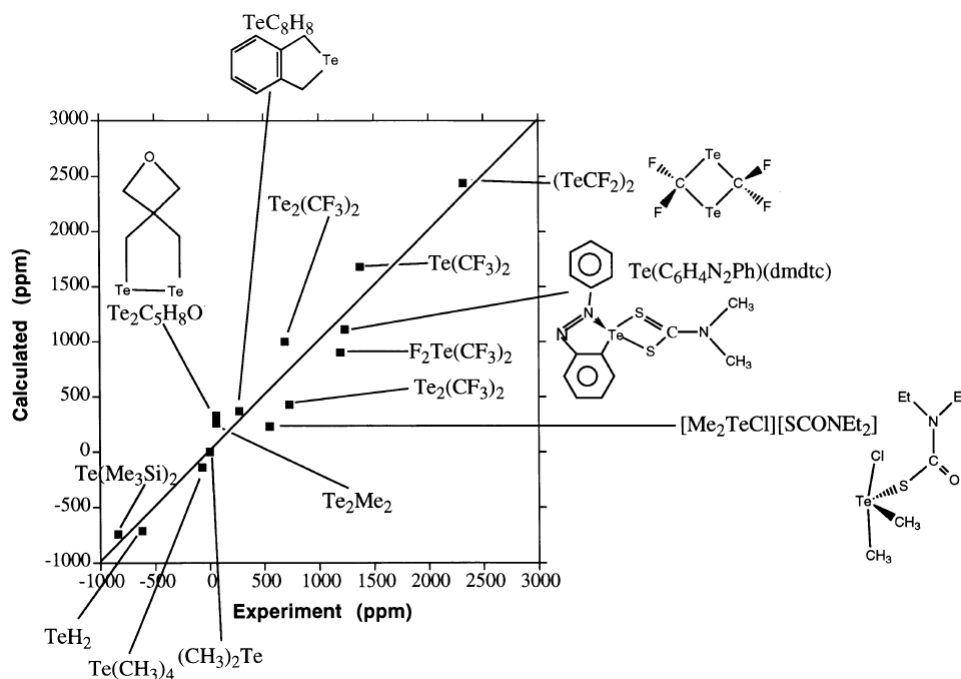
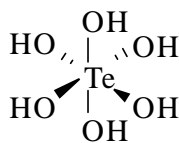


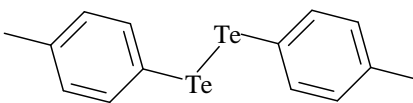
**Figure 3.1** Comparison of calculated and experimental  $^{125}\text{Te}$  NMR chemical shifts for selected organotellurium compounds. Reproduced with permission from reference 136.

### 3.4 Results and Discussion

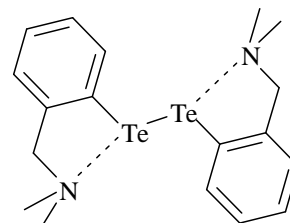
#### 3.4.1 Choice of Model Compounds



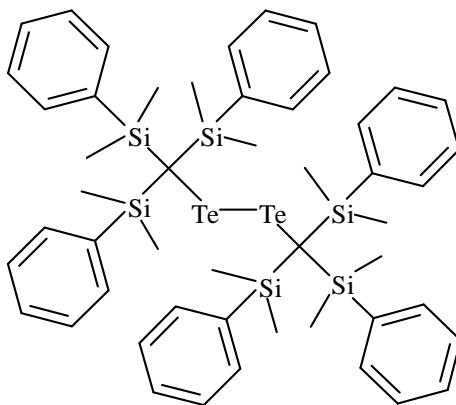
13



14



15

**16**

A NMR study of the association of main-group species with electron donors could in principle be conducted with a number of systems. For example, molecular iodine readily forms adducts with Lewis bases;<sup>136</sup> the formation of the  $I_3^-$  anion from  $I^-$  and molecular iodine would be the covalent extreme. However, the  $^{127}I$  nucleus has spin 5/2 with a quadrupole moment of  $-0.79 \times 10^{-28} \text{ m}^2$ . Because of this property, NMR studies of the iodine nucleus are most commonly performed on simple species with very small electric field gradients.<sup>140</sup> The Te-Te bond of ditellurides is analogous to the I-I bond in molecular iodine in that the Te-Te  $\sigma^*$  antibonding orbital is capable of acting as an electron acceptor. Indeed, secondary bonding is frequently observed to be collinear with the Te-Te bond of the ditellurides in the solid state.<sup>123,135,141-142</sup> The formation of SBIs in solution and other effects of the local environment on the tellurium nuclei could in principle be effectively studied using  $^{125}Te$  NMR.

Telluric acid (**13**) was chosen as a system of reference for this study, being a simple and stable compound in which the chalcogen is surrounded by oxygen atoms in an octahedral arrangement that prevents any SBIs. Its reported  $^{125}\text{Te}$  NMR spectrum consists of one resonance at 707 ppm.<sup>144</sup>

The bis *p*-tolyl ditelluride, **14**, was chosen as a "typical ditelluride". It consists of one aromatic ring at each extreme of the Te-Te bridge and the tellurium atoms are readily available for interaction with other molecules, as it is the case of most other ditellurides. The methyl group in the *para* position provides a convenient spectroscopic handle to monitor the integrity of the samples. The solid state geometry of **14** features a gauche conformation, with a C-Te-Te-C dihedral angle of  $85.7(4)^\circ$  and a Te-Te distance of  $2.6962(5) \text{ \AA}$ .<sup>5</sup> Its reported  $^{125}\text{Te}$  NMR chemical shift is 432.2 ppm in chloroform-d.<sup>145</sup>

Bis(*o*-(dimethylaminomethyl)phenyl)-ditelluride **15** was selected as a system with intramolecular SBIs which could compete with the interactions between tellurium and the molecules of donor solvents. Acting as donors, the dialkylamino groups block access to the tellurium atom through the interaction with the Te-Te  $\sigma^*$  orbital. In the solid state, **15** exhibits an average Te $\cdots$ N SBI distance of  $2.876(3) \text{ \AA}$ . This donation results in a Te-Te distance of  $2.7480(7) \text{ \AA}$ , somewhat longer than in **14**, and a wider C-Te-Te-C dihedral angle of  $95.2(1)^\circ$ .<sup>82</sup> In addition to these structural differences, the compound is prone to photolysis, presumably as a result of the weakening of the ditelluride bond induced by the SBI. **15** has a reported  $^{125}\text{Te}$  chemical shift of 355 ppm in chloroform-d.<sup>82</sup>

Bis(tris-dimethylphenylsilyl)methyl ditelluride (**16**) was selected as an example of a ditelluride completely protected from any SBI interactions by the steric bulk of the substituents. The steric demands of the substituents force the C-Te-Te-C dihedral angle to  $180.0(1)^\circ$  and the Te-Te bond distance to  $2.7716(3) \text{ \AA}$ .<sup>146</sup> Although the solid is stable, the compound in solution is only stable for short periods of time, even in the absence of light.<sup>146</sup> It has a  $^{125}\text{Te}$  chemical shift of 442 ppm using chloroform-d as a solvent.<sup>146</sup>

### 3.4.2 Synthesis of Ditellurides

The synthetic procedures used for these compounds were all adapted from the literature. All methods begin with the synthesis of a telluroate anion, which is then oxidized in mild conditions. The final product is usually recovered by extraction and purified by recrystallization, sublimation or chromatography. Specifically, bis-*p*-tolyl ditelluride **14**<sup>147</sup> was obtained from the reaction of the *p*-tolyl Grignard reagent and elemental tellurium followed by oxidation with pure oxygen; for compounds **15**<sup>123</sup> and **16**,<sup>146</sup> dimethyl-benzylamine and tris(dimethylphenylsilyl)-methane were lithiated in-situ, followed by treatment with elemental tellurium and oxidation (with oxygen and iodine, respectively). Because the last two compounds are reportedly photosensitive, their syntheses required rigorous exclusion of light and their manipulations were performed under light of appropriate wavelengths. There was a remarkable difference in the physical appearance of the products; while **14** is a red crystalline solid (as with most other ditellurides), **15** is light yellow and the sterically

encumbered **16** forms dark-green prismatic crystals. The difference of colour, and consequently the difference of  $\lambda_{\max}$  in their UV-vis spectra is a reflection of the geometry around the ditelluride moiety, as discussed below.

### 3.4.3 Conformational Effects Assessed by Computational Modeling

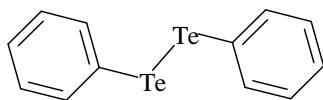
#### 3.4.3.1 Structural Benchmarking and Basis Set Selection

Initial geometry optimisations were conducted to determine which basis set would provide the best balance between accuracy and computational expense in the reproduction of the experimental structures of ditellurides by the GGA PW91 exchange-correlation potential. In first instance, due to the nearly flat potential profile from the rotation of the methyl moiety in a p-tolyl group, diphenyl ditelluride (**17**) was calculated as a model for the structure of **14**. There are no single- $\zeta$  (SZ), and double- $\zeta$  with one polarization set (DZP) basis sets for tellurium; in those cases the double- $\zeta$  (DZ) and triple- $\zeta$  with one polarization set (TZP) were respectively used for the heavy atoms. A summary of the most important bond lengths and angles is provided in **Table 3.1**. Bond angles are reproduced very well and are consistent across basis sets. The bond lengths are more dependent on the basis set; the largest deviations are observed for the Te-Te and C-Te distances, although not to unacceptable magnitudes.<sup>†</sup> The most serious deviation corresponds to the dihedral angle, which is always underestimated to an extent dependent

---

<sup>†</sup> For a detailed discussion of the ability of DFT methods to reproduce experimental structures, see Cramer, C. J. *Essentials of Computational Chemistry*, John Wiley and Sons: Etobicoke, 2002.

on the basis set, the quadruple- $\zeta$  with four-polarization sets (QZ4P) was required to bring the error below 0.5 degrees.

**17**

**Table 3.1** A comparison of calculated and experimental<sup>147</sup> bond lengths and angles of **17**.

Bond	Bond Lengths (Å)						Experimental
	SZ <sup>a</sup>	DZ	DZP <sup>b</sup>	TZP	TZ2P	QZ4P	
C1-Te1	2.137	2.158	2.156	2.154	2.145	2.145	2.081(18)
Te1-Te2	2.881	2.829	2.777	2.779	2.734	2.732	2.711(2)
Te2-C1'	2.138	2.158	2.156	2.155	2.145	2.145	2.150(15)
Bond Angles (°)							
C6-C1-Te1	120.1	120.2	120.0	120.2	120.4	120.1	121.4(13)
C1-Te1-Te2	100.9	97.2	99.6	100.7	100.5	101.1	100.3(5)
Te1-Te2-C1'	101.0	97.1	99.5	100.6	100.5	101.0	97.4(4)
Te2-C1'-C2'	120.1	120.3	120.1	120.2	120.5	120.2	119.9(12)
Dihedral Angle (°)							
C1-Te1-Te2-C7	84.4	81.6	86.2	84.8	82.4	88.9	88.5

a) DZ basis set used for tellurium.

b) TZP basis set used for tellurium.

The larger basis sets (TZP, TZ2P, and QZ4P) were then applied to optimize the complete structure of **14**, from the experimental geometry as the starting point. The results are summarized in **Table 3.2**. The largest deviations between the model and experimental geometries correspond again to the C-Te-Te-C dihedral angle. The angle is less sensitive to the basis set and appears to also be sensitive to the methyl groups. It is conceivable that crystal packing could account for the observed deviation; this premise could be examined by modeling the potential energy surface defined by the rotation of

the Te-Te bond. More importantly, this analysis is also required to explore possible conformational changes in solution and their effect on the shielding tensor of the tellurium nuclei.

**Table 3.2** A comparison of calculated and experimental<sup>148</sup> bond lengths and angles of **14**.

Bond	Bond Lengths (Å)			Experimental
	TZP	TZ2P	QZ4P	
C1-Te1	2.147	2.138	2.131	2.13(1)
Te1-Te2	2.778	2.743	2.715	2.697(3)
Te2-C1'	2.149	2.138	2.131	2.13(1)
Bond Angles (°)				
C6-C1-Te1	119.2	119.3	118.2	118.1(1.0)
C1-Te1-Te2	99.1	98.9	101.5	100.0(0.3)
Te1-Te2-C1'	99.1	98.9	101.5	101.5(0.3)
Te2-C1-C2'	119.2	119.3	118.2	118.8(0.9)
Dihedral Angle (°)				
C1-Te1-Te2-C1'	73.0	73.4	73.6	85.7(4)

The potential energy surface was evaluated by rotating the C-Te-Te-C torsion angle of **17** from 200° to -20° in increments small enough to provide a smooth curve (2.5°); all other molecular dimensions were fully optimized at each step. The potential energy calculated as a function of the dihedral angle is displayed in **Figure 3.2-I**. Two trajectories were identified in the course of mapping the surface; they are distinguished by the orientation of the aromatic rings, as illustrated in **Figure 3.3**. The trajectories provide numerically different surfaces, but the differences are small enough (< 2.1 kJ/mol) to be blurred by thermal effects. The surfaces have well-defined minima at

90° but changes of up to 30 degrees from the minimum would cost less than 5 kJ/mol. Indeed, 90% of the 48 structurally characterized diaryl ditellurides do exhibit C-Te-Te-C dihedral angle values from 60° to 120°. The maxima at 0° and 180° are the result of repulsion between lone-pairs on the tellurium atoms. The energy difference between the maxima is due to the steric interaction between aromatic rings at small C-Te-Te-C dihedral angles. A jump was initially observed in surface A at 60° but was smoothed out using a small step size. This is a consequence of rotation around the C-Te bonds which takes place because of the proximity of the phenyl rings to each other. Similarly, the jump visible in surface B is the result of rotation around the C-Te bonds which takes place as the distance between phenyl rings increases.

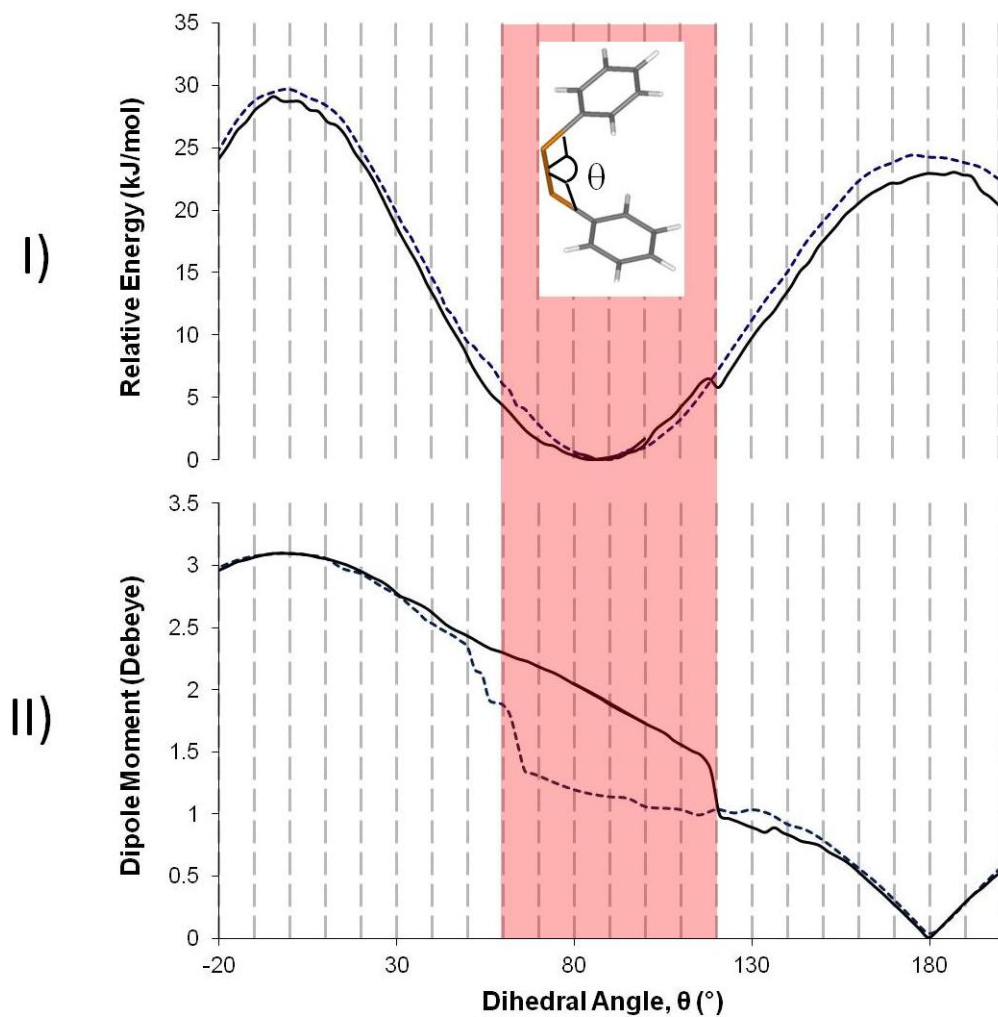


**Figure 3.2** The effect of the dihedral angle on I) the relative energy, and II) the dipole moment of **17** ( --- Trajectory A, — Trajectory B). The shaded area highlights the dihedral angles of 90% of crystallographically characterized ditellurides.

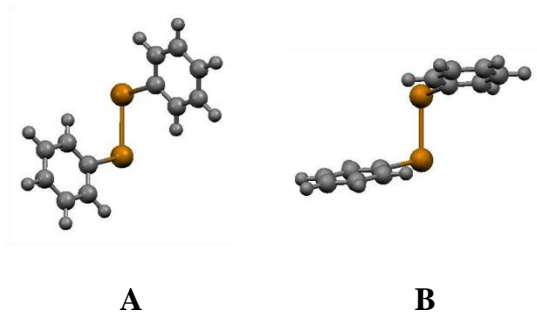


**Figure 3.3** Two distinct optimized geometries of **17** obtained at the C-Te-Te-C torsion angle of  $90^\circ$  for trajectories A and B.

Such conformational changes are accompanied by changes in molecular dipole moment **Figure 3.2-II**,<sup>67</sup> its value is strongly dependent on the orientation of the aromatic rings, thus curves A and B are distinct, especially at C-Te-Te-C torsion angles between  $50^\circ$  and  $120^\circ$ . The interaction of the tellurium p-orbital lone pairs and the adjacent phenyl  $\pi$ -systems are likely the main contributors to this effect. The change of calculated dipole moment between  $60^\circ$  and  $120^\circ$  spans 0.95 D. This observation implies that the molecular geometry could be influenced by the polarity of a solvent, especially considering the small energetic cost of geometric change within that angle range.

### 3.4.3.2 Electronic Excitations

In the most stable geometry, the frontier orbitals of **17** are centred on the tellurium atoms (>80%) (**Figure 3.4**). The HOMO consists of a combination of their lone pairs and the LUMO is the  $\sigma^*_{\text{Te-Te}}$  orbital. The first excitation would have a  $\sigma^* \leftarrow n$  character and a modest transition dipole moment. Moreover, the conformation of the Te-Te bond is likely

to influence the repulsion between lone pairs, the HOMO-LUMO gap, electronic excitations and the paramagnetic component of the NMR shielding constant.

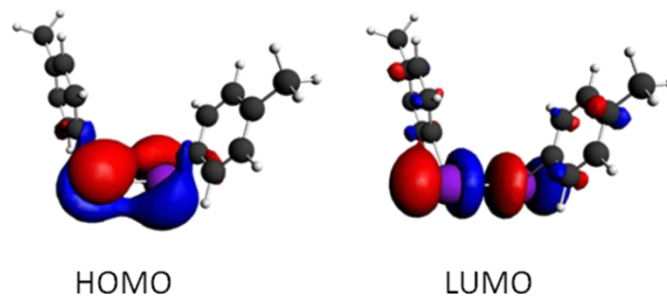


**Figure 3.4** Kohn-Sham frontier molecular orbitals of **14**. Isosurfaces plotted at 0.05 au.

TD-DFT calculations were carried out to assess the effect of the C-Te-Te-C dihedral angle on the energy of electronic excitations for angles between  $0^\circ$  and  $180^\circ$ , the results are graphically presented in **Figure 3.5** for the first electronic excitation and the two trajectories discussed above.

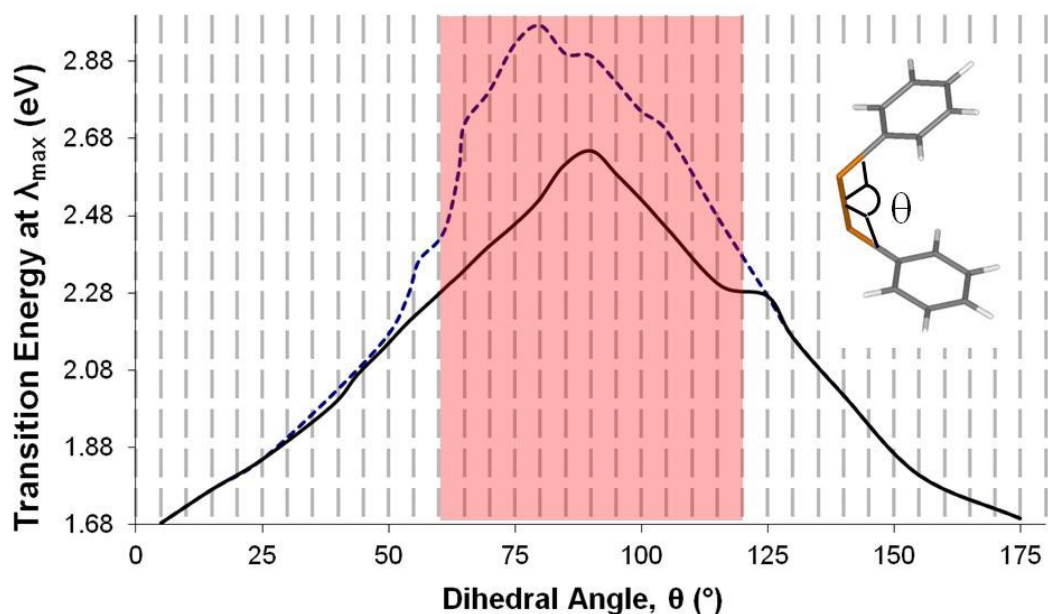


**Figure 3.5** Effect of the dihedral angle on the energy of the first electronic excitation of **17**. ( --- Trajectory A, — Trajectory B) The shaded area highlights the dihedral angles of 90% of crystallographically characterized ditellurides.

For **17**, the geometry of minimum energy shows the largest HOMO-LUMO gap, as the energy of the HOMO depends on the C-Te-Te-C dihedral angle (**Figure 3.6**). Any geometric distortion would result in a decrease of the gap, and thus the excitation energy, as the nature of the HOMO changes from one combination of p-orbital lone pairs to the other. The repulsion between tellurium lone pairs causes a contraction of the HOMO-LUMO gap, which would be smallest at  $0^\circ$  and  $180^\circ$ . These principles are in agreement with the calculated trends in excitation energies. The difference between the curves for trajectories A and B indicates that the orientation of the phenyl ring also has an effect on the transition energies (**Figure 3.5**). In addition to affecting the HOMO and LUMO, rotation of the Te-Te bond also alters the order of orbitals, and excitations (**Figure 3.6**).

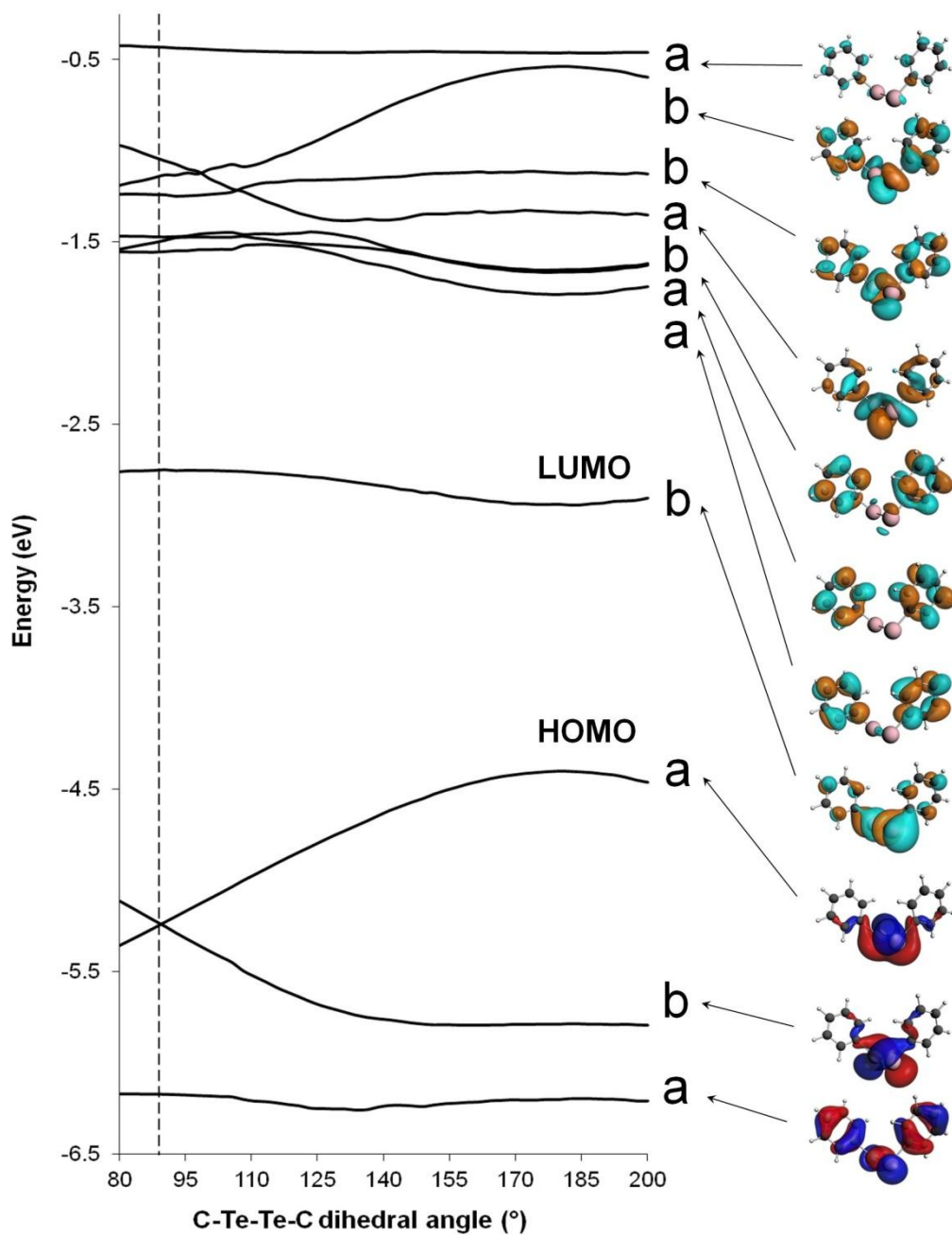


**Figure 3.6** Walsh diagram illustrating the effect of the C-Te-Te-C dihedral angle on the frontier orbitals of **17**. Orbitals are labeled according to C<sub>2</sub> molecular symmetry. (--- dihedral angle for energetic minimum)

### 3.4.3.3 $^{125}\text{Te}$ NMR Chemical Shift

DFT GIAO-NMR calculations were performed to examine the effect of the C-Te-Te-C dihedral angle on the  $^{125}\text{Te}$  chemical shift, using the geometries optimized as described above. The results of these calculations are displayed in **Figure 3.8**. The diamagnetic and paramagnetic contributions to the shielding tensor are presented separately. The latter includes four tensors related to the mixing of orbitals caused by the applied magnetic field, as well as the *gauge*.<sup>‡</sup> The relative contributions of these tensors are presented in **Figure 3.7**. The mixing of occupied and virtual orbitals dominates the shielding constant while the contribution from the mixing of all-occupied orbitals has only a small effect on the shielding. The contribution of the gauge tensor to the total paramagnetic shielding is also small. The sum of the total paramagnetic and diamagnetic terms yields the total shielding, which can be compared to the sum of tensors calculated for a reference compound (dimethyl telluride) to yield the chemical shift.

While the calculation of the electronic excitations for the two trajectories found a small effect of the orientation of the aromatic rings, the impact on the  $^{125}\text{Te}$  chemical shift is significant. Trajectory B (solid line) displays changes of 200 ppm throughout the whole range, but less than 50 ppm from  $60^\circ$  to  $120^\circ$ , the most commonly observed values for the C-Te-Te-C dihedral angle. In contrast, trajectory A (dashed line) displays changes of

---

<sup>‡</sup> Within the calculation, the components of the paramagnetic term are denoted as the  $s^{(1)}$ ,  $u^{(1)}$ ,  $b^{(1)}$  and  $g$  tensors. The dominant contribution,  $u^{(1)}$ , pertains the mixing of occupied and virtual orbitals that result from the application of the magnetic field. There is a moderate contribution from the mixing of occupied orbitals,  $s^{(1)}$ , and no contribution from the  $b^{(1)}$  tensor. The gauge tensor is chosen by the ADF-NMR program to minimize the effect of the frame of reference on the *observed* movement of electrons. Within this thesis, these components are described by the relevant orbitals. The diamagnetic term is comprised of two tensors related to contributions from the motion of the valence electrons and the core electrons; as these calculations were performed using all-electron basis sets, the core has a value of zero.

up to 400 ppm and the most significant variations are between 60 to 120°. The difference can be traced to the orientation of the aromatic rings, which in trajectory A enables interaction of the aromatic system with the tellurium lone pair; an effect that is dependent on the orientation of the rings and the C-Te-Te-C torsion angle. Similar calculations showed similar dependency of the  $^{125}\text{Te}$  NMR chemical shift on the dihedral angles in other molecules, with the total change ranging from 100 ppm ( $\text{Te}(\text{OH})_4$ ) up to 1200 ppm ( $\text{Te}(\text{SH})_2$ ).<sup>149</sup>

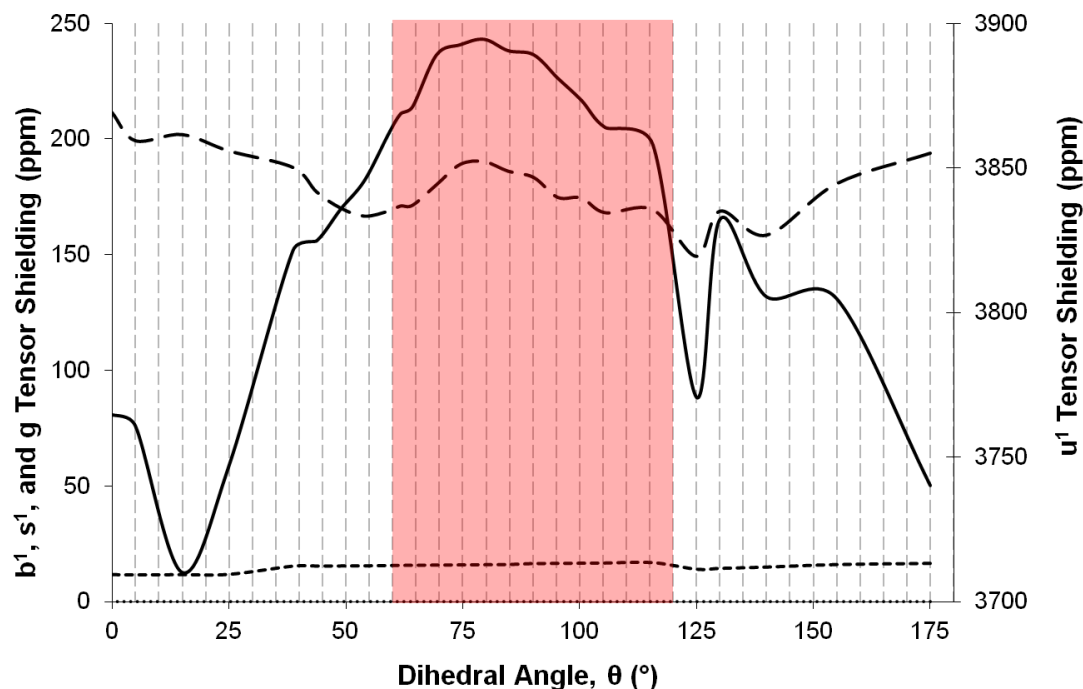


**Figure 3.7** The relative contributions of the components of the shielding constant for each calculated geometry of trajectory B (— — — occupied-occupied ( $s^{(1)}$ ), — occupied-virtual ( $u^{(1)}$ ), ••• virtual-virtual ( $b^{(1)}$ ), --- gauge tensor ( $g$ )).

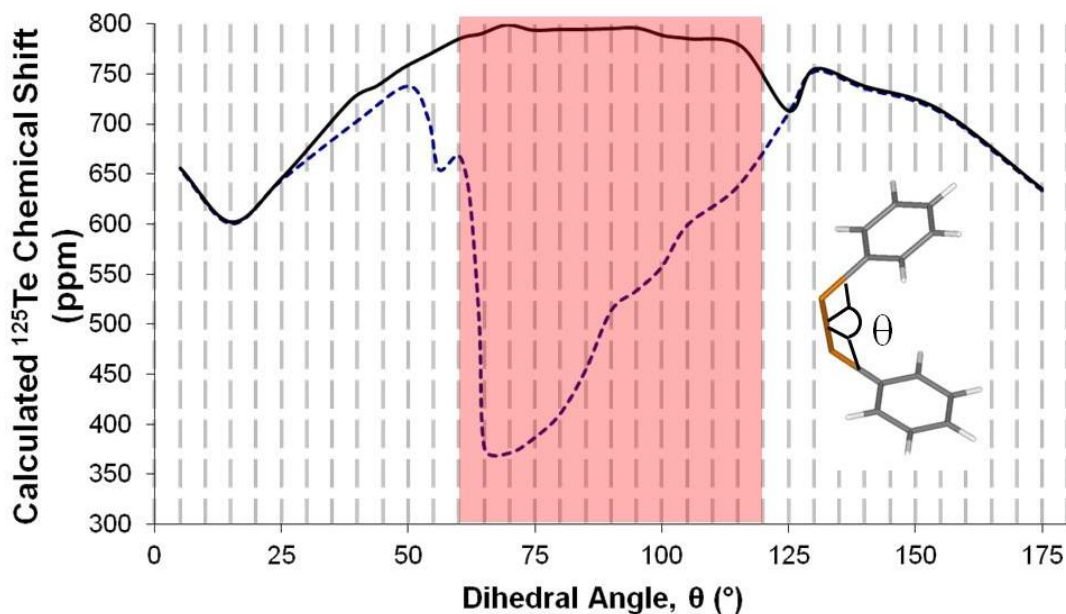


**Figure 3.8** The effect of the dihedral angle on the  $^{125}\text{Te}$  chemical shift of **17**. ( --- Trajectory A, — Trajectory B) The shaded area represents the dihedral angles of 90% of crystallographically characterized ditellurides.

#### 3.4.3.4 Molecular Conformation, Electronic Excitations and NMR Shielding

The computational results discussed above indicate that the  $^{125}\text{Te}$  NMR chemical shift of organoditellurides is very variable because of the flexibility of the C-Te-Te-C bridge. The calculated chemical shifts change by about 200 ppm within the range of dihedral angle values most commonly observed in the solid state. Similarly, and according to the TD-DFT results, the energy of the first electronic excitation is also dependent on the conformation of the molecule. There is in fact an approximate correlation between the calculated paramagnetic shielding and the calculated transition energies (**Figure 3.9**). However, the magnitude of the paramagnetic shielding decreases as the inverse of the transition energy increases; this is opposite to the prediction of the

“closure” approximation<sup>136</sup> (Eq. 3.5). This type of approximation has often been applied to simple diatomic<sup>150-152</sup> and linear systems in which the virtual orbitals (and hence average excitation energy) are relatively easy to calculate,<sup>150-152</sup> but modern computational methods allow for its application to more complex systems.<sup>153</sup> That a correlation exists indicates that the paramagnetic shielding is a major contributor to the shielding constant and the chemical shift. As a comparison, the overall change observed in the diamagnetic term is less than 1 ppm over the same range. However, the closure approximation is not applicable to this system according to the calculations. The calculated trend appears to change for  $1/\Delta E < 0.45$ , when the chemical shielding levels out close to 3700 ppm.

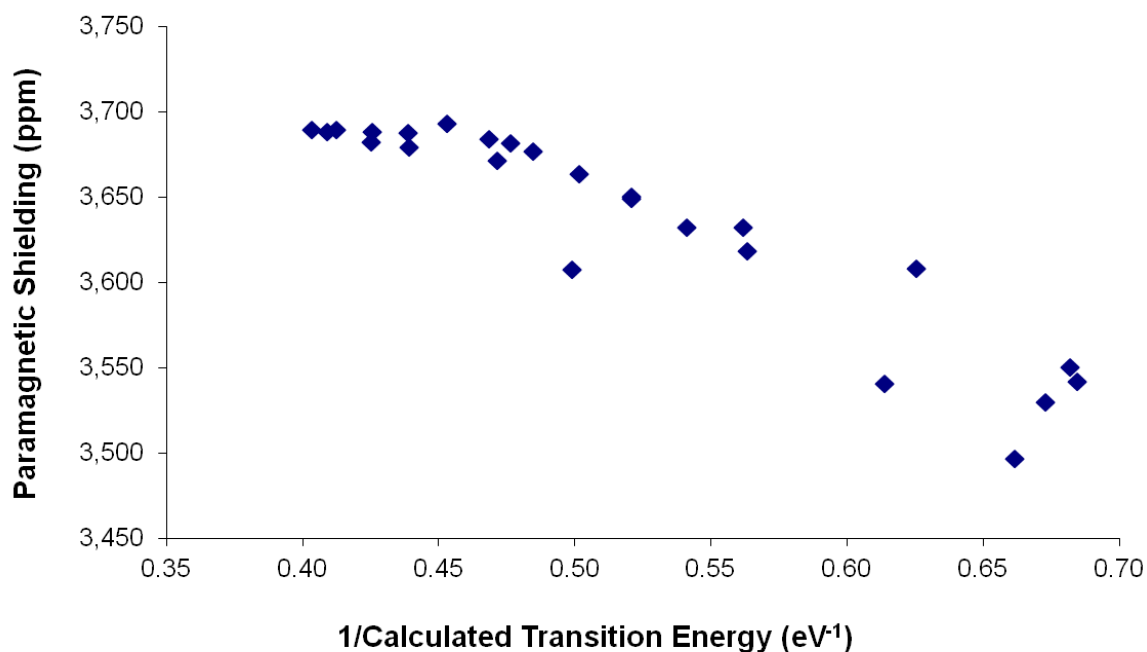


**Figure 3.9** Correlation between the magnitude of the calculated paramagnetic shielding and the calculated transition energy of **17** as a result of changes in the molecular geometry (Trajectory B).

### 3.4.4 Environmental Effects through Computational and Experimental Studies

The preceding discussion is based on computational modeling that necessarily refers to individual molecules in gas phase. Practical  $^{125}\text{Te}$  NMR studies are conducted in condensed media, either solid or liquid. In the case of a liquid solution, the effect of the environment on the  $^{125}\text{Te}$  NMR chemical shift can be approached at two scales, one macroscopic in which the solvent is a homogeneous medium with continuous dielectric and diamagnetic properties, the other microscopic in which the molecular identity of the solvent and its specific interactions with the sample molecule are acknowledged.

#### 3.4.4.1 Dielectric Properties

The polarity of a solvent can impact the  $^{125}\text{Te}$  NMR chemical shift of **14** through two mechanisms, which are not strictly independent from each other. The first would be a consequence of the stabilization of the more polar conformations by polar solvents; the other would be the result of changes in the stability of the electronic ground and excited states (solvatochromic effect) for a particular geometry.

To account for solvent effects, calculations were performed on the minimized structure of **17** using the conductor-like screening model (COSMO). This method approximates the electrostatic effects of solvation by surrounding the molecule with a dielectric continuum and assuming a mean solvent molecular radius. In this manner, the structure of **17** was re-optimized in solvents with varying dielectric constants: hexane, carbon tetrachloride ( $\text{CCl}_4$ ), benzene, toluene, triethylamine ( $\text{Et}_3\text{N}$ ), carbon disulfide

(CS<sub>2</sub>), diethyl ether (Et<sub>2</sub>O), tetrahydrofuran (THF), dichloromethane (DCM), pyridine (py), isopropanol (*i*-PrOH), nitromethane (MeNO<sub>2</sub>), acetonitrile (ACN) and dimethyl sulfoxide (DMSO). In all cases, the length of the Te-Te bond increased, while the other structural parameters were slightly influenced (**Table 3.3**). The most significant changes were calculated for the C-Te-Te-C dihedral angle, which increased slightly with solvent polarity. These changes in the geometry around tellurium are consistent with a stabilization of more polar conformations by polar solvents.

**Table 3.3** A comparison of optimized gas phase and COSMO structures of **17**.

	Te1-Te2 bond length (Å)	C1-Te1-Te2 Bond angle (°)	Te1-Te2-C1' Bond angle (°)	C1-Te1-Te2-C1' dihedral angle (°)	Angle Between Mean Planes of Phenyl Rings (°)
gas phase	2.732	101.06	101.13	88.89	23.23
hexanes	2.741	100.32	100.32	84.74	22.56
CCl <sub>4</sub>	2.740	100.38	100.38	86.30	18.42
C <sub>6</sub> H <sub>6</sub>	2.739	100.56	100.56	85.78	22.71
toluene	2.741	100.41	100.41	85.34	23.12
Et <sub>3</sub> N	2.740	100.38	100.38	86.25	17.72
CS <sub>2</sub>	2.749	100.47	100.47	85.31	22.68
Et <sub>2</sub> O	2.741	100.33	100.33	86.11	18.44
THF	2.742	100.42	100.42	88.11	18.77
DCM	2.740	99.99	99.99	85.85	18.16
Py	2.738	100.23	100.23	87.03	18.58
<i>i</i> -PrOH	2.741	100.32	100.32	87.07	21.63
MeNO <sub>2</sub>	2.740	100.37	100.37	87.17	22.02
MeOH	2.741	100.36	100.36	86.44	22.69
ACN	2.739	100.51	100.51	87.59	21.81
DMSO	2.742	100.32	100.32	87.11	22.25

To experimentally assess the magnitude of the solvatochromic effect, the UV-visible spectra of **14** was acquired from 0.137 mol L<sup>-1</sup> solutions in several solvents at 303.0 K.

**Figure 3.10** presents the experimental transition energies at the wavelength of maximum of absorption plotted as a function of the solvent dielectric constant. The excitation energies span a window of 0.19 eV with a small correlation. In general the excitation energy increases as the dielectric constant of the medium increases but there is significant dispersion of the points.

The solvatochromic effect can also be approximated with COSMO TD-DFT calculations applied to each COSMO-minimized structure. The trend resulting from this analysis (**Figure 3.11**) closely resembles the experimental observation (**Figure 3.10**) although there is a difference of 0.5 eV in the corresponding energies. That the trend is reproduced indicates that the dielectric properties of the solvent are indeed critical to the energy of excitation. The large deviation observed for CS<sub>2</sub> is likely due to large the polarizability of the sulfur atoms and van der Waals interactions with the ditelluride molecule, which these calculations cannot account for. A comparison of the calculated transition energy and the experimental energy at  $\lambda_{\text{max}}$ , **Figure 3.12**, shows a correlation, but there is great dispersion in the data. In addition to the previously mentioned carbon disulfide, large deviations from the trend are observed for DMSO and pyridine (the strong donor solvents) where the orientation of solvent molecules is likely to result from orbital interactions.

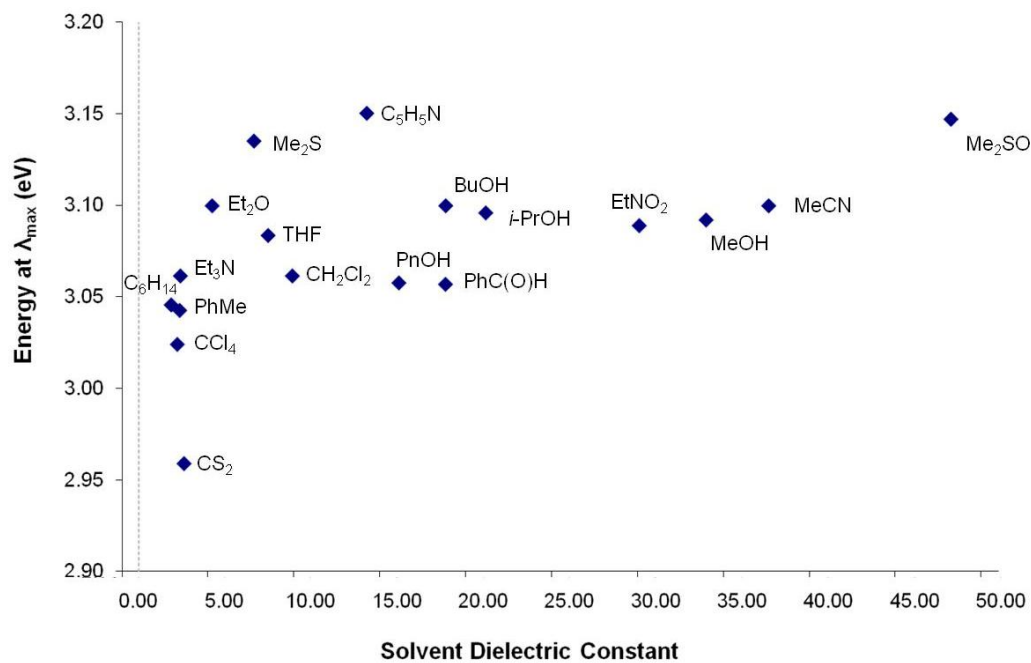


**Figure 3.10** Experimentally determined energy of excitation of **14** (0.137 M, 303.0 K) as a function of solvent dielectric constant.

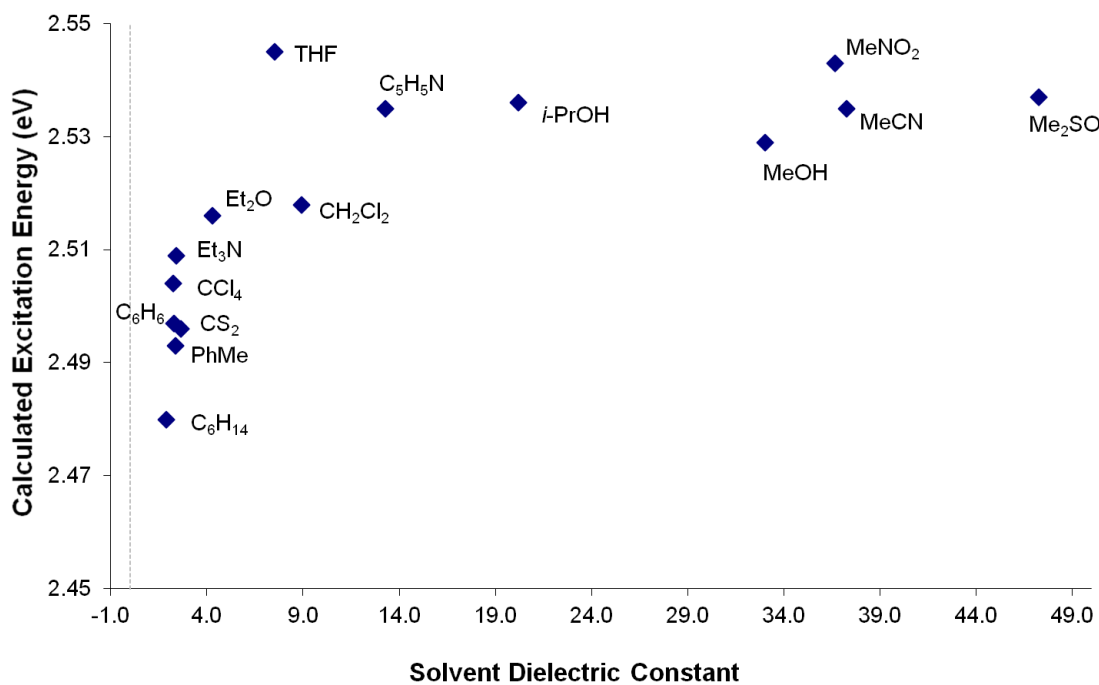


**Figure 3.11** Calculated excitation energy of **17** as a function of solvent dielectric constant.

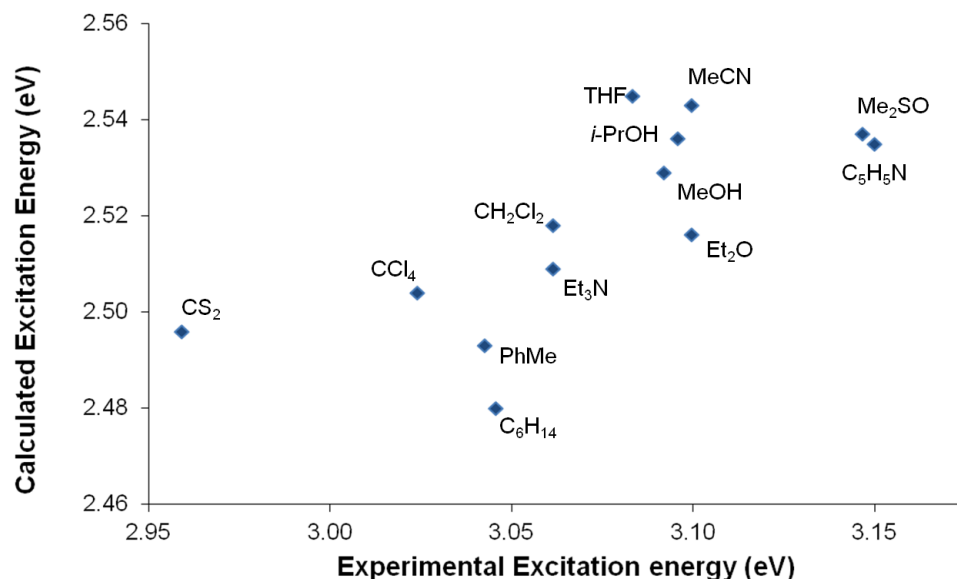


**Figure 3.12** Comparison of calculated and experimental excitation energies for the first transition of **17** and **14** in a number of solvents.

The COSMO formalism cannot be directly applied to the GAIO-NMR calculations in ADF, thus the solvation effect on the <sup>125</sup>Te chemical shifts could only be approximated by performing calculations on the COSMO-optimized geometries. The results are displayed in **Table 3.4**. In all cases, the calculated chemical shifts were smaller than in the gas-phase minimized geometry, with changes in the calculated values of up to 33 ppm observed for solvents with high dielectric constant.

In order to better account for solvent effects, a correction to the chemical shift was also applied using equation **3.7** and the known volume susceptibilities of the solvents.<sup>154-</sup>

<sup>156</sup> These corrections do bring the calculated chemical shifts about 2-3 ppm closer to the experimental values, but the overall contributions are small.

$$\delta_{corr} = \left( \frac{\sigma_{ref} - \sigma}{1 - \sigma_{ref}} \right) - \left( \frac{4\pi}{3} \right) [\chi_v - \chi_{v(ref)}] \quad 3.7$$

**Table 3.4** Calculated  $^{125}\text{Te}$  chemical shifts for **17** using COSMO-optimized geometries.

	$\delta \text{ }^{125}\text{Te}$ (ppm)	$\chi_v (\times 10^6)$	Corrected $\delta \text{ }^{125}\text{Te}$ (ppm)
gas phase	794.2	-	-
DMSO	761.9	-0.624	759.3
Py	780.0	-0.611	777.4
DCM	759.3	-0.733	756.2
$\text{C}_6\text{H}_6$	760.9	-0.611	758.3
$\text{C}_7\text{H}_8$	767.7	-0.620	765.1
$\text{C}_6\text{H}_{14}$	761.6	-0.565	759.2
$\text{CS}_2$	763.5	-0.699	760.6
$\text{CH}_3\text{CN}$	759.6	-0.534	757.3
$\text{CCl}_4$	767.9	-0.691	765.0
$\text{Et}_2\text{O}$	774.4	-0.534	772.1
<i>i</i> -PrOH	779.2	-0.599	776.7
$\text{MeNO}_2$	763.4	-0.391	761.7
MeOH	762.0	-0.530	759.8
$\text{NEt}_3$	767.5	-0.586	765.0
THF	779.8	-0.650	777.1

The  $^{125}\text{Te}$  chemical shift of **14** (0.137 M, 303.0 K) was measured in the same solvents (**Figure 3.13**). The resonances were found between 402.9 ppm and 455.9 ppm, displaying some correlation with the polarity of the solvent. All chemical shifts were derived from the measured absolute frequency of each resonance. The spread of this data is larger than the dispersion ranges reported for 5 mol % solutions of diorganyl

tellurides:<sup>157,158</sup> dimethyl telluride (32.3 ppm), methylphenyl telluride (29.8 ppm), and methyl 1-hexynyl telluride (15.5 ppm). However, the overall trends are comparable.<sup>157</sup>

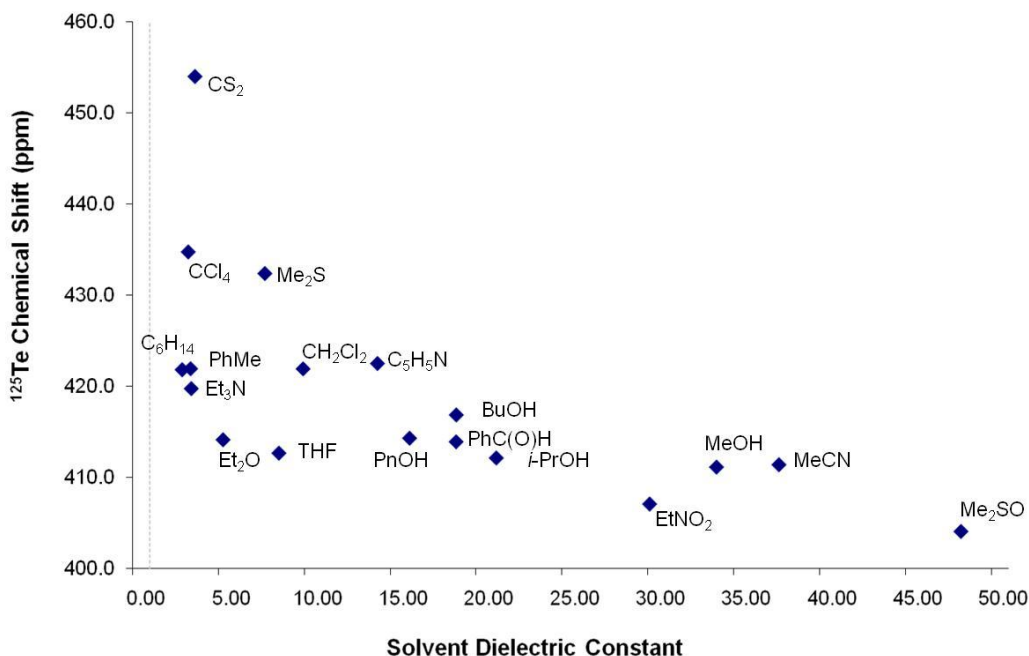


**Figure 3.13** Experimentally determined <sup>125</sup>Te chemical shift of **14** (0.137 M, 303.0 K) as a function of solvent dielectric constant.

Interestingly, the plot of the experimental chemical shift vs. energy of excitation at the first maximum of absorption displays a trend opposite to that predicted from the calculations for the system in gas phase, i.e. the chemical shift increases as the excitation energy increases. Similar trends have been observed in the NMR spectra of <sup>17</sup>O- and <sup>13</sup>C-enriched acetone in water mixtures.<sup>160</sup> The interpretation considers that, due to the polarity of the medium, as the proportion of acetone increases there would be an increase in the  $\pi^* \leftarrow n$  transition energy and a decrease in the <sup>17</sup>O chemical shift. Hydrogen-bonding is also more prevalent in highly polar systems, which results in the opposite

effect and increases the HOMO-LUMO gap.<sup>159</sup> In the present case the difference between calculation and experiment highlights an important limitation of the computational method.

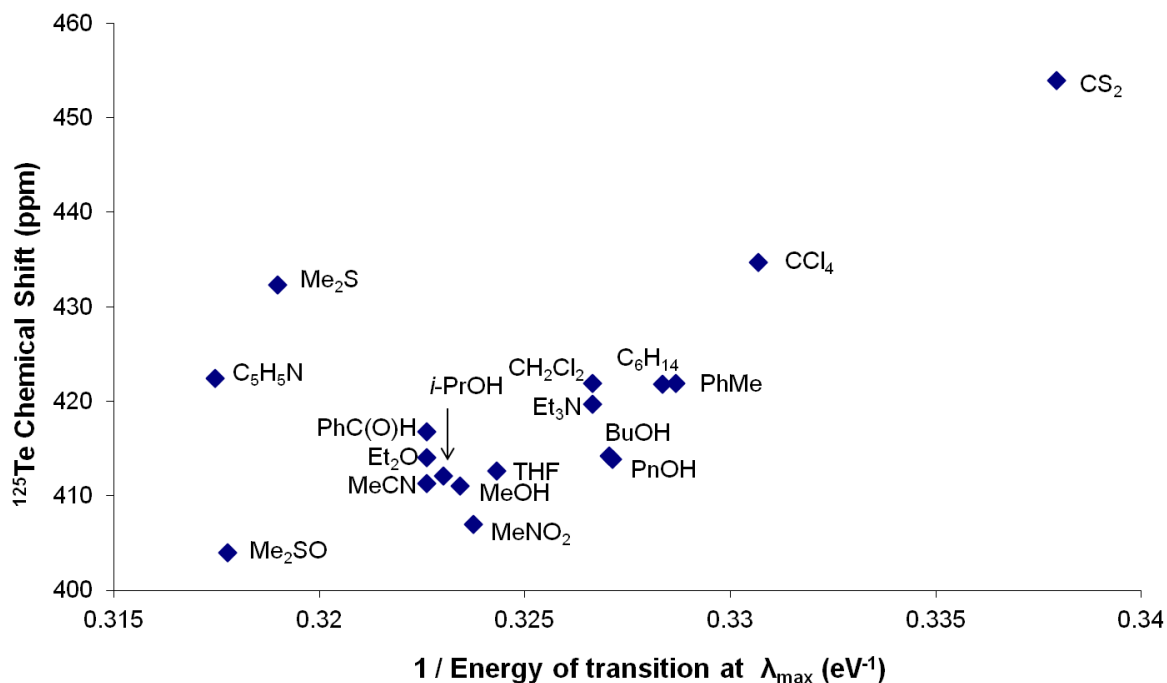


**Figure 3.14** Experimental  $^{125}\text{Te}$  chemical shift as a function of excitation energy for **14** in different solvents.

### 3.4.4.2 Explicit Solvation Models

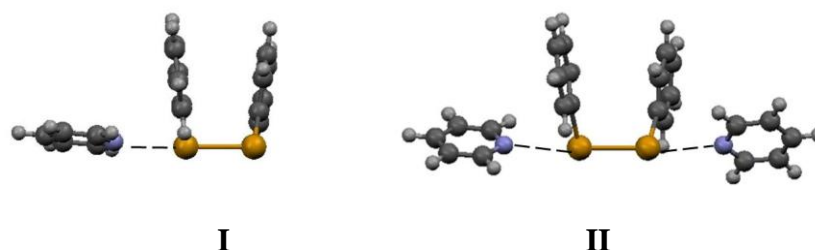
Although the trends in **Figure 3.5** - **Figure 3.12** can be easily identified and reasonably explained based on the properties of the ditelluride **14** and the solvents, the experimental points are widely scattered. The degree of dispersion indicates that the effect of each solvent cannot be fully accounted for with approximate continuous models.

It is necessary to take into consideration the specific interactions that solvent molecules can have with ditellurides.

The changes observed in the excitation spectra of **14** in different solvents closely resemble those observed for molecular iodine ( $I_2$ ) as it forms addition compounds with a variety of donor molecules (D)<sup>160-163</sup> thanks to its low-lying  $\sigma^*_{I-I}$  orbital. Such molecular adducts feature D-I bonds that range from weak (SBIs) to very strong (hypervalent covalent bonds). Formation of these adducts is usually accompanied by a blue shift of the maximum of absorption in the visible spectrum, which can be correlated to the enthalpy of coordination.<sup>164,165</sup> As discussed in **3.4.1**, compound **14** can interact with the molecules of donor solvents through the  $\sigma^*_{Te-Te}$  antibonding orbital. In principle such an interaction would result in a change of the HOMO-LUMO gap and increased shielding of the tellurium nucleus. In **Figure 3.13**, the solvents with available lone pairs (which also tend to have the larger dielectric constants) cause an increase in excitation energy and a decrease in  $^{125}Te$  chemical shift.

To explicitly explore the effect of solvation on the structure and properties of **14**, calculations were performed on models of the solvates that would be made by coordination of one and two molecules of benzene, carbon disulfide, dichloromethane, dimethyl sulfoxide (DMSO) and pyridine on **17** (**Scheme 3.1**). The optimized structural parameters of the ditelluride solvates are displayed in **Table 3.5** and **Table 3.6**. The solvent molecules in the optimized structure acquire the expected orientation, opposite to the Te-Te bond, with the exception of  $CS_2$  which minimized to a structure where solvent

molecules are far removed from the tellurium nuclei and can only be interpreted as a nonbonded system. The presence of both Te-Cl and H-aryl interactions with DCM gave reasonably strong association energies despite the weak donor ability of the solvent. The calculated association energies are small, but significant in solution.



**Scheme 3.1** Schematic representation of the structures of the pyridine solvates of **17** with 1:1 (**I**) and 2:1 (**II**) stoichiometries.

**Table 3.5** Binding energies (not Zero Point Energy (ZPE) corrected) and selected structural parameters for **17** and its mono-solvates.

	Bond Lengths (Å)				
	<b>17</b>	<b>17</b> •DMSO	<b>17</b> •C <sub>6</sub> H <sub>6</sub>	<b>17</b> •DCM	<b>17</b> •Py
D-Te1	-	2.904	4.261	3.934	2.929
D-Te2	-	-	-	-	-
Te1-Te2	2.732	2.760	2.736	2.731	2.769
Bond Angles (°)					
C1-Te1-Te2	101.6	98.92	100.18	100.32	97.88
Te1-Te2-C1'	101.13	96.47	100.47	100.32	99.59
Dihedral Angle (°)					
C1-Te1-Te2-C1'	88.89	89.46	84.42	83.20	84.89
Angle between mean planes of phenyl rings (°)					
	23.23	25.56	24.98	39.56	13.9
Binding Energy per solvent molecule (kJ/mol)					
	-	-15.17	-4.49	-8.98	-18.06

**Table 3.6** Binding energies (not ZPE corrected) and selected structural parameters for **17** and its di-solvates.

	Bond Lengths (Å)					
	<b>17</b>	<b>17</b> •DMSO <sub>2</sub>	<b>17</b> •(C <sub>6</sub> H <sub>6</sub> ) <sub>2</sub>	<b>17</b> •CS <sub>2</sub>	<b>17</b> •DCM <sub>2</sub>	<b>17</b> •Py <sub>2</sub>
D-Te1	-	3.097	3.82	3.857	3.877	3.075
D-Te2	-	3.097	3.82	3.857	3.877	3.075
Te1-Te2	2.732	2.766	2.738	2.748	2.736	2.779
	Bond Angles (°)					
C1-Te1-Te2	101.6	97.76	99.33	100.49	101.08	97.76
Te1-Te2-C1'	101.13	97.76	99.33	100.49	101.08	97.76
	Dihedral Angle (°)					
C1-Te1-Te2-C1'	88.89	92.09	83.89	79.57	89.03	79.60
	Angle between mean planes of phenyl rings (°)					
	23.23	23.62	7.48	15.97	25.79	11.8
	Binding Energy per solvent molecule (kJ/mol)					
	-	-10.52	-3.88	-8.09	-8.28	-13.02

According to the calculations, solvent binding has only a small effect on the structure of the ditelluride. The Te-Te bond distance increases in all cases, with a maximum change of 0.066 Å observed in **17**•py<sub>2</sub>. Changes in the C-Te-Te bond angles display no defined trend, but can be as large as 4.8°. More significant changes were observed in the C-Te-Te-C dihedral angle, which ranged from 79.57° with two molecules of carbon disulfide to 92.09° with two molecules of oxygen-bonded DMSO. While DMSO increases the dihedral angle, all other solvents contract it. This effect was enhanced by the coordination of the second solvent molecule in each case, with the exception of dichloromethane which shows contraction of the dihedral angle with one solvent molecule and increase with two.

DFT GIAO-NMR calculations were performed to obtain the <sup>125</sup>Te chemical shift of the solvation models described above. The results of these calculations are compiled in

**Table 3.7.** In general, solvation results in a shift of the calculated resonances to lower frequency, but there are exceptions, particularly in the case of mono-solvates. Addition of one solvent molecule mostly affects the resonance of the bound tellurium nucleus ( $\text{Te}_A$ ); with pyridine and benzene the resonance of ( $\text{Te}_B$ ) is shifted to higher frequency. The presence of a second solvent molecule reduces the overall effect observed in mono-solvation, resulting in smaller changes of chemical shift. Solvent molecules with the largest binding energies yield also the greatest changes of the chemical shift relative to the gas phase calculation.

**Table 3.7** Calculated  $^{125}\text{Te}$  chemical shifts for the gas phase structure of **17** and explicit solvation models.  $\Delta\delta$  refers to the change from the gas phase value.

	$\delta \text{Te}_A$ (ppm) <sup>a</sup>	$\Delta \delta$	$\delta \text{Te}_B$ (ppm)	$\Delta \delta$
<b>17</b>	794.2	-	794.2	-
<b>17</b> •DMSO	615.1	-179.1	761.2	-33.0
<b>17</b> •DMSO <sub>2</sub>	693.9	-100.4	693.9	-100.4
<b>17</b> •Py	634.0	-160.2	821.8	27.6
<b>17</b> •Py <sub>2</sub>	714.5	-79.7	714.5	-79.7
<b>17</b> •DCM	724.5	-69.7	774.6	-19.6
<b>17</b> •DCM <sub>2</sub>	768.9	-25.3	768.9	-25.3
<b>17</b> •C <sub>6</sub> H <sub>6</sub>	707.3	-86.9	825.0	30.8
<b>17</b> •(C <sub>6</sub> H <sub>6</sub> ) <sub>2</sub>	772.3	-21.9	772.3	-21.9
<b>17</b> •(CS <sub>2</sub> ) <sub>2</sub>	825.0	30.8	825.0	30.8

a) In the mono-substituted species,  $\text{Te}_A$  refers to the solvent bound atom.

### 3.4.4.3 Summary of Solvent Effects

The commonly accepted chemical shift reference for tellurium NMR is neat dimethyl telluride, which by definition is independent of solvation.<sup>§166-168</sup> In the present study, using hexanes as a solvent provides the closest mimic of the environment in the standard. The other solvents can be classified in three groups: those that gave larger chemical shifts (they contain chlorine or sulfur heteroatoms), those that gave smaller chemical shifts (they contain oxygen atoms), and those that had little to no effect (nitrogen containing solvents, and other hydrocarbons). This is in stark contrast with the effect of the solvent on the UV-vis spectrum, where all solvents (except CS<sub>2</sub> and CCl<sub>4</sub>) resulted in an increase of the excitation energy.

DFT-COSMO calculations were then applied to determine the effect of the solvent dielectric on the ditelluride molecule. The molecular shape was strongly affected by the dielectric net of COSMO. The <sup>125</sup>Te chemical shifts were calculated from the COSMO-optimized geometries. The COSMO results reproduced the experimental trend in the energy of excitation as a function of the solvent's dielectric constant.

Explicit solvation models showed only small modifications to the structure of the ditelluride. The largest deviations were for the C-Te-Te-C dihedral angle, which was increased with DMSO solvation, but decreased for all others. The effect of the solvent molecules on the calculated chemical shift is significant. In all cases, solvent-bound tellurium atoms were most strongly affected, causing changes in the chemical shift on the

---

<sup>§</sup> The most recent IUPAC recommendation for a standard is "neat" TeMe<sub>2</sub> with a "small amount" of C<sub>6</sub>D<sub>6</sub> added as a lock.<sup>175</sup> Most published <sup>125</sup>Te NMR studies are referenced to pure dimethyl telluride with an insert of a deuterated lock solvent.

order of 180 ppm compared to the gas-phase structure. The solvents which resulted in the largest changes also gave the largest binding energies.

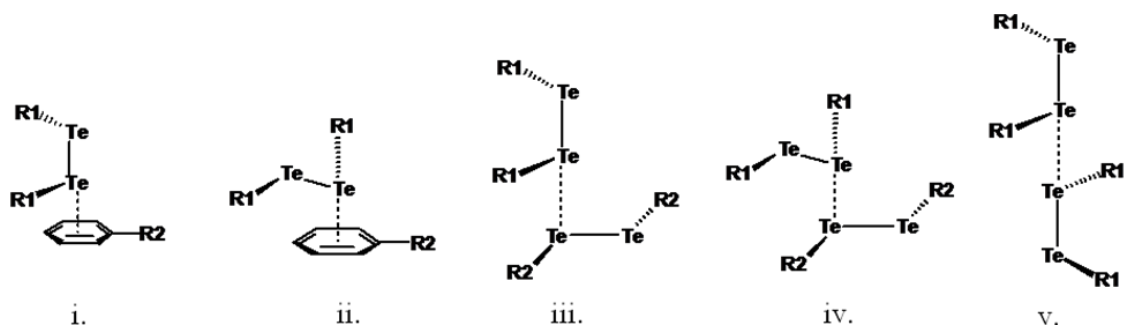
### 3.4.5 Dynamic Effects

The models discussed up to this point are approximations to reality, even with inclusion of explicit solvation and a dielectric envelope, because they consist of individual molecules treated as if they were rigid atom assemblies. More realistic models would have to take in account that molecules are in dynamic motion, distributed amongst a number of vibrational states. The simple conformational study made it evident that even small deviations from the equilibrium structure can cause significant changes in the  $^{125}\text{Te}$  chemical shift; the measured value would be statistically determined by the dynamic exchange of the nuclei in different geometries and environment. Complete modeling of such effects would require the application of molecular dynamics methods<sup>137</sup> that are not yet widely accessible for heavy main-group systems. Dynamic effects would be sensitive to temperature and concentration, therefore the  $^{125}\text{Te}$  chemical shift of **14** was measured in different solvents over a range of temperature and concentration.

#### 3.4.5.1 Auto-association Models

There is, however, an added complication in that the molecules of **14** can undergo association with each other. A survey of the Cambridge structural database (WEBCSD 1.1.1, May. 2011, 570 474 structures) found 48 entries for diaryl ditellurides; only 4

exhibit no short contacts to tellurium as a result of steric hindrance or packing effects. The rest are associated and can be classified by the type of interaction in two groups: those involving an Aryl...Te interaction, and those involving Te...Te interactions. Within the first group, one can distinguish cases in which the aryl group is opposite to the Te-Te bond (**Scheme 3.2 i**) or a Te-C bond (**Scheme 3.2 ii**). Similarly, in the second group a Te atom is opposite to the Te-Te bond (**Scheme 3.2 iii**) or a Te-C bond (**Scheme 3.2 iv**), in a third category the ditellurides form linear  $(\text{Te}_2)_n$  chains (**Scheme 3.2 v**).



**Scheme 3.2** Auto-association bonding schemes present in the solid-state structures of ditellurides.

DFT geometry optimizations were applied in order to assess whether those structures are relevant in solution. Bonding motifs i, iii, and v could all be minimized; their dimensions are summarized in **Table 3.8**. The association energies are small but enough to influence NMR measurements in concentrated solution and at low temperatures. No minimum could not be found for ii and iv; this problem suggests that

the corresponding association energies are even smaller.\*\* In each case, association causes only modest changes in the structural parameters; the Te-Te bond is typically lengthened by 0.02 to 0.05 Å, while the C-Te-Te-C torsion angle decreased less than 9°.

**Table 3.8** Calculated bond lengths, angles, and interaction energies of association models of **17**<sub>2</sub>.

Geometry	Association Energy (kJ/mol)	Te1-Te2 (Å)	C-Te-Te-C torsion angle (donor)	Te...Te SBI (Å)	Te3-Te4 (Å)	C-Te-Te-C torsion angle (acceptor)
i.	-3.38	2.731	79.2	3.918	2.732	85.3
iii.	-9.92	2.738	84.7	3.835	2.764	87.2
v.	-3.02	2.739	86.6	3.738	2.739	86.4

### 3.4.5.2 Concentration and Temperature Dependence

**Bis-*p*-tolyl-ditelluride (14).** If **14** underwent an auto-association equilibrium in solution such as equation **3.8**, the proportion of associated molecules would rise with an increase of the total concentration.



Such equilibrium would be fast enough for the NMR experiment to observe only an averaged resonance of <sup>125</sup>Te nuclei. Therefore the observed chemical shift would depend on the total concentration and temperature. The <sup>125</sup>Te chemical shift of **3** was measured

\*\* All geometry optimizations were carried out using the PW91 potential for exchange and correlation. This method is unable to deal with dispersion, which likely contributes to the supramolecular association in these systems. Dispersion-supplemented functionals are now available, but the empirical corrections employed by them are not satisfactory for systems that combine light and heavy elements.

over three orders of magnitude of concentration, and temperatures between 270.0 and 305.0 K, in solvents of different donor ability and dielectric constant: hexanes, DMSO, carbon tetrachloride, and pyridine. **Figure 3.15** and **Table 3.9** present the results obtained at 303 K; in each solvent the  $^{125}\text{Te}$  chemical shift decreased with each dilution step following a linear trend.<sup>††</sup> It is not possible to extract a thermodynamic constant from this trend line because the actual resonances of the structures involved in the equilibrium are unknown. However, it is clear that the  $^{125}\text{Te}$  chemical shifts measured in different solvents can only be compared once the effect of concentration dependence is removed at *infinite dilution*, i.e. by extrapolating the trend lines to zero concentration.

---

<sup>††</sup> In addition to the association equilibrium, the chemical shift would be influenced by the change in diamagnetic susceptibility that results from the change in composition. This is generally considered to be a small contribution for  $^1\text{H}$  and  $^{13}\text{C}$  spectra, but is more significant in systems containing heavy elements.

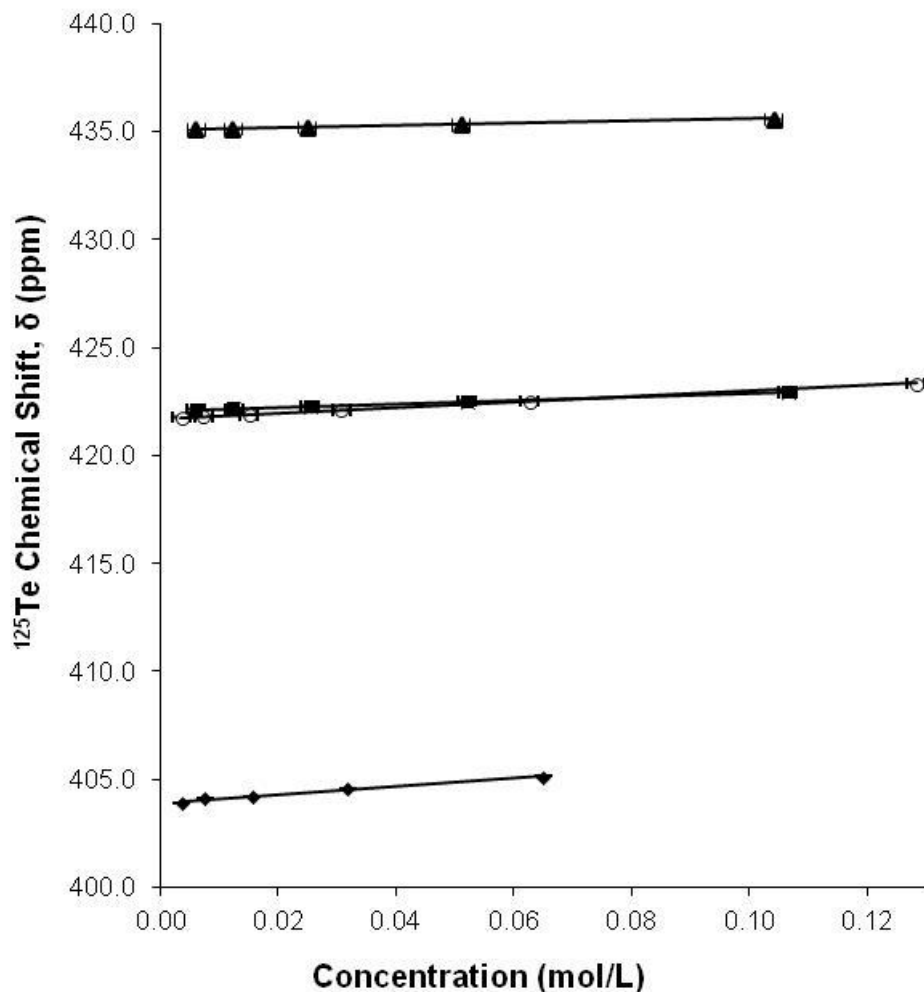


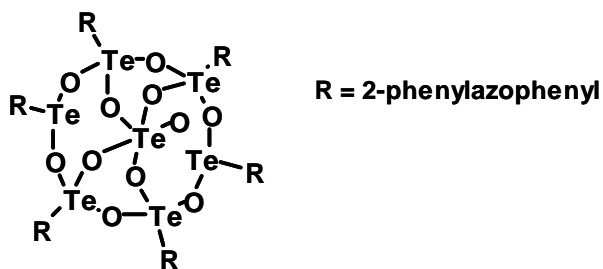
**Figure 3.15** Effect of the concentration on the  $^{125}\text{Te}$  NMR chemical shift of **14** in solution at 303.0 K. (▲ =  $\text{CCl}_4$ , ○ = Hexanes, ■ = Pyridine, ◆ = DMSO). The error in the measured chemical shift ( $\leq 0.005$  ppm) is too small to be noticeable in this plot.

**Table 3.9** Regression parameters\* of the concentration dependence of the  $^{125}\text{Te}$  NMR chemical shift of **14** at 303.0 K.

Solvent	$\text{CCl}_4$	Hexanes	Pyridine	DMSO
$\delta(\text{ppm})_{\text{infinite dilution}}$	$435.1 \pm 0.02$	$421.7 \pm 0.01$	$422.1 \pm 0.04$	$403.9 \pm 0.2$
Slope ( $\text{ppm L mol}^{-1}$ )	$5.1 \pm 0.3$	$12.7 \pm 0.2$	$7.9 \pm 0.8$	$18.8 \pm 4.4$

\*Confidence range at 95%

Measurements in DMSO and pyridine were complicated by the instability of the ditelluride in these solvents. A white precipitate formed from solutions of **14** over time. Formation of this solid could be slowed by shielding samples from light and keeping them in tightly sealed containers to exclude oxygen. Such decomposition has been observed before<sup>169,170</sup> but the products have not been conclusively identified. Proposed products include a variety of oxygen-containing species ( $R_2Te_2O$ ,  $R_2Te_2O_2$ ,  $R_2Te_2O_3$ ) based on IR and elemental analysis (EA), but it is likely that these are species related to **18**.<sup>171</sup>

**18**

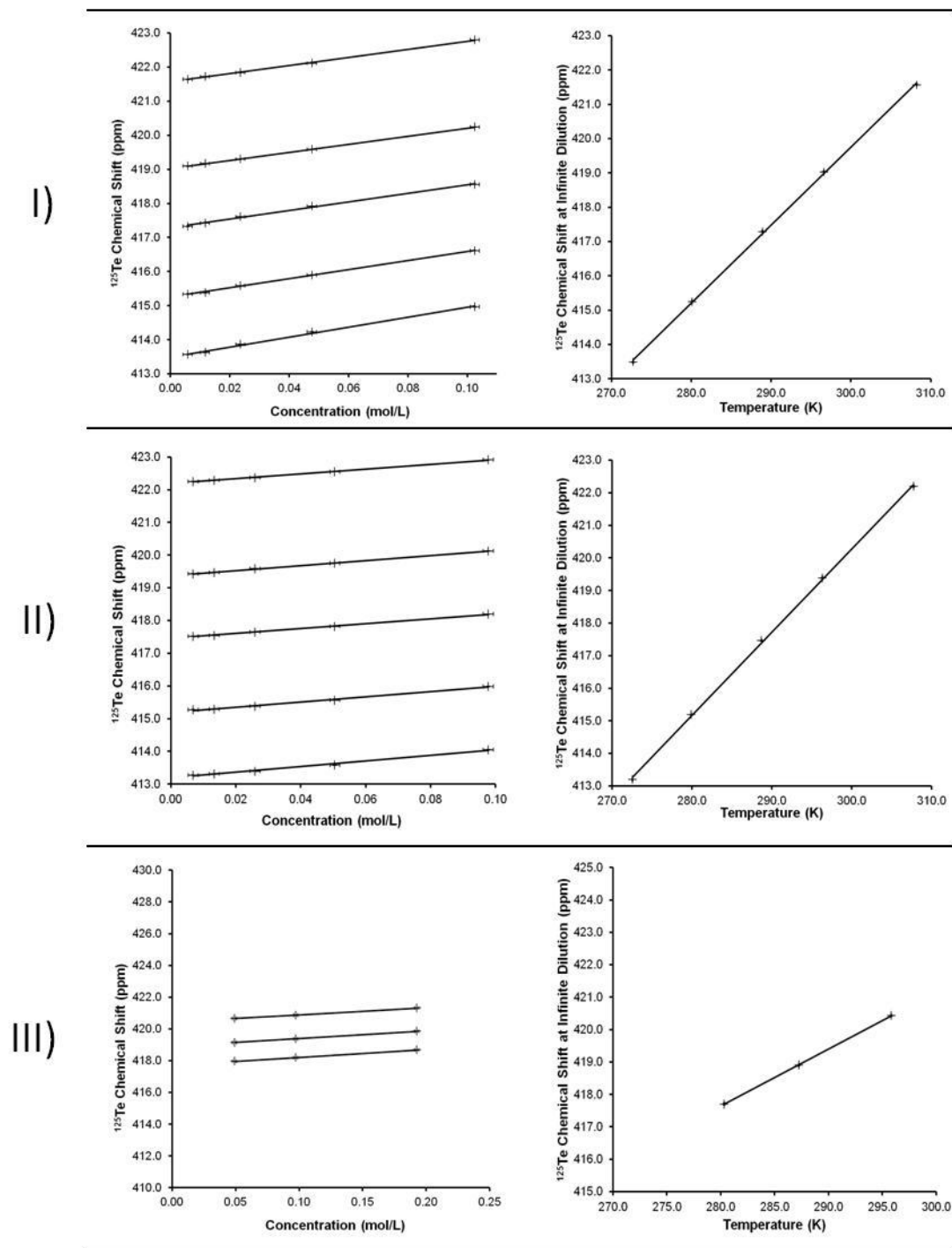


**Figure 3.16** Effect of concentration and temperature on the  $^{125}\text{Te}$  NMR chemical shift of **14** in I) hexanes, II) toluene, and III) dichloromethane. The errors in the measured chemical shift ( $\leq 0.005$  ppm) and temperature ( $\leq 0.045$  K) are too small to be noticeable in this plot.

**Table 3.10** The dependence of the  $^{125}\text{Te}$  NMR chemical shift on the concentration of **14** in hexanes.\*

Temperature ( $\pm 0.1\text{K}$ )	Slope ( $\text{ppm L mol}^{-1}$ )	Intercept (ppm)
308.2	$11.9 \pm 0.8$	$421.6 \pm 0.0$
296.6	$11.8 \pm 0.2$	$419.0 \pm 0.0$
288.9	$12.6 \pm 1.6$	$417.3 \pm 0.1$
280.1	$13.3 \pm 1.0$	$415.3 \pm 0.1$
272.7	$14.6 \pm 1.9$	$413.5 \pm 0.1$

\*Confidence range at 95%

**Table 3.11** The dependence of the  $^{125}\text{Te}$  NMR chemical shift on the concentration of **14** in toluene.\*

Temperature ( $\pm 0.1\text{K}$ )	Slope ( $\text{ppm L mol}^{-1}$ )	Intercept (ppm)
307.7	$7.3 \pm 0.7$	$422.2 \pm 0.0$
296.3	$7.6 \pm 0.5$	$419.4 \pm 0.0$
288.7	$7.5 \pm 0.7$	$417.5 \pm 0.0$
279.9	$8.0 \pm 1.2$	$415.2 \pm 0.1$
272.6	$8.5 \pm 1.7$	$413.2 \pm 0.1$

\*Confidence range at 95%

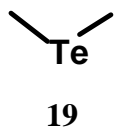
**Table 3.12** The dependence of the  $^{125}\text{Te}$  NMR chemical shift on the concentration of **14** in dichloromethane.\*

Temperature ( $\pm 0.1\text{K}$ )	Slope ( $\text{ppm L mol}^{-1}$ )	Intercept (ppm)
295.6	$4.5 \pm 1.1$	$420.4 \pm 0.1$
287.2	$4.9 \pm 1.2$	$418.9 \pm 0.2$
280.3	$5.0 \pm 0.6$	$417.7 \pm 0.1$

\*Confidence range at 95%

In order to avoid the possible interference of such side reactions, measurements at other temperatures were completed only for the solutions in hexanes, toluene, and dichloromethane; the results are summarized in **Figure 3.16** and **Table 3.10**, **Table 3.11**,

and **Table 3.12**. In all cases the  $^{125}\text{Te}$  NMR chemical shift displayed a linear dependence on concentration. For each solvent, the slopes and the infinite dilution chemical shifts are temperature dependent. The infinite dilution chemical shifts exhibit a linear dependence on the temperature; the slopes of these lines are  $0.2 \pm 0.0 \text{ ppm K}^{-1}$  in hexanes,  $0.3 \pm 0.0 \text{ ppm K}^{-1}$  in toluene, and  $0.2 \pm 0.0 \text{ ppm K}^{-1}$  in dichloromethane; interpolated chemical shifts at 298.0 K are 419.3 ppm, 419.8 ppm and 420.8 ppm respectively. In order to appreciate the significance of this data it is necessary to compare the behaviour of other tellurium systems.



**Dimethyl telluride (19)**. The chemical shift measured from a neat sample of dimethyl telluride (**19**) changed by  $0.10 \text{ ppm} \pm 0.0 \text{ K}^{-1}$  between 270.0 and 305.0 K; this value is comparable within experimental error to literature data.<sup>172</sup> By definition, the chemical shift at 298.0 K is 0.0 ppm.

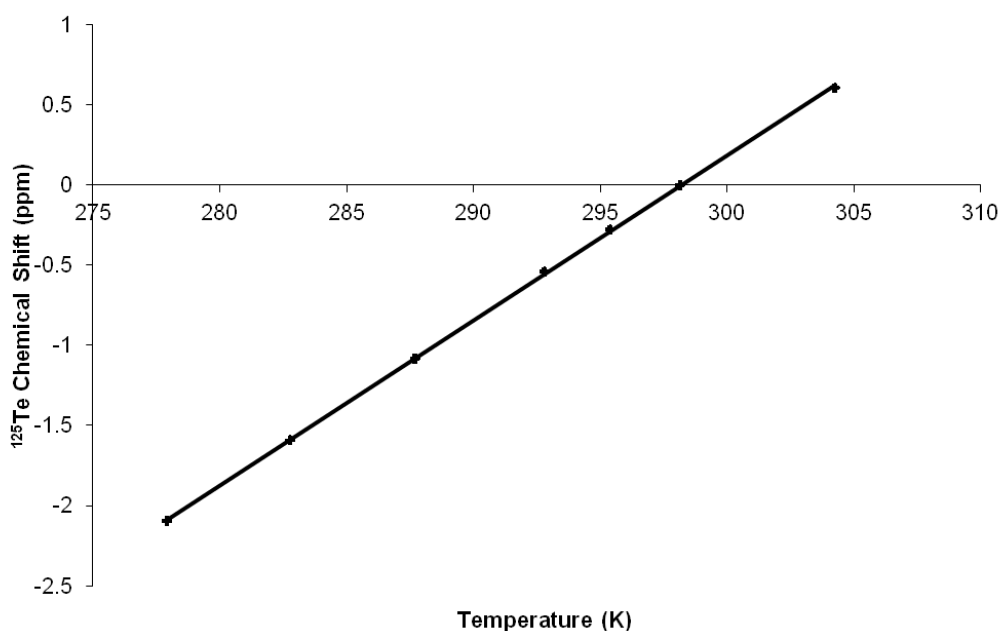


**Figure 3.17** Effect of the temperature on the  $^{125}\text{Te}$  NMR chemical shift of **19**. The errors in the measured chemical shift ( $\leq 0.005$  ppm) and temperature ( $\leq 0.045$  K) are too small to be noticeable in this plot.

**Telluric Acid (13).** **Figure 3.18** graphically summarizes the concentration and temperature dependence of the  $^{125}\text{Te}$  chemical shift of telluric acid (**13**) in water. The chemical shift depends on concentration by  $-0.5 \pm 0.3$  ppm  $\text{L mol}^{-1}$  at 296.2 K. This small negative slope is likely an effect of the change of diamagnetic susceptibility. The data for **13** can be corrected using the reported volume susceptibilities of the solvent<sup>154</sup> and the solute.<sup>173</sup> The volume susceptibility of dimethyl telluride was approximated using literature methods.<sup>174</sup> The temperature dependence of **13** in water was just  $0.1 \pm 0.0$  ppm  $\text{K}^{-1}$  with an interpolated chemical shift of 711.8 ppm at 298.0 K.

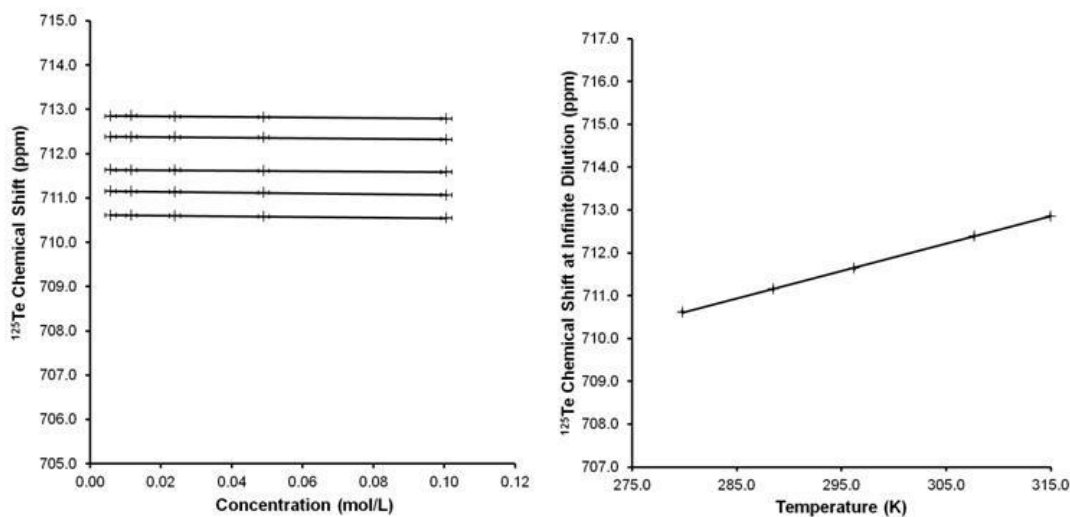


**Figure 3.18** Effect of concentration and temperature on the  $^{125}\text{Te}$  NMR chemical shift of **13** in water. The errors in the measured chemical shift ( $\leq 0.005$  ppm) and temperature ( $\leq 0.045$  K) are too small to be noticeable in this plot.

**Table 3.13** The dependence of the  $^{125}\text{Te}$  NMR chemical shift on the concentration of **13** in water. Corrections are applied according to Eq. 3.7.\*

Temperature ( $\pm 0.1\text{K}$ )	Slope ( $\text{ppm L mol}^{-1}$ )	Corrected Slope ( $\text{ppm L mol}^{-1}$ )	Intercept (ppm)	Corrected Intercept (ppm)
315.0	$-0.7 \pm 0.3$	$-0.6 \pm 0.3$	$712.9 \pm 0.0$	$710.8 \pm 0.0$
307.7	$-0.5 \pm 0.4$	$-0.4 \pm 0.4$	$712.4 \pm 0.0$	$710.2 \pm 0.0$
296.2	$-0.5 \pm 0.3$	$-0.4 \pm 0.4$	$711.6 \pm 0.0$	$709.4 \pm 0.0$
288.5	$-0.9 \pm 0.3$	$-0.8 \pm 0.3$	$711.2 \pm 0.0$	$709.0 \pm 0.0$
279.8	$-0.7 \pm 0.1$	$-0.6 \pm 0.1$	$710.6 \pm 0.0$	$708.4 \pm 0.0$

\*Confidence range at 95%

**Bis-N,N-dimethylbenzylamino-*o*-ditelluride (15)**. The  $^{125}\text{Te}$  chemical shift of the benzyl amino derivative **15** was measured in hexanes or toluene over a concentration range and temperatures between 270.0 and 305.0 K. The results are graphically summarized in **Figure 3.19**. Within each temperature data set there was again a clear

concentration dependence of the chemical shift, increasing with lower temperatures. When compared to the concentration dependence of **14** in hexanes ( $11.8 \pm 0.2$  ppm L mol<sup>-1</sup> at 296.6 K), the observed dependence of **15** was notably smaller ( $9.3 \pm 0.9$  ppm L mol<sup>-1</sup> at 296.2 K); a similar result was observed in toluene ( $3.5 \pm 0.7$  ppm L mol<sup>-1</sup> at 297.6 K compared with  $7.6 \pm 0.5$  ppm L mol<sup>-1</sup> at 296.3 K). In the two solvents tested, the temperature dependences were found to be  $0.1$  ppm  $\pm 0.0$  K<sup>-1</sup>, with interpolated chemical shifts of 344.1 ppm at 347.4 K.

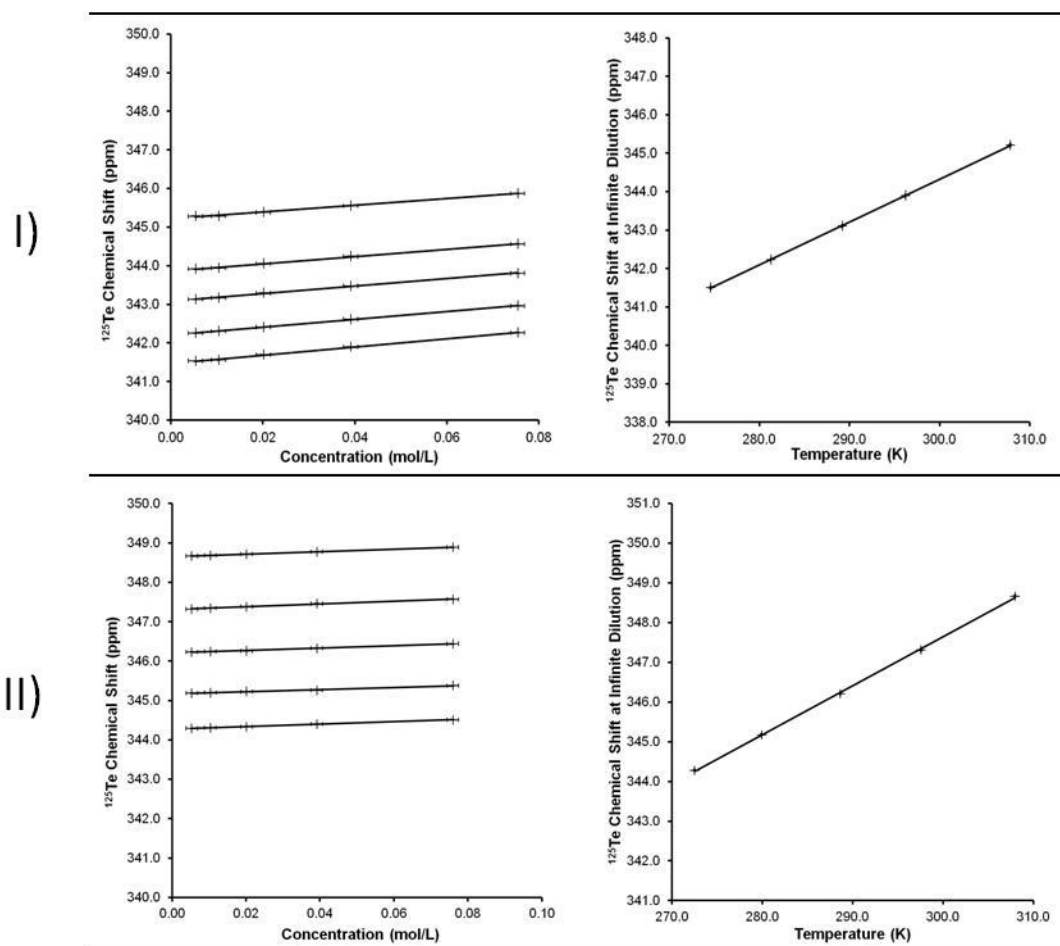


**Figure 3.19** Effect of concentration and temperature on the  $^{125}\text{Te}$  NMR chemical shift of **15** in I) hexanes, and II) toluene. The errors in the measured chemical shift ( $\leq 0.005$  ppm) and temperature ( $\leq 0.045$  K) are too small to be noticeable in this plot.

**Table 3.14** The dependence of the  $^{125}\text{Te}$  NMR chemical shift on the concentration of **15** in hexanes.\*

Temperature ( $\pm 0.1\text{K}$ )	Slope ( $\text{ppm L mol}^{-1}$ )	Intercept (ppm)
307.8	$8.7 \pm 1.1$	$345.2 \pm 0.0$
296.2	$9.3 \pm 0.9$	$343.9 \pm 0.0$
289.2	$9.8 \pm 0.1$	$343.1 \pm 0.0$
281.3	$10.1 \pm 0.0$	$342.2 \pm 0.0$
274.6	$10.6 \pm 0.0$	$341.5 \pm 0.0$

\*Confidence range at 95%

**Table 3.15** The dependence of the  $^{125}\text{Te}$  NMR chemical shift on the concentration of **15** in toluene.\*

Temperature ( $\pm 0.1\text{K}$ )	Slope ( $\text{ppm L mol}^{-1}$ )	Intercept (ppm)
308.0	$3.1 \pm 0.2$	$348.7 \pm 0.0$
297.6	$3.5 \pm 0.7$	$347.3 \pm 0.0$
288.6	$3.0 \pm 0.4$	$346.2 \pm 0.0$
279.9	$2.6 \pm 0.7$	$345.2 \pm 0.0$
272.5	$3.1 \pm 0.3$	$344.3 \pm 0.0$

\*Confidence range at 95%

**bis(tris-dimethylphenylsilyl)methyl ditelluride (16)**. In the case of the sterically hindered bis(tris-dimethylphenylsilyl)methyl ditelluride (**16**), measurements could only be performed in dichloromethane due to the limited solubility in other solvents. The  $^{125}\text{Te}$  chemical shift dependence on concentration and temperature (**Figure 3.20**) displayed a different behavior from that of the other ditelluride molecules. In this case the dependence on concentration was negative ( $-7.2 \pm 4.0 \text{ ppm L mol}^{-1}$  at 296.0 K) with a temperature dependence of  $0.4 \text{ ppm} \pm 0.0 \text{ K}^{-1}$ . Interpolation of the temperature dependence plot to 298.0 K provides a chemical shift of 418.8 ppm.

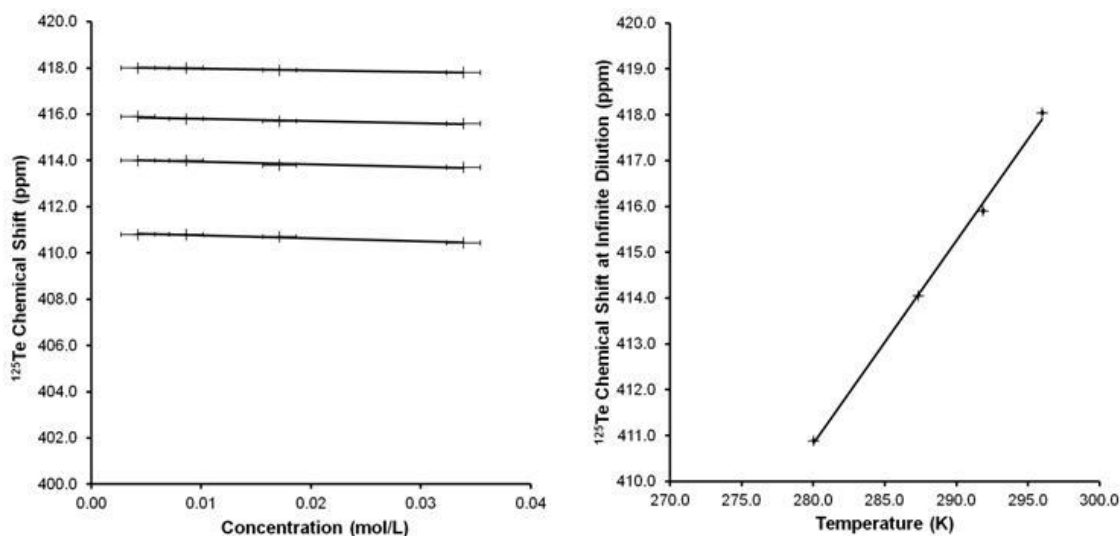


**Figure 3.20** Effect of concentration and temperature on the  $^{125}\text{Te}$  NMR chemical shift of **16** in dichloromethane. The errors in the measured chemical shift ( $\leq 0.005$  ppm) and temperature ( $\leq 0.045$  K) are too small to be noticeable in this plot.

**Table 3.16** The dependence of the  $^{125}\text{Te}$  NMR chemical shift on the concentration of **16** in dichloromethane.\*

Temperature ( $\pm 0.1\text{K}$ )	Slope ( $\text{ppm L mol}^{-1}$ )	Intercept (ppm)
296.0	$-7.2 \pm 4.0$	$418.0 \pm 0.1$
291.9	$-9.5 \pm 8.3$	$415.9 \pm 0.1$
287.3	$-10.9 \pm 10.7$	$414.1 \pm 0.2$
280.0	$-13.0 \pm 7.4$	$410.9 \pm 0.2$

\*Confidence range at 95%

**Comparison.** Being the recommended standard for  $^{125}\text{Te}$  NMR, measurements for  $\text{Te}(\text{CH}_3)_2$  were useful to set the absolute frequency of reference from which the chemical shifts of all other species were measured. It was also used to validate the measurements of temperature dependence, in that the observed thermal shift of its  $^{125}\text{Te}$  resonance was in agreement with literature reports. Telluric acid, **13**, features tellurium in oxidation state

+6, with an idealized octahedral coordination geometry defined by binding of six hydroxyl groups. Here the chalcogen is effectively shielded from interaction with other molecules, although intermolecular hydrogen-bonding between hydroxyl groups is possible. In clear contrast with the behaviour of **14**, the  $^{125}\text{Te}$  chemical shift of this compound exhibits a small and negative dependence on temperature. This trend can be explained by the effect of the volume susceptibility of the sample and how it relates to the chemical shift (Eq. **3.7**). An increase in concentration results in increased magnitude of the diamagnetic (negative) susceptibility of the sample, while that of the reference does not change. The intramolecular N $\cdots$ Te SBI in **15** would compete with the binding of solvent molecules to the tellurium atoms and disrupt the self-association equilibrium. Indeed, the slopes that characterize the concentration dependence at each temperature are consistently smaller than the values measured for **14**. However, the intramolecular SBI does not eliminate the concentration dependence, which suggests that the molecule of **15** is likely in a dynamic equilibrium between the conformation with intramolecular SBIs and a conformation without SBIs that permits the solvent molecules to reach the tellurium atoms. The behaviour of the  $^{125}\text{Te}$  chemical shift of the hindered ditelluride **16**, decreasing with concentration, is likely due in part to the change of diamagnetic susceptibility.

The only way in which the concentration dependence could be discounted entirely was through the use of steric hindrance. The possible association of the ditelluride molecules could account for some of this dependence, and competition with the solvent is

likely to attenuate the observed dependence. At these low concentrations, the weakly coordinating  $\pi$ -system of toluene would shield the tellurium nuclei, preventing any auto-association of ditelluride molecules. Electrostatic dipolar interactions with the chlorine atoms in dichloromethane would more effectively prevent this association, and decrease the concentration dependence.

In all compounds, the temperature dependency of the  $^{125}\text{Te}$  chemical shift at infinite dilution appears to correlate with the size of the molecule; the largest slope is displayed by **16**. This could be an entropic effect, considering the number of vibrational degrees of freedom of each molecule. On this consideration, the infinite dilution chemical shifts of **13–16** and **19** at each temperature were divided by the total number of atoms in each molecule; the resulting plot of the change in chemical shift as a result of changes in temperature (**Figure 3.21**) suggests that in the presence of protecting groups (steric or SBI), the temperature dependence is decreased significantly.

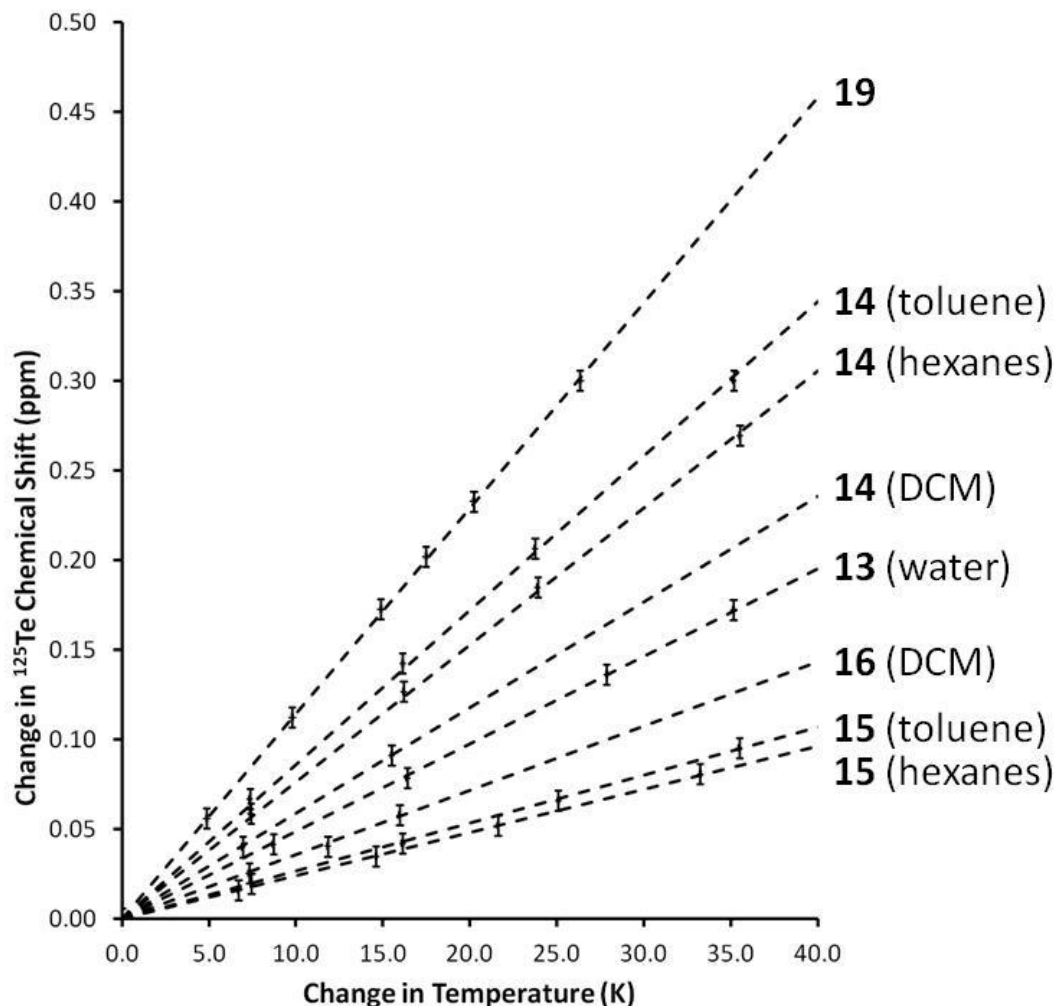


**Figure 3.21** Effect of temperature on the  $^{125}\text{Te}$  NMR chemical shift of **13-16**, and **19**. The chemical shift values have been divided by the number of atoms in the molecule. The errors in the measured temperature ( $\leq 0.045$  K) are too small to be noticeable in this plot.

### 3.5 Summary and Conclusions

Calculations of dipole-moment changes as a function of the C-Te-Te-C dihedral angle of diphenyl ditelluride indicate that the solvent can have influence on the molecular geometry. Such deviations from the gas-phase energy minimum can in turn induce

significant changes in the UV-vis and  $^{125}\text{Te}$  chemical shifts. Experimental and computational studies of bis-*p*-tolyl ditelluride in a variety of solvents show some degree of correlation between the  $^{125}\text{Te}$  chemical shift and the energy of electronic excitation. Concentration and temperature dependences of three ditellurides showed that those effects are also dependent on the nature of the solvent. The presence of SBIs resulted in attenuation of the concentration dependence, but only with the use of large steric bulk could it be removed completely. Explicit solvation models indicate that donor solvents coordinate the ditellurides through donation into the Te-Te  $\sigma^*$  antibonding orbital, but this causes only minor changes of molecular geometry. The increased shielding caused by the solvent on the tellurium nucleus was apparent in the calculated  $^{125}\text{Te}$  chemical shifts for both explicit and implicit solvation models. The auto-association of ditelluride molecules in solution was modeled using the bonding arrangements observed in the solid state; although changes to the structural parameters are modest, the corresponding binding energies suggest these interactions play a role in the observed dependence of  $^{125}\text{Te}$  NMR chemical shift on concentration and temperature.

Although these results did identify some effects of the SBIs, and in general molecular association, on the  $^{125}\text{Te}$  NMR chemical shift of organo-ditellurides, their interpretation is not straightforward. However, this study does show that comparisons of the  $^{125}\text{Te}$  NMR chemical shifts must be approached with great caution. Even differences of concentration and temperature can significantly influence the measurements for a

compound. At very least, details of sample preparation (e.g. concentration, actual temperature) should be reported along with measured  $^{125}\text{Te}$  NMR chemical shift values.

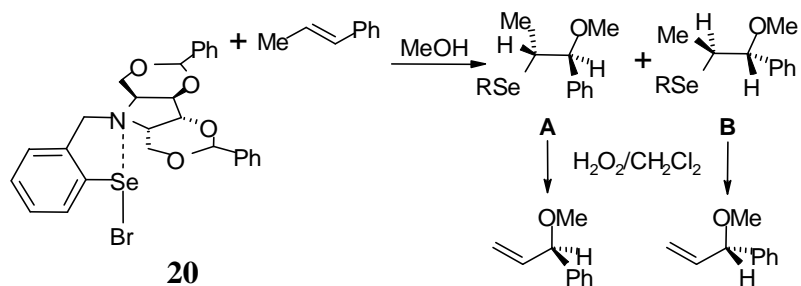
Moreover, these results do indicate that the current standard for Te NMR, "*a solution of less than 10% benzene- $d_6$  in dimethyl telluride*"<sup>175</sup> as defined by IUPAC, should be reconsidered for more accurate chemical shift measurements. Such a mixture is likely to exhibit significant concentration dependency due to solvent-solute interactions and auto-association. The use of an absolute scale, in which the resonances are referenced to the frequency of TMS protons, has already been recommended.<sup>176</sup> Until that approach is accepted for the routine measurement of  $^{125}\text{Te}$  chemical shifts, telluric acid would make a more reliable standard because of its small concentration and temperature dependence. In addition, solid telluric acid can be handled more safely and weighed with greater precision than  $\text{Me}_2\text{Te}$ .

## 4 Investigations of the Reactivity, Electronic Structure and Optical Properties of Dipolar Azobenzenes that Feature Intramolecular E...N SBIs (E = S, Se, Te)

### 4.1 Introduction

The formation of virtual rings and intramolecular secondary bonds is a recurrent feature of molecules that contain a combination of chalcogen atoms (divalent or tetravalent) and heteroatoms with lone pairs available for donation.<sup>177</sup> In most cases, intramolecular SBIs to tellurium involve electron donation from N, P, O, S, or Cl atoms<sup>1</sup> in functional groups such as nitrogen heterocycles,<sup>178</sup> organic carbonyls,<sup>179</sup> amines,<sup>56</sup> phosphines,<sup>180</sup> and nitro groups.<sup>181</sup>

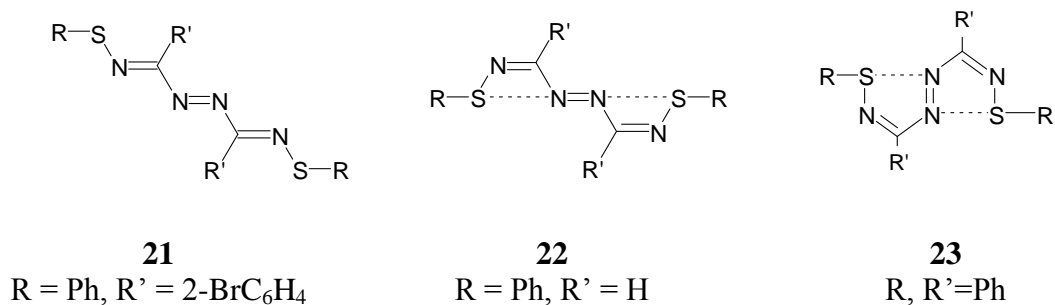
In spite of their modest interaction energies, intramolecular SBIs are sufficiently strong not only to determine the conformation observed in the solid state but also to influence the electronic structure and reactivity of a molecule. For example, compound **20** contains a chiral amine in close interaction with the selenium atom and reacts with olefins yielding up to a 97% enantiomeric excess of one stereoisomer (for example, A in **Scheme 4.1**).<sup>182</sup>



**Scheme 4.1** Asymmetric methoxyselenenylation of an olefin.

Intramolecular SBIs can stabilize certain chalcogen centres in unusual oxidation states; as in the case of the heavier aryl-chalcogenyl halides Ar-E-X (E = Se, Te; X = Cl, Br, I). Such species readily disproportionate into the dichalcogenides and the aryl-chalcogen trihalides but can be stabilized with steric protection<sup>146,183,184</sup> by bulky substituents or through intramolecular coordination.<sup>52,185-187</sup>

As discussed in section 1.1.2, main group SBIs are primarily stabilized by the  $\sigma$  donation of a lone pair into an antibonding orbital. Calculations, however, indicate that in some cases there is an additional stabilizing  $\pi$  interaction in which, akin to *back-bonding*, a lone pair of a divalent chalcogen is delocalized into the antibonding orbital of a N=N double bond.<sup>17</sup> Indeed, the colour of diazenes of type RSN=C(R')N=NC(R')=NSR (**Scheme 4.2**) is influenced by the conformation of the molecule. While compounds **21** and **22** are red-brown, compound **23** has a characteristic purple colour.<sup>17</sup>



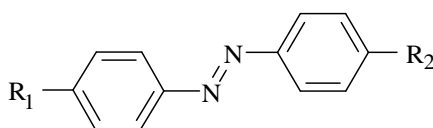
**Scheme 4.2** Structural isomers of the type  $\text{RSN}=\text{C}(\text{R}')\text{N}=\text{NC}(\text{R}')=\text{NSR}$ .

#### 4.1.1 Proposed System of Study and Objectives

In principle, the delocalization of electron density of a chalcogen atom into a conjugated  $\pi$  system through an intramolecular SBI in a virtual ring could be used to manipulate the electronic structure and properties of a molecule. Conversely, changes in the molecular structure that affect the strength of an intramolecular SBI could be monitored through spectroscopic methods that are sensitive to changes in the electronic structure (e.g. UV-vis absorption). This chapter explores the interplay of these concepts based on organo-chalcogen chemistry and the optical properties of a family of simple and well understood chromophores: the *azobenzenes*.

In general, diphenyldiazenes ("azobenzenes", **24**) exhibit characteristic strong absorption bands in the UV and visible due to  $\pi^* \leftarrow \pi$  and  $\pi^* \leftarrow n$  transitions. The *E* configuration is most stable but irradiation with light (between 300 and 400 nm for the parent azobenzene) can induce *Z* isomerisation; this process has received much attention due to multiple demonstrations of practical applications.<sup>188,189</sup> Substituted azobenzenes can be classified in three general groups, based on the effect of the substituent on the

electronic structure of the molecule. Azobenzene-type describes substituent groups which are electronically inert (**Scheme 4.3, 24**). Aminoazobenzenes exhibit an amino donor substituent, typically *para*- to the azo bridge (**Scheme 4.3, 25**). Pseudostilbenes (also called dipolar, D- $\pi$ -A or push pull azobenzenes) describe combined effects of electron donor and acceptor groups placed at opposite ends of the molecule (**Scheme 4.3, 26**). Azobenzenes find actual applications in dyes and pigments, acid-base indicators, liquid crystals, electro-optical devices and nonlinear optical materials.<sup>190-195</sup> At least in part, they are frequently studied because they can be readily synthesized through long-established methods and from inexpensive reagents, e.g. by the reaction of diazonium cations with electron rich compounds or reductive coupling of nitro-aromatics.



- 24**  $R_1, R_2 = \text{Alkyl, H}$   
**25**  $R_1 = \text{N(alkyl)}_2, R_2 = \text{Alkyl, H}$   
**26**  $R_1 = \text{N(alkyl)}_2, R_2 = \text{NO}_2, \text{F, S(O)}_2\text{Me}$

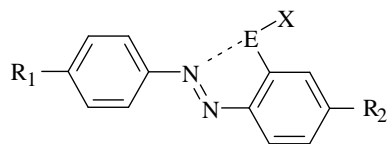
**Scheme 4.3** Classification of substituted azobenzenes.

The specific system chosen for the investigations described in this chapter consists of a chalcogen atom placed *ortho* to the azo bridge (**Scheme 4.4**). In this position the chalcogen is able to form a virtual five-membered ring and delocalize electron density onto the  $\pi^*_{\text{N=N}}$  orbital. As the SBI must be sensitive to the nature of the group X, the UV-vis spectrum could be used to monitor the process of exchange of X and other chalcogen-

centered reactions. Amongst the available options, azobenzenes which feature a combination of one electron donor and one electron acceptor groups are especially interesting because of their large hyperpolarisabilities.

The overall objectives of these investigations included:

- To examine the impact of the intramolecular SBI on the electronic structure & UV-vis spectra of the modified chromophore.
- To take advantage of such changes to monitor a reaction at the chalcogen centre.
- To establish the effect of the intramolecular SBI on the NLO properties of the chromophore.

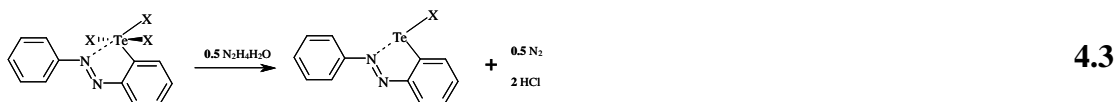
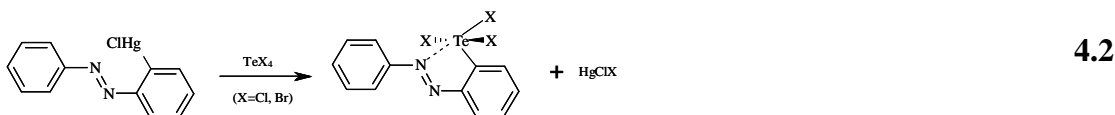
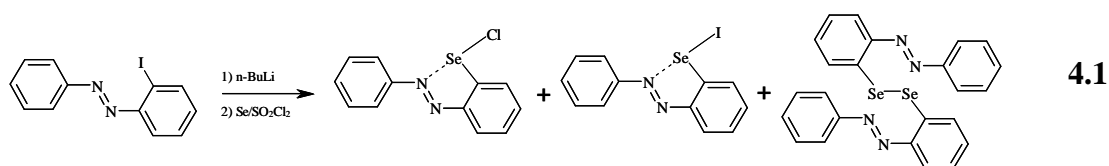


**Scheme 4.4** Azodye chalcogen-substituted *ortho*- to the azo bridge.

#### 4.1.2 Proposed Methods and Scope of this Chapter

Based on literature reports, two methods were considered for the synthesis of the target azobenzenes, the first would proceed through a lithiated intermediate, the second would employ an organomercury alternative reagent. As an example of the first method, the addition of *n*-BuLi to 2-iodoazobenzene, followed by the 1:1 addition product of elemental selenium and  $\text{SO}_2\text{Cl}_2$  yields a mixture of starting material, bis(2-phenylazophenyl-C-N')selenide, and the 2-selenenyl chloride and iodide substituted dyes

(Eq. 4.1);<sup>196</sup> a similar reaction using instead selenium tetrabromide yields the selenenyl-bromide. However, working with lithiated azobenzenes is complicated because of their propensity to decompose at temperatures over  $-78^{\circ}\text{C}$ . In this respect organomercurials are more convenient intermediates thanks to their kinetic stability. Reaction of a chloromercuro-substituted azobenzene with tellurium tetrachloride or tetrabromide gives rise to the corresponding trihalotellurenyl substituted species; subsequent reduction with hydrazine affords the Te(II) analogues (Eq. 4.2, and 4.3).<sup>197,198</sup> The synthesis of a mercurated intermediate was attempted but soon it became evident that the dipolar azobenzenes are much less reactive than azobenzene and once the reaction was enabled it occurred on the ring that in principle bears less electron density. This observation led to detailed experimental and computational investigations that provide a rationale for our observations and are summarised in the next section. The application of the mercurated intermediate in the synthesis of the substituted chromophores and the study of such species is discussed in the subsequent sections.



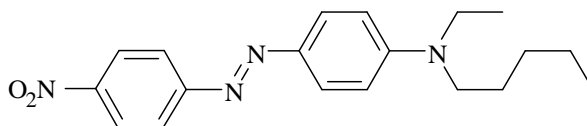
## 4.2 Mercuration of a Push-Pull Azobenzene

A vast variety of aryl-mercurials have been obtained in over 100 years of research.<sup>36,199</sup> The field has been reinvigorated by studies of the unique Lewis-acid properties of perfluorinated phenylmercurials. Their ability to form complexes with a variety of molecules,<sup>200,201</sup> including conjugated alkynes,<sup>202</sup> metallocenes,<sup>203</sup> organic esters,<sup>204</sup> and arenes<sup>205</sup> can be applied to the assembly of remarkable supramolecular structures.<sup>206</sup> Recent work has shown that mono- and di-functional Lewis acids containing bridging mercury atoms exhibit affinities for fluoride ions that rival those of their diboron counterparts, but possess greater stability in the presence of water.<sup>207</sup> Many of these species are synthesized through transmetallation of the corresponding lithiated intermediates or Grignards with mercuric salts; but organo-mercury compounds can also be prepared through simple metallation. Activated aromatic molecules easily react with mercury (II) oxide, chloride, acetate or trifluoroacetate (in increasing order of reactivity).<sup>208</sup>

Direct mercuration of aromatic rings is strongly influenced by the nature of the substituent groups. Such effects are usually explicable by considering an electrophilic aromatic substitution (EAS) mechanism and the resonance of multiple canonical structures;<sup>209,210</sup> in the classical formalism, electron-donating groups are *ortho/para*-directors while electron-withdrawing groups are *meta*-directors. However, the reactions of mercuric salts with aromatic species often yield results that - at first glance - are unexpected. For example, the mercuration of toluene exhibits at first a strong preference for *para*-substitution but equilibrium between all three possible isomers will ensue over

long reaction times, especially in acidic medium.<sup>211</sup> This has been attributed to the ability of mercury in the arenemercuronium ions to shift when there is no kinetic control over the site of substitution.<sup>212</sup> The low yield of *ortho*-mercurated products obtained from some monoalkyl-benzenes does suggest steric effects also impact these reactions.<sup>213</sup> Interestingly, while the mercuration of nitrobenzene yields predominantly *meta*-substituted species there is also a significant proportion of *ortho*-mercuration.<sup>210</sup> In general, substituents bearing electron lone pairs promote mercuration at the *ortho* position, which is usually assumed to be the consequence of an attractive interaction with the mercury ion.<sup>209,210</sup>

However, the regiochemistry of the mercuration of larger molecules with extensively conjugated  $\pi$ -systems and a combination of competing donor and acceptor groups is difficult to predict, as is the case with the direct mercuration of diphenyl Schiff bases.<sup>59</sup>

**27**

For this project we required the mercuration of a push-pull azodye (N-Ethyl-4-[4-nitrophenyl]diazenyl] N-pentylaniline, **27**). Most of what is already known about the mercuration of azobenzenes derives from early studies that meticulously examined the reaction of the parent compound and several *ortho*-substituted derivatives.<sup>214,215</sup> In

general, azobenzenes are not very reactive and do require stringent mercuration conditions. For example, 22 h of reflux in methanol with one equivalent of mercury acetate yields just 40% of *ortho*-monomercurated and 3% of each *o,o*- and *o,o'*-dimercurated products. Addition of a small amount of perchloric acid increases the corresponding yields to 55%, 8% and 9%. Similarly, reflux with mercury trifluoroacetate salt in neat trifluoroacetic acid yields 57% of *ortho*-monometallated product. The effect of individual substituents is complicated. *Ortho*-methylazobenzene experiences 71% monomercuration on the substituted ring after 22 h of reflux methanol with one equivalent of mercury acetate. *o,o'*-dimethylazobenzene gives 51% monomercuration, and 4% *o,o'*-disubstitution under the same conditions, while *o*-methoxyazobenzene yields 63% monomercuration and 1% and 4% of *o,o*- and *o,o'*-dimercurials respectively.<sup>214</sup> Interestingly, electron withdrawing groups in the *ortho* position appear to promote substitution of their own ring and noticeably decrease the yields (-I: 22%, -NO<sub>2</sub>: 6%, -CN: 1%) of monomercurials. In most cases, the limited solubility of the mercurated products is a problem that can be solved by treatment with elemental iodine; the reaction replaces the HgR group for an iodine atom without isomerization. The iodo products usually are soluble enough to permit their identification by <sup>1</sup>H NMR; this procedure assumes that iodine will be attached only at the position that is already substituted.<sup>214</sup>

## 4.2.1 Results and Discussion

### 4.2.1.1 Synthesis

In a typical experiment, compound **27** and mercury trifluoroacetate were combined with anhydrous trifluoroacetic acid under an atmosphere of nitrogen. The sample was maintained at 68 °C with vigorous stirring before quenching with a solution of sodium chloride and sodium acetate in water. After treatment with ultrasound for 10 min, the insoluble maroon product was treated with base then treated with a solution of iodine in chloroform for 48 h. After removing the solvent, the solids were washed with aqueous sodium thiosulfate and water to remove residual iodine.

The distribution of products with time was monitored through the use of six reaction tubes of a parallel synthesis reactor (Argonaut FirstMate™). The samples were treated as above, and quenched at prescribed times. Each sample was treated with ultrasound for 10 min, washed repeatedly with aqueous sodium bicarbonate, centrifuged, and the supernatant was removed by pipette. The solid residues were then treated with iodine as above. NMR spectra were measured on the entirety of each sample dissolved in dichloromethane.

### 4.2.1.2 Molecular Structure of 2,2'-Diiodo Azobenzene (**28**)

Preliminary experiments tested several methods for the synthesis and purification of the products of mercuration of azobenzene. The corresponding observations were consistent with Roling's original reports.<sup>214,215</sup> From the mixture obtained by stepwise reaction with Hg(CF<sub>3</sub>CO<sub>2</sub>)<sub>2</sub>, NaCl and I<sub>2</sub>, fractional crystallization afforded single needle-like purple crystals of 2,2'-diiodo azobenzene (**28**). In view of the lack of structural data

on iodo-azobenzenes, the X-ray diffraction pattern was collected and the structure solved. Although the structure of **28** (**Figure 4.1**) shows a planar arrangement of the rings, there is elongation of the ellipsoids of C5' and C6' as well as I1' out of the plane. This elongation is likely the cause of thermal motion, as the data was collected at room temperature and the molecule does not lie on a mirror plane. Although the planar conformation of the rings is consistent with the 2,2'-dichloro analog,<sup>216</sup> there does seem to be flexibility in the azobenzene molecule; the rings retain a parallel geometry, but are staggered relative to one another.<sup>217</sup> The C-N (1.419(4) Å) and N=N (1.236(3) Å) bond distances are within error of those observed in azobenzene (1.431(1) Å and 1.2562(8) Å respectively) but there is an increase in the C-N-N bond angle from 113.52(4)° to 115.10(2)°.<sup>217</sup> Details on the refinement of the crystal structure of **28** can be found in **Table 4.1**.

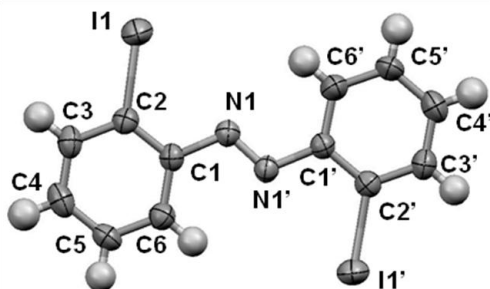
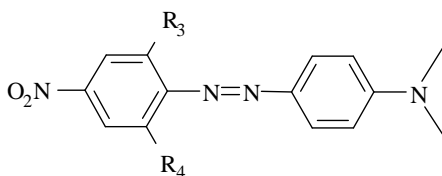


**Figure 4.1** ORTEP of 2,2'-diiodo azobenzene, **28** (50% displacement ellipsoids).

#### 4.2.1.3 Mercuration of Dipolar Azodyes

Although the observations summarised in section 4.2 do provide an excellent overview of the influence of individual substituents on the mercuration reaction of

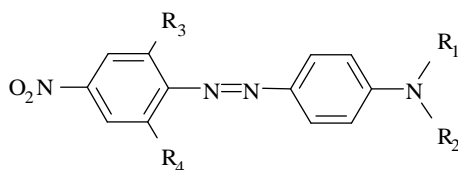
azobenzene, molecules that contain two substituents with competing effects, as would be the case of push-pull azobenzenes, are notably absent from that list. Our preliminary work on the mercuration of azodyes was based on [(4-nitrophenyl)diazenyl]N,N-dimethylaniline (**29**).



**29** R<sub>3</sub>, R<sub>4</sub> = H  
**30** R<sub>3</sub> = H, R<sub>4</sub> = I

Mercuration attempts with mercury (II) chloride and acetate were unsuccessful. Chromatographic evidence of partial mercuration of **29** was obtained with the trifluoroacetate in anhydrous trifluoroacetic acid.<sup>214</sup> However, the yield was small and the limited solubility of the product hampered optimization of the method. Longer alkyl groups were placed on the amino group in order to increase the solubility of the azodye. Satisfactory results were obtained for the N-Ethyl-[(4-nitrophenyl)diazenyl] N-pentylaniline (**27**), therefore this compound was used for a full study of the reaction. After mercuration, the trifluoroacetate anion was exchanged for chloride in order to facilitate the isolation of the products. The crude mercurated materials were usually obtained as dark-maroon solids which could not be thoroughly purified on their own due to their limited solubility in common solvents. Instead, iodine treatment in chloroform afforded a soluble fraction that was shown by NMR and HPLC to be a mixture. The

custom HPLC separation method combined gradient and isocratic water/acetonitrile regimes. Three major bands were observed, and the separation method was scaled up to collect samples large enough to permit their spectroscopic characterization. Up to 7% of the material obtained from the iodination reaction eluted in 12 small bands which could not be conclusively identified. Also, a significant amount of starting material (10%) was recovered.

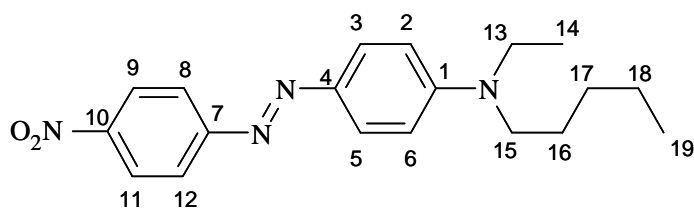


**31**  $R_1 = C_2H_5$ ,  $R_2 = n-C_5H_{11}$ ,  $R_3 = H$ ,  $R_4 = HgCl$

**32**  $R_1 = C_2H_5$ ,  $R_2 = n-C_5H_{11}$ ,  $R_3, R_4 = HgCl$

**33**  $R_1 = C_2H_5$ ,  $R_2 = n-C_5H_{11}$ ,  $R_3 = H$ ,  $R_4 = I$

**34**  $R_1 = C_2H_5$ ,  $R_2 = n-C_5H_{11}$ ,  $R_3, R_4 = I$



**Scheme 4.5** Atom numbering for **27**.

#### 4.2.1.4 Structures of the Isolated Compounds

Each species was initially identified using two-dimensional  $^1H$  NMR spectroscopy, taking advantage of the changes in the patterns of the aromatic region. The first band to

elute ( $t = 8.78$  min) corresponded to unreacted azodye (**27**). Its NMR spectrum displays characteristic pairs of doublets of the amino [ $\delta = 6.82, 7.93$  ppm ( $^3J_{\text{H-H}} = 9.02$  Hz)] and nitro rings [ $\delta = 7.95, 8.31$  ppm ( $^3J_{\text{H-H}} = 8.85$  Hz)] with equal integrations. The second band ( $t = 12.37$  min) belongs a di-substituted species giving three equally intense resonances in the aromatic region: two doublets at 6.68 ppm ( $^3J_{\text{H-H}} = 9.11$  Hz) and 7.90 ppm ( $^3J_{\text{H-H}} = 9.11$  Hz) which would belong to the amino ring and one singlet at 8.76 ppm which indicated that two iodine atoms are in equivalent positions, likely ortho to the azo bridge. The third band ( $t = 14.21$  min) corresponds to a product of mono-substitution. While the chemical shifts of the protons in the amino ring are essentially unchanged [ $\delta = 6.82, 7.94$  ppm ( $^3J_{\text{H-H}} = 9.00$  Hz)] the nitro ring protons produce two doublets at  $\delta$  7.68 ppm ( $^3J_{\text{H-H}} = 9.00$  Hz) and 8.81 ppm ( $^3J_{\text{H-H}} = 2.52$  Hz) which couple to the resonance centred at 8.24 ppm. On the basis of their  $^1\text{H}$  NMR spectra the second and third major bands in the chromatogram were assigned to compounds **34** and **33** respectively.

#### 4.2.1.5 Molecular Structure of **30**

Although the NMR characterization of the species in the second band does show functionalization of the nitro ring, there remains some ambiguity about the exact position of metallation. Both the nitro group and the azo-bridge are known to have an ortho-directing effect. An assignment based only on the  $^1\text{H}$  NMR chemical shifts would be uncertain because the aromatic protons are subject to both the inductive effect of the substituents and the anisotropic shielding from the  $\pi$ -electron cloud. Single-crystal x-ray

diffraction would be the best way to make a definitive structural assignment. However, attempts to grow single crystals of the second band species were unsuccessful and only dendritic microcrystals were observed.

Instead the product of monosubstitution of **29** did yield crystals of good enough quality for structural determination. The structure of **30** (**Figure 4.2**) does show the iodine atom *ortho*- to the azo bridge on the nitro-substituted ring. Data from the final refinement is provided in **Table 4.1** and selected bond distances and angles are provided in **Table 4.2**. The molecule exhibits a perfectly planar structure, which is somewhat unexpected. Although there are no structurally characterized *ortho*-iodo azobenzenes, the structures of similarly *ortho*-halogenated azodyes<sup>218-221</sup> show the halogenated ring rotated between 2.05°-8.60° from the average plane and, in one notable extreme, 2'-Bromo-4-(N-(2-cyanoethyl)-N-(2-phenylethyl)amino)-4'-nitro-azobenzene has rings which are rotated 38.19° from each other.<sup>222</sup>

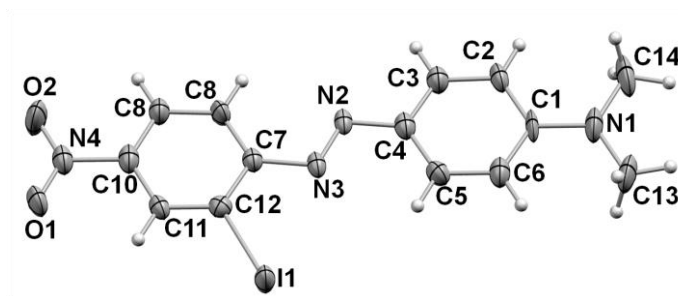


**Figure 4.2** ORTEP of 4-nitro, 2-iodo, 4-dimethylamino azobenzene, **30** (50% displacement ellipsoids). For clarity, all hydrogen atoms are displayed as spheres of  $\text{\AA} = 0.15$ .

The crystal structure of **30** does show displacement ellipsoids somewhat elongated along *b*. This fact suggests that there might be some disorder in the orientation of the

rings with respect to each other and the observed flat structure might be the average; however, a satisfactory model for such a disorder could not be found. Despite these limitations, the structural determination did establish the position at which **29** underwent metallation. Given the similarities of their NMR spectra, **30** and the mono iodo derivative of **33** must have analogous connectivities, which confirms the identification of **34** as the species eluting at 14.2 min. This observation confirms by extension the identification of **34** and implies that the products of the mercuration reaction are **31** and **32**.

**Table 4.1** Summary of crystal data, collection and refinement conditions for **28** and **30**.

	<b>28</b>	<b>30</b>
Formula	C <sub>12</sub> H <sub>8</sub> N <sub>2</sub> I <sub>2</sub>	C <sub>14</sub> H <sub>13</sub> N <sub>4</sub> O <sub>2</sub> I
Formula weight	433.98	396.18
Radiation (wavelength, Å)	0.71073	0.71073
Temperature	296(2)	173 (2)
Crystal system	Monoclinic	Monoclinic
Space group	P2 <sub>1</sub> /c	I2/m
a (Å)	4.6306(3)	13.447(4)
b (Å)	18.1105(12)	6.6929(18)
c (Å)	15.3748(10)	16.799(6)
α (°)	90.00	90.00
β (°)	98.5320(10)	99.083(3)
γ (°)	90.00	90.00
Volume (Å <sup>3</sup> )	1275.10(14)	1492.9(8)
Z	4	4
δ <sub>calcd.</sub> (g/cm <sup>3</sup> )	2.261	1.763
μ (mm <sup>-1</sup> )	4.907	2.155
R <sub>1</sub> <sup>a</sup>	0.0398	0.069
wR <sub>2</sub> <sup>b</sup>	0.0262	0.113

$$^a R_1 = \frac{\sum ||F_o| - |F_c||}{\sum |F_o|}$$

$$^b wR_2 = (\sum w ||F_o| - |F_c||^2 / \sum w |F_o|^2)^{1/2}$$

**Table 4.2** Selected bond lengths (Å) and bond angles (°) for **30**.

Average Bond Distances (Å)	
C-C (aryl)	1.389 (14)
N1-O	1.212 (12)
N4-C (methyl)	1.443 (16)
Bond Distances (Å)	
N1-C1	1.474 (13)
C3-I1	2.092 (10)
C4-N2	1.426 (12)
N2-N3	1.257 (11)
N3-C7	1.382 (12)
C10-N4	1.337 (12)
Bond Angles (°)	
O1-N1-O2	123.4 (9)
O2-N1-C1	117.6 (9)
C2-C3-I1	117.1 (7)
C3-C4-N2	116.6 (9)
C4-N2-N3	114.1 (8)
N2-N3-C7	114.6 (9)
N3-C7-C8	125.4 (9)
C9-C10-N4	122.1 (11)
C10-N4-C13	119.7 (10)
C13-N4-C14	120.1 (10)

#### 4.2.1.6 Temporal Distribution of Products

Once the  $^1\text{H}$  NMR spectra of the predominant species were assigned, it became possible to use the 8.76-ppm singlet of **34**, the 8.81-ppm doublet of **33** and the 8.31-ppm doublet of **27** to probe the composition of the reaction mixture over time (after treatment of an aliquot with iodine). This method permitted an examination of the evolution of the system in the form of the plot presented in **Figure 4.3**. The reaction clearly proceeds in two steps; the consumption of the monomercurated species to form the dimercurated is

only significant after an induction period of 2 h. However, the reaction does not appear to proceed to completion, with 10% of starting material remaining unreacted after 24 h. These features suggest that the mercuration steps might have a reversible character; alas the high concentrations and especially the formation of multiple by-products precluded the completion of a proper kinetic study in this case. In spite of the limitations, this information is still useful to determine the reaction time that maximizes the yield of the monosubstituted species.

**Table 4.3** The relative yields of products of substitution.

Time (h)	<b>27</b>	<b>33</b>	<b>34</b>
0	1.00	0.00	0.00
1	0.54	0.45	0.00
2	0.25	0.71	0.03
4	0.15	0.79	0.06
8	0.12	0.76	0.11
12	0.12	0.73	0.15
24	0.10	0.67	0.23

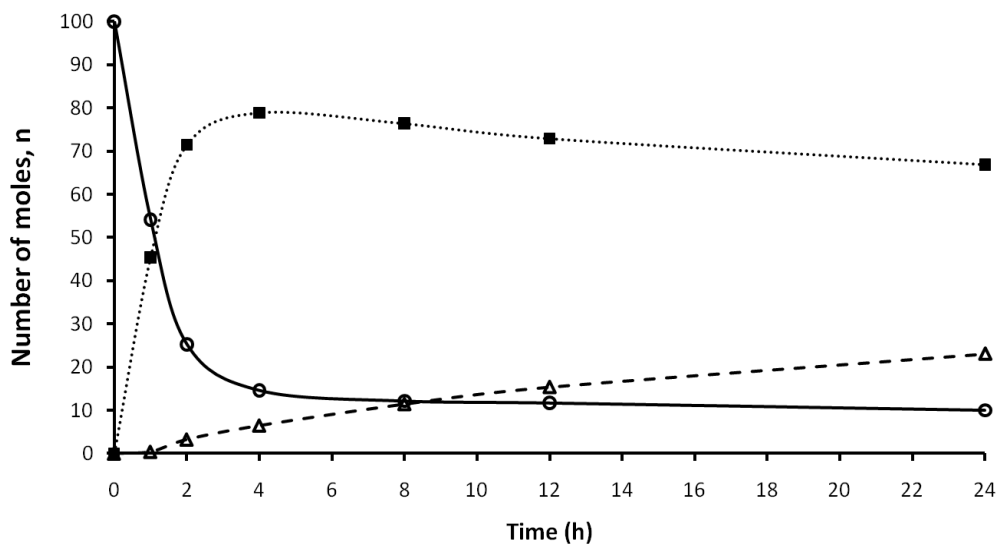


**Figure 4.3** Amounts of the reactant and products of mercuration as a function of reaction time (— **27**, •••**34**, --- **33**). Spline lines highlight the trends but were not obtained by fitting.

#### 4.2.1.7 Computational modeling

The most intriguing characteristic of the azodye mercuration process is the definite preference for reaction at the nitro-substituted ring. Invoking a conventional EAS mechanism, the reaction should occur on the amino-substituted ring because it is more electron rich. DFT calculations were carried out in an attempt to rationalize the experimental observations, first for azobenzene and later for the push-pull dye. In order to simplify modeling of the system, the calculations were performed on derivatives of the N,N-dimethyl dye, **29**, and chloride was used in lieu of the trifluoro acetate anion. The relative thermodynamic stabilities of all possible products of monomercuration were assessed by means of the comparison of the total bonding energies of their minimized structures; the results are graphically presented in **Figure 4.4** and **Figure 4.5**.

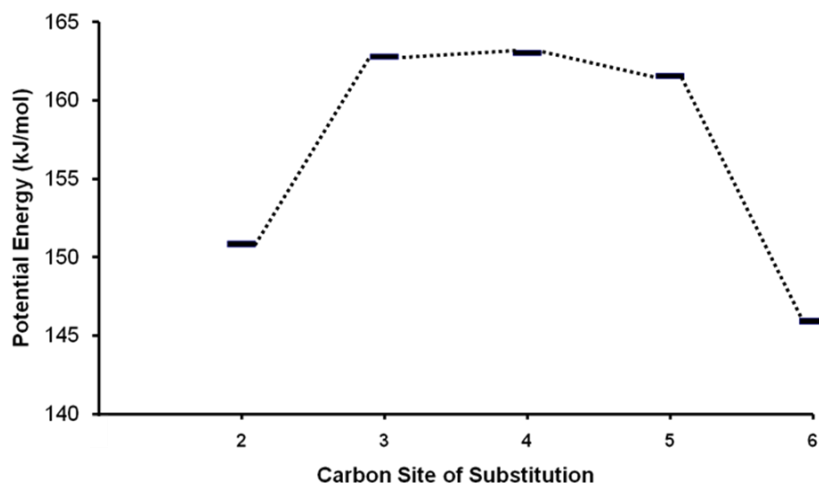


**Figure 4.4** Differences of total bonding energies of the possible products of metallation of azobenzene, **24**. (The carbon atoms and the positions of substitution are numbered as in **Figure 4.1**).

According to the DFT results in the case of azobenzene, substitution at the positions *ortho* to the azo bridge (C2, C6) is preferred by >12 kJ/mol over all other positions, including *para* (C4). For the push-pull dye, substitution at the positions *ortho* to the amino (C2, C6) and nitro (C9, C11) groups is less favorable than *ortho* to the azo bridge (C3, C5, C8, C12). There is little preference (< 7 kJ/mol) for functionalization at C5 and C8 over C3 and C12 but overall the calculations do suggest there is no preference for reaction on either aromatic ring. Therefore, if the reaction were under thermodynamic control an approximately equimolar distribution of all the products of metallation *ortho* to the azo bridge would be obtained. Thermal rotation of the rings would exchange positions C3 and C5 as well as C8 and C12, but at least two isomer products of monometallation would be observed.

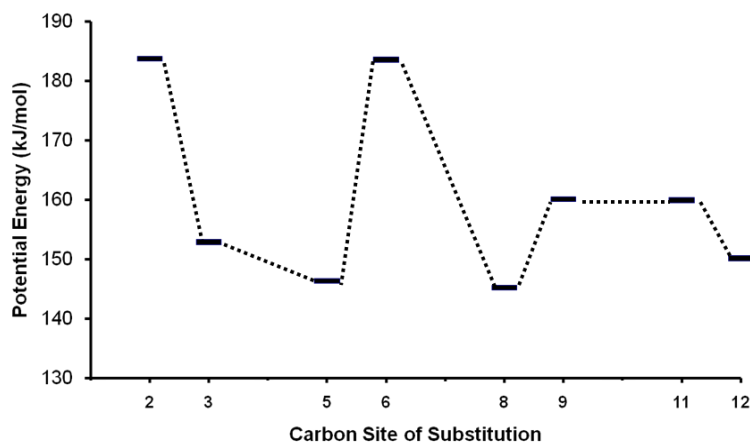
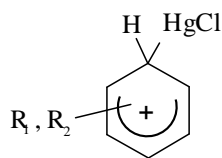


**Figure 4.5** Differences of total bonding energies of the possible products of metallation of **29**. (The carbon atoms and the positions of substitution are numbered as in **Scheme 4.5**).

As the experimental observations are in conflict with the thermodynamic arguments, attention was devoted to the reaction mechanism. In the initial stages of the reaction, the mercuric salt would dissociate generating a  $\text{Hg-X}^+$  cation which would add to the azodye, forming a transient species of general structure **35**. The most likely sites for electrophilic attack could be identified by the nucleophilic Fukui function,<sup>223,224</sup> i.e. the projection of the HOMO onto the total electron density, which is shown in **Figure 4.6**. Mapped in blue, C2, C4, C6, C8, C10, C12 and N3 would be the most favourable points for an initial electrophilic attack.



**35**  
**Chart 4.2**

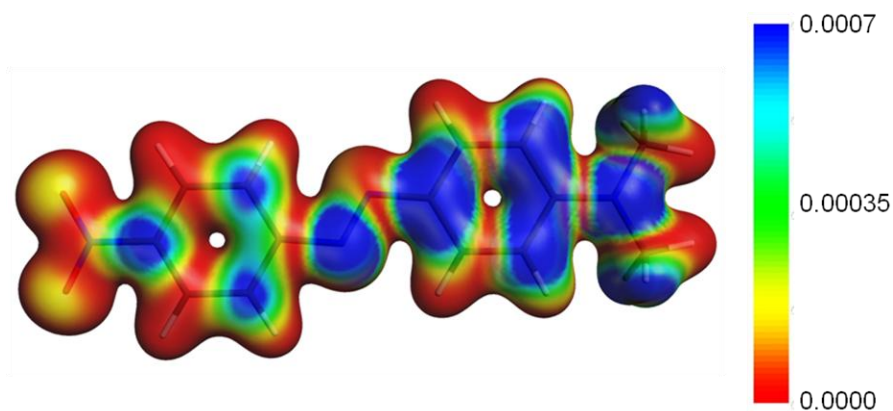


**Figure 4.6** HOMO of **29** projected onto the electron density (0.03 a.u. isosurface).

However, steric repulsion would hinder reaction at C2 and C6; similarly C4 and C10 are unreactive because the nitro group and the azo bridge cannot be displaced and N3 would preferably coordinate the cation through the  $\sigma$  lone pair. Although this result appears to agree with the experiment, a more rigorous analysis requires examination of the activation barrier. In this respect the mechanism of EAS reactions, including metallation, is suitable for quantum mechanical modeling because the barriers can be approximated by calculating the relative energies of **35**, which in most cases can be optimized.<sup>225-227</sup> In the present case, we calculated the geometries of the transition states which would lead to the substitution of each hydrogen on the aromatic rings of azobenzene and the push-pull derivative. The relative energies of the structures are presented graphically in **Figure 4.7** and **Figure 4.8**. In the case of azobenzene, there is a significant stabilization of the transition state that leads to *para* substitution (on C4) to the extent that it is even slightly preferred over the *ortho* intermediates. For the push-pull

dye, the results do show preference for the structure that would lead to metallation at C8, as experimentally observed. The next structure in order of energy is 14.7 kJ/mol above and would lead to mercuration at C2.

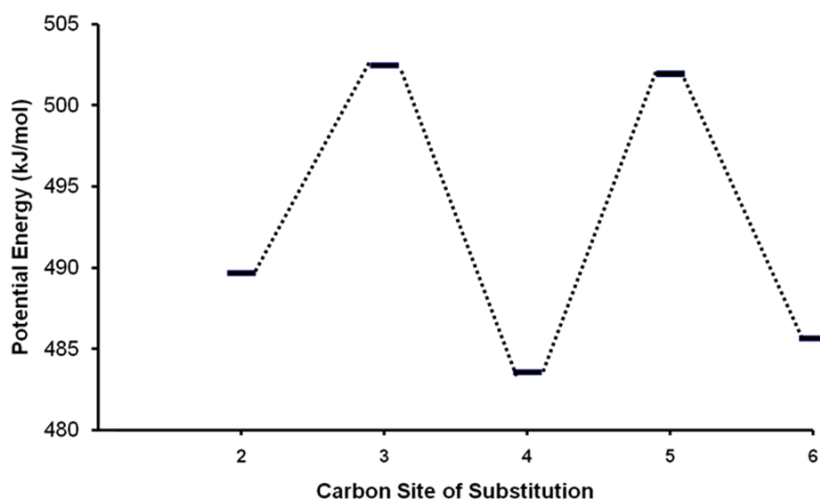


**Figure 4.7** Differences of total bonding energies of the transition states corresponding to the possible products of metallation of **24**. (The carbon atoms and the positions of substitution are numbered as in **Figure 4.1**).

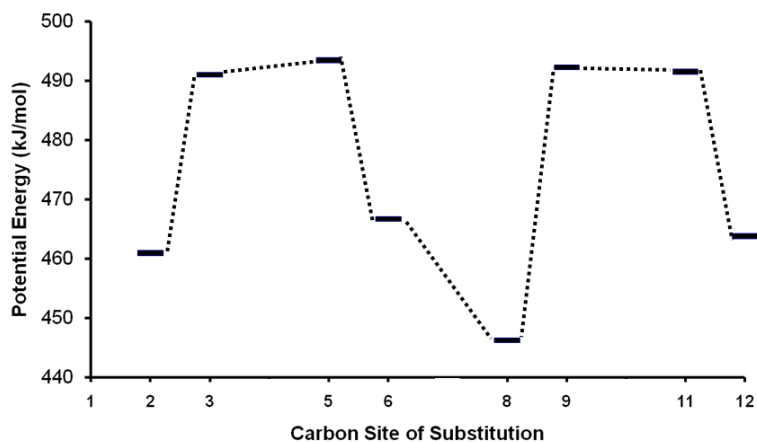


**Figure 4.8** Differences of total bonding energies of the transition states that would lead to each possible product of metallation of **29**. (The carbon atoms and the positions of substitution are numbered as in **Scheme 4.5**).

#### **4.2.2 Summary of the Mercuration Studies**

The combination of electron donating and withdrawing groups reduces the reactivity of azobenzene towards direct mercuration, thus very aggressive conditions such as mercury (II) trifluoroacetate in anhydrous trifluoroacetic acid are necessary to achieve the functionalization of the chromophore. Even then, the reaction does not proceed quantitatively, leaving behind a significant proportion of starting material. The two major products are the result of sequential metallation of the nitro substituted ring, at the positions ortho to the azo bridge. The DFT study of the reagent and models of the possible isomers of the first product and the corresponding transition states points to a system under kinetic control. The results and methods of this study constitute a tool for the preparation of intermediates in the synthesis of functional molecules and materials derivatized with organic chromophores.

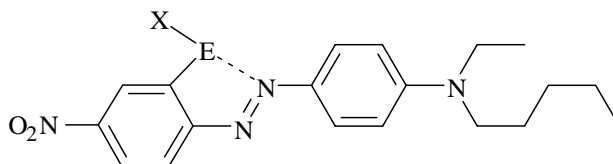
#### **4.3 Spectrophotometric Study of the 2-Halochalcogenyl-Substituted Azobenzenes and their Halide Exchange Reaction**

UV-vis absorption has played a central role in the study of the thermodynamics and kinetics of inorganic reactions, mostly in the case of transition metal species. Being characterized by partly-filled valence shells and modest ligand-field splitting, many ions of the d-block elements and their environment can be conveniently probed using electronic spectroscopy. Some main-group systems (e.g. free radicals, polystannanes, interhalogen compounds) are coloured and can also be studied in a spectrophotometer but many saturated main-group systems are excited deep in the UV and/or their relevant

excitations are weak, appearing as shoulders that are not fully resolved from other more intense excitation bands. In such cases a plausible alternative for spectroscopic probing could rely on coupling the reactive main-group centre to a chromophore which would be sensitive to changes of environment of the p-block element.

#### 4.3.1 Experimental Design

We chose to place a chalcogenyl-halide (E-X; E = Se, Te, X = Cl, Br, I) moiety *ortho* to the azo bridge of a push-pull azodye (**Chart 4.3**). The SBI, and the excitation spectrum in this structure would be sensitive to the nature of the X, enabling facile study of processes such as halide exchange.



- 36** E = S, X = F  
**37** E = S, X = Cl  
**38** E = S, X = Br  
**39** E = S, X = I  
**40** E = Se, X = F  
**41** E = Se, X = Cl  
**42** E = Se, X = Br  
**43** E = Se, X = I  
**44** E = Te, X = F  
**45** E = Te, X = Cl  
**46** E = Te, X = Br  
**47** E = Te, X = I

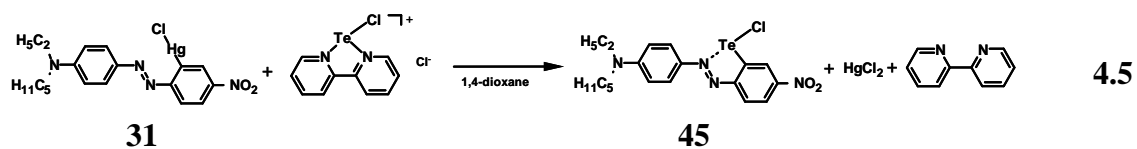
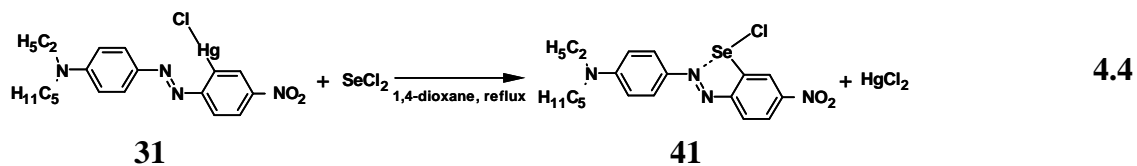
**Chart 4.3**

A number of synthetic investigations have demonstrated that it is possible to exchange the halide in similar compounds by metathesis with the concomitant precipitation of a salt. Reaction of tellurenyl bromide-substituted C,N-diphenyl Schiff bases have been reported with sodium azide and methoxide, and silver fluoride, acetate, and perchlorate.<sup>228,229</sup> Addition of molecular iodine in chloroform to the tellurenyl bromide substituted azobenzene<sup>197,198</sup> results in halide exchange to the iodide;<sup>198</sup> a compound which can also be obtained from the same starting material through salt metathesis using sodium iodide in acetone.<sup>230</sup> Salt metathesis with silver fluoride in toluene yields the fluoride analogue.<sup>198</sup> Chalcogen substitution on larger azobenzenes is possible but rare.<sup>231,232</sup> However, none of these studies has ever examined the equilibrium or the rate constants of such processes.

## 4.3.2 Results and Discussion

### 4.3.2.1 Preparation of 2-Halochalcogenyl-Azobenzenes

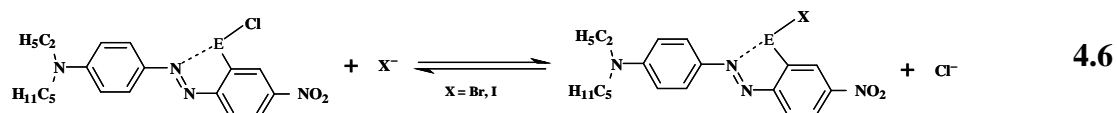
The synthesis was based on literature procedures reported for simpler (not dipolar) azobenzenes.<sup>198,233</sup> Those methods begin with the synthesis of an *ortho*-mercurated intermediate (**Section 4.2**), which is then treated with a chalcogen (II) halide source in anhydrous dioxane. We employed a 1:1 mixture of SeCl<sub>4</sub> and elemental selenium, in one case and the bipyridyl adduct of tellurium dichloride<sup>78</sup> in the other. The 2-chloroselenenyl dye (**41**), was isolated as a dark blue solid after elution with DCM through silica gel. The synthesis of the 2-chlorotellurenyl derivative (**45**) was nearly quantitative after removing 2,2'-bipyridyl, along with the solvent, under dynamic vacuum.



The UV-vis absorption spectrum of **27** is characterised by one intense absorption above 300 nm ( $\lambda_{\text{max}} = 493 \text{ nm}$ ,  $\epsilon = 19000 \text{ cm}^2/\text{mol}$ ). The product of substitution with the chloroselenenyl group (**41**) displays a blue shift of ca. 100 nm ( $\lambda_{\text{max}} = 589 \text{ nm}$ ,  $\epsilon = 27000 \text{ cm}^2/\text{mol}$ ) and an additional absorption maximum at shorter wavelength (426 nm,  $\epsilon = 17500 \text{ cm}^2/\text{mol}$ ). The tellurenylchloride substitution (**45**) results in a blue shift which is more significant than that observed in the selenium homologue ( $\lambda_{\text{max}} = 614 \text{ nm}$ ,  $\epsilon = 18500 \text{ cm}^2/\text{mol}$ , **Figure 4.9**) and also displays an additional maximum at shorter wavelength (480 nm,  $\epsilon = 6900 \text{ cm}^2/\text{mol}$ ).

#### 4.3.2.2 Exchange Reactions

The halide exchange reactions in acetonitrile were performed by stepwise addition of a tetra-alkyl ammonium halide solution to the chalcogenyl-substituted dyes in the presence of an ionic strength buffer (a 10-fold excess of tetra-*n*-butylammonium hexafluorophosphate). The high solubility of the tetra-*n*-butylammonium salts made these compounds ideal for the study.



Using a specially designed quartz cuvette outfitted with a gas adapter and a Teflon valve, a solution of the chalcogenyl halides **41** and **45** were titrated with concentrated solutions of  $\text{Cl}^-$ ,  $\text{Br}^-$  and  $\text{I}^-$ . In both instances, addition of tetrabutylammonium chloride induced negligible changes in the absorption spectrum of for **41** and **45** ( $< 0.05$  AU). The result for chloride addition indicated that both **41** and **45** are not significantly dissociated. Similarly the bromide anion does not exchange with chloride in these experimental conditions. On the other hand, the titration of **45** with tetrabutylammonium iodide, at 25 °C, did induce significant changes (**Figure 4.9a**). Changes in absorption are most significant at 330 nm and provide the data in the second plot (**Figure 4.9a**). Fitting the curve made by plotting the absorption at 330 nm against the iodide ion concentration to the equation of a binding isotherm (See Appendix), an equilibrium constant of  $1.7 \times 10^{-2}$  was obtained. That the equilibrium (Eq. **4.6**) is shifted towards the chloride is expected based on the E-X bond strengths. For the same reason, it is puzzling that  $\text{Br}^-$  cannot displace the chloride anion. A preliminary study with **41** showed a similar exchange but precise measurements have yet to be performed.

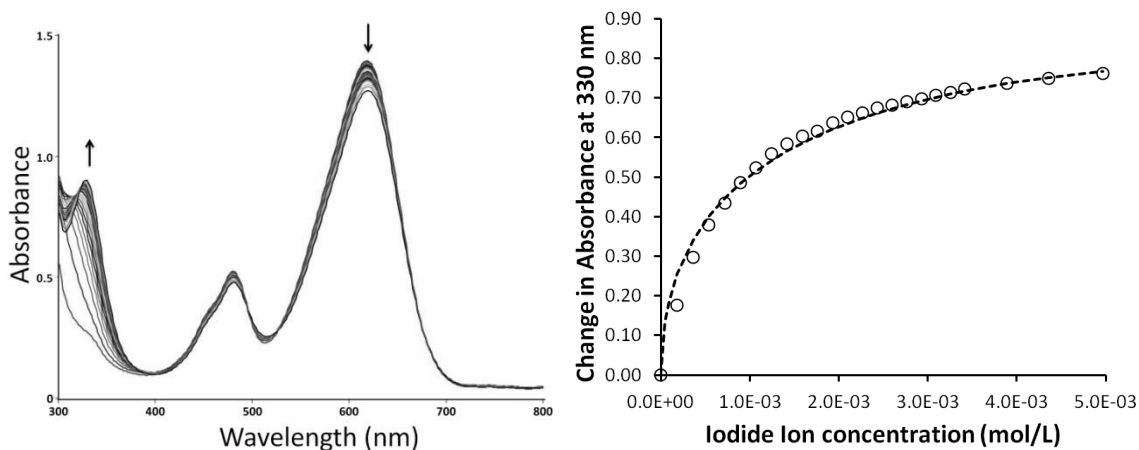


**Figure 4.9** Changes in the UV-vis spectra and absorbance at 330 nm of **45** as a result of addition of I<sup>-</sup> (from 0 to 100 equivalents) at 25 °C.

#### 4.4 Second Harmonic Generation from 2-Arylchalcogenyl Azobenzenes

##### 4.4.1 Molecular Origin of Nonlinear Optical Properties

Nonlinear Optical (NLO) phenomena can be understood as a consequence of the redistribution of electron density induced by an external electric field. This results in an induced dipole moment or polarisation that can be described in a macroscopic medium by the following expansion in a series of powers of the electric field:

$$P_{bulk} = \chi^{(1)}E + \chi^{(2)}E^2 + \chi^{(3)}E^3 + \dots \quad 4.7$$

In which each  $\chi^{(n)}$  is the dielectric susceptibility of order n. A similar equation can be written for the phenomenon at the molecular level:

$$P_{molecular} = \alpha E + \beta E^2 + \gamma E^3 + \dots$$

4.8

The  $\alpha$  coefficient is a tensor quantity that refers to the polarisability while  $\beta$  and  $\gamma$  are the first (second order) and second (third order) hyperpolarisability tensors. The higher order terms are the origin of NLO effects, but are only significant when the electric field is intense. In such a field, a NLO material can generate the harmonic frequencies of a laser beam, change its refractive index and exhibit other unusual phenomena.<sup>234</sup> NLO properties can be classified by the order of the coefficient that originates them, i.e., second-, third-order, etc.

The induced polarisation of electron density can be regarded as the result of orbital mixing (**Figure 4.10**). In the simple case of a hydrogen atom in the gas phase under no external electric field, the electron density is equally distributed in all directions and can be described using the square of the 1s orbital. When placed in an electric field, the electron cloud will be polarised, and the 1s orbital alone would be insufficient to account for the cloud's shape. An approximate wavefunction can be built in such case by combining the 1s and the 2p orbitals; in other words, the electric field is a perturbation that enables mixing of orbitals that would otherwise be orthogonal.

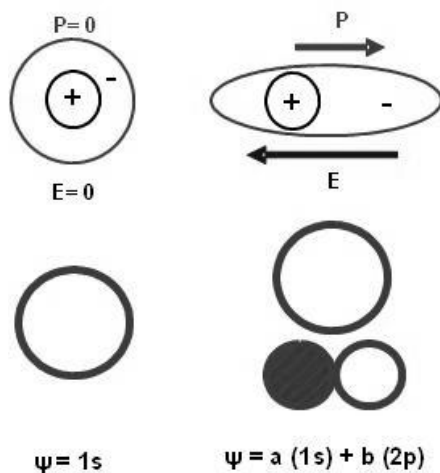


**Figure 4.10** Schematic representation of polarisation as orbital mixing.

In principle this phenomenon involves all occupied and all empty orbitals of a molecule (or atom), but that is an infinite number of functions. The simplest approximate model considers only the ground and first excited states. This “two-level” approximation<sup>235</sup> yields an equation that describes the intrinsic (frequency independent) first hyperpolarisability as a function of the transition dipole moment  $\mu_{ge}$ , the change in dipole moment between the two states  $\Delta\mu_{ge}$ , and the energy of the transition  $\omega_{ge}$ .

$$\beta(0) = \frac{3 \Delta\mu_{ge} \mu_{ge}^2}{2 \varepsilon_0 (\hbar\omega_{ge})} \quad 4.9$$

In the process of Rayleigh scattering, the collision of a photon of light with a molecule results in an excitation to a virtual state; followed by relaxation to the ground state and emission of a photon of equal frequency. If two photons are simultaneously

picked up, excitation can occur to a higher virtual state, and relaxation would result in the emission of a single photon with twice the frequency of the incident light (**Figure 4.11**).

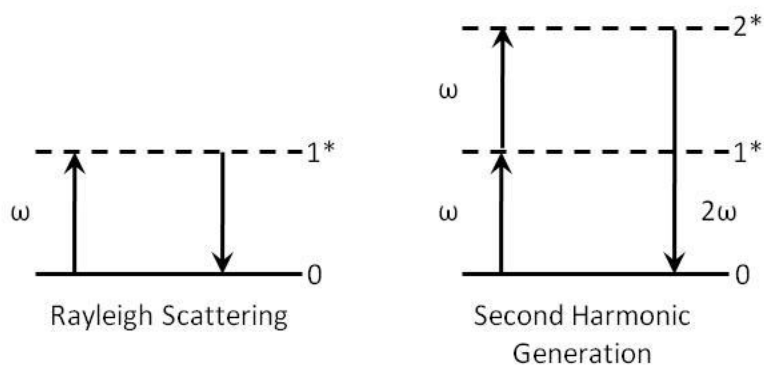


**Figure 4.11** A Comparison of Rayleigh scattering and SHG processes.

Alternately, the time dependence of an oscillating electric field can also be used to explain this effect. For an oscillating field:

$$E = E(t) = Ee^{-i\omega t} + E^*e^{i\omega t} \tag{4.11}$$

Substitution into the second term of Equation 4.5 yields the following equation

$$\beta E^2 = 2\beta EE^* + \beta \left[ E^2 e^{-2i\omega t} + (E^*)^2 e^{2i\omega t} \right] \tag{4.12}$$

The  $2\omega$  term in Equation 4.12 corresponds to the field oscillating with double the frequency of the original field.

The intensity of NLO processes depends on the magnitudes of the corresponding NLO coefficients. In addition, even-order NLO phenomena can only be observed when the system (either a molecule or a macroscopic structure) is non-centrosymmetric. The search for suitable NLO chromophores has focused mostly on organic systems; in particular conjugated unsaturated molecules with delocalized  $\pi$ -orbitals. These are usually incorporated into a polymeric matrix in order to prepare a NLO material.

The most common approach to enable molecular NLO properties consists in the placement of electron donating and accepting groups at opposing ends of a chromophore. This dipolar architecture, maximizes the change in the molecular dipole moment upon excitation, and in turn increases the hyperpolarisability of the molecule.<sup>236</sup>

Due to the inherent polarisability of heavy atom electron clouds, the incorporation of a large heteroatom into an organic framework should in principle increase the hyperpolarisability. **Table 4.4** summarizes the effect of heavy atoms in the furan, thiophene and selenophene family of molecules.<sup>237</sup> There is a notable increase in the second hyperpolarisability ( $\gamma$ ) with the substitution of increasingly heavy atoms.

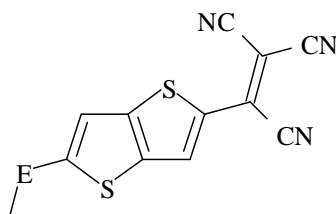


- a) O
  - b) S
  - c) Se
- 48**

**Table 4.4** Hyperpolarisabilities for a series of chalcogen containing heterocycles.

	$\gamma$ ( $\times 10^{-31}$ esu)
<b>48a</b>	0.72
<b>48b</b>	1.06
<b>48c</b>	1.53

The location of the chalcogen within the  $\pi$ -framework is also important; chalcogen-containing donor groups induce only a modest increase in NLO activity, which is not necessarily progressive as shown by the values of  $\beta$  in **Table 4.5**.<sup>238</sup>



- a) O
  - b) S
  - c) Se
  - d) Te
- 49**

**Table 4.5** The effect of chalcogen donation on the hyperpolarisability of a series of thiophene-based molecules (**49**).

	$\beta$ ( $\times 10^{-30}$ esu)
<b>49a</b>	25
<b>49b</b>	43
<b>49c</b>	39
<b>49d</b>	37

Interestingly, when a heavy chalcogen atom is grafted into the  $\pi$ -system of a dipolar biphenyl system,<sup>239</sup> there is a stepwise increase in the second hyperpolarisability with the heavier heteroatoms (**Table 4.6**).

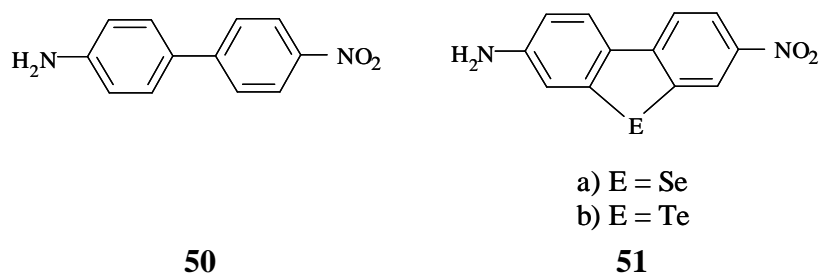
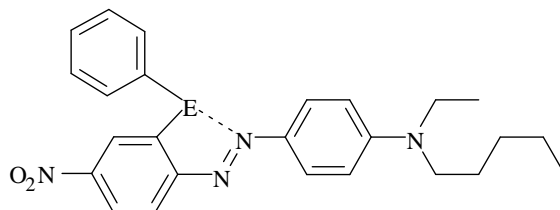


**Table 4.6** Hyperpolarisabilities for a series of chalcogen-containing D- $\pi$ -A molecules.

	$\gamma$ ( $\times 10^{-31}$ esu)
<b>50</b>	0.5
<b>51a</b>	1.0
<b>51b</b>	1.4

Though the evidence indicates that the incorporation of heavy main-group atoms increases the NLO properties of a chromophore, the synthesis of fully conjugated heterocycles is often difficult. As an alternative, we considered the use of intramolecular SBIs to promote the delocalization of electron density of a heavy chalcogen into the  $\pi$ -framework of a NLO chromophore. In this section we describe the preparation of such a modified chromophore and report the initial measurements of their NLO response by hyper-Rayleigh scattering (HRS). Because the measurements could not be performed under an inert atmosphere, the model systems (**52-54**) had a phenyl ring appended to the chalcogen instead of a halogen atom to avoid degradation by hydrolysis.



**52** E = S

**53** E = Se

**54** E = Te

**Chart 4.4**

## 4.4.2 Results and Discussion

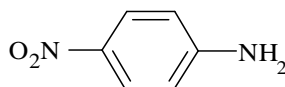
### 4.4.2.1 Syntheses

Early synthetic attempts considered two different approaches, using mercurated or lithiated intermediates, based on literature reports of the preparation of similar compounds; the former was preferred due to the thermal instability of the lithiated intermediate. The *ortho*-mercurated azodye (**31**, Section **4.2**) was reacted with Aryl-chalcogen chlorides; PhECl in the case of E = S, Se, and PhTeCl<sub>3</sub>. In the case of Te, the Te(IV) product would have to be reduced to afford the target compound in a subsequent step; for example 2-trichlorotellurenyl azobenzene reacts in this way with hydrazine hydrate.<sup>233</sup> The reaction with phenyl sulfenyl chloride in 1,4-dioxane produced a complex mixture from which the target could not be conclusively identified even after HPLC separation. The corresponding reaction with phenyl tellurium trichloride gave a dark purple solid, which was equally challenging to purify and characterize.<sup>240</sup> Small amounts of mono, and di-functionalized products were identified from the stepwise reaction of the mercurated dye with *t*-butyl lithium and phenyl sulfenyl chloride.<sup>241</sup>

This part of the project was successful with the reaction of PhSeCl and purified **31** in a very concentrated dioxane solution. After mixing, a gradual change from red to pink/purple was observed over 4 hours. After removing the solvent under vacuum, the resulting residue was dissolved in acetonitrile and separated by HPLC to give **53** in 65% yield.

#### 4.4.2.2 Hyperpolarisability determination

Hyper-Rayleigh scattering measurements were performed in acetonitrile solution for **27** and **53**. The orientational average of the first hyperpolarisability tensor for second harmonic generation was determined at 532 nm (from a 1064 nm fundamental) by comparison to standard 5% (w/v) solution of *para*-nitroaniline (**55**,  $\langle\beta\rangle 13 \times 10^{-30} \pm 0.3 \times 10^{-30}$  esu) in acetonitrile.<sup>242</sup> For the azodye derivatives,  $\langle\beta\rangle$  values were found to be  $290 \times 10^{-30}$  esu ( $\pm 3 \times 10^{-30}$  esu) for **27** and  $242 \times 10^{-30}$  esu ( $\pm 10 \times 10^{-30}$  esu) for **53**, representing an increase in the tensor average by factors of 20 and 18 respectively. Although these responses are significantly higher than that of the standard and comparable to reported values for related compounds,<sup>243-245</sup> the presence of the chalcogen in the *ortho* position appears to have no effect on the NLO coefficient relative to the non-substituted dye **27**.



**55**

## 4.5 Computational Studies of Chalcogenyl-Substituted Azobenzenes

### 4.5.1 Molecular Structures

Geometry optimisations of models of the substituted azobenzenes (**36-47**) were performed as the initial point of this study. The models featured Me<sub>2</sub>N- groups for simplicity. As most of the crystallographically characterized dipolar azodyes have a planar structure<sup>246-248</sup> due to the extended  $\pi$ -conjugation, the models were optimised under  $C_s$  symmetry. A summary of the most important bond lengths and angles is provided in **Table 4.7**, **Table 4.8** and **Table 4.9**.

In the case of the chalcogenyl-halide derivatives, introduction of the chalcogen results in lengthening of the azo bridge by up to 0.02Å, significant changes (0.04 Å) are also observed in the C7-N3 bonds on the nitro-substituted ring. In contrast, the nature of X has no effect on these bond lengths. The length of the SBI (N2-E) is more dependent on the nature of X, resulting in changes of 0.092 Å, 0.078 Å, and 0.047 Å for S, Se, and Te respectively. Bond angles show a similar dependence on the chalcogen and the halide. Upon chalcogen substitution, the C4-N2-N3 bond angles increased, while the magnitude of the N2-N3-C7 angle decreased. With heavier halogens, these same angles increased between 1 and 2°. Interestingly, the N2-E-X angle varied between 162 and 180°, with the smallest angles observed with Te, and the largest with Se. Although the substitution of the dye results in only minor modifications to the geometry, the effect on the electronic structure is expected to be more significant.

**Table 4.7** A comparison of calculated bond lengths and angles of **27** and the sulfenyl halide substituted derivative.

	Bond Lengths (Å)				
	<b>27</b>	<b>36</b> X = F	<b>37</b> X = Cl	<b>38</b> X = Br	<b>39</b> X = I
C4-N2	1.391	1.398	1.393	1.392	1.389
N2-N3	1.277	1.297	1.291	1.288	1.284
N3-C7	1.407	1.368	1.368	1.368	1.370
C8-S	-	1.737	1.746	1.747	1.751
N2-S	-	1.945	1.970	1.984	2.037
S-X	-	1.791	2.312	2.482	2.683
	Bond Angles (°)				
C4-N2-N3	115.49	119.42	120.61	121.01	121.37
N2-N3-C7	114.16	108.61	109.20	109.48	109.95
C8-S-N2	-	82.10	82.26	82.18	81.52
N2-S-X	-	175.05	179.72	179.86	177.89

**Table 4.8** A comparison of calculated bond lengths and angles of **27** and the selenenyl halide substitution.

	Bond Lengths (Å)				
	<b>27</b>	<b>40</b> X = F	<b>41</b> X = Cl	<b>42</b> X = Br	<b>43</b> X = I
C4-N2	1.391	1.397	1.394	1.393	1.391
N2-N3	1.277	1.294	1.289	1.287	1.284
N3-C7	1.407	1.371	1.372	1.372	1.373
C8-Se	-	1.881	1.894	1.896	1.901
N2-Se	-	2.116	2.145	2.158	2.194
Se-X	-	1.909	2.380	2.540	2.744
Bond Angles (°)					
C4-N2-N3	115.49	118.59	119.26	119.57	119.81
N2-N3-C7	114.16	111.08	111.39	111.56	111.85
C8-Se-N2	-	78.17	78.01	77.99	77.45
N2-Se-X	-	170.34	174.42	175.7	177.16

**Table 4.9** A comparison of calculated bond lengths and angles of **27** and the tellurenyl halide substitutions.

	Bond Lengths (Å)				
	<b>27</b>	<b>44</b> X = F	<b>45</b> X = Cl	<b>46</b> X = Br	<b>47</b> X = I
C4-N2	1.391	1.401	1.399	1.396	1.396
N2-N3	1.277	1.295	1.291	1.290	1.288
N3-C7	1.407	1.373	1.374	1.374	1.375
C8-Te	-	2.075	2.088	2.092	2.097
N2-Te	-	2.293	2.314	2.320	2.340
Te-X	-	2.027	2.502	2.663	2.878
Bond Angles (°)					
C4-N2-N3	115.49	117.31	117.66	117.84	118.02
N2-N3-C7	114.16	113.13	113.35	113.45	113.56
C8-Te-N2	-	73.44	73.29	73.22	72.75
N2-Te-X	-	162.8	166.49	167.59	168.85

In the phenyl-chalcogenyl derivatives, the azo bridge (N2-N3) and the C4-N2 bond lengths remain unchanged, while the N3-C6 bond distance was decreased by 0.02 Å. The nature of the chalcogen appears to have no effect on these bond lengths. The length of the SBI (N2-E) for sulfur (2.605 Å), selenium (2.605 Å) and tellurium (2.605 Å) correspond to 73%, 76% and 73% of the  $\sum r_{vdw}$  respectively. The bond angles show a similar dependence on the chalcogen. Upon substitution, the C4-N2-N3 bond angles increase slightly (1°), while the N2-N3-C7 angle decreased by no more than 0.47°. For increasing chalcogen size, the C8-E-N2 bond angles decreased from 74.77° to 68.84°; the N2-E-X angles also decreased from 176.58° to 162.80°. Although the substitution of the dye results in only minor modifications to the geometry, the effect of the SBI on the electronic structure should be more significant.

**Table 4.10** A comparison of calculated bond lengths and angles of **27** and phenyl chalcogenyl substituted species **52**, **53**, and **54**.

	Bond Lengths (Å)			
	<b>27</b>	<b>52</b> E = S	<b>53</b> E = Se	<b>54</b> E = Te
C4-N2	1.391	1.388	1.389	1.392
N2-N3	1.277	1.276	1.278	1.279
N3-C7	1.407	1.389	1.388	1.386
C8-E	-	1.774	1.921	2.117
N2-E	-	2.613	2.605	2.635
E-Ph	-	1.801	1.964	2.175
	Bond Angles (°)			
C4-N2-N3	115.49	116.48	116.70	116.36
N2-N3-C7	114.16	113.74	113.62	114.18
C8-E-N2	-	74.77	72.67	68.84
N2-E-Ph	-	176.58	171.67	162.80

#### 4.5.2 Electronic Structure

**Figure 4.12** compares the energies of selected frontier orbitals of the azobenzenes **27**, **40** - **47**, **53**, and **54**. Introduction of the chalcogen substituent is reflected in additional orbitals which correspond in first instance to lone-pairs on S, Se, Te and on the halogens. The shape of the HOMO and LUMO of **45** are shown as representative examples in **Figure 4.13**.

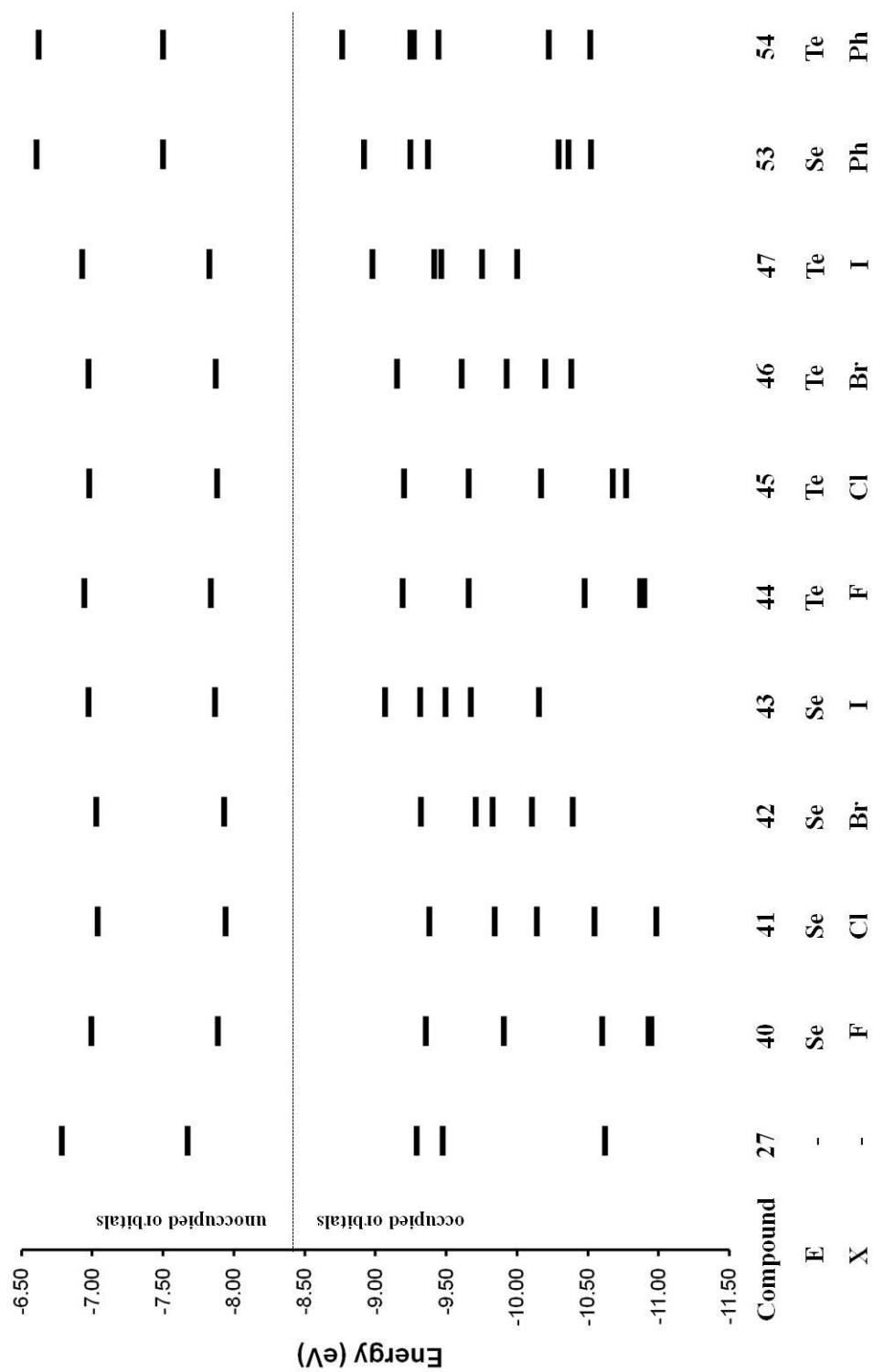
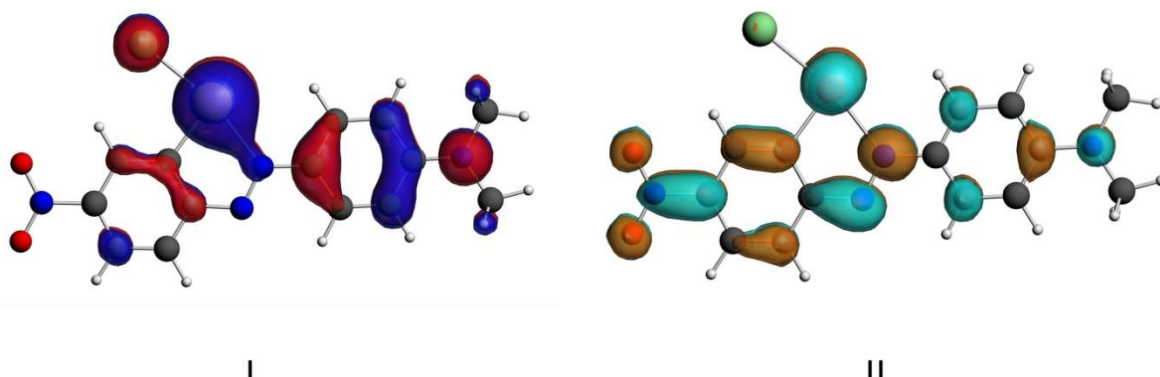
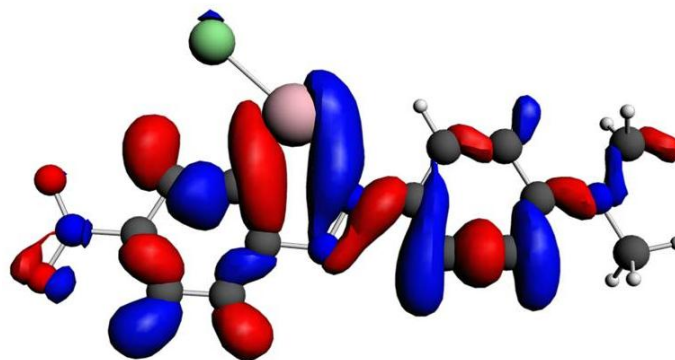


Figure 4.12 Selected frontier orbitals of the azobenzenes 27, 40 - 47, 53, and 54.



**Figure 4.13** Composition of the I) HOMO and II) LUMO of **45**.

In each of the systems, the shape of the LUMO is consistent; the presence of the chalcogen only provides another lobe, as observed in **Figure 4.13 II**. The effect of the chalcogen on the occupied orbitals of **40-47** is more significant; much of the HOMO is located on the chalcogen, and even with the lighter analogues this orbital shows  $\pi$ -overlap along the SBI. The spacing of molecular orbitals decreases as the weight of the halogen increases due to the larger number of closely spaced orbitals in the more polarisable halogen atoms and the energy high of the lone pairs. In the cases of **43** and **47**, for example, two of the frontier orbitals are comprised entirely of the iodine lone pairs. Similarly, the presence of the aromatic rings in **53** and **54** provides two orbitals localised entirely on the pendant phenyl ring. Stabilisation from a  $\sigma$ -interaction is found only in orbitals of much lower in energy; for example, the HOMO-16 of **45** (**Figure 4.14**). The contribution from the  $\sigma^*_{\text{Te-Cl}}$  orbital however, is not clearly visible in this figure, as it must be spread over multiple molecular orbitals.



**Figure 4.14** Graphical representation of the HOMO-16 of **45**, which illustrates the sigma stabilization interaction of the SBI. Isosurface plotted at 0.03 a.u.

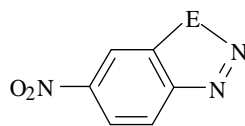
### 4.5.3 Electron Delocalization Through the SBIs

The composition of molecular orbitals such as **Figure 4.13** indicates that the electronic density of the chalcogen is indeed delocalized into the  $\pi$  manifold of the chromophore through the virtual ring formed by the SBI. In order to explore this concept in greater detail we considered ideas developed in the study of aromatic systems. Low chemical reactivity, thermodynamic stability, planar geometry, and characteristic spectroscopic signatures (UV absorption,  $^1\text{H}$  chemical shifts) are features commonly associated with aromaticity.<sup>249</sup> Although there is an on-going debate on the definition of the property,<sup>250</sup> it has been proposed that the shielding effects observed in the  $^1\text{H}$  NMR spectrum provide the best criterion of aromaticity: *diatropic* (aromatic) systems exhibit a diamagnetic ring current, *atropic* systems exhibit no ring current, and *paratropic* (anti-aromatic) systems exhibit a paramagnetic current.<sup>251</sup> Attempts to apply a quantitative measure to these arguments have led to the development of a number of aromaticity

indices, including the harmonic oscillator model of aromaticity (HOMA),<sup>252</sup> aromatic stabilization energies (ASE)<sup>253</sup>, magnetic susceptibility exaltation<sup>254</sup> and the nucleus-independent chemical shift (NICS)<sup>255</sup>. Of these methods, perhaps the most easily interpreted is NICS.

The evaluation of the NICS consists of the calculation of the chemical shift of a point in space, most commonly at the geometric centre of an unsaturated ring formed by covalent bonds. The results of a series of calculations on a number of five-membered heterocycles indicate that a negative NICS value corresponds to a diatropic system, while a positive value suggests a paratropic ring current is present.<sup>255</sup> With chalcogen-substituted azodyes (**36-47**), the formation of the virtual heterocycle could provide a diatropic ring current, if delocalization through the SBI is sufficiently strong.

NICS calculations were undertaken for compounds **36-47**, as well as reference compounds **27**, **33**, C<sub>6</sub>H<sub>6</sub>, and the 1,2,3-benzochalcogenazoles **56**, **57**, and **58** at the points indicated in **Figure 4.15**. The results are compiled in **Table 4.11**. While the NICS calculated for the unsubstituted chromophore (**27**) and its 2-iodo derivative (**33**) are positive, they are negative for all the chalcogenyl-halide bearing molecules, indicating the presence of a diatropic ring current on the virtual ring. However, the NICS magnitudes are smaller than those observed in fully "covalent" heterocycles such as the 1,2,3-chalcogenadiazoles, **56-58**.



**56** E = S

**57** E = Se

**58** E = Te

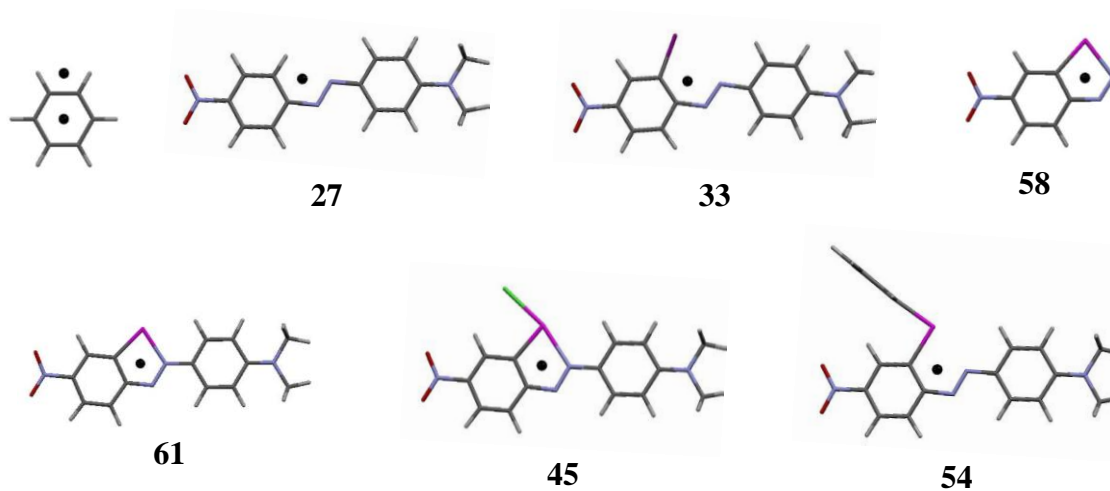
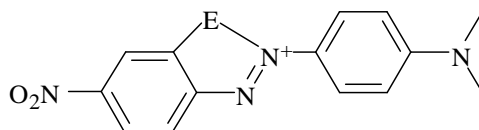


**Figure 4.15** Representative structures of  $C_6H_6$ , **27**, **33**, **58**, **61**, **45**, and **54** showing the location of calculated centroids used in NICS calculations.

**Table 4.11** Calculated NICSs for compounds, **27, 33,36-47, 52-54, 56-62.**

	NICS (ppm)
$C_6H_6$ (inner)	-6.78
$C_6H_6$ (outer)	-2.28
<b>27</b>	5.06
<b>33</b>	1.73
<b>59</b>	-8.27
<b>36</b>	-5.40
<b>37</b>	-3.20
<b>38</b>	-3.11
<b>39</b>	-2.62
<b>52</b>	9.33
<b>60</b>	-8.04
<b>40</b>	-3.72
<b>41</b>	-2.77
<b>42</b>	-2.59
<b>43</b>	-2.21
<b>53</b>	1.76
<b>61</b>	-7.38
<b>44</b>	-3.65
<b>45</b>	-2.75
<b>46</b>	-2.57
<b>47</b>	-2.25
<b>54</b>	0.18
<b>56</b>	-10.23
<b>57</b>	-9.11
<b>58</b>	-7.23

In the case of the halochalcogenyl derivatives, the magnitude of the NICS is larger with  $X = F$ . This could be interpreted as the result of the stronger SBI and delocalization created by the most electronegative halogen. The extreme case of ring covalency was considered using the model cationic species **59**, **60**, and **61**. As expected, this model possesses the most diatropic ring current, **Figure 4.16**. The correlation between the strength of the chalcogen-nitrogen interaction and the NICS is also apparent in a plot of the NICS parameter as a function of the  $E \cdots N$  SBI length.



**59** E = S

**60** E = Se

**61** E = Te

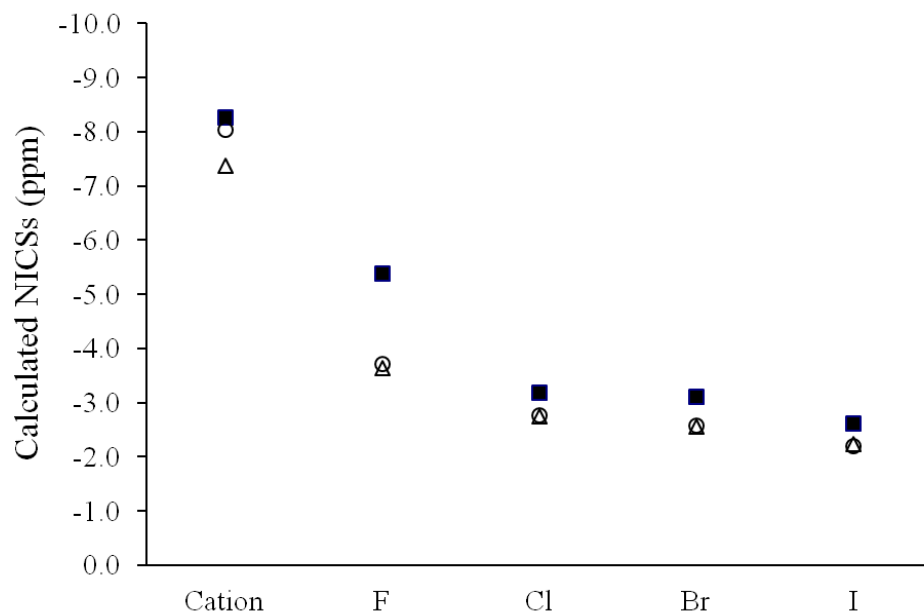


**Figure 4.16** Calculated NICs as a function of the halide X in compounds **36-47** and **59-61**. (■ = sulfur, ○ = selenium, Δ = tellurium)

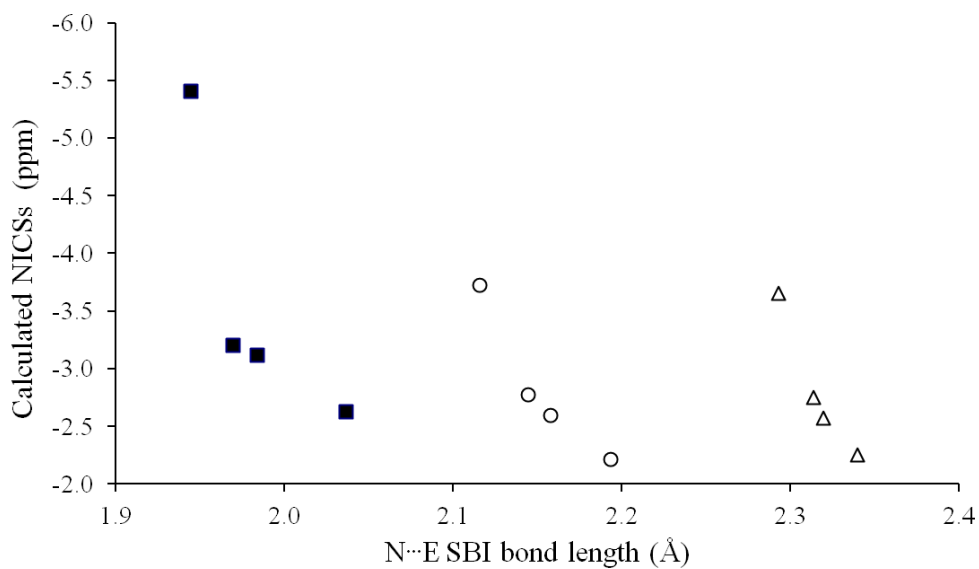


**Figure 4.17** Correlation between the SBI bond length of **36-47** on the calculated NICs. (■ = sulfur, ○ = selenium, Δ = tellurium)

The NICS results are significantly different for the phenylchalcogenyl derivatives **52-54** in that all indicate paratropic ring currents at the centre of the virtual rings. The implication is that delocalization through their SBIs is less efficient because the Te-C  $\sigma^*$  orbital in **54** is a poor electron acceptor. Consistently, the SBIs in this case are long compared to those of the halochalcogenyl species. These results provide a plausible explanation for the results from the NLO experiment; delocalization of selenium electrons into the  $\pi$  manifold is not efficient enough to significantly enhance the nonlinear response of the chromophore.

#### 4.5.4 Analysis of the Excitation Spectra

TD-DFT calculations were used to aid in the interpretation of the UV-vis absorption spectra, probing the effect of the chalcogen E, and halide X. In each case, the lowest 120 transitions were calculated with the Davidson approximation<sup>100</sup> for **36-47**. The lowest 50 transitions of each compound are listed in the Supplementary. Approximate gaussian envelopes of 180-nm width were used to model the spectra. In each calculated spectrum, the transitions were found not to be simple orbital-to-orbital excitations. For example, the first transition of **27** results from the mixing of 8 molecular orbitals, including significant contributions from the HOMO and LUMO. Chalcogen functionalisation results in a wavelength shift of the first transition, but also gives rise to a number of new transitions. For **27**, there are two intense transitions above 300 nm which are primarily confined to the molecular  $\pi$ -system. As shown in **4.5.2**, the presence of an appended chalcogen element (**Figure 4.12**) results in a significant perturbation of the electronic structure; the

transition densities for the first three transitions, calculated as equation **4.13**, are shown in **Figure 4.18**. Three intense transitions were predicted, each of which would include strong contributions from the halochalcogenyl moiety. The shape of the plotted transition densities is consistent for all chalcogens and is largely independent of X; the energy of the transitions are more strongly affected by nature of the halide (**Figure 4.19**).

$$\rho_{ge}(r) = \psi_g^*(r)\psi_e(r) \quad 4.13$$

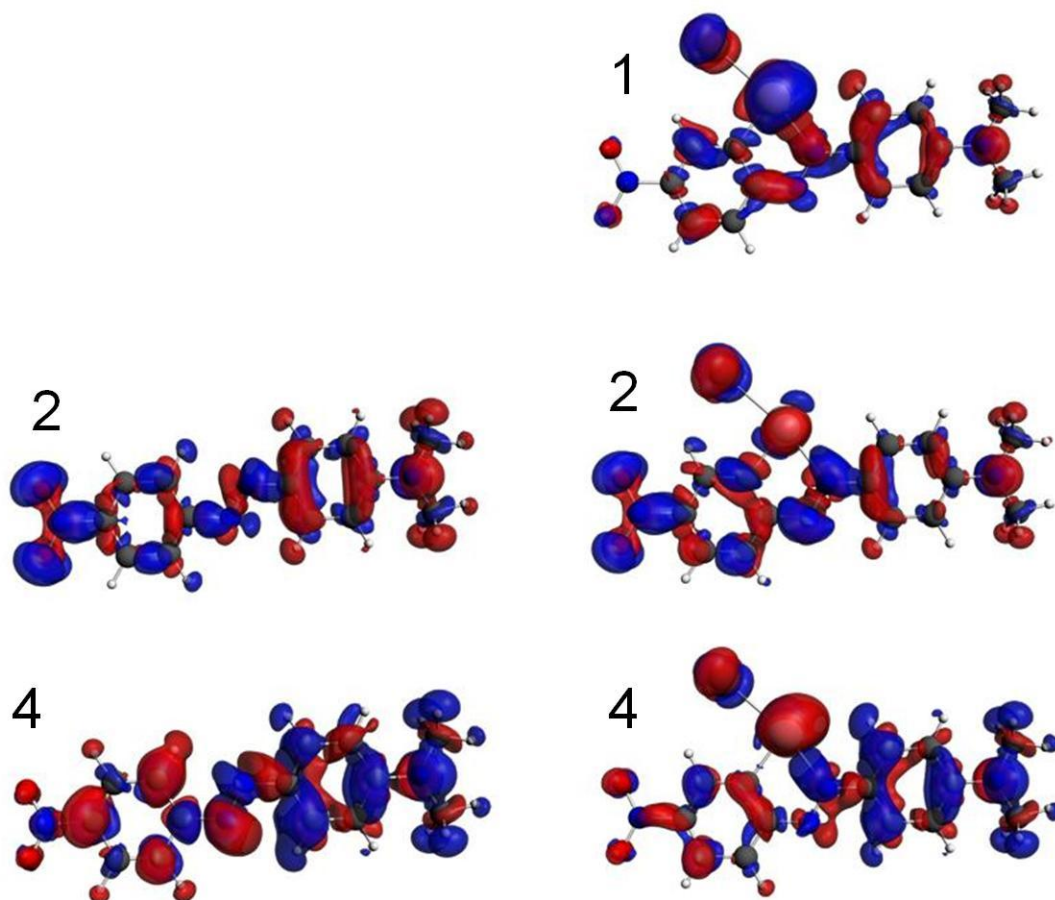


**Figure 4.18** Transition densities for the most intense transitions in the electronic spectra of **27** and **45**. The transition number (in order of increasing energy) is indicated beside each plot.

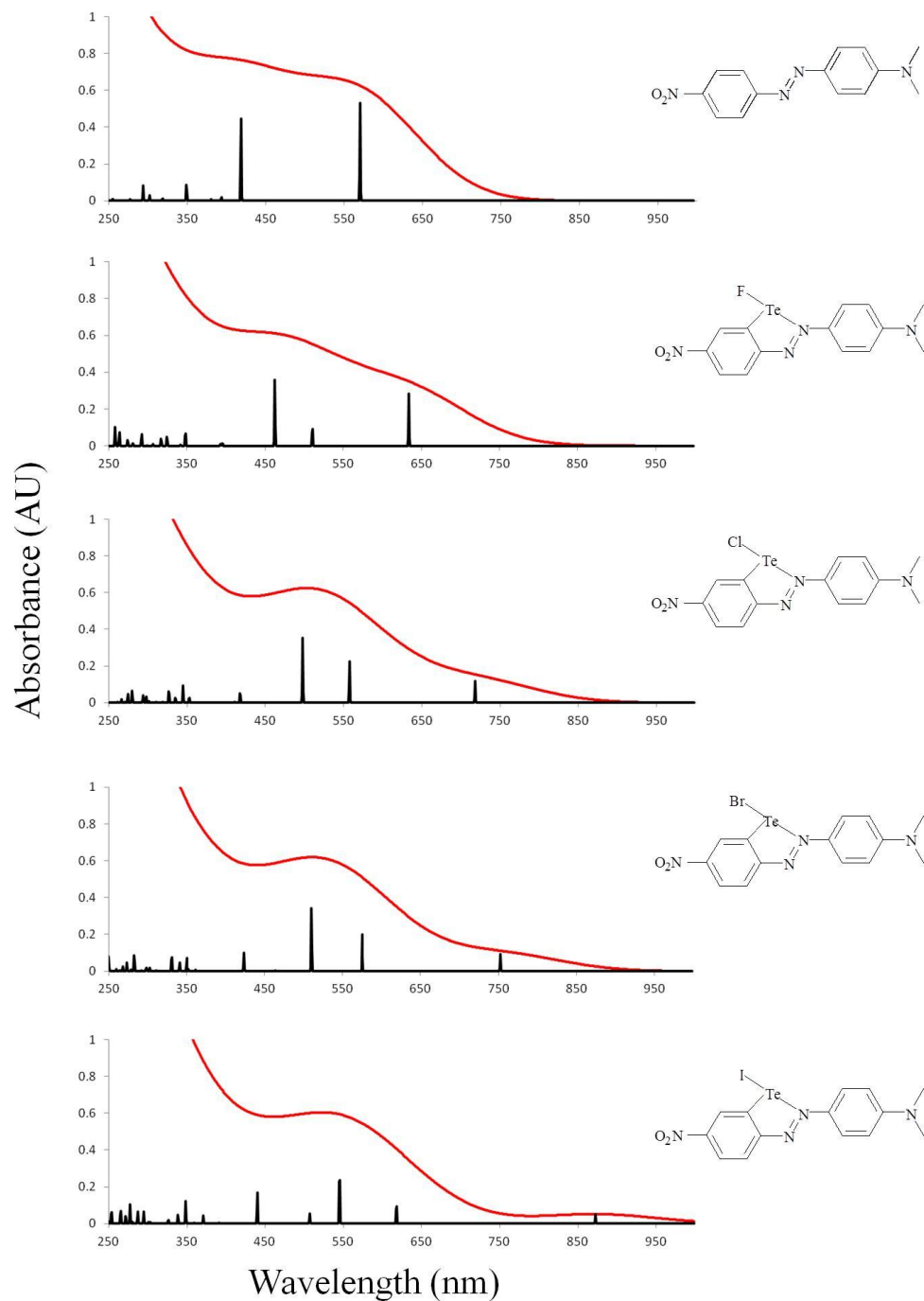


**Figure 4.19** Calculated UV-vis absorption spectra and absorption bands for **27**, **44**, **45**, **46**, and **47**.

#### 4.5.5 Calculated SHG Hyperpolarisabilities

DFT and TD-DFT calculations were extended to estimate the orientational averages of the static molecular hyperpolarisabilities and the SHG hyperpolarisabilities at 1064 nm of **52**, **53** and **54** as well as **27**. For the azodye derivatives, the calculated SHG values are between 40 and 70 times the experimental value for *para*-nitroaniline, **55**.<sup>242</sup> The TD-DFT results suggest that although there is a significant increase in hyperpolarisability for the dipolar azodye relative to the reference standard there is no enhancement of the NLO activity as a result of incorporating the heavy chalcogens; functionalization with each sequentially larger chalcogen would further decrease the calculated SHG efficiency.

**Table 4.12** DFT and TD-DFT calculated values pertaining to NLO activity of **27**, the phenylchalcogenyl derivatives (**52**, **53**, **54**), and **55**.

	<b>27</b>	<b>52</b>	<b>53</b>	<b>54</b>	<b>55</b>
static $\langle\beta\rangle$ (esu $\times 10^{30}$ )	139.71	139.64	133.54	129.29	8.44
SHG <sub>1064</sub> $\langle\beta\rangle$ (esu $\times 10^{30}$ )	1646.64	1477.57	1393.17	1021.16	18.62
$\mu$ (D)	12.823	11.234	11.421	11.769	7.91
HOMO-LUMO Gap (eV)	1.661	1.576	1.559	1.461	2.67

#### 4.6 Summary and Conclusions

Initial stages of this project were concerned with the optimisation of the procedure for mercurating a push-pull azodye. This important intermediate in the synthesis of the chalcogen-substituted species could only be obtained through harsh reaction conditions and with high concentration. Treatment of **27** with mercury trifluoroacetate resulted in

direct mercuration at a position *ortho*- to the azo bridge on the nitro-substituted ring; with longer reaction times, a second substitution occurs at the other *ortho*- position of the same ring. Although the regiochemistry was at first unexpected, experimental and computational studies showed that the reaction is under kinetic control. By monitoring the distribution of species with time, we were able to determine the optimum time to stop the reaction in order to maximize the yield of mono-mercurial for subsequent reactions.

The mercurated azodye **31** was efficiently converted to the halochalcogenyl species **41** and **45** using chalcogenyl halide reagents. The presence of the chalcogen atoms results in a blue shift in the UV-vis absorptions, suggesting a strong perturbation of the  $\pi$ -system of the molecule. Titrations of tetrabutylammonium salts, in the presence of an ionic buffer, showed a measurable exchange process only in the case of the iodide, allowing for the determination of a rate constant for the conversion between **45** and **47** ( $k_{\text{eq}} = 1.7 \times 10^{-2}$ ). The possibility of dissociation of **45** in solution was discounted by these same methods, using the chloride salt.

DFT calculations indicate that although the molecular structures of the chromophores are unlikely to be significantly altered by the presence of the chalcogen, the electronic structure is more strongly affected. The shape of the virtual orbitals is consistent before and after chalcogen substitution, while the occupied frontier orbitals have strong chalcogen contributions. As the weight of the halogen increases, the spacing of the orbitals decreases.

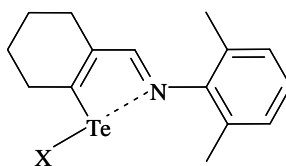
Reaction of the mercurated dye with phenylselenenyl chloride afforded a dye with sufficient stability to determine the NLO response in solution. Both **53** and the non-

functionalized chromophore **27**, showed strong hyperpolarisabilities in solution, but the results suggest that the chalcogen does not have a significant the effect. DFT calculated geometries and NICSs suggest that this may be the result of a weak SBI and poor delocalization because of the low electronegativity of the aryl ring.

## 5 Synthetic, Structural and Computational Investigations of a Macrocycle Featuring -O-Te-N- Catenation

### 5.1 Introduction

One of the more common structural features in systems that display intramolecular secondary bonding interactions to chalcogens is a virtual five-membered ring. As discussed in Chapter 4, derivatives of azobenzenes and Schiff bases are among the most common systems that contain these interactions. Donation from the imine or azo nitrogen into the chalcogen-X  $\sigma^*$  antibonding orbital, when X is a very electronegative atom, can result in SBIs so short that they approach the length of "covalent bonds". Two of the shortest Te $\cdots$ N SBI distances are observed in **62a** and **62b**; those SBIs are almost indistinguishable from the corresponding covalent two-centre, two-electron bonds (2.147 Å and 2.202 Å respectively, compared with 2.11 Å).<sup>228</sup>



- a) X = Br  
b) X = CH<sub>3</sub>COO

### 62

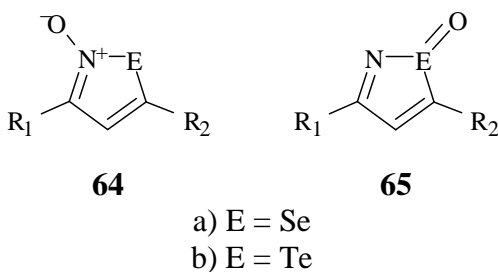
Although the Lewis structure with N $\rightarrow$ Te bonds (**Scheme 5.1 b**) has been used in the description of these and related compounds<sup>61,228,256</sup> and is arguably appropriate in



## 5.2 Results and Discussion

### 5.2.1 Synthesis and Isolation

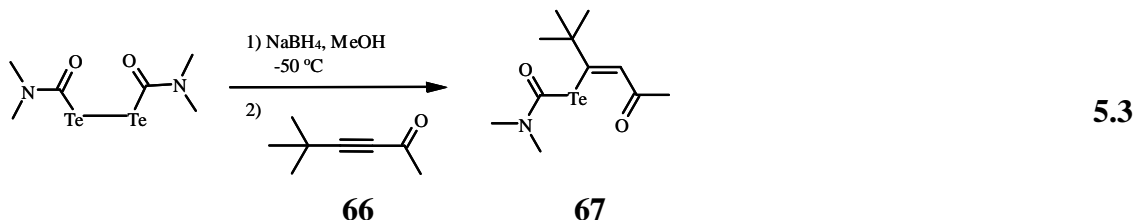
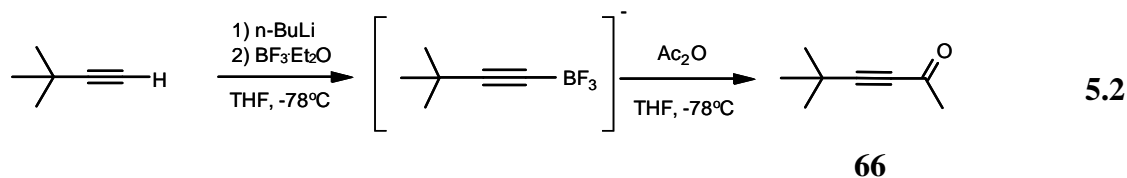
As a step in a recently published<sup>258</sup> general method for the synthesis of 1,2-chalcogenazoles, treatment of  $\beta$ -(N,N-dimethylcarbamoyl-chalcogeno)-alkenyl ketones with hydroxylamine-O-sulfonic acid leads to ring closure by formation of a chalcogen nitrogen bond. While the selenium reagents did produce the structurally authenticated N-oxide (**64a**), the products obtained from the tellurium analogues were tentatively identified by the authors as the Te-oxides (**65b**) on the basis of their unusual <sup>125</sup>Te NMR chemical shifts ranging from 3782 to 3831 ppm, although no crystal structure could be obtained for corroboration. In both cases, reaction with mild reducing agents yielded the 1,2-chalcogenazole.<sup>258</sup>

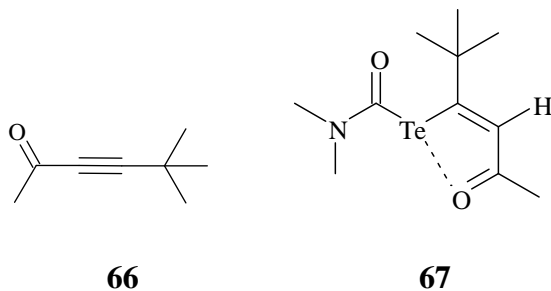


**Scheme 5.2** 1,2-Chalcogenazole oxides.

The above method was considered for the synthesis of the 5-*t*-butyl-3-methyl 1,2-tellurazole as follows (Eq. **5.1-5.4**). Based on literature procedures,<sup>80,258,259</sup> ynone **66** was obtained by lithiation of *t*-butyl acetylene, followed by rapid addition of acetic anhydride; the selectivity of the reaction was enhanced using boron trifluoride etherate. Addition of

elemental tellurium to a hot mixture of dimethylformamide (DMF) and sodium formed a thick slurry which, upon oxidation with oxygen, yielded the corresponding ditelluride. After reduction of this with sodium borohydride, the reactive intermediate underwent addition to the ynone **66** in methanol. The  $\beta$ -(N,N-dimethylcarbamoyltelluro)alkenyl ketone (**67**) produced in this manner was purified by column chromatography. While  $^1\text{H}$  and  $^{13}\text{C}$  NMR spectra indicate that only one product had been obtained, there were two resonances present in the  $^{125}\text{Te}$  NMR spectrum; these were identified as a doublet due to the  $^3\text{J}(\text{Te-H})$  coupling of 13.6 Hz in **67**. Geometry optimisations indicated that the Z-isomer of **67** is 233 kJ/mol more stable than the E-isomer due to an intramolecular  $\text{Te}\cdots\text{O}$  SBI.





The next step in the reaction consisted of the addition of hydroxylamine-*o*-sulfonic acid to form the isotellurazole oxide. After an aqueous workup and extraction with toluene, the product could be recrystallized from hot chloroform to yield small yellow crystals of quality appropriate for X-ray diffraction. Such a study revealed the actual nature of the product.

### 5.2.2 Structure

The structure of **63** obtained by X-ray diffraction is shown in **Figure 5.1**. Data from the final refinement is provided in **Table 5.1**, and selected bond distances and angles are provided in **Table 5.2**. The asymmetric unit consists of one quarter of the molecule; the macrocycle ring appears to be comprised of four 1,2-tellurazole heterocycles linked by oxygen bridges between tellurium and nitrogen. The 12-membered (-O-Te-N-)<sub>4</sub> cycle belongs to the S<sub>4</sub> point group and displays a cavity with a trans-annular Te---Te distance of 5.5382(7) Å. The 1,2-tellurazole ring is essentially planar, with the largest deviation (0.033 Å) corresponding to the nitrogen atom. Within the 1,2-tellurazole heterocycle the

C-N and C-C distances denote localized double bonds for the azabutadiene (-C=C-C=N-) fragment. The C<sub>1</sub>-Te<sub>1</sub> distance is in the range of typical single bonds, 1.91-2.20 Å.<sup>260,261</sup>

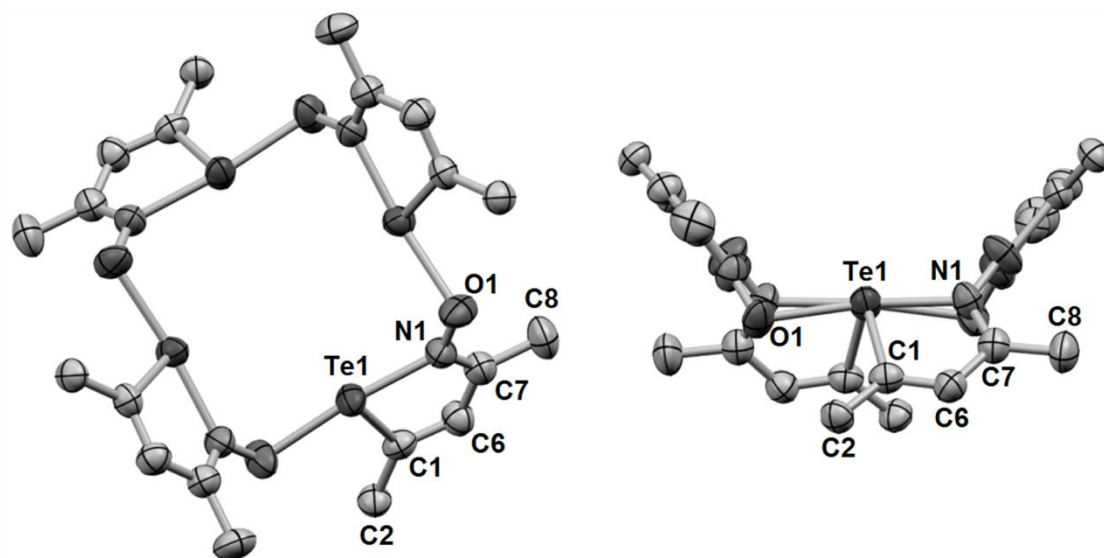


**Figure 5.1** ORTEP of two perspectives of the molecular structure of **63** (95% probability ellipsoids, methyl groups of t-butyl and hydrogen atoms omitted for clarity). Reproduced with permission from reference 263.

**Table 5.1** Summary of crystal data, collection and refinement conditions for **63**.

<b>63</b>	
Formula	C <sub>32</sub> H <sub>52</sub> N <sub>4</sub> O <sub>4</sub> Te <sub>4</sub>
Formula weight	1067.18
Radiation (wavelength, Å)	0.71073
Temperature	100(2)
Crystal system	Tetragonal
Space group	I4 <sub>1</sub> /a
a (Å)	13.7474(6)
b (Å)	13.7474(6)
c (Å)	20.696(2)
α (°)	90.00
β (°)	90.00
γ (°)	90.00
Volume (Å <sup>3</sup> )	3911.38
Z	4
ρ <sub>calcd.</sub> (g/cm <sup>3</sup> )	1.812
μ (mm <sup>-1</sup> )	2.991
R <sub>1</sub> <sup>a</sup>	0.0245
wR <sub>2</sub> <sup>b</sup>	0.0629

$$^a R_1 = \frac{\sum ||F_o| - |F_c||}{\sum |F_o|}$$

$$^b wR_2 = \left( \frac{\sum w ||F_o| - |F_c||^2}{\sum w |F_o|^2} \right)^{1/2}$$

**Table 5.2** Selected bond lengths (Å) and bond angles (°) for **63**.

Bond Lengths (Å)	
Te1-C1	2.105(2)
Te1-N1	2.154(2)
Te1-O1	2.299(2)
N1-O1	1.355(2)
N1-C7	1.306(3)
C7-C6	1.434(3)
C6-C1	1.363(3)
C2-C1	1.526(3)
C7-C8	1.487(3)
Bond Angles (°)	
O1-N1-Te1	123.4(1)
C7-N1-O1	121.1(2)
C7-N1-Te1	115.4(1)
N1-Te1-C1	77.88(7)
O1-Te1-C1	93.57(7)
Te1-C1-C6	111.0(1)
C1-C6-C7	121.4(2)
C6-C7-N1	114.0(2)
N1-O1-Te1	107.2(1)
O1-Te1-N1	171.45(6)
Dihedral Angles (°)	
C7-N1-O1-Te1	112.0(2)
Te1-O1-N1-Te1	70.8(1)
O1-Te1-N1-O1	172.2(3)
N1-Te1-C1-C6	3.0(1)
C1-C6-C7-N1	2.3(3)
C8-C7-N1-O1	5.4(3)
N1-Te1-O1-N1	176.5(4)
C1-Te1-N1-C7	98.2(2)

All of the structural features along the -O-Te-N- sequence are consistent with single covalent bonds. The Te1-N1 bond length is somewhat longer than the intramolecular Te-N distances observed in the structures of 1,2,5-telluradiazoles and tellurium diamides

(2.00-2.10 Å)<sup>43,263</sup> and in the cyclic imide (tBuNTe)<sub>3</sub> (2.033(6) Å).<sup>264</sup> The N1-O1 distance is longer than in pyridine-N-oxide (1.29(2) Å)<sup>265</sup> and 3-methyl-5-phenyl-1,2-isoselenazole-N-oxide (1.283(3) Å)<sup>258</sup> but shorter than the average in oximes (1.400 Å).<sup>266</sup> The oxygen atom sits opposite to the Te1-N1 bond at a distance that is longer than that observed for the axial bonds of  $\alpha$ -TeO<sub>2</sub> (2.122(1)Å).<sup>267</sup> Due to the magnitude of the C1-Te1-N1 bond angle, the environment of the tellurium atom is best described as distorted T-shaped. The local environment for tellurium is similar to that of **63b**, which exhibits small differences in the Te-N (2.202(3) Å) and the Te-O (2.197(3) Å) distances and the O-Te-N angle (162.3(1)°). The oxygen atom in **64** is closer to the average plane of the 1,2-tellurazole bonded by tellurium (0.071 Å) than to that of the heterocycle attached by nitrogen (0.175 Å). The N1-O1-Te1 angle in **63** is typical of unstrained oxygen bridges. The Te1-O1-N1-Te1 torsion angle determines the observed twist-boat conformation of the macrocycle and the relative orientation of the 1,2-tellurazole rings. The angles between average planes of the 1,2-tellurazole rings are 66.9° and 77.6° for the vicinal and opposite rings, respectively.

### 5.2.3 Modeling the Assembly from the Isotellurazole Oxide

Given its tetrameric nature, **63** is likely formed by addition of four C<sub>8</sub>H<sub>13</sub>NOTe units. These could be either the N- or Te-oxide of 1,2 tellurazole, generated as intermediates in the reaction (**Scheme 5.2**). The assembly of **63** from **65b** could be proposed in view of the frequent aggregation of tellurium-oxygen compounds. The

phenomenon has been interpreted as a reluctance of tellurium to make double bonds with oxygen,<sup>268</sup> but recent reports<sup>269-271</sup> have demonstrated kinetically stabilized compounds with Te=O bonds. Moreover, if **65b** were to be formed under our reaction conditions, the oxygen atom would have to migrate onto the chalcogen and subsequent aggregation would likely result in oxygen bridges between tellurium atoms, not the observed N-O-Te links. DFT calculations showed that **64b** is 178 kJ mol<sup>-1</sup> more stable than **65b**, thus the former is the most likely intermediate in the mechanism of formation. The calculations also gave an association energy of 226 kJ mol<sup>-1</sup> for the assembly of **63** from four molecules of **64b**.

The links between tellurium and oxygen are in great part electrostatically stabilized by the contributions presented in the coulombic potential map of **64b** (**Figure 5.2**). In addition, because the LUMO of **64b** is rather low in energy, tellurium can readily accept a lone pair of electrons from oxygen. The predominantly Te-N  $\sigma$  antibonding character of the acceptor orbital (**Figure 5.3**) leads to the observed geometry around tellurium.

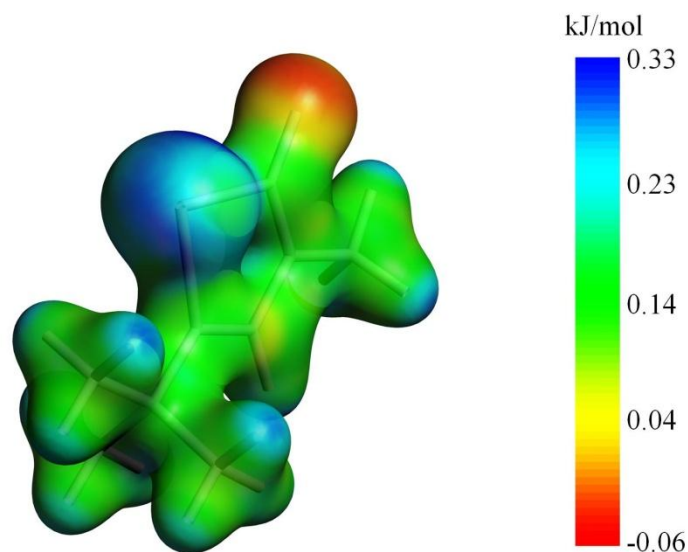


**Figure 5.2** SCF potential of **64b** projected onto the electron density (0.04 a.u. isosurface).

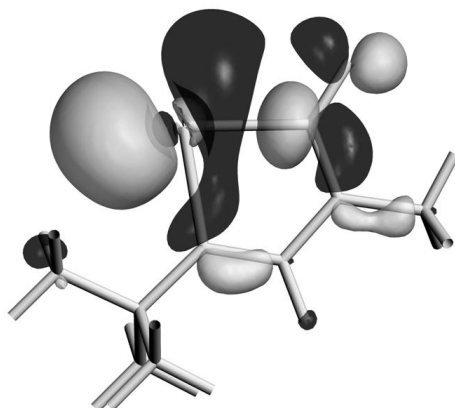


**Figure 5.3** LUMO of **64b** (0.03 a.u. isosurface).

The assembly of **63** from **64b** would be a case of intermolecular association by very strong SBIs. Interestingly, the most significant change of calculated bond lengths between **64b** and **63** corresponds to the N-O bond: 1.254 and 1.337 Å in their respective models. Intermolecular association has been observed in the structures of **64a**, but in such

cases only cyclic dimers are formed by 2.931 Å Se--O interactions<sup>258</sup> with geometric features that are very different from those of **63**.

#### 5.2.4 Stability

Attempts to reduce the isotellurazole oxide with an excess of triphenylphosphine (10 molar equivalents) in a vacuum sealed NMR tube provided no evidence of reduction. This result was reproduced after heating the sample overnight; compared to similar compounds<sup>258</sup> such stability is unusual. In light of this, and given the covalency observed in the crystal structure bond distances, an investigation was undertaken to determine whether the macrocycle was preserved in solution.

Mass spectrometric methods (EI, CI, ESI, MALDI) could not detect the molecular ion of **63**; the heaviest fragments observed had the composition of the 1,2-tellurazole and its oxide, with comparable intensities. The crystal structure of **63** places the methyl and *t*-butyl groups on vicinal isotellurazole rings in close proximity. The shortest distance between these groups ( $d_{\text{H-H}} = 2.84 \text{ \AA}$ ) would be short enough to enable observation of the nuclear Overhauser effect (NOE) if the ring were to remain intact in solution. The structural integrity of **63** in solution was then investigated using nuclear Overhauser effect spectroscopy (NOESY) NMR experiments at variable temperatures (VT). These studies showed cross-relaxation of the methyl and *t*-butyl <sup>1</sup>H nuclei at 180 K (**Figure 5.4**). This effect would only be possible if the methyl and *t*-butyl functional groups were in close proximity as observed in the macrocyclic structure. The effect is lost upon

warming, presumably due to a dynamic process in solution (e.g. ring inversion or a conformational change) which would also explain our failure to locate the  $^{125}\text{Te}$  resonance of **63** within this temperature range.

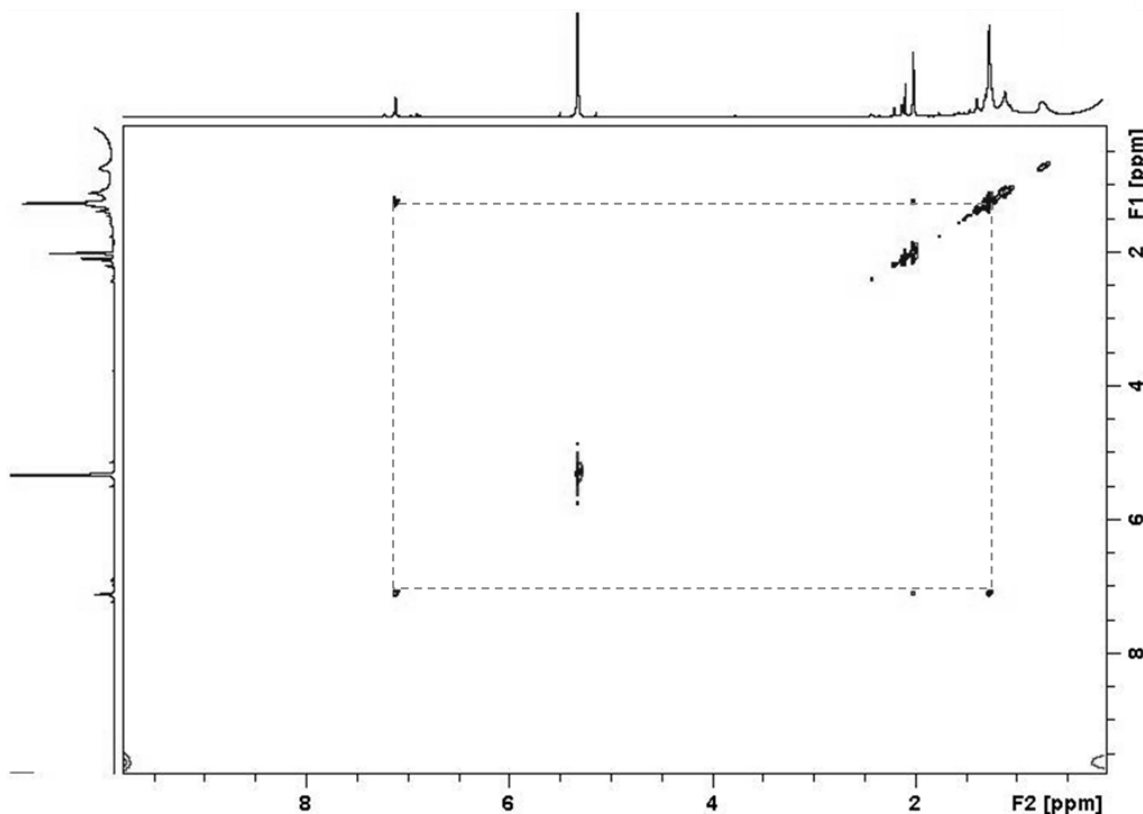
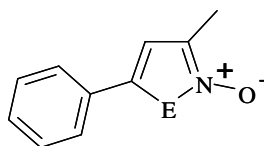


**Figure 5.4** 2-D NOESY spectrum of **63** in dichloromethane- $d_2$  collected at 180 K. ( $\delta(\text{Me}) = 2.17$  ppm,  $\delta(t\text{-Bu}) = 1.42$  ppm,  $\delta(\text{C-H}) = 7.00$  ppm)

### 5.2.5 Bonding

The crystal structure of **68a** exhibits short Se-O contacts through donation of oxygen electron density into the Se-C  $\sigma^*$  orbital, resulting in dimers.<sup>258</sup> This is in stark contrast to the macrocyclic structure **63**, in which a nearly linear O-Te-N axis is observed. DFT calculations were performed to investigate the nature of these bonding schemes for both

the tellurium and selenium cases. A constrained space orbital variation (CSOV) analysis of the optimised structures indicates that the virtual orbitals are less significant for the selenium case than for tellurium (**Table 5.3**). Removal of the virtual  $\pi$ -orbitals of **68a** has little effect on the association energy of the molecule; if the  $\sigma$ -orbitals are treated in a similar fashion, the dimer is unstable. The covalent nature of the Te-N SBI has been studied in detail in the case of 1,2,5-telluradiazoles.<sup>16</sup>



a) E = Se

b) E = Te

**68**

**Table 5.3** CSOV analysis for  $C_{2h}$  dimers of **68a** and **68b**.

	Total bonding Energy (kJ/mol)			
	All virtual	no $\pi$	no $\pi$	no virtual
<b>68a</b>	-8.96	-8.51	-6.71	-5.98
<b>68b</b>	-35.53	-26.88	16.40	24.86

The dimers of **68a** and **68b** would be, in principle stable structures, though the stabilization energy is small. When the monomer, dimer (**64b**<sub>2</sub>), trimer (**64b**<sub>3</sub>), and tetrameric (**63**) assemblies of **64b** were considered, the energies were more significant; on a per unit basis, dimerization results in a 3.5 kJ/mol stabilization, while formation of the trimer provides 51.0 kJ/mol, and the tetramer affords 56.5 kJ/mol. Relief of ring strain upon addition of isotellurazole units is the likely cause of this added stabilization.

Interestingly, in the structure of **64b**<sub>2</sub> and **64b**<sub>3</sub> the methyl and t-butyl groups are too far apart (5.43 Å and 3.12 Å respectively) for cross-relaxation to occur in the NOESY experiment.

### 5.3 Summary

The solid-state structure of **63** revealed an unexpected environment around tellurium, with a seemingly tetrameric structure. It is likely that this macrocycle is assembled through a combination of electrostatic attraction between oxygen and tellurium, and donation of an oxygen lone pair into the  $\sigma^*$  Te-N bond. All of the bond lengths within the macrocycle are within the ranges reported for single covalent bonds, and the compound exhibits unusual stability in the presence of reducing agents. A VT-NOESY experiment has provided some evidence that this macrocycle is preserved in solution. Computational studies have indicated that although it should be possible observe a dimer or trimer of **64b**, the tetramer is the most stable structure.

## 6 Conclusions and Suggestions for Future Work

### 6.1 Conclusions

The results of the work described in this thesis constitute a valuable contribution to the study of inter- and intramolecular SBIs through spectroscopic means. The viability of electronic absorption spectroscopy and  $^{125}\text{Te}$  NMR for this purpose was assessed through a combination of computational and experimental studies. The results of DFT calculations showed that changes in molecular geometry can have a significant effect on the UV-vis and  $^{125}\text{Te}$  NMR spectra, with a small energetic cost. Experimentally, those spectroscopic techniques were found to be sensitive to the nature of the solvent used. These results were interpreted using DFT calculations for explicit solvation models as well as the COSMO formalism. The concentration and temperature dependence of the  $^{125}\text{Te}$  NMR chemical shift of three ditellurides with different ability to interact with other molecules showed that those effects also depend on the nature of the solvent. The presence of SBIs attenuated the concentration dependence, but significant steric protection was required to completely remove it. The possibility of auto-association of ditelluride molecules in solution was modeled using the bonding arrangements observed in the solid state. The overall results of these investigations indicate that the current methods available for  $^{125}\text{Te}$  NMR could not be used to conclusively identify SBIs in solution in a straightforward way; small changes due to SBI formation are easily overshadowed by other effects in solution.

The optimisation of a procedure for mercurating a difunctional azodye provided a useful intermediate in the grafting of an SBI into the  $\pi$ -manifold of a chromophore. Direct reaction of a dipolar azodye with mercury trifluoroacetate in high concentrations resulted in substitution at a position *ortho*- to the azo bridge on the nitro-substituted ring. Experimental and computational studies suggest the reaction is under kinetic control, directed to that position by the cooperation of the other substituents. After 4 h reaction time the maximum yield of mono-substituted compound is obtained. The mercurated azodye was efficiently converted to halochalcogenyl derivatives. The presence of the chalcogen results in a blue shift in the UV-vis absorptions, indicating a strong perturbation of the molecular  $\pi$ -system. Titrations with tetrabutylammonium salts showed that in the case of the iodide, there is a chemical equilibrium present. DFT calculations indicated only small effect of the chalcogen on the chromophore structure; frontier molecular orbitals were more significantly altered. The size of the halogen affects the spacing of the orbitals. An analogous phenylselenenyl functionalized dye showed a strong NLO response in solution. This response was consistent with that of the non-functionalized dye. DFT calculations suggest that this may be the result of a weak SBI resulting from the poor electronegativity of the aryl ring.

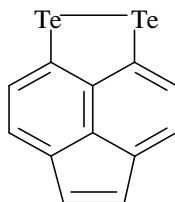
The solid-state structure of an intermediate in the synthesis of isotellurazoles revealed an unexpected geometry around tellurium, with a seemingly tetrameric structure. The macrocycle is likely assembled through electrostatic attraction between oxygen and tellurium, and donation of an oxygen lone pair into the  $\sigma^*_{\text{Te-N}}$  bond, of isotellurazole oxide monomers. All of the bond lengths within the macrocycle are within the ranges

reported for single covalent bonds, and the compound exhibits unusual stability in the presence of reducing agents. Preliminary studies have provided some evidence the macrocycle is preserved in solution. Computational studies suggest smaller rings should be stable but an additional  $C_8H_{13}NOTe$  unit relieves ring strain and increases stabilization.

## 6.2 Suggestions of Future Work

### 6.2.1 $^{125}Te$ NMR Spectroscopy of Ditellurides

Although the compounds selected for the investigations discussed in Chapter 3 are simple,  $^{125}Te$  NMR spectroscopy made it evident that their solutions are far from simple systems; there are multiple variables simultaneously affecting the chemical shift. The NMR study could be extended using ditellurides which should display a simpler behaviour. The conformational effects due to the freedom of rotation of the C-Te-Te-C dihedral angle could be removed with a rigid structure, for example **69**.<sup>128</sup> Here the geometry around the Te-Te bond is highly constrained, with a C-Te-Te-C dihedral angle of  $4.6^\circ$  imposed by the rigid acenaphthylene backbone.



**69**

Another method of reducing complications in the NMR would be to use compounds that have no  $\pi$ -systems with which the tellurium atoms could interact. This can possibly be achieved using structures containing aromatic rings with multiple bulky substituents to prevent coordination. The known structure of the bis(2,4,6-tri-*t*-butylphenyl) ditelluride for example, shows no short contacts to tellurium in the solid state, though the *t*-butyl groups are likely too small to prevent association entirely in solution. For the same reason ditellurides with dialkyl groups (e.g., cyclohexyl or adamantyl)<sup>272</sup> could also be studied but (**CAUTION!**) this and the dialkyl monotellurides (which would likely be impurities) are in general readily absorbed through skin and can result in acute poisoning and death.

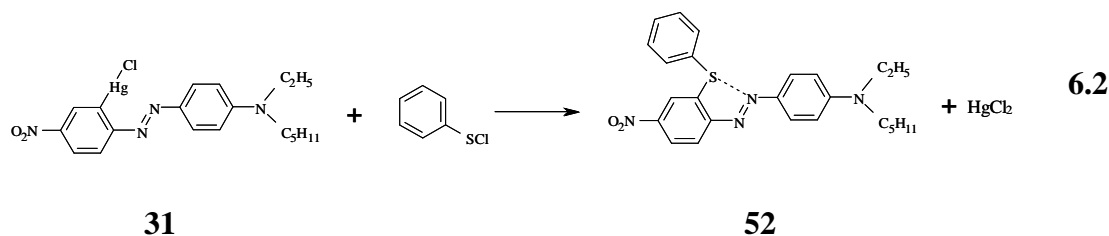
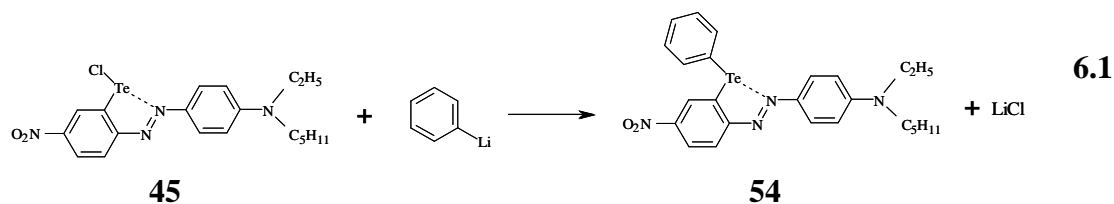
### 6.2.2 UV-vis Studies of Chalcogen-Substituted Azodyes

Titration of **45** and **41** with iodide salts were monitored using UV-vis spectroscopy at 25 °C but the studies should be expanded to determine the temperature dependence of the equilibria. Additionally, complete conversion of **45** to the iodide **47** through salt metathesis can be used to obtain a more reactive chromophore. A series of titrations using both chloride and bromide salts at a number of temperatures will provide a more complete picture of the system.

### 6.2.3 Nonlinear Optical Properties

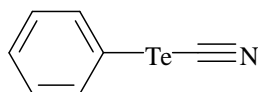
The results in section 4.4.2.2 show no significant enhancement of the second-order NLO response of the 2-phenylselenenyl-substituted azodye relative to the non-substituted chromophore. Measurements should be performed for the other chalcogen analogues to provide a comparison with these results. The phenyltellurenyl dye could be obtained by treatment of **45** with phenyl-lithium (Eq. 6.1). The sulfur analogue could be prepared from the reaction of **33** with using phenylsulfenyl chloride (Eq.6.2). Although the TD-DFT calculations for those compounds predict hyperpolarisability magnitudes similar to those of **53**, the three congeners are necessary to complete the study.

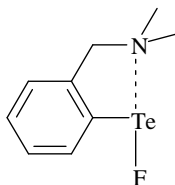
It is possible that the NLO response of these dyes could be improved by manipulating the strength of the Te-N SBI. The NICS calculations indicate that the phenyl group has a detrimental effect for the delocalisation of electrons through the virtual five-membered ring and that the more electronegative substituents favour delocalization. Therefore it would be desirable to examine the effect of the X group in the NLO activity of chalcogen-substituted azodyes. The TD-DFT calculations indicated that fluorine should significantly enhance the NLO response of these compounds. However, performing measurements with the halochalcogenyl substituted molecules would be difficult considering their moisture sensitivity, this would require the use of calibrated cells which would be loaded with the sample solution and sealed for measurements in the laser spectrometer. Alternatively, the pentafluorophenyl group could be used.



#### 6.2.4 Delocalization of Electron Density by SBI formation

It is necessary to find experimental evidence to support the conclusion from the NICS calculations regarding the establishment of diatropic ring currents on virtual heterocycles formed by SBIs centred on chalcogen atoms with very electronegative substituents. In chalcogenyl-substituted azodyes, an X substituent containing an NMR active nucleus X could be used to probe such a phenomenon. Salt metathesis with silver fluoride or sodium cyanide from **45** could provide the necessary derivatives to allow for these measurements using the  $^{19}\text{F}$  or  $^{13}\text{C}$  nuclei. Their chemical shifts would then be compared with those from derivatives related to **70**<sup>273</sup> and **71**.<sup>274</sup> A decreased shielding would be diagnostic of the diatropic current.

**70**



71

### 6.2.5 Stability of the (-Te-O-N)<sub>4</sub> Macrocycle

Because of its apparent tetrameric nature, it is conceivable that the macrocycle **46** could dissociate in solution. The NOESY results discussed in section **5.2.4** do indicate the macrocycle does not dissociate in solution but additional evidence would further support this point. For example, a VT study should look for the temperature at which the NOE stops being observable. Over that temperature, diffusion ordered spectroscopy (DOSY)<sup>275-277</sup> experiments could be used to determine the rate of diffusion of and measure the size of the species in solution. Alternatively, an analogue (or an actual isotellurazole oxide) with different substituents could be prepared to probe the possibility of a scrambling equilibrium in a solution containing both species.

### 6.2.6 Coordination Complexes of the (-Te-O-N)<sub>4</sub> Macrocycle

The lone pairs on the chalcogens and the Te---Te trans-annular distance (5.54 Å) in **63** suggest that this molecule is suitable for host-guest chemistry with some metal ions. This is supported by preliminary DFT calculations of coordination complexes, for example the derivative of mercury (II) chloride shown in **Figure 6.1**; in this case the

binding energy has been estimated at 40 kJ/mol. Similar calculations for cadmium, platinum, and palladium also indicate that the macrocycle would undergo only minor deviations in the geometry to accommodate ions of different size.

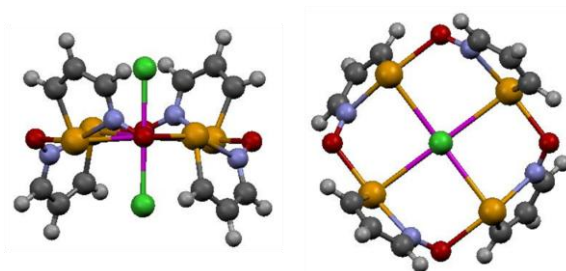
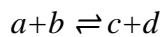


**Figure 6.1** Two views of the DFT optimized structure of mercury (II) chloride bound by a (-Te-O-N)<sub>4</sub> macrocycle.

**Appendix**

**A.1** Binding isotherm for the spectrophotometric determination of a double exchange equilibrium.



$$K_{eq} = \frac{C_c C_d}{C_a C_b} = \frac{C_c^2}{C_a C_b}$$

$$C_a = C_a^0 - C_c$$

$$C_a = \frac{C_c^2}{K_{eq} C_b}$$

$$C_a^0 - C_c = \frac{C_c^2}{K_{eq} C_b}$$

$$K_{eq} C_b C_a^0 - K_{eq} C_b C_c = C_c^2$$

$$C_c^2 + K_{eq} C_b C_c - K_{eq} C_b C_a^0 = 0$$

$$A = \varepsilon C l$$

$$\frac{\Delta A}{l} = \Delta \varepsilon C_c$$

$$\frac{\Delta A}{l} = \Delta \varepsilon \left( \frac{-K_{eq} C_b + \sqrt{(K_{eq} C_b)^2 - 4(K_{eq} C_b C_a^0)}}{2} \right)$$

**A.2** Chemical shielding correction by volume susceptibility.

$$\frac{B}{B_0} = (1 - \sigma)$$

$$\frac{B}{B'} = (1 - \sigma')$$

$$B' = B_0 + \frac{4}{3} \pi I$$

$$\frac{B'}{B_0} = 1 + \frac{4}{3} \pi \chi_v$$

$$B' = B_0 + \frac{4}{3} \pi \chi_v B_0$$

$$\frac{B}{B_0 + \frac{4}{3} \pi \chi_v B_0} = (1 - \sigma')$$

$$\sigma' = 1 - \frac{B}{B_0 + \frac{4}{3} \pi \chi_v B_0}$$

$$\sigma' = \frac{B_0 + \frac{4}{3} \pi \chi_v B_0 - B}{B_0 + \frac{4}{3} \pi \chi_v B_0}$$

$$\sigma' = \frac{1 + \frac{4}{3} \pi \chi_v - \frac{B}{B_0}}{1 + \frac{4}{3} \pi \chi_v}$$

$$\frac{4}{3} \pi \chi_v \ll 1$$

$$\sigma' = 1 + \frac{4}{3} \pi \chi_v - \frac{B}{B_0}$$

$$\sigma' = 1 + \frac{4}{3} \pi \chi_v - (1 - \sigma)$$

$$\sigma' = \sigma + \frac{4}{3} \pi \chi_v$$

### References

- (1) Nic, M.; Jirat, J.; Kosata, B.; Jenkins, A. In *IUPAC Compendium of Chemical Terminology, 2nd ed. (the "Gold Book")*. Compiled by A. D. McNaught and A. Wilkinson; Blackwell Scientific Publications: Oxford, 1997.
- (2) Puddephatt, R. J. *Coord. Chem. Rev.* **2001**, 216-217, 313-332.
- (3) Pyykkö, P. *Chem. Rev.* **1997**, 97, 597-636.
- (4) Haiduc, I. In *Secondary Bonding*; Steed, J., Atwood, J., Eds.; Encyclopedia of Supramolecular Chemistry; Marcel Dekker, Inc.: New York, 2004; p 1215-1224.
- (5) du Mont, W. -W.; Martens-von Salzen, A.; Ruthe, F.; Seppälä, E.; Mugesh, G.; Devillanova, F. A.; Lippolis, V.; Kuhn, N. *J. Organomet. Chem.* **2001**, 623, 14-28.
- (6) Bleiholder, C.; Werz, D. B.; Köppel, H.; Gleiter, R. *J. Am. Chem. Soc.* **2006**, 128, 2666-2674.
- (7) Mohajeri, A.; Pakiari, A. H.; Bagheri, N. *Chem. Phys. Lett.* **2009**, 467, 393-397.
- (8) Newton, M. G.; King, R. B.; Haiduc, I.; Silvestru, A. *Inorg. Chem.* **1993**, 32, 3795-3796.
- (9) Clark, T.; Hennemann, M.; Murray, J.; Politzer, P. *J. Mol. Model.* **2007**, 13, 291-296.
- (10) Chen, J. -M.; Santra, B. K.; Liu, C. W. *Inorg. Chem. Commun.* **2004**, 7, 1103-1105.
- (11) Vargas-Baca, I.; Chivers, T. *Phosphorus, Sulfur Silicon Relat. Elem.* **2000**, 164, 207-227.

- (12) Chivers, T. In *A Guide To Chalcogen-nitrogen Chemistry*; World Scientific Publishing: Hackensack, NJ, 2006.
- (13) Svensson, P. H.; Kloo, L. *Chem. Rev.* **2003**, *103*, 1649-1684.
- (14) Alcock, N. W. *Adv. Inorg. Chem. Radiochem.* **1972**, *15*, 1-58.
- (15) Angyan, J. G.; Poirer, R. A.; Kucsman, A.; Csizmadia, I. G. *J. Am. Chem. Soc.* **1987**, *109*, 2237-2245.
- (16) Cozzolino, A. F.; Vargas-Baca, I.; Mansour, S.; Mahmoudkhani, A. H. *J. Am. Chem. Soc.* **2005**, *127*, 3184-3190.
- (17) Chivers, T.; Krouse, I.; Parvez, M.; Vargas-Baca, I.; Ziegler, T.; Zoricak, P. *Inorg. Chem.* **1996**, *35*, 5836-5842.
- (18) Iwaoka, M.; Tomoda, S. *J. Am. Chem. Soc.* **1996**, *118*, 8077-8084.
- (19) Politzer, P.; Murray, J. S.; Lane, P. *Int. J. Quantum Chem.* **2007**, *107*, 3046-3052.
- (20) Israelachvilli, J. N. In *Intermolecular and Surface Forces*; Academic Press: London, 1985; p 83-90, 96-99, 109-117.
- (21) Steed, J. W.; Atwood, J. L. In *Supramolecular Chemistry*; Wiley: New York, 2000.
- (22) Haas, A.; Kasproski, J.; Pryka, M. *Chem. Ber.* **1992**, *125*, 789-792.
- (23) Cozzolino, A. F.; Elder, P. J. W.; Vargas-Baca, I. *Coord. Chem. Rev.* **2011**, *255*, 1426-1438.
- (24) Starbuck, J.; Norman, N. C.; Orpen, A. G. *New J. Chem.* **1999**, *23*, 969-972.

- (25) James, S. C.; Norman, N. C.; Orpen, A. G.; Starbuck, J. *Cryst. Eng. Commun.* **2000**, *2*, 67-72.
- (26) Haiduc, I.; Zuckerman-Schpector, J. *Phosphorus, Sulfur Silicon Relat. Elem.* **2001**, *171-172*, 73-112.
- (27) Gleiter, R.; Werz, D. B.; Rausch, B. J. *Chem. Eur. J.* **2003**, *9*, 2676-2683.
- (28) Werz, D. B.; Gleiter, R.; Rominger, F. *J. Am. Chem. Soc.* **2002**, *124*, 10638-10639.
- (29) Werz, D. B.; Staeb, T. H.; Benisch, C.; Rausch, B. J.; Rominger, F.; Gleiter, R. *Org. Lett.* **2002**, *4*, 339-342.
- (30) Sarma, J. A. R. P.; Allen, F. H.; Hoy, V. J.; Howard, J. A. K.; Thaimattam, R.; Biradha, K.; Desiraju, G. R. *Chem. Commun.* **1997**, 101-102.
- (31) Farina, A.; Meille, S. V.; Messina, M. T.; Metrangolo, P.; Resnati, G.; Vecchio, G. *Angew. Chem., Int. Ed. Engl.* **1999**, *38*, 2433-2436.
- (32) Metrangolo, P.; Carcenac, Y.; Lahtinen, M.; Pilati, T.; Rissanen, K.; Vij, A.; Resnati, G. *Science* **2009**, *323*, 1461-1464.
- (33) Clemente-Juan, J.; Coronado, E.; Minguez Espallargas, G.; Adams, H.; Brammer, L. *Cryst. Eng. Commun.* **2010**, *12*, 2339-2342.
- (34) Desiraju, G. R. *Angew. Chem., Int. Ed. Engl.* **1995**, *34*, 2311-2327.
- (35) Sijbesma, R. P.; Beijer, F. H.; Brunsveld, L.; Folmer, B. J. B.; Hirschberg, J. H. K.; Lange, R. F. M.; Lowe, J. K. L.; Meijer, E. W. *Science* **1997**, *278*, 1601-1604.
- (36) Greenwood, N. N.; Earnshaw, A. In *Chemistry of the Elements*, 2<sup>nd</sup> Ed. Butterworth Heinemann: Oxford, 1997; p 1222-1224.

- (37) Cooper, W. C. In *Tellurium*; Van Nostrand Reinhold Co.: New York, 1971; p 437.
- (38) Zuckerman-Schpector, J.; Haiduc, I. *Cryst. Eng. Commun.* **2002**, *4*, 178-193.
- (39) Allen, F. H. *Acta Crystallogr. B.: Struct. Sci.* **2002**, *58*, 380-388.
- (40) Bertini, V.; Dapporto, P.; Lucchesini, F.; Sega, A.; Munno, A. D. *Acta Crystallogr., Sect. C* **1984**, *40*, 653-655.
- (41) Neidlein, R.; Knecht, D.; Gieren, A.; Ruiz-Perez, C. *Z. Naturforsch. B: Chem. Sci.* **1987**, *42*, 84-90.
- (42) Chivers, T.; Gao, X.; Parvez, M. *Inorg. Chem.* **1996**, *35*, 9-15.
- (43) Cozzolino, A. F.; Britten, J. F.; Vargas-Baca, I. *Cryst. Growth Des.* **2006**, *6*, 181-186.
- (44) Cozzolino, A. F.; Vargas-Baca, I. *Cryst. Growth Des.* **2011**, *11*, 668-677.
- (45) Cozzolino, A. F.; Whitfield, P. S.; Vargas-Baca, I. *J. Am. Chem. Soc.* **2010**, *132*, 17265-17270.
- (46) Cozzolino, A. F.; Yang, Q.; Vargas-Baca, I. *Cryst. Growth Des.* **2010**, *10*, 4959-4964.
- (47) Bazan, G. C.; Liu, B. U.S. Pat. 2006-US3498 2006083932, 2006.
- (48) Pasquier, C.; Charriere, V.; Braun, H. -J. Eur. Pat. 2001-EP7494 2002022093, 2001.
- (49) Umbricht, G.; Braun, H. -J.; Oberson, S. Eur. Pat. 2001-10114426, 2001.
- (50) Dutton, J. L.; Tindale, J. J.; Jennings, M. C.; Ragogna, P. J. *Chem. Commun.* **2006**, 2474-2476.

- (51) Berionni, G.; Pégot, B.; Marrot, J.; Goumont, R. *Cryst. Eng. Commun.* **2009**, *11*, 986-988.
- (52) Sudha, N.; Singh, H. B. *Coord. Chem. Rev.* **1994**, *135/136*, 469-515.
- (53) Sadekov, I. D.; Maksimenko, A. A.; Abakarov, G. M.; Maslakov, A. G.; Minkin, V. I. *Khim. Geterotsikl. Soedin.* **1988**, 1426-1427.
- (54) Mbogo, S. A.; McWhinnie, W. R.; Lobana, T. S. *J. Organomet. Chem.* **1990**, *384*, 115-119.
- (55) Mbogo, S. A.; McWhinnie, W. R.; Lobana, T. S. *Inorg. Chim. Acta* **1990**, *172*, 221-224.
- (56) Singh, H. B.; Sudha, N.; Butcher, R. J. *Inorg. Chem.* **1992**, *31*, 1431-1433.
- (57) Al-Salim, N.; McWhinnie, W. R. *Polyhedron* **1989**, *8*, 2769-2776.
- (58) Abid, K. Y.; Al-Salim, N.; Greaves, M.; McWhinnie, W. R. *J. Chem. Soc. Dalton Trans.* **1989**, 1697-1703.
- (59) Singh, H. B.; McWhinnie, W. R. *J. Chem. Soc. Dalton Trans.* **1985**, 821-824.
- (60) Minkin, V. I.; Sadekov, I. D.; Maksimenko, A. A.; Maslakov, A. G.; Mehrotra, G. K.; Fedotov, M. A. *Zh. Obshch. Khim.* **1988**, *58*, 1684-1685.
- (61) Ahmed, M. A. K.; McCarthy, A. E.; McWhinnie, W. R.; Berry, F. J. *J. Chem. Soc. Dalton Trans.* **1986**, 771-775.
- (62) Mugesh, G.; Panda, A.; Singh, H. B.; Puneekar, N. S.; Butcher, R. J. *Chem. Commun.* **1998**, *20*, 2227-2228.

- (63) Iwaoka, M.; Tomoda, S. *J. Chem. Soc. Chem. Commun.* **1992**, 1165-1167.
- (64) Nishibayashi, Y.; Singh, J. D.; Fukazawa, S.; Uemura, S. *J. Org. Chem.* **1995**, *60*, 4114-4120.
- (65) Fujita, K.; Murata, K.; Iwaoka, M.; Tomoda, S. *Tetrahedron Lett.* **1995**, *36*, 5219-5222.
- (66) *RLATT*. Bruker AXS Inc., Madison, Wisconsin, USA. 1998.
- (67) *APEX2*. Bruker AXS Inc., Madison, Wisconsin, USA. 2006.
- (68) *SMART and SAINT*. Siemens Analytical X-ray Instruments Inc., Madison, Wisconsin, USA. 1995.
- (69) *SADABS*. Bruker AXS Inc., Madison, Wisconsin, USA., 2001.
- (70) a) Sheldrick, G. M. *SHELX97* [Includes SHELXS97, SHELXL97, CIFTAB]. Programs for Crystal Structure Analysis. Release 97-2. Institut für Anorganische Chemie der Universität, Göttingen, Germany, 1997. b) Sheldrick, G. M. (2008). *Acta Cryst.* **A64**, 112-122.
- (71) Farrugia, L. *J. Appl. Cryst.* **1999**, *32*, 837-838.
- (72) Farrugia, L. *J. Appl. Cryst.* **1997**, *30*, 565.
- (73) Macrae, C. F.; Edgington, P. R.; McCabe, P.; Pidcock, E.; Shields, G. P.; Taylor, R.; Towler, M.; van de Streek, J. *J. Appl. Crystallogr.* **2006**, *39*, 453-457.
- (74) Ammann, C.; Meier, P.; Merbach, A. E. *J. Magn. Reson.* **1982**, *46*, 319-321.

- (75) Zhang, W.; Cozzolino, A. F.; Mahmoudkhani, A. H.; Tulumello, M.; Mansour, S.; Vargas-Baca, I. *J. Phys. Chem. B* **2005**, *109*, 18378-18384.
- (76) Ashby, E. C.; Oswald, J. *J. Org. Chem.* **1988**, *53*, 6068-6076.
- (77) Finkelstein, H. *Chem. Ber.* **1910**, *43*, 1528-1532.
- (78) Dutton, J. L.; Farrar, G. L.; Sgro, M. J.; Battista, T. L.; Ragogna, P. *J. Chem. – Eur. J.* **2009**, *15*, 10263-10271.
- (79) Liu, S. -L.; Ma, M. -M. *J. Organomet. Chem.* **1970**, *24*, 89-90.
- (80) Shimada, K.; Oikawa, S.; Nakamura, H.; Moro-oka, A.; Kikuchi, M.; Maruyama, A.; Suzuki, T.; Kogawa, H.; Inoue, Y.; Gong, Y.; Aoyagi, S.; Takikawa, Y. *Bull. Chem. Soc. Jpn.* **2005**, *78*, 899-905.
- (81) Haller, W.; Irgolic, K. *J. Organomet. Chem.* **1973**, *38*, 97-103.
- (82) Kaur, R.; Singh, H.; Butcher, R. *Organometallics* **1995**, *14*, 4755-4763.
- (83) Lepley, A. R.; Khan, W. A. *J. Org. Chem.* **1968**, *33*, 4362-4368.
- (84) Shin, D. M.; Schanze, K. S.; Whitten, D. G. *J. Am. Chem. Soc.* **1989**, *111*, 8494-8501.
- (85) te Velde, G.; Bickelhaupt, F. M.; Baerends, E. J.; Fonseca Guerra, C.; van Gisbergen, S. J. A.; Snijders, J. G.; Ziegler, T. *J. Comp. Chem.* **2001**, *22*, 931-967.
- (86) Guerra, C. F.; Snijders, J. G.; te Velde, G.; Baerends, E. J. *Theor. Chem. Acc.* **1998**, *99*, 391-403.

- (87) Baerends, E. J.; Autschbach, J.; Bérces, A.; Bo, C.; Boerrigter, P. M.; Cavallo, L.; Chong, D. P.; Deng, L.; Dickson, R. M.; Ellis, D. E.; Faassen, M. v.; Fan, L.; Fischer, T. H.; Fonseca Guerra, C. F.; van Gisbergen, S. J. A.; Groeneveld, J. A.; Gritsenko, O. V.; Grüning, M.; Harris, F. E.; van der Hoek, P.; Jacobsen, H.; Jensen, G.; van Kessel, G.; Kootstra, F.; van Lenthe, E.; McCormack, D. A.; Michalak, A.; Osinga, V. P.; Patchkovskii, S.; Philipsen, P. H. T.; Post, D.; Pye, C. C.; Ravenek, W.; Ros, P.; Schipper, P. R. T.; Schreckenbach, H. G.; Snijders, J. G.; Solà, M.; Swart, M.; Swerhone, D.; te Velde, G.; Vernooijs, P.; Versluis, L.; Visser, O.; Wang, F.; van Wezenbeek, E.; Wiesenekker, G.; Wolff, S. K.; Woo, T. K.; Ziegler, T. Amsterdam, The Netherlands <http://www.scm.com>, ADF, *Versions 2005.01 - 2010.02*.
- (88) van Gisbergen, S. J. A.; Snijders, J. G.; Baerends, E. J. *Phys. Rev. Lett.* **1997**, *78*, 3097-3100.
- (89) van Gisbergen, S. J. A.; Snijders, J. G.; Baerends, E. J. *J. Chem. Phys.* **1998**, *109*, 10644-10656.
- (90) Vosko, S. H.; Wilk, L.; Nusair, M. *Can. J. Phys.* **1980**, *58*, 1200-1211.
- (91) Becke, A. D. *Phys. Rev. A* **1988**, *38*, 3098-3100.
- (92) Perdew, J. P. *Phys. Rev. B* **1986**, *33*, 8822-8824.
- (93) Perdew, J. P.; Wang, Y. *Phys. Rev. B* **1992**, *45*, 13244-13249.
- (94) van Lenthe, E.; Ehlers, A.; Baerends, E. J. *J. Chem. Phys.* **1999**, *110*, 8943-8953.
- (95) van Lenthe, E.; Baerends, E. J.; Snijders, J. G. *J. Chem. Phys.* **1993**, *99*, 4597-4610.
- (96) van Lenthe, E.; Baerends, E. J.; Snijders, J. G. *J. Chem. Phys.* **1994**, *101*, 9783-9792.

- (97) van Lenthe, E.; Snijders, J. G.; Baerends, E. J. *J. Chem. Phys.* **1996**, *105*, 6505-6516.
- (98) van Lenthe, E.; van Leeuwen, R.; Baerends, E. J.; Snijders, J. G. *Int. J. Quant. Chem.* **1996**, *57*, 281-293.
- (99) Gross, E.; Ullrich, C.; Gossmann, U. In *Density Functional Theory of Time-Dependent systems*; Plenum: New York, 1995.
- (100) van Gisbergen, S. J. A.; Snijders, J. G.; Baerends, E. J. *Comput. Phys. Commun.* **1999**, *118*, 119-138.
- (101) Rosa, A.; Baerends, J. E.; van Gisbergen, S. J. A.; van Lenthe, E.; Groenveld, J. A.; Snijders, J. G. *J. Am. Chem. Soc.* **1999**, *121*, 10356-10365.
- (102) Bishop, D. M. . *Adv. Quant. Chem.* **1994**, *25*, 1-45.
- (103) Willets, A.; Rice, J. E.; Burland, D. M.; Shelton, D. P. *J. Chem. Phys.* **1992**, *97*, 7590-7600.
- (104) Shelton, D. P.; Rice, J. E. *Chem. Rev.* **1994**, *94*, 3-29.
- (105) Gritsenko, O. V.; Schipper, P. R. T.; Baerends, E. J. *Chem. Phys. Lett.* **1999**, *302*, 199-207.
- (106) Gritsenko, O. V.; Schipper, P. R. T.; Baerends, E. J. *Int. J. Quant. Chem.* **2000**, *76*, 407-419.
- (107) Schipper, P. R. T.; Gritsenko, O. V.; van Gisbergen, S. J. A.; Baerends, E. J. *J. Chem. Phys.* **2000**, *112*, 1344-1352.
- (108) Schreckenbach, G.; Ziegler, T. *J. Phys. Chem.* **1995**, *99*, 606-611.

- (109) Schreckenbach, G.; Ziegler, T. *Int. J. Quantum Chem.* **1996**, *60*, 753-766.
- (110) Schreckenbach, G.; Ziegler, T. *Int. J. Quantum Chem.* **1997**, *61*, 899-918.
- (111) Wolff, S.; Ziegler, T. *J. Chem. Phys.* **1998**, *109*, 895-905.
- (112) Klamt, A.; Schüürmann, G. *J. Chem. Soc. Perkin Trans.* **1993**, *2*, 799-805.
- (113) Klamt, A. *J. Phys. Chem.* **1995**, *99*, 2224-2235.
- (114) Klamt, A.; Jones, V. *J. Chem. Phys.* **1996**, *105*, 9972-9982.
- (115) Visser, O.; Leyronnas, P.; van Zeist, W. -J.; Luppi, M. Amsterdam, The Netherlands <http://www.scm.com>, ADF-GUI, *Version 2008.01*.
- (116) Ugo Varetto, Swiss National Supercomputing Centre: Manno, Switzerland, MOLEKEL 4.0.
- (117) Gabrys, B.; Pusztai, L.; Pettifor, D. *J. Phys. Condens. Matter* **2007**, *19*, 335205-335215.
- (118) Cozzolino, A. F.; Gruhn, N. E.; Lichtenberger, D. L.; Vargas-Baca, I. *Inorg. Chem.* **2008**, *47*, 6220-6226.
- (119) McFarlane, H. C. E.; McFarlane, W. In *Selenium-77 and Tellurium-125*; Laszlo, P., Ed.; NMR of Newly Accessible Nuclei; Academic press, Inc.: New York, 1983; Vol. 2, p 275-299.
- (120) McFarlane, H. C. E.; McFarlane, W. *J. Chem. Soc. Dalton Trans.* **1973**, 2416-2418.
- (121) Schrobilgen, G. J.; Burns, R. C.; Granger, P. *J. Chem. Soc. Chem. Commun.* **1978**, *21*, 957-960.

- (122) Iwaoka, M.; Katsuda, T.; Tomoda, S.; Harada, J.; Ogawa, K. *Chem. Lett.* **2002**, 518-519.
- (123) Mugesh, G.; Panda, A.; Kumar, S.; Apte, S.; Singh, H.; Butcher, R. *Organometallics* **2002**, *21*, 884-892.
- (124) Mugesh, G.; Panda, A.; Singh, H.; Butcher, R. *Chem.–Eur. J.* **1999**, *5*, 1411-1421.
- (125) Panda, A.; Mugesh, G.; Singh, H.; Butcher, R. *Organometallics* **1999**, *18*, 1986-1993.
- (126) Ludlow, S.; McCarthy, A. E. *J. Organomet. Chem.* **1981**, *219*, 169-176.
- (127) Kumar, S. K.; Singh, H. B.; Das, K.; Sinha, U. C. *J. Organomet. Chem.* **1990**, *397*, 161-167.
- (128) Aso, Y.; Yui, K.; Miyoshi, T.; Otsubo, T.; Ogura, F.; Tanaka, J. *Bull. Chem. Soc. Jpn.* **1988**, *61*, 2013-2018.
- (129) Bhasin, K. K.; Arora, V.; Klapötke, T. M.; Crawford, M. -J. *Eur. J. Inorg. Chem.* **2004**, 4781-4788.
- (130) Edelmann, A.; Brooker, S.; Bertel, N.; Noltemyer, M.; Roesky, H. W.; Sheldrick, G. M.; Edelmann, F. T. *Z. Naturforsch., B: Chem. Sci.* **1992**, *47*, 305-309.
- (131) Tripathi, S. K.; Patel, U.; Roy, D.; Sunoj, R. B.; Singh, H. B.; Wolmershauser, G.; Butcher, R. J. *J. Org. Chem.* **2005**, *70*, 9237-9247.
- (132) Schulz Lang, E.; Burrow, R. A.; Silveira, E. T. *Acta Crystallogr. Sect. C.: Cryst. Struct. Commun.* **2002**, *58*, o397-o398.

- (133) Zingaro, R. A.; Herrera, C.; Meyers, E. A. *J. Organomet. Chem.* **1986**, *306*, C36-C40.
- (134) Jones, P. G.; Jeske, J. *Private Communication* **2004**.
- (135) Drago, R. In *Physical Methods for Chemists, 2nd Ed.* Surfside Scientific: Gainesville, 1992.
- (136) Schreckenbach, G.; Ziegler, T. *Theor. Chem. Acc.* **1998**, *99*, 71-82.
- (137) Sterzel, M.; Autschbach, J. *Inorg. Chem.* **2006**, *45*, 3316-3324.
- (138) Sutter, K.; Truflandier, L. A.; Autschbach, J. *ChemPhysChem* **2011**, *12*, 1448-1455.
- (139) Truflandier, L. A.; Sutter, K.; Autschbach, J. *Inorg. Chem.* **2011**, *50*, 1723-1732.
- (140) Lindman, B.; Forsén, S. In *The Halogens-Chlorine, Bromine and Iodine*; Harris, R. K., Mann, B. E., Eds.; NMR and the Periodic Table; Academic Press, Inc.: New York, 1978; p 421-438.
- (141) Kruse, F. H.; Marsh, R. E.; McCollough, J. D. *Acta Crystallogr.* **1957**, *10*, 201-209.
- (142) Kandasamy, K.; Kumar, S.; Singh, H. B.; Wolmershauser, G. *Organometallics* **2003**, *22*, 5069-5078.
- (143) Fronczek, F. R.; Junk, T. *Private Communication* **1996**.
- (144) Tötsch, W.; Peringer, P.; Sladky, F. *J. Chem. Soc. Chem. Commun.* **1981**, *16*, 841-842.

- (145) Granger, P.; Chapelle, S.; McWhinnie, W. R.; Al-Rubaie, A. *J. Organomet. Chem.* **1981**, *220*, 149-158.
- (146) Klapötke, T. M.; Krumm, B.; Nöth, H.; Gálvez-Ruiz, J. C.; Polborn, K.; Schwab, I.; Suter, M. *Inorg. Chem.* **2005**, *44*, 5254-5265.
- (147) Llabres, G.; Dideberg, O.; Dupont, L. *Acta Crystallogr. B.: Struct. Sci.* **1972**, *28*, 2438-2444.
- (148) Spirlet, M.; van den Bossche, G.; Dideberg, O.; Dupont, L. *Acta Crystallogr. B.: Struct. Sci.* **1979**, *B35*, 1727-1729.
- (149) Fleischer, H.; Mitzel, N. W.; Schollmeyer, D. *Eur. J. Inorg. Chem.* **2003**, 815.
- (150) Kern, C. W.; Lipscome, W. N. *J. Chem. Phys.* **1962**, *37*, 260-266.
- (151) Reid, R. V. *Phys. Rev. A* **1975**, *11*, 403-408.
- (152) O'Reilly, D. E. *Progress in NMR spectroscopy* **1967**, *2*, 1-61.
- (153) Facelli, J. C. *Concepts Magn. Reson. A* **2004**, *20A*, 42-69.
- (154) Smith, G. W. In *Appendix C: Compilation of Volume Diamagnetic Susceptibilities of Organic Compounds*; Emsley, J. W., Feeney, J. and Sutcliffe, L. H., Eds.; *High Resolution Nuclear Magnetic Resonance Spectroscopy*; Pergamon Press, Ltd.: Toronto, 1967; Vol. 1, p 605-623.
- (155) Guillaume, I. *Compt. Rend. Congr. Soc. Savantes Paris Dept., Sect. Sci.* **1962**, *87*, 469-475.
- (156) Kennedy, M. B.; Lister, M. W.; Marson, R.; Poyntz, R. B. *Can. J. Chem.* **1973**, *51*, 674-679.

- (157) Kalabin, G. A.; Valeev, R. B.; Kushnarev, D. F. *Zh. Org. Khim.* **1981**, *17*, 947-953.
- (158) Taft, R. W.; Kamlet, M. J. *Inorg. Chem.* **1983**, *22*, 250-254.
- (159) de Jeu, W. H. *Mol. Phys.* **1970**, *18*, 31-37.
- (160) Drago, R. S.; Meek, D. W.; Longhi, R.; Joesten, M. *Inorg. Chem.* **1963**, *2*, 1056-1060.
- (161) Keefer, R. M.; Andrews, L. J. *J. Am. Chem. Soc.* **1955**, *77*, 2164-2168.
- (162) Yada, H.; Tanaka, J.; Nagakura, S. *Bull. Chem. Soc. Jpn.* **1960**, *33*, 1660-1667.
- (163) Middaugh, R. L.; Drago, R. S.; Niedzielski, R. J. *J. Am. Chem. Soc.* **1964**, *86*, 388-392.
- (164) Foster, R. In *Organic Charge Transfer Complexes*; Academic Press: London, 1969.
- (165) Kusakawa, H.; Nishizaki, S. *Bull. Chem. Soc. Jpn.* **1965**, *38*, 313-315.
- (166) Karaghiosoff, K.; Klapötke, T. M.; Krumm, B.; Ruscitti, O. P. *J. Organomet. Chem.* **1999**, *577*, 69-75.
- (167) O'Brien, D. H.; Dereu, N.; Huang, C. -K.; Irgolic, K. J. *Organometallics* **1983**, *2*, 305-307.
- (168) Chadha, R. K.; Miller, J. M. *Can. J. Chem.* **1982**, *60*, 2256-2258.
- (169) Sharma, M.; Bhasin, K. K.; Mehta, S. K.; Singh, N.; Kumar, S. *Radiat. Phys. Chem.* **2006**, *75*, 2029-2038.
- (170) Mehdi, R. T.; Miller, J. D.; Tahir, T. A. *Inorg. Chim. Acta* **1984**, *90*, 85-89.

- (171) Srivastava, K.; Sharma, S.; Singh, H. B.; Singh, U. P. *Chem. Commun.* **2010**, *46*, 1130-1132.
- (172) Granger, P.; Chapelle, S. *J. Magn. Reson.* **1980**, *39*, 329-334.
- (173) Kido, K. *Rept. Yokohama Tech. Coll. Jpn.* **1934**, *2*, 233.
- (174) Bain, G. A.; Berry, J. F. *J. Chem. Ed.* **2008**, *85*, 532-536.
- (175) Harris, R. K.; Becker, E. D.; Cabral de Menezes, S. M.; Granger, P.; Hoffman, R. E.; Zilm, K. W. *Magn. Reson. Chem.* **2008**, *46*, 582-598.
- (176) Harris, R. K.; Becker, E. D.; Cabral de Menezes, S. M.; Goodfellow, R.; Granger, P. *Pure Appl. Chem.* **2001**, *73*, 1795-1818.
- (177) Milov, A. A.; Minyaev, R. M.; Minkin, V. I. *J. Phys. Chem. A* **2011**, *115*, 12973-12982.
- (178) Singh, H. B.; Sudha, N. *J. Organomet. Chem.* **1990**, *397*, 161-167.
- (179) Piette, J. -L.; Thibaut, P.; Renson, M. *Tetrahedron* **1978**, *34*, 655-669.
- (180) Gysling, H. J.; Luss, H. R. *Organometallics* **1984**, *3*, 596-598.
- (181) Wiriyaichitra, P.; Falcone, S. J.; Cava, M. P. *J. Org. Chem.* **1979**, *44*, 3957-3959.
- (182) Fujita, K.; Murata, K.; Iwaoka, M.; Tomoda, S. *Tetrahedron* **1997**, *53*, 2029-2048.
- (183) Beckmann, J.; Hesse, M.; Poleschner, H.; Seppelt, K. *Angew. Chem., Int. Ed. Engl.* **2007**, *46*, 8277-8280.
- (184) Beckmann, J.; Heitz, S.; Hesse, M. *Inorg. Chem.* **2007**, *46*, 3275-3282.

- (185) Kumar, S.; Singh, H. B.; Wolmerhauser, G. *J. Organomet. Chem.* **2005**, *690*, 3149-3153.
- (186) Mugesh, G.; Panda, A.; Singh, H. B. *Proc. Indian Acad. Sci. (Chem. Sci. )* **2000**, *112*, 239-248.
- (187) Engman, L.; Wojton, A.; Oleksyn, B. J.; Sliwinski, J. *Phosphorus, Sulfur Silicon Relat. Elem.* **2004**, *179*, 285-292.
- (188) Savant, G. J.; Jansson, T. P. U.S. Patent 1995/5384221, 1995.
- (189) Sawatari, N.; Okabe, M. U.S. Patent 2006/0083868, 2006.
- (190) Li, Z.; Wu, W.; Li, Q.; Gui, Y.; Xiao, L.; Liu, Y.; Ye, C.; Qin, J.; Li, Z. *Angew. Chem, Int. Ed.* **2010**, *49*, 2763-2767.
- (191) Garcia-Amorós, J.; Finkelmann, H.; Velasco, D. *Chem.– Eur. J.* **2011**, *17*, 6518-6523.
- (192) Chen, A. G.; Brady, D. J. *Appl. Phys. Lett.* **1993**, *62*, 2920.-2922
- (193) Lee, M.; Katz, H. E.; Erben, C.; Gill, D. M.; Gopalan, P.; Heber, J. D.; McGee, D. *J. Science* **2002**, *298*, 1401-1403.
- (194) Gopalan, P.; Katz, H. E.; McGee, D. J.; Erben, C.; Zielinski, T.; Bousquet, D.; Muller, D.; Grazul, J.; Olsson, V. *J. Am. Chem. Soc.* **2004**, *126*, 1741-1747.
- (195) Raposo, M. M. M.; Castro, M. C. R.; Fonseca, A. M. C.; Schellenberg, P.; Belsley, M. *Tetrahedron* **2011**, *67*, 5189-5198.
- (196) Srivastava, K.; Chakraborty, T.; Singh, H. B.; Butcher, R. J. *Dalton Trans.* **2011**, *40*, 4489-4496.

- (197) Cobbleddick, R. E.; Einstein, F. W. B.; McWhinnie, W. R.; Musa, F. H. *J. Chem. Research (M)* **1979**, 1901-1934.
- (198) Majeed, Z.; McWhinnie, W. R.; Hamor, T. A. *J. Organomet. Chem.* **1997**, *549*, 257-262.
- (199) Coates, G. E. In *Organometallic Compounds*; Wiley: London, 1960, p 72-87.
- (200) Tschinkl, M.; Schier, A.; Riede, J.; Gabbai, F. P. *Organometallics* **1999**, *18*, 2040-2042.
- (201) Tschinkl, M.; Gabbai, F. P. *J. Chem. Crystallogr.* **2003**, *33*, 595-598.
- (202) Taylor, T.; Elbjeirami, O.; Burress, C.; Tsunoda, M.; Bodine, M.; Omary, M.; Gabbai, F. P. *J. Inorg. Organomet. Polym.* **2008**, *18*, 175-179.
- (203) Haneline, M. R.; Gabbai, F. P. *Angew. Chem., Int. Ed.* **2004**, *43*, 5471-5474.
- (204) Yakovenko, A. A.; Gallegos, J. H.; Antipin, M. Y.; Masunov, A.; Timofeeva, T. V. *Cryst. Growth Des.* **2011**, *11*, 3964-3978.
- (205) Taylor, T. J.; Burress, C. N.; Pandey, L.; Gabbai, F. P. *Dalton Trans.* **2006**, 4654-4656.
- (206) Taylor, T. J.; Burress, C. N.; Gabbai, F. P. *Organometallics* **2007**, *26*, 5252-5263.
- (207) Dorsey, C. L.; Jewula, P.; Hudnall, T. W.; Hoefelmeyer, J. D.; Taylor, T. J.; Honesty, N. R.; Chiu, C. -.W.; Schulte, M.; Gabbai, F. P. *Dalton Trans.* **2008**, 4442-4450.
- (208) Kobe, K. A.; Doumani, T. F. *Industrial & Engineering Chemistry* **1941**, *33*, 170-176.

- (209) Ogata, Y.; Tsuchida, M. *J. Org. Chem.* **1955**, *20*, 1637-1643.
- (210) Ogata, Y.; Tsuchida, M. *J. Org. Chem.* **1955**, *20*, 1644-1649.
- (211) Brown, H. C.; McGary, C. W. *J. Am. Chem. Soc.* **1955**, *77*, 2300-2306.
- (212) Olah, G. A.; Hashimoto, I.; Lin, H. C. *Proc. Natl. Acad. Sci. U. S. A.* **1977**, *74*, 4121-4125.
- (213) Brown, H. C.; McGary, C. W. *J. Am. Chem. Soc.* **1955**, *77*, 2310-2312.
- (214) Roling, P. V.; Kirt, D. D.; Dill, J. L.; Hall, S.; Hollstrom, C. *J. Organomet. Chem.* **1976**, *116*, 39-53.
- (215) Roling, P. V.; Pickering, R. A. *J. Organomet. Chem.* **1976**, *122*, 289-293.
- (216) Komeyama, M.; Yamamoto, S.; Nishimura, N.; Hasegawa, S. *Bull. Chem. Soc. Jpn.* **1973**, 26062607.
- (217) Harada, J.; Ogawa, K. *J. Am. Chem. Soc.* **2004**, *126*, 3539-3544.
- (218) You, X. -L.; Zhang, Y.; Zhang, Y.; Zhang, D. -C. *Acta Crystallogr. Sect. E.: Struct. Rep. Online* **2005**, *61*, o2656-o2658.
- (219) Woode, K. A.; Bart, J. C. J.; Calcaterra, M. *Dyes Pigm.* **1981**, *2*, 271-278.
- (220) He, L.; El-Shafei, A.; Freeman, H. S.; Boyle, P. *Dyes Pigm.* **2009**, *82*, 299-306.
- (221) Gong, L.; Lu, L. *Acta Crystallogr. Sect. E.: Struct. Rep. Online* **2011**, *67*, o662.
- (222) Glowka, M. L.; Olubek, Z. *Acta Crystallogr. C.: Cryst. Struct. Commun.* **1994**, *50*, 458-460.

- (223) Yang, W.; Parr, R. G.; Pucci, R. *J. Chem. Phys.* **1984**, *81*, 2862-2863.
- (224) Parr, R. G.; Yang, W. *J. Am Chem. Soc.* **1984**, *106*, 4049-4050.
- (225) Kolboe, S.; Svelle, S.; Arstad, B. *J. Phys. Chem. A.* **2009**, *113*, 917-923.
- (226) Kolboe, S. *J. Phys. Chem. A.* **2011**, *115*, 3106-3115.
- (227) Kudavalli, J. S.; Boyd, D. R.; Coyne, D.; Keeffe, J. R.; Lawlor, D. A.; MacCormac, A. C.; O'Ferrall, R. A. M.; Rao, S. N.; Sharma, N. D. *Org. Lett.* **2010**, *12*, 5550-5553.
- (228) Sadekov, I. D.; Minkin, V. I.; Zakharov, A. V.; Starikov, A. G.; Borodkin, G. S.; Aldoshin, S. M.; Tkachev, V. V.; Shilov, G. V.; Berry, F. J. *J. Organomet. Chem.* **2005**, *690*, 103-116.
- (229) Sadekov, I. D.; Maksimenko, A. A.; Maslakov, A. G.; Minkin, V. I. *J. Organomet. Chem.* **1990**, *391*, 179-188.
- (230) Hamor, T. A.; Chen, H.; McWhinnie, W. R.; McWhinnie, S. L. W.; Majeed, Z. *J. Organomet. Chem.* **1996**, *523*, 53-61.
- (231) Jones, P. G.; Ramirez de Arellano, M. C. *Chem. Ber.* **1995**, *128*, 741-742.
- (232) Al-Rubaie, A. Z.; Al-Fregi, A. A.; Al-Jadaan, S. A. S. *Phosphorus, Sulfur Silicon Relat. Elem.* **2011**, *186*, 115-124.
- (233) Cobblestick, R. E.; Einstein, F. W. B.; McWhinnie, W. R.; Musa, F. H. *J. Chem. Research (M)* **1979**, 1901-1934.
- (234) Davis, C. C. In *Lasers and Electro-Optics - Fundamentals and Engineering*; Cambridge University Press: New York, 1996, p 720.

- (235) Marder, S.; Kippelen, B.; Jen, A.; Peyghambarian, N. *Nature* **1997**, 388, 845-851.
- (236) Verbiest, T.; Houbrechts, S.; Kauranen, M.; Clays, K.; Persoons, A. *J. Mater. Chem.* **1997**, 7, 2175-2189.
- (237) Kamada, K.; Ueda, M.; Sakaguchi, T.; Ohta, K.; Fukima, T. *Chem. Phys. Lett.* **1996**, 263, 215-222.
- (238) Blenkle, M.; Boldt, P.; Bräuchle, C.; Grahn, W.; Ledoux, I.; Nerenz, H.; Stadler, S.; Wichern, J.; Zyss, J. *J. Chem. Soc. Perkin Trans.* **1996**, 2, 1377-1384.
- (239) Suzuki, H.; Nakamura, T.; Sakaguchi, T.; Ohta, K. *J. Org. Chem.* **1995**, 60, 5274-5280.
- (240) Parker, K. D. J. *Nonlinear Optical Chromophores with Heavy Chalcogen Atoms*, Undergraduate Senior Thesis, McMaster University, 2006.
- (241) Chapman, A. E. A. *Summer research project*, **2003**.
- (242) Clays, K. *Phys. Rev. Lett.* **1991**, 66, 2980-2983.
- (243) Moylan, C. R.; Twieg, R. J.; Lee, V. Y.; Swanson, S. A.; Betterton, K. M.; Miller, R. D. *J. Am. Chem. Soc.* **1993**, 115, 12599-12600.
- (244) Ulman, A.; Willand, C. S.; Kohler, W.; Robello, D. R.; Williams, D. J.; Handley, L. *J. Am. Chem. Soc.* **1990**, 112, 7083-7090.
- (245) Singer, K. D.; Sohn, J. E.; King, L. A.; Gordon, H. M.; Katz, H. E.; Dirk, C. W. *J. Opt. Soc. Am. B.* **1989**, 6, 1339-1350.
- (246) Adams, H.; Allen, R. W. K.; Chin, J.; O'Sullivan, B.; Styring, P.; Sutton, L. R. *Acta Crystallogr. Sect. E.: Struct. Rep. Online* **2004**, 60, o289-o290.

- (247) Centore, R.; Tuzi, A. *Cryst. Eng.* **2003**, *6*, 87-97.
- (248) Yousefi, M.; Hosseini, H.; Amani, V.; Chamjangali, M. A.; Khavasi, H. R. *Acta Crystallogr., Sect. E: Struct. Rep. Online* **2008**, *64*, o789.
- (249) Merino, G.; Heine, T.; Seifert, G. *Chem.–Eur. J.* **2004**, *10*, 4367-4371.
- (250) Lazzeretti, P. *Phys. Chem. Chem. Phys.* **2004**, *6*, 217-223.
- (251) Garratt, P. J. In *Aromaticity*; Wiley: New York, 1986.
- (252) Krygowski, T. M.; Cyrański, M. *Tetrahedron* **1996**, *52*, 1713-1722.
- (253) Hehre, W. J.; McIver, R. T.; Pople, J. A.; von Ragué Schleyer, P. *J. Am. Chem. Soc.* **1974**, *96*, 7162-7163.
- (254) Dauben, H. J.; Wilson, J. D.; Laity, J. I. *J. Am. Chem. Soc.* **1968**, *90*, 811-813.
- (255) von Ragué Schleyer, P.; Maerker, C.; Dransfield, A.; Jiao, H.; van Eikema Hommes, N. J. R. *J. Am. Chem. Soc.* **1996**, *118*, 6317-6318.
- (256) Maslakov, A. G.; McWhinnie, W. R.; Perry, M. C.; Shaikh, N.; McWhinnie, S. L. W.; Hamor, T. A. *J. Chem. Soc. Dalton Trans.* **1993**, 619-624.
- (257) Kübel, J. *Experimental and Computational Studies of Te-N-C heterocycles as Supramolecular Building Blocks*, Undergraduate Senior Thesis, McMaster University, 2010.
- (258) Shimada, K.; Moro-oka, A.; Maruyama, A.; Fujisawa, H.; Saito, T.; Kawamura, R.; Kogawa, H.; Sakuraba, M.; Takata, Y.; Aoyagi, S.; Takikawa, Y.; Kabuto, C. *Bull. Chem. Soc. Jpn.* **2007**, *80*, 567-577.

- (259) Brown, H. C.; Racherla, U. S.; Singh, S. M. *Tetrahedron Lett.* **1984**, 25, 2411-2414.
- (260) Werz, D. B.; Gleiter, R.; Rominger, F. *Organometallics* **2003**, 22, 843-849.
- (261) Minoura, M.; Mukuda, T.; Sagami, T.; Akiba, K. *J. Am. Chem. Soc.* **1999**, 121, 10852-10853.
- (262) Allan, R. E.; Gornitzka, H.; Kaercher, J.; Paver, M. A.; Rennie, M.; Russell, C. A.; Raithby, P. R.; Stalke, D.; Steiner, A.; Wright, D. S. *J. Chem. Soc. Dalton Trans.* **1996**, 1727-1730.
- (263) Kübel, J.; Elder, P. J. W.; Jenkins, H. A.; Vargas-Baca, I. *Dalton Trans.* **2010**, 39, 11126-11128.
- (264) Chivers, T.; Gao, X.; Parvez, M. *J. Am. Chem. Soc.* **1995**, 117, 2359-2360.
- (265) Chiang, J. F. *J. Chem. Phys.* **1974**, 61, 1280-1284.
- (266) Politzer, P.; Murray, J. S. In *Structural Analysis of Hydroxylamines, Oximes and Hydroxamic Acids: Trends and Patterns*; Rappoport, Z., Liebman, J. F., Eds.; The Chemistry of Hydroxylamines, Oximes and Hydroxamic Acids; Wiley: 2009.
- (267) Thomas, P. A. *J. Phys. C: Solid State Phys.* **1988**, 21, 4611-4627.
- (268) Schatte, G.; Chivers, T.; Tuononen, H. M.; Suontamo, R.; Laitinen, R.; Valkonen, J. *Inorg. Chem.* **2005**, 44, 443-451.
- (269) Oba, M.; Okada, Y.; Nishiyama, K.; Shimada, S.; Ando, W. *Chem. Commun.* **2008**, 42, 5378-5380.
- (270) Konaka, S.; Ozawa, Y.; Yagasaki, A. *Inorg. Chem.* **2008**, 47, 1244-1245.

- (271) Klapötke, T. M.; Krumm, B.; Scherr, M. *Phosphorus, Sulfur Silicon Relat. Elem.* **2009**, *184*, 1347-1354.
- (272) Duddeck, H.; Biallaß, A. *Mag. Reson. Chem.* **1994**, *32*, 303-311.
- (273) Falcone, S. J.; Cava, M. P. *J. Org. Chem.* **1980**, *45*, 1044-1045.
- (274) Hammerl, A.; Klapötke, T. M.; Krumm, B.; Scherr, M. *Z. Anorg. Allg. Chem.* **2007**, *633*, 1618-1626.
- (275) Morris, K. F.; Johnson, C. S. *J. Am. Chem. Soc.* **1993**, *115*, 4291-4299.
- (276) Morris, K. F.; Johnson, C. S. *J. Am. Chem. Soc.* **1992**, *114*, 3139-3141.
- (277) Morris, K. F.; Stilbs, P.; Johnson, C. S. *Anal. Chem.* **1994**, *66*, 211-215.